

## **NOTICE**

The quality of this microform is heavily dependent upon the quality of the original thesis submitted for microfilming. Every effort has been made to ensure the highest quality of reproduction possible.

If pages are missing, contact the university which granted the degree.

Some pages may have indistinct print especially if the original pages were typed with a poor typewriter ribbon or if the university sent us an inferior photocopy.

Reproduction in full or in part of this microform is governed by the Canadian Copyright Act, R.S.C. 1970, c. C-30, and subsequent amendments.

## **AVIS**

La qualité de cette microforme dépend grandement de la qualité de la thèse soumise au microfilmage. Nous avons tout fait pour assurer une qualité supérieure de reproduction.

S'il manque des pages, veuillez communiquer avec l'université qui a conféré le grade.

La qualité d'impression de certaines pages peut laisser à désirer, surtout si les pages originales ont été dactylographiées à l'aide d'un ruban usé ou si l'université nous a fait parvenir une photocopie de qualité inférieure.

La reproduction, même partielle, de cette microforme est soumise à la Loi canadienne sur le droit d'auteur, SRC 1970, c. C-30, et ses amendements subséquents.

**Canada**

THE UNIVERSITY OF ALBERTA

IMAGING OF REFLECTION SEISMIC AND RADAR WAVEFIELDS:  
MONITORING OF STEAM-HEATED OIL RESERVOIRS AND  
CHARACTERIZATION OF NUCLEAR WASTE REPOSITORIES

by

FOTIOS KALANTZIS



A THESIS

SUBMITTED TO THE FACULTY OF GRADUATE STUDIES AND RESEARCH  
IN PARTIAL FULFILLMENT OF THE REQUIREMENTS FOR THE DEGREE  
OF DOCTOR OF PHILOSOPHY  
IN  
GEOPHYSICS

DEPARTMENT OF PHYSICS

EDMONTON, ALBERTA

Fall 1994



National Library  
of Canada

Acquisitions and  
Bibliographic Services Branch

395 Wellington Street  
Ottawa, Ontario  
K1A 0N4

Bibliothèque nationale  
du Canada

Direction des acquisitions et  
des services bibliographiques

395, rue Wellington  
Ottawa (Ontario)  
K1A 0N4

*Votre titre - Votre référence*

*Notre titre - Notre référence*

**The author has granted an irrevocable non-exclusive licence allowing the National Library of Canada to reproduce, loan, distribute or sell copies of his/her thesis by any means and in any form or format, making this thesis available to interested persons.**

**L'auteur a accordé une licence irrévocable et non exclusive permettant à la Bibliothèque nationale du Canada de reproduire, prêter, distribuer ou vendre des copies de sa thèse de quelque manière et sous quelque forme que ce soit pour mettre des exemplaires de cette thèse à la disposition des personnes intéressées.**

**The author retains ownership of the copyright in his/her thesis. Neither the thesis nor substantial extracts from it may be printed or otherwise reproduced without his/her permission.**

**L'auteur conserve la propriété du droit d'auteur qui protège sa thèse. Ni la thèse ni des extraits substantiels de celle-ci ne doivent être imprimés ou autrement reproduits sans son autorisation.**

ISBN 0-315-95204-0

**Canada**

Name FOTIOS KALANTZIS

Dissertation Abstracts International is arranged by broad, general subject categories. Please select the one subject which most nearly describes the content of your dissertation. Enter the corresponding four-digit code in the spaces provided.

**0373 U.M.I.**

SUBJECT TERM

SUBJECT CODE

**Subject Categories**

**THE HUMANITIES AND SOCIAL SCIENCES**

**COMMUNICATIONS AND THE ARTS**  
 Architecture ..... 0729  
 Art History ..... 0377  
 Cinema ..... 0900  
 Dance ..... 0378  
 Fine Arts ..... 0357  
 Information Science ..... 0723  
 Journalism ..... 0391  
 Library Science ..... 0399  
 Mass Communications ..... 0708  
 Music ..... 0413  
 Speech Communication ..... 0459  
 Theater ..... 0465

**EDUCATION**  
 General ..... 0515  
 Administration ..... 0514  
 Adult and Continuing ..... 0516  
 Agricultural ..... 0517  
 Art ..... 0273  
 Bilingual and Multicultural ..... 0282  
 Business ..... 0688  
 Community College ..... 0275  
 Curriculum and Instruction ..... 0727  
 Early Childhood ..... 0518  
 Elementary ..... 0524  
 Finance ..... 0277  
 Guidance and Counseling ..... 0519  
 Health ..... 0680  
 Higher ..... 0745  
 History of ..... 0520  
 Home Economics ..... 0278  
 Industrial ..... 0521  
 Language and Literature ..... 0279  
 Mathematics ..... 0280  
 Music ..... 0522  
 Philosophy of ..... 0998  
 Physical ..... 0523

Psychology ..... 0525  
 Reading ..... 0535  
 Religious ..... 0527  
 Sciences ..... 0714  
 Secondary ..... 0533  
 Social Sciences ..... 0534  
 Sociology of ..... 0340  
 Special ..... 0529  
 Teacher Training ..... 0530  
 Technology ..... 0710  
 Tests and Measurements ..... 0288  
 Vocational ..... 0747

**LANGUAGE, LITERATURE AND LINGUISTICS**

Language  
 General ..... 0679  
 Ancient ..... 0289  
 Linguistics ..... 0290  
 Modern ..... 0291

Literature  
 General ..... 0401  
 Classical ..... 0294  
 Comparative ..... 0295  
 Medieval ..... 0297  
 Modern ..... 0298  
 African ..... 0316  
 American ..... 0591  
 Asian ..... 0305  
 Canadian (English) ..... 0352  
 Canadian (French) ..... 0355  
 English ..... 0593  
 Germanic ..... 0311  
 Latin American ..... 0312  
 Middle Eastern ..... 0315  
 Romance ..... 0313  
 Slavic and East European ..... 0314

**PHILOSOPHY, RELIGION AND THEOLOGY**

Philosophy ..... 0422  
 Religion  
 General ..... 0318  
 Biblical Studies ..... 0321  
 Clergy ..... 0319  
 History of ..... 0320  
 Philosophy of ..... 0322  
 Theology ..... 0469

**SOCIAL SCIENCES**

American Studies ..... 0323  
 Anthropology  
 Archaeology ..... 0324  
 Cultural ..... 0326  
 Physical ..... 0327

Business Administration  
 General ..... 0310  
 Accounting ..... 0272  
 Banking ..... 0770  
 Management ..... 0454  
 Marketing ..... 0338  
 Canadian Studies ..... 0385

Economics  
 General ..... 0501  
 Agricultural ..... 0503  
 Commerce-Business ..... 0505  
 Finance ..... 0508  
 History ..... 0509  
 Labor ..... 0510  
 Theory ..... 0511  
 Folklore ..... 0358  
 Geography ..... 0366  
 Gerontology ..... 0351  
 History  
 General ..... 0578

Ancient ..... 0579  
 Medieval ..... 0581  
 Modern ..... 0582  
 Black ..... 0328  
 African ..... 0331  
 Asia, Australia and Oceania ..... 0332  
 Canadian ..... 0334  
 European ..... 0335  
 Latin American ..... 0336  
 Middle Eastern ..... 0333  
 United States ..... 0337  
 History of Science ..... 0585  
 Law ..... 0398  
 Political Science  
 General ..... 0615  
 International Law and Relations ..... 0616  
 Public Administration ..... 0617  
 Recreation ..... 0814  
 Social Work ..... 0452  
 Sociology  
 General ..... 0626  
 Criminology and Penology ..... 0627  
 Demography ..... 0938  
 Ethnic and Racial Studies ..... 0631  
 Individual and Family Studies ..... 0628  
 Industrial and Labor Relations ..... 0629  
 Public and Social Welfare ..... 0630  
 Social Structure and Development ..... 0700  
 Theory and Methods ..... 0344  
 Transportation ..... 0709  
 Urban and Regional Planning ..... 0999  
 Women's Studies ..... 0453

**THE SCIENCES AND ENGINEERING**

**BIOLOGICAL SCIENCES**

Agriculture  
 General ..... 0473  
 Agronomy ..... 0285  
 Animal Culture and Nutrition ..... 0475  
 Animal Pathology ..... 0476  
 Food Science and Technology ..... 0359  
 Forestry and Wildlife ..... 0478  
 Plant Culture ..... 0479  
 Plant Pathology ..... 0480  
 Plant Physiology ..... 0817  
 Range Management ..... 0777  
 Wood Technology ..... 0746

Biology  
 General ..... 0306  
 Anatomy ..... 0287  
 Biostatistics ..... 0308  
 Botany ..... 0309  
 Cell ..... 0379  
 Ecology ..... 0329  
 Entomology ..... 0353  
 Genetics ..... 0369  
 Limnology ..... 0793  
 Microbiology ..... 0410  
 Molecular ..... 0307  
 Neuroscience ..... 0317  
 Oceanography ..... 0416  
 Physiology ..... 0433  
 Radiation ..... 0821  
 Veterinary Science ..... 0778  
 Zoology ..... 0472

Biophysics  
 General ..... 0786  
 Medical ..... 0760

**EARTH SCIENCES**  
 Biogeochemistry ..... 0425  
 Geochemistry ..... 0996

Geodesy ..... 0370  
 Geology ..... 0372  
 Geophysics ..... 0373  
 Hydrology ..... 0388  
 Mineralogy ..... 0411  
 Paleobotany ..... 0345  
 Paleocology ..... 0426  
 Paleontology ..... 0418  
 Paleozoology ..... 0985  
 Palynology ..... 0427  
 Physical Geography ..... 0368  
 Physical Oceanography ..... 0415

**HEALTH AND ENVIRONMENTAL SCIENCES**

Environmental Sciences ..... 0768  
 Health Sciences  
 General ..... 0566  
 Audiology ..... 0300  
 Chemotherapy ..... 0992  
 Dentistry ..... 0567  
 Education ..... 0350  
 Hospital Management ..... 0769  
 Human Development ..... 0758  
 Immunology ..... 0982  
 Medicine and Surgery ..... 0564  
 Mental Health ..... 0347  
 Nursing ..... 0569  
 Nutrition ..... 0570  
 Obstetrics and Gynecology ..... 0380  
 Occupational Health and Therapy ..... 0354  
 Ophthalmology ..... 0381  
 Pathology ..... 0571  
 Pharmacology ..... 0419  
 Pharmacy ..... 0572  
 Physical Therapy ..... 0382  
 Public Health ..... 0573  
 Radiology ..... 0574  
 Recreation ..... 0575

Speech Pathology ..... 0460  
 Toxicology ..... 0383  
 Home Economics ..... 0386

**PHYSICAL SCIENCES**

**Pure Sciences**  
 Chemistry  
 General ..... 0485  
 Agricultural ..... 0749  
 Analytical ..... 0486  
 Biochemistry ..... 0487  
 Inorganic ..... 0488  
 Nuclear ..... 0738  
 Organic ..... 0490  
 Pharmaceutical ..... 0491  
 Physical ..... 0494  
 Polymer ..... 0495  
 Radiation ..... 0754  
 Mathematics ..... 0405

Physics  
 General ..... 0605  
 Acoustics ..... 0986  
 Astronomy and Astrophysics ..... 0606  
 Atmospheric Science ..... 0608  
 Atomic ..... 0748  
 Electronics and Electricity ..... 0607  
 Elementary Particles and High Energy ..... 0798  
 Fluid and Plasma ..... 0759  
 Molecular ..... 0609  
 Nuclear ..... 0610  
 Optics ..... 0752  
 Radiation ..... 0756  
 Solid State ..... 0611  
 Statistics ..... 0463

**Applied Sciences**  
 Applied Mechanics ..... 0346  
 Computer Science ..... 0984

Engineering  
 General ..... 0537  
 Aerospace ..... 0538  
 Agricultural ..... 0539  
 Automotive ..... 0540  
 Biomedical ..... 0541  
 Chemical ..... 0542  
 Civil ..... 0543  
 Electronics and Electrical ..... 0544  
 Heat and Thermodynamics ..... 0348  
 Hydraulic ..... 0545  
 Industrial ..... 0546  
 Marine ..... 0547  
 Materials Science ..... 0794  
 Mechanical ..... 0548  
 Metallurgy ..... 0743  
 Mining ..... 0551  
 Nuclear ..... 0552  
 Packaging ..... 0549  
 Petroleum ..... 0765  
 Sanitary and Municipal ..... 0554  
 System Science ..... 0790  
 Geotechnology ..... 0428  
 Operations Research ..... 0796  
 Plastics Technology ..... 0795  
 Textile Technology ..... 0994

**PSYCHOLOGY**

General ..... 0621  
 Behavioral ..... 0384  
 Clinical ..... 0622  
 Developmental ..... 0620  
 Experimental ..... 0623  
 Industrial ..... 0624  
 Personality ..... 0625  
 Physiological ..... 0989  
 Psychological ..... 0349  
 Psychometrics ..... 0632  
 Social ..... 0451



THE UNIVERSITY OF ALBERTA

**RELEASE FORM**

NAME OF AUTHOR      Fotios Kalantzis  
TITLE OF THESIS      Imaging of Reflection Seismic and Radar Wavefields:  
                                 Monitoring of Steam Heated Oil Reservoirs and  
                                 Characterization of Nuclear Waste Repositories  
DEGREE FOR WHICH THESIS WAS PRESENTED      Doctor of Philosophy  
YEAR THIS DEGREE GRANTED                              Fall 1994

Permission is hereby granted to THE UNIVERSITY OF ALBERTA LIBRARY to reproduce single copies of this thesis and to lend or sell such copies for private, scholarly or scientific research purposes only. The author reserves other publication rights, and neither the thesis nor extensive extracts from it may be printed or otherwise reproduced without the author's written permission.

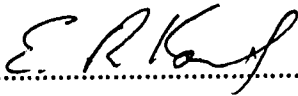
(SIGNED) ..... 

PERMANENT ADDRESS:  
124 Elmview Road  
Regina, Saskatchewan  
Canada S4R 0B3

DATED *Sept. 30*, 1994


THE UNIVERSITY OF ALBERTA  
FACULTY OF GRADUATE STUDIES AND RESEARCH

The undersigned certify that they have read, and recommend to the Faculty of Graduate Studies and Research, for acceptance, a thesis entitled IMAGING OF REFLECTION SEISMIC AND RADAR WAVEFIELDS: MONITORING OF STEAM-HEATED OIL RESERVOIRS AND CHARACTERIZATION OF NUCLEAR WASTE REPOSITORIES submitted by FOTIOS KALANTZIS in partial fulfillment of the requirements for the degree of DOCTOR OF PHILOSOPHY in GEOPHYSICS.

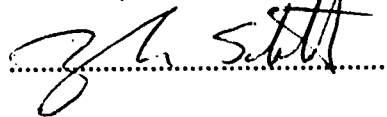
  
.....

Supervisor

E.R. Kanasewich (Geophysics)

  
.....

T.J.T. Spanos (Geophysics)

  
.....

D.R. Schmitt (Geophysics)

  
.....

R.F. Egerton (Physics)

  
.....

J.H. Masliyah (Chemical Engineering)

  
.....

External Examiner

L. R. Lines (Geophysics, Memorial Univ.)

Date Sept 23, 1994

Dedicated to

*Jo-Anna, Kristoforos and Nikolas*

I could not do this without your sacrifices

## ABSTRACT

In this research new and existing seismic modeling and migration methods were developed and modified, respectively, and were used in a number of different geophysical applications. Innovative utilization of recent advances in computing based on the vector computations and the subdivision of the computational sequence into parallel components led to the development of highly vectorized and parallel algorithms. The algorithms were vectorized using sophisticated techniques such as matrix multiplication by diagonals. Some of the algorithms were highly parallelized by utilizing the inherent parallelism that the seismic equations have in the frequency, space and partially in time domains. Their implementation on vector and parallel supercomputers resulted in pronounced CPU, parallelization and vectorization performance.

A new 3-D acoustic modeling method was developed using a first order hyperbolic wave system which was solved with explicit finite differences using the MacCormack splitting scheme. The numerical solution of the 3-D wave system provides a useful method for simulating the evolution of a pressure field which corresponds to the P or compressional type of body waves which is most frequently recorded. Also, existing 2-D elastic modeling algorithms were modified and fine-tuned for computationally efficient and realistic wave propagation simulations in complex structures.

2-D depth migration parallel algorithms in the frequency-space domain using implicit finite differences were developed. Furthermore, 3-D depth migration parallel algorithms were developed in the frequency-space domain that use a one-pass or alternative direction implicit (ADI) finite difference method.

An original formulation of the 3-D reverse time migration method was developed employing either a full or a one-way wave hyperbolic system that is solved with explicit finite differences using the MacCormack scheme. This method is very accurate, does not suffer from the unwanted evanescent energy, can image dips beyond 90 degrees and does not generate multiple energy.

Enormous reserves of bitumen or heavy oil are present in sands of Lower Cretaceous age in Alberta, Canada. Enhanced oil recovery (EOR) methods such as steam stimulation are used to reduce the viscosity of the bitumen and produce it by driving it into a production well. However, during the steaming process, the movement of fluids away from the heated sources at the perforation level is controlled by permeability heterogeneities and even small heterogeneities or anisotropy, caused from fracturing due to high pressure injected steam, can play an important factor in the efficiency of the EOR process. Therefore, it is important



to image the shape and areal extent of the steam-heated zone and determine the direction and rate of movement of the thermal front. Petrophysical alterations in the heavy oil reservoirs during steam stimulation are caused by pressure, temperature, the replacement of bitumen by steam or steam condensate, etc., contribute to velocity changes, attenuation and velocity dispersion of seismic waves in the effected reservoir.

Two case studies were performed that involve steam stimulation projects (Mobil Oil Canada and Imperial Oil of Canada) in the heavy oil sands of Cold Lake, Alberta. Seismic monitoring of the reservoir during the thermal process was performed by the oil companies with 3-D surface high resolution seismic surveys repeated over specified time intervals. Extensive 2-D elastic and 3-D acoustic wave propagation simulations were performed during different phases of the steam stimulation process in order to examine the relation between reservoir properties and conditions with seismic characteristics. Furthermore, an extensive seismic attribute analysis was performed on all 3-D seismic (base and monitors) before and after our own processing such as one-pass 3-D depth migration. This resulted in high resolution seismic attribute images such as amplitude anomalies, time and depth pushdowns, and velocity reduction that mapped the areal and vertical extent of the steam-heated zones (areal and vertical conformance), tracked the steam front and detected some fractures. Furthermore, the attribute anomalies were correlated to the areal location and pressure and temperatures states of the wells. A knowledge of the evolving reservoir properties and conditions in real time allows the possibility of controlling and modifying steam injection and production strategies. Thus, 3-D surface seismic monitoring has the potential of becoming a powerful tool for the efficient management of EOR projects.

Atomic Energy of Canada is investigating the suitability of plutonic rocks of the Canadian Shield as a repository medium for nuclear wastes. Ground-Penetrating radar (GPR) data were processed using seismic processing algorithms such as our own 2-D frequency-space depth migration algorithm. Our migration algorithm enabled us to detect and image fracture zones in the plutonic rock with a resolution never before achieved. Furthermore, this depth migration algorithm was applied on LITHOPROBE's Alberta Transect seismic data and succeed to image structures in the crust down to depths of 50 Km and the crust/mantle boundary (Moho) at about 40 Km depth.

## ACKNOWLEDGEMENTS

I am grateful to my supervisor Dr. E.R. Kanasevich for his guidance and encouragement throughout this work. I would like to thank Dr. A. Vafidis for invaluable assistance on 3-D modeling and reverse time migration and euphoria of discussions on many other geophysical topics. Dr. S. Kapotas and Dr. S. Phadke are greatly thanked for sharing their expertise on parallel computers. Dr. Kostyukevich and Dr. N. Dai are thanked for their assistance with the elastic modeling performed in this work. Dr. N. Udey is thanked for his assistance with the normalization of the seismic monitoring data. My colleagues, M. Burianyk and R. Lu are thanked for their help in many occasions and for creating a pleasant working environment. I would like to thank the staff of the Physics Department. I am also grateful to professors T. Spanos, D. Schmitt, R. Egerton, J. Masliyeh and L. Lines for their comprehensive and careful review of this work.

I would like to acknowledge Imperial Oil of Canada for providing the 3-D seismic monitoring data and financial assistance for this research. Dr J Eastwood of Imperial Oil is greatly thanked for his support and advise during the analysis of these data. Also, I wish to acknowledge Mobil Oil of Canada for providing 3-D seismic monitoring data and in particular, Mr. A. Siewert for his advise during the analysis of the data. Also, I am grateful Mr. P. Allen of Mobil Oil for enlightening discussions on many concepts of seismology during my summer jobs with Mobil. I wish to acknowledge Atomic Energy of Canada (AECL) and in particular, Dr. P. Lodha and Mr. K. Stevens for the GPR data and their assistance during the analysis of these data.

I am thankful to the Alberta Government for awarding me with the Province of Alberta Graduate Fellowship. I would like to thank the Society of Exploration Geophysicists (SEG) and the Canadian Society of Exploration Geophysicists (CSEG) for awarding me scholarships during my Ph.D. studies. I wish to acknowledge the Alberta Oil Sands Technology and Research Authority for providing financial support for this project.

I wish to acknowledge the Canadian Space Research Network of the University of Alberta for allowing to use their Myrias parallel computer. Also, I am thankful to the High Performance Computing Center in Calgary for awarding me a scholarship for free use of their Fujitsu supercomputer and in particular, Dr P. Masiar for his support and assistance.

I am grateful to my wife Jo-Anna and my sons Kristoforos and Nikolas for their understanding, enormous support and encouragement, and sacrifices during all these years. I promise that you will not have to go through similar stages again. I am also thankful to my parents and my parents-in-law for their support and encouragement.

# TABLE OF CONTENTS

CHAPTER	PAGE
<b>1. INTRODUCTION</b>	<b>1</b>
1.1 SEISMIC MODELING AND IMAGING	1
1.2 SEISMIC MONITORING OF OIL RESERVOIRS	4
1.3 RADAR IMAGING OF NUCLEAR WASTE REPOSITORIES	7
1.4 OUTLINE OF THE THESIS	8
<b>2. VECTOR AND PARALLEL COMPUTERS FOR SEISMIC DATA PROCESSING</b>	<b>10</b>
2.1 INTRODUCTION	10
2.2 VECTOR SUPERCOMPUTERS	10
2.3 PARALLEL COMPUTERS	13
2.3.1 Parallel Computer Architectures	13
2.3.2 Massively Parallel Processors (MPPs)	14
2.3.3 Workstation Clusters	16
2.3.4 Problems and Solutions in Parallel Computers	17
2.4 SUPERCOMPUTING AND SEISMIC DATA PROCESSING	19
2.5 CONCLUSION	24
REFERENCES	25
<b>3. SEISMIC MODELING</b>	<b>28</b>
3.1 INTRODUCTION	28
3.2 ELASTIC MODELING IN TWO DIMENSIONS	32
3.2.1 Introduction	32
3.2.2 The Equations and the Numerical Method	33
3.2.3 Absorbing Boundaries for 2-D Elastic Modeling	36
3.3 ACOUSTIC MODELING IN THREE DIMENSIONS	38
3.3.1 Introduction	38
3.3.2 Problem Formulation: Equations	40
3.3.3 Source Excitation	42
3.3.4 Numerical Solution	43
3.3.5 Absorbing Boundary Conditions for 3-D Acoustic Modeling	46
3.3.6 Numerical Examples	51

<b>CHAPTER</b>	<b>PAGE</b>
3.4 VECTORIZATION OF THE FINITE DIFFERENCE MODELING ALGORITHMS	52
3.5 SEISMIC MODELING IN PARALLEL	57
3.6 2-D ELASTIC AND 3-D ACOUSTIC MODELING APPLICATIONS	63
3.6.1 Introduction	63
3.6.2 Simulations during Thermal EOR Processes at Cold Lake	63
3.6.3 Three-dimensional Acoustic Wave Simulations for the French Model	64
3.10 CONCLUSION	69
REFERENCES	70
<b>4. SEISMIC REFLECTION IMAGING</b>	<b>74</b>
4.1 INTRODUCTION	74
4.1.1 Migration	74
4.1.2 Migration: Extrapolation and Imaging	74
4.1.3 Poststack versus Prestack Migration	77
4.1.4 Migration Methods	78
4.1.5 3-D Migration	80
4.1.7 Migration Methods and Algorithms Developed in this Thesis	84
4.2 2-D $\omega$ -x FINITE DIFFERENCE DEPTH MIGRATION	85
4.2.1 Introduction	85
4.2.2 Depth Extrapolation with a $65^\circ$ Approximation to the One-way Wave Equation	85
4.2.2 Poststack 2-D $\omega$ -x Depth Migration	90
4.2.3 Prestack 2-D $\omega$ -x Depth Migration	91
4.3 ONE-PASS 3-D FINITE DIFFERENCE DEPTH MIGRATION	93
4.3.1 Introduction	93
4.3.2 Problem Formulation: Equations	93
4.3.3 One-Pass 3-D Poststack Depth Migration	97
4.3.4 One-Pass 3-D Prestack Depth migration	98
4.4 FORWARD MODELING IN THE FREQUENCY DOMAIN AND OTHER APPLICATIONS	99
4.5 PARALLEL IMPLICIT FINITE DIFFERENCE DEPTH MIGRATION AND MODELING ALGORITHMS	100

<b>CHAPTER</b>	<b>PAGE</b>
4.6 APPLICATION OF THE IMPLICIT FINITE DIFFERENCE MIGRATIONS FOR IMAGING SEISMIC AND RADAR DATA	109
4.7 3-D REVERSE TIME MIGRATION	110
4.7.1 Introduction	110
4.7.2 Reverse time migration with a 3-D full acoustic wave first order hyperbolic system	111
4.7.3 Reverse time migration with a 3-D one-way acoustic wave first order hyperbolic system	112
4.7.4 Reverse-Time Extrapolation	113
4.7.5 3-D poststack reverse time migration	114
4.7.6 3-D prestack reverse time migration	114
4.7.7 Advantages and Disadvantages with the two Approaches - Implementation of reverse time migration	116
4.7.8 Applications of the Reverse Time Migration	118
4.8 DISPERSION ANALYSIS FOR 3-D MIGRATION	119
4.9 MIGRATION VELOCITY ANALYSIS	123
4.10 CONCLUSION	127
REFERENCES	128
<b>5 . THERMALLY ENHANCED OIL RECOVERY OF THE COLD LAKE OIL SANDS AND WAVE PROPAGATION</b>	<b>136</b>
5.1 INTRODUCTION	136
5.2. THE GEOLOGY OF THE ALBERTA OIL SANDS	139
5.3 RESERVOIR DESCRIPTION	140
5.4 ENHANCED OIL RECOVERY: THE CYCLIC STEAM STIMULATION PROCESS	142
5.5 SEISMIC WAVE PROPAGATION IN FLUID SATURATED POROUS ROCKS	143
5.5.1 The quality factor Q and velocity dispersion	143
5.5.2 Attenuation mechanisms	147
5.5.3 Laboratory measurements of attenuation and velocities	151
5.5.4 Summary on attenuation and velocity	158
5.6 RESERVOIR CONDITIONS AND SEISMIC CHANGES DURING EOR PROCESSES	159

<b>CHAPTER</b>	<b>PAGE</b>
5.6.1 Effects of Pressure	159
5.6.2 Effects of Temperature	160
5.6.3 Effects of Gas	161
5.6.4 Effects of pore fluid type and saturation	162
5.6.5 Utilizing seismic attributes	163
5.7 CONCLUSION	166
REFERENCES	167
<b>6. SEISMIC MONITORING OF THERMALLY ENHANCED OIL RECOVERY PROCESSES AT COLD LAKE</b>	<b>174</b>
6.1 INTRODUCTION	174
6.2 U OF A PROCESSING AND ANALYSIS OF THE 3-D SEISMIC MONITORING SURVEYS	176
6.2.1 Simulations of Seismic Wave Propagation at Cold Lake Oil Sands	176
6.2.2 Energy Balancing	177
6.2.3 One-pass 3-D Depth Migration	178
6.2.4 Seismic Attribute Analysis	179
6.3 SEISMIC MONITORING STUDIES AT IMPERIAL OIL'S D3 PAD	180
6.3.1 Cyclic Steam Stimulation recovery of the Cold Lake bitumen	180
6.3.2 3-D Seismic Monitoring Reflection Surveys	181
6.3.3 Seismic Wave Simulations during Thermal EOR Processes	182
6.3.4 Processing of the 3-D Reflection Surface Seismic Monitoring Data	197
6.3.5 Seismic Attribute Analysis of the Time and Depth Migrated Data	198
6.3.6 Discussion of Imperial Oil Project's Results	215
6.4 SEISMIC MONITORING OF MOBIL'S PILOT EOR PROJECT	217
6.4.1 The Vertical Pilot EOR project	217
6.4.2 3-D Seismic Reflection Surveys	217
6.4.3. Seismic Wave Propagation Simulations	219
6.4.4 Processing of the 3-D Seismic Data	227
6.4.5 Attribute Analysis	228
6.4.6 Discussion of Results from Mobil's Experiment	230
6.5 CONCLUSION ON SEISMIC MONITORING OF EOR PROCESSES	241
REFERENCES	243
<b>7. IMAGING OF GROUND-PENETRATING RADAR DATA FOR</b>	

<b>CHAPTER</b>	<b>PAGE</b>
<b>CHARACTERIZATION OF NUCLEAR WASTE REPOSITORIES</b>	<b>245</b>
7.1 INTRODUCTION	245
7.2 GEOPHYSICAL METHODOLOGY	246
7.3 GEOLOGY OF THE WHITESHELL RESEARCH AREA	247
7.4 GROUND-PENETRATING RADAR METHOD	247
7.5 FREQUENCY-SPACE DEPTH MIGRATION FOR GPR DATA	251
7.6 ACQUISITION OF GPR DATA IN GRANITE	251
7.7 PROCESSING OF GPR DATA USING SEISMIC ALGORITHMS	256
7.8 INTERPRETATION OF THE GPR MIGRATED IMAGES	257
7.9 CONCLUSION	263
REFERENCES	263
<b>8. CONCLUSIONS</b>	<b>266</b>
<b>APPENDIX A. VECTOR AND PARALLEL SUPERCOMPUTERS</b>	<b>271</b>
A.1 THE MYRIAS SPS3 PARALLEL COMPUTER	271
A.2 THE FUJITSU VPX240/10 SUPERCOMPUTER	273
A.3 THE CONVEX C210 VECTOR MINI-SUPERCOMPUTER	275
<b>APPENDIX B. FUNDAMENTALS OF SEISMIC WAVES</b>	<b>277</b>
B.1 STRESS AND STRAIN	277
B.2 SEISMIC WAVES	280
B.3 THE ACOUSTIC WAVE EQUATION	283
<b>APPENDIX C. 3-D EXPLICIT FINITE DIFFERENCE MODELING</b>	<b>285</b>
C.1 THE MACCORMACK TYPE SPLITTING SCHEME	285
<b>APPENDIX D. IMPLICIT FINITE-DIFFERENCE MIGRATION</b>	<b>287</b>
D.1 IMPLICIT FINITE DIFFERENCE FOR THE $65^{\circ}$ PARABOLIC APPROXIMATION	287
D.2 SOLUTION OF THE TRIDIAGONAL SYSTEM OF EQUATIONS	290
D.3 STABILITY ANALYSIS FOR THE $65^{\circ}$ PARABOLIC APPROXIMATION	291
D.4 ABSORBING BOUNDARY CONDITIONS	293
<b>E. LITHOPROBE ALBERTA BASEMENT TRANSECT</b>	<b>295</b>
E.1 ACQUISITION	295
E.2 PROCESSING AND IMAGING	296

## LIST OF FIGURES

FIGURE		PAGE
2.1	Cartoons illustrating the different processing architectures as they evolved with time: (a) scalar processing; (b) vector processing; (c) vector/parallel processing; and (d) parallel processing (modified after Moriarty, 1987).	11
3.1	Reflectivity versus the wave propagating angles.	53
3.2	The two-layer model used for testing the 3-D acoustic modeling method.	54
3.3	The analytical (theoretical) and numerical solutions at a source-receiver distance of 48 m for the two layer model that was excited by point source whose time function is Gaussian with peak frequency at 30 Hz and a time delay of 100 ms.	55
3.4	Portion of the 3-D synthetic seismograms (shot gathers) for the pressure field (a) and for the particle velocity field (b) from 3-D acoustic modeling for the two-layer model	56
3.5	Finite difference solution for the operator in the x-direction. Up to second order neighbours in every direction are required for calculations at each time step.	60
3.6	Coarse grain parallelism for 2-D elastic modeling. (a) A model submatrix is assigned on each processor. (b) Communication between tasks / processors is required.	61
3.7	Dependence decomposition for partial parallelism over time for 2-D elastic modeling. (a) 1-D domain decomposition and (b) 2-D domain decomposition.	62
3.8	A depth slice and a vertical cut of the French model (two domes and a fault) used for 3-D acoustic modeling.	66
3.9	Portions of the 3-D shot gather (vertical particle velocity component) from the 3-D acoustic wave simulation for the French model (Figure 3.8): (a) along inline 45 and (b) along crossline 16.	67
3.10	(a) A depth slice (77 m) and (b) a vertical cut (along inline 45) from the 3-D snapshot (150 ms) for the pressure field from the 3-D acoustic wave simulation for the French model (Figure 3.8).	68



<b>FIGURE</b>	<b>PAGE</b>
<b>4.1</b>	The code structure models used for parallelization of the migration and modeling algorithms in the frequency domain. 103
<b>4.2</b>	Parallel pseudocode for 2-D $\omega$ -x $65^\circ$ poststack depth migration as was implemented on a Myrias SPS3 parallel computer. 104
<b>4.3</b>	Parallel pseudocode for 2-D $\omega$ -x $65^\circ$ prestack depth migration. 105
<b>4.4</b>	Parallel pseudocode for one-pass 3-D $\omega$ -x-y $65^\circ$ poststack depth migration. 106
<b>4.5</b>	Parallel pseudocode for one-pass 3-D $\omega$ -x-y $65^\circ$ prestack depth migration. 107
<b>4.6</b>	Parallel pseudocode for 2-D or 3-D zero-offset forward modeling (for 2-D set everywhere $y=0$ ). 108
<b>4.7</b>	Slices parallel to the $\phi$ - $\theta$ plane from the 3-D surfaces of the dispersion relations of the 3-D scalar wave equation (hemisphere), the proposed one-way system and the 65 degree paraxial approximation for different values of the $k_z$ : (a) high; (b) intermediate; and (c) zero. 121
<b>4.8</b>	Comparison of the dispersion relations of the 3-D scalar wave equation (hemisphere), the proposed one-way system and the 65 degree paraxial approximation in: (a) the inline or crossline direction and (b) in the diagonal direction. 122
<b>4.9</b>	The algorithmic flow for velocity analysis, 3-D depth migration and modeling by utilizing the algorithms developed in this thesis. 126
<b>5.1</b>	Map of the Alberta oil sands, outlining the major heavy oil accumulation regions of the Lower Cretaceous deposits that occur in the Western Canadian basin (modified after Harrison et al., 1979). 137
<b>6.3.1</b>	The site map of the Imperial Oil's D-3 pad (under CSS) at Cold Lake, shows the location of the producer/injection wells (D3-1 to D3-15) at reservoir depth level, the observation wells (OB1 to OB6) and the inline 42 of the seismic grid (8x8 m bins). 183
<b>6.3.2</b>	The basic velocity model used for 2-D elastic wave propagation simulations before steaming (no steam zone) and during steaming (with the steam zone) at Imperial Oil's D3-pad at Cold Lake, Alberta. 187
<b>6.3.3</b>	Synthetic zero offset sections (vertical particle velocity component) from 2-D elastic wave propagation simulations for the model (Figure 6.3.2) without (a) and with (b) the steam zone. 188

<b>FIGURE</b>	<b>PAGE</b>
6.3.4 Synthetic shot gathers (vertical particle velocity component) from 2-D elastic wave propagation simulations for the model (Figure 6.3.2) without (a) and with (b) the steam zone.	189
6.3.5 The 3-D GEOSET model from Imperial Oil's D3-pad at Cold Lake, Alberta.	190
6.3.6 2-D velocity models based on the basic model (Figure 6.3.2) and the GEOSET model (Figure 6.3.5): (a) without steam zone (base model) and (b) with a steam zone (monitor-steam model).	191
6.3.7 2-D elastic wave simulations for the base model (Figure 6.3.6.a): (a) shot gather (vertical particle velocity component) and (b) stacked section.	192
6.3.8 Zero offset sections from elastic wave simulations for the models in Figure 6.3.6: (a) without a steam zone (base) and (b) with a steam zone (monitor-steam).	193
6.3.9 (a) Inline 42 of the 3-D synthetic zero offset section from 3-D acoustic wave propagation simulations for the modified 3-D GEOSET model; (b) the depth migrated section (inline 42) after 3-D poststack reverse time migration.	194
6.3.10 Velocity models, incorporating (a) a crosswell velocity tomogram and (b) additionally, a steam zone, used for elastic modeling during production (6th cycle) and steam injection (8th cycle).	195
6.3.11 Synthetic zero offset sections (vertical particle velocity component) from 2-D elastic wave simulations for the models in Figure 6.3.10 during the 6th production cycle (a) and the 8th steam cycle (b).	196
6.3.12 The processing flows as they were applied on both data sets (production 1990 and steam 1992) by Imperial Oil and the Seismology Laboratory, University of Alberta (this research).	202
6.3.13 Time migrated data, inline 42 from the production 1990 (a) and the steam 1992 (b) seismic data volumes.	203
6.3.14 (a) Devonian amplitude difference and (b) Devonian two-way travel time delay (pushdown) between the steam (1990) and the production (1992) normalized time migrated data.	204
6.3.15 Inline 42 from: (a) the production (1990) and (b) the steam (1992) depth migrated data volumes.	205
6.3.16 Crossline 37 from: (a) the production (1990) and (b) the steam (1992)	

<b>FIGURE</b>	<b>PAGE</b>
depth migrated data volumes.	206
<b>6.3.17</b> Cosine of phase for inline 42 from: (a) the production (1990) and (b) the steam (1992) depth migrated data volumes.	207
<b>6.3.18</b> Instantaneous frequency for inline 42 from: (a) the production (1990) and (b) the steam (1992) depth migrated data volumes.	208
<b>6.3.19</b> Depth slices summed over 5 m interval, 450~455 m, from: (a) the production (1990) and (b) the steam (1992) depth migrated data volumes.	209
<b>6.3.20</b> Depth slices summed over 5 m interval, 470~475 m, from: (a) the production (1990) and (b) the steam (1992) depth migrated data volumes.	210
<b>6.3.21</b> Amplitude difference between the production (1990) and the steam (1992) depth migrated data over 5 m depth interval: (a) between 450 and 455 m, and (b) between 470 and 475 m.	211
<b>6.3.22</b> A 3-D perspective of the apparent depth structure of the Devonian horizon during the production 1990 (a) and the steam 1992 (b) cycles.	212
<b>6.3.23</b> (a) Devonian apparent depth pushdown between steam (1992) and production (1990) depth migrated data. (b) The velocity reduction ( $\Delta v$ ) in the steam-heated reservoir as it is seen by the Devonian horizon.	213
<b>6.3.24</b> Devonian amplitude difference (a) and ratio (b) between the production (1990) and the steam (1992) depth migrated data volumes.	214
<b>6.4.1</b> The site map of Mobil's pilot project showing the locations of the injection/production and observation wells, and the seismic grid.	218
<b>6.4.2</b> The steam zones used to simulate steam injection in the Sparky Sands.	222
<b>6.4.3</b> Acoustic $\omega$ -x modeling generated zero offset sections without (a) and with steam zone (b). 2-D $\omega$ -x depth migration of the zero offset section with the steam zone generated the depth migrated section (c).	223
<b>6.4.4</b> Velocity models used for 2-D elastic wave propagation simulations: (a) before the steaming process (base, no steam zones) and (b) during steam injection (monitor, steam zones).	224
<b>6.4.5</b> Synthetic shot gathers (vertical particle velocity component) from elastic wave simulations for the models (Figure 6.4.4): (a) before the steaming process (base, no steam zones) and (b) during steam injection (monitor, steam zones).	225
<b>6.4.6</b> Stacked sections for the models (Figure 6.4.4): (a) before the steam	

<b>FIGURE</b>	<b>PAGE</b>
stimulation process (base) and (b) during steam injection (monitor-steam).	226
<b>6.4.7</b> The processing flows as they were applied on both data sets (base and steam-monitor) by Mobil Oil and the Seismology Laboratory, University of Alberta (this research).	231
<b>6.4.8</b> The inline 12 from the stacked data sets: (a) base and (b) steam-monitor.	232
<b>6.4.9</b> Time slices from the stacked data volumes: (a) base and (b) steam-monitor.	233
<b>6.4.10</b> The Colony horizon from the stacked data: (a) the amplitude difference and (b) the time difference (pushdown) between the monitor and the base surveys.	234
<b>6.4.11</b> The Devonian horizon from the stacked data after normalization: (a) the amplitude difference and (b) the time delay (pushdown) between monitor and base surveys.	235
<b>6.4.12</b> The inline 12 from the depth migrated data: (a) base and (b) steam-monitor surveys.	236
<b>6.4.13</b> The crossline 44 from the depth migrated data: (a) base and (b) steam-monitor surveys.	237
<b>6.4.14</b> The inline 60 from the depth migrated data: (a) base and (b) steam-monitor surveys.	238
<b>6.4.15</b> The Devonian horizon from the depth migrated data: (a) the amplitude difference between base and monitor and (b) the apparent depth pushdown between monitor and base.	239
<b>6.4.16</b> The Sparky horizon from the depth migrated data: (a) the amplitude difference between base and monitor and (b) the apparent depth pushdown between monitor and base.	240
<b>7.1</b> Location and area map of AECL's (Atomic Energy of Canada Limited) Whiteshell Research Area and the Underground Research Lab in Manitoba, Canada.	248
<b>7.2</b> A cross section showing geological and structural features across the URL area and through the URL shaft. The major fracture zones shown have been confirmed by a number of different geophysical methods.	249
<b>7.3</b> The location of the GPR profiles and boreholes in (a) Permitt area B and (b) the URL area.	253
<b>7.4</b> Raw GPR profile: (a) profile-b3 from the Permitt area B, and (b) profile-u2 from the URL area.	254

<b>FIGURE</b>	<b>PAGE</b>
7.5	Raw GPR profiles: (a) profile-pgl1 and (b) profile-pgl3, both from the URL area. 255
7.6	The GPR profile-u2 from the URL area. (a) The processed data after AGC, static shift, deconvolution, and bandpass and signal-to-noise ratio enhancement filtering; (b) The core log from borehole M-10 (located near the northwest end of the profile); and (c) The depth migrated data after $\omega$ -x finite difference migration, random noise attenuation and trace balancing. 259
7.7	The GPR profile-b3 from area B: (a) The processed data after static shift, gain, deconvolution, and bandpass and signal-to-noise enhancement filtering; (b) The core log from borehole WB1 (about 40 m west from the profile); and (c) The depth migrated data after $\omega$ -x finite difference migration, random noise attenuation and trace balancing. 260
7.8	GPR profiles after processing and migration: (a) The depth migrated profile-pgl1; and (b) The depth migrated profile-pgl3. 261
7.9	The algorithmic flow used for processing and migration of GPR data. 262
E.1	Portions of the depth migrated line 10 (LITHOPROBE Alberta Basement transect) with interpretation (Seismology Laboratory, University of Alberta). 297

# CHAPTER 1

## INTRODUCTION

### 1.1 SEISMIC MODELING AND IMAGING

The seismic reflection method is essentially an echo technique making use of artificially induced elastic waves from seismic sources such as explosions (dynamite) and mechanical vibrations (vibrators). The seismic waves are reflected, transmitted and attenuated due to the changes of acoustic impedance in the subsurface geologic structure and stratigraphy. The seismic reflection method seeks to image the structure of the Earth from the recorded seismic wavefields at the surface. The seismic signal recorded by a geophone, is a superposition of seismic waves originating from all possible directions in the subsurface. Thus, much of the recorded energy is not from reflectors directly below the receiver but from horizons far away from the point of recording.

In the last decades, several techniques have been developed for simulating and imaging seismic wavefields. Because of the large amount of data, the use of certain theoretical assumptions in the development of the algorithms, the use of 2-dimensional approximations, and the requirement of a very large number of computations, the conventional modeling and processing schemes produced limited results in many cases. However, recent advances in computing based on vector computation and subdivision of the computational sequence into parallel components can allow the development and implementation of advanced techniques that are more accurate and cost effective than were possible in practice in the past. These advanced techniques are distinguished mainly by their use of the wave equation (acoustic or elastic in two or three dimensions) which introduces mathematical rigor and computational complexity. However, 3-D seismic wave-equation modeling and imaging has the potential of becoming feasible, efficient and more accurate for any complex subsurface geologic structure.

In forward modeling one starts with an assumed earth model and generates a wave field by solving wave equations. In order to gain an acceptable geological model, comparisons are often made between the synthetic and observed seismograms. In contrast, in imaging one attempts to construct a possible model from the observed seismic wave field. One of the most commonly used inverse methods in advanced seismic processing is

the migration technique in which the recorded wave amplitudes with the use of the wave equation are redistributed to their true spatial positions to better image a two-dimensional or three-dimensional subsurface reflecting structure.

Migration can be performed in a number of different domains such as in the time, frequency, space and wavenumber domains. Also, it can be performed before or after stacking the recorded seismic data. Stacking the data consists of adding together multiple traces after applying normal moveout (a Pythagorean operation based on the assumption of flat horizontal reflecting interfaces and a velocity field estimate). The resultant stacked sections, representing the estimated seismic responses, may be regarded as data obtained from coincident sources and receivers at each spatial location. Stacking of recordings from many source receiver combinations improves the signal to noise ratio of weak subsurface echoes and reduces the large amount of data for further processing. Poststack migration attempts to correct a stacked section for the effect of the reflector dip since the obtained stack sections with dipping or discontinuous reflectors are distorted. Poststack migration is an important component of conventional processing. However, in complex geologic areas, where seismic velocity varies strongly, poststack migration is inadequate due to inherent assumptions and only prestack migration can place energy in the true subsurface position and provide an accurate image of the complex subsurface. However, prestack migration is computationally expensive since it uses the vast amount of recording data (e.g., a typical 3-D seismic survey can generate 30 million traces which translate in the order of 200 Gbytes of recorded data).

One group of approaches for seismic wave-equation modeling are the discrete-coordinate methods such as finite difference methods, finite element methods and other methods that combine time advancing algorithms and integral transformations with respect to space variables such as the pseudo spectral method. Also, the numerical techniques employed by migration processes can be divided in three general categories, namely, the finite difference method, the summation or integral approach and the transformation method. However, this thesis utilizes finite difference methods for the development of seismic modeling and migration methods and algorithms.

The finite difference method, since its introduction into computational seismology in the late sixties, has proved to be particularly versatile in extending the scope of solvable problems. The finite difference method offers a most direct solution to the problem expressed in terms of the basic equations, and the initial and boundary conditions. In the elastic case, the method automatically accounts not only for direct waves, primary and multiple reflection waves but also converted waves, head waves, diffraction waves and

waves observed in ray-theoretical shadow zones. The finite difference method for both modeling and migration generally require large computer memory and high performance speed. However, with the advent of computer power they have received special attention because they are capable of producing a complete synthetic seismogram for a realistic earth model and image accurately the subsurface, respectively.

Finite difference schemes can generally be placed in two broad categories: *explicit* and *implicit*. In explicit schemes the response is evaluated exclusively at one space location at an advanced time directly from the response on the neighboring grid points already determined at previous times. In implicit schemes the response is evaluated simultaneously at all space locations at an advanced time from known values at previous times through a matrix inversion technique. The explicit operators are easier and more economical to implement but suffer from stability problems. For hyperbolic equations explicit schemes are preferred because the stability conditions are not as severe as with parabolic equations.

This thesis explores new and existing wave-equation based modeling methods. A new 3-D acoustic modeling method is formulated and a computationally efficient algorithm is developed for it. The second order differential wave equation is formulated into a first order hyperbolic system which is solved with explicit finite differences using the MacCormack splitting scheme. Also, existing 2-D elastic modeling algorithms are modified and fine-tuned for computationally efficient and realistic wave propagation simulations in complex structures.

Also, this thesis explores new and existing migration methods in two and three dimensions. Two new 3-D reverse time migration methods are formulated employing a full and a one-way wave system that is solved with explicit finite differences. Based on these methods four new algorithms are developed for poststack and prestack migration of 3-D complex seismic data. Also, 2-D poststack and depth migration algorithms are developed in the frequency-space domain using implicit finite differences. These 2-D migration algorithms are adapted for applications that range from deep crustal imaging of seismic wavefields that involve 18 seconds long travel times (50 Km depth) and frequencies in the order of 1~ 100 Hz, to imaging of radar wavefields that involve 2000 nano-seconds (ns) long travel times and frequencies in the order of 50 MHz. Furthermore, a 3-D poststack and prestack depth migration parallel algorithm is developed in the frequency domain that uses an one-pass or alternative direction implicit (ADI) finite difference method.

Implementation of the above algorithms fully utilizes the existing current supercomputer technology such as vector and parallel supercomputers (e.g., the Convex 210 vector mini-supercomputer, the Fujitsu VPX 240/10 vector/parallel supercomputer, and the Myrias



SPS-3 MIMD parallel computer) and single workstations and workstation clusters (e.g., SUN, IBM RISC 6000). Advanced modeling and imaging algorithms require a great deal of numerical operations as well as a large number of data transfer operations. In order to overcome these problems we explore all possible inherent vectorization and parallelization techniques that can make the developed codes computationally fast. On the one hand, many of the developed algorithms are highly vectorized using sophisticated approaches such as matrix multiplication by diagonals to take full advantage of the computational power of vector supercomputers. On the other hand, some of the algorithms are highly parallelized by utilizing the inherent parallelism in the frequency, space and partially in time domains that the seismic equations have and thus they can take full advantage of the computational power of massively parallel computers and workstation clusters.

## **1.2 SEISMIC MONITORING OF OIL RESERVOIRS**

As we head into the 21st century, it is recognized that an integrated approach to reservoir description, development and management is necessary. Some of the reasons are that new fields tend to be smaller and more complex, difficult economic times, focus on increasing reserves by better characterization of existing fields and enhanced recovery. Also, we tend to recover a fairly small fraction of the oil in the ground (30-40%). This integrated approach requires that geophysicists, geologists and engineers successfully analyze and integrate all available data into a single consistent description of the reservoir.

For a successful reservoir management a number of major objectives must be met: such as cost reduction of field development, optimization of total reserves, optimization of production recovery, reduction of operating costs of the developed field, and enhanced recovery if economically justified. Geophysics plays a very important role in efficient reservoir management, since, geophysical methods can lead to the identification of reserves, accurate characterization of the reservoir in terms of volume, fluid properties lithology and continuation, and reservoir surveillance for accurate monitoring. During all phases of the field management high resolution 3-D surface seismic data and borehole seismic data can play a key role as they are integrated with geological and reservoir engineering data within a single model of the reservoir.

In the predevelopment phase, where delineation of the reservoir (characterization of the trap and determination of its structural nature, limits and volume) takes place, high resolution seismic data can define structures and continuity of pay and nonpay zones and can indicate the presence of gas or oil. 3-D seismic data can effectively reduce the risk of

dry holes and the cost of delineation wells by predicting drilling hazards such faults and overpressure zones.

In the initial development phase, where reservoir and aquifer description and characterization takes place, geophysical data are beginning to play an active role. This characterization involves estimating lateral facies and porosity variations, determining 3-D distribution and continuity of the pore-fluid system of the reservoir and the aquifer system, determining formation pressures and fluid saturations, analyzing reservoir fractures, building a complete geological model and performing reservoir simulations based on this model. Seismic stratigraphy provides information on depositional patterns and lateral facies variations. Seismic data integrated with well data can improve the spatial description of rock properties such as lithology and porosity which are input into reservoir flow simulation models. Also, 3-D seismic data can help to determine reservoir continuity, define reservoir subzones and map discontinuous shales and tight streaks that can act as permeability barriers.

In the operating phase of a field development, where efficient reservoir management (reduce operating costs and maximize hydrocarbon recovery) must take place, 3-D high resolution data and borehole seismic data integrated with core, well and reservoir performance data are beginning to impact reservoir monitoring. During this phase, reservoir surveillance is important since actual and predicted performance is usually different. It is critical to detect permeability barriers, estimate reservoir continuity and plan an accurate infill drilling program.

In the enhanced recovery phase a number of processes such as steam stimulation, steam drive, combustion (fire-flooding), CO<sub>2</sub> stimulation, can be used to initiate recovery in the case of heavy oil sands or increase recovery efficiency. Reservoir characterization is very important before starting an Enhanced Oil Recovery (EOR) project because of the possibility of failure due to reservoir heterogeneities and anisotropy. Also, reservoir surveillance during an EOR process is critical for the evaluation of the EOR efficiency. 3-D high resolution surface seismic and cross-well seismic data can be used for defining and monitoring EOR processes. Time-lapse seismic images can monitor reservoir changes that are induced during EOR processes.

Although field development and recovery phases appear distinct, in the reality they are not because reservoir management is an iterative process. For example, a 3-D seismic data volume can evolve into a continuously utilized and updated management tool that can impact oil recovery strategies and evaluation for years after the seismic data were originally acquired. As a result seismic interpretation and reservoir model become more detailed and

sophisticated.

3-D seismic data analysis can image with high resolution the “geometric framework” of such as structures as faults and fracture patterns, structural and stratigraphic traps, and the position and orientation of unconformities. Furthermore, a major shift in the use of the 3-D seismic method is taking place since it has been realized that reservoirs are more complex and heterogeneous than assumed in the past and are evolving during development and enhanced oil recovery. This shift involves the use of 3-D seismic monitoring to qualitatively and quantitatively correlate seismic attributes (e.g., amplitudes, phase changes, interval traveltimes between events and frequency) with reservoir properties and conditions (e.g., porosity, fluid type, lithology, fluid and gas saturation, permeability, pressure and temperature) over time. Furthermore, the estimation of reservoir properties may be possible by integrating information from 3-D seismic data analysis, borehole logs, cores, mud logs, production and pressure data, temperature logs and other data. Although the 3-D surface seismic method does not have the vertical resolution of borehole logs and cores, it is the only method which can give details about areal distributions.

Enormous reserves of bitumen or heavy oil are present in sands of Lower Cretaceous age in Alberta, Canada. However, most of the heavy oil can be extracted only by *in situ* enhanced oil recovery (EOR) processes that consist of increasing the mobility of the oil and then driving it into a production well. Two case studies are performed in this thesis that involve steam stimulation projects (Mobil Oil Canada and Imperial Oil of Canada) in the heavy oil sands of Cold Lake, Alberta. Seismic monitoring of the reservoir during the thermal process (steam stimulation) is performed with 3-D surface high resolution seismic surveys repeated over specified time intervals carried out over the EOR sites. The modeling and migration algorithms developed here are used for advanced processing and interpretation of the recorded 3-D data volumes and integration of the seismic data with other geological and engineering data. Furthermore, an extensive seismic attribute analysis is performed on the 3-D seismic data in order to generate 4-D images (3-D plus calendar time). The seismic images have the potential to map the areal extent of the steam-heated zone, track the steam front, define fractures and reservoir permeability anisotropy, and be used as reservoir temperature, pressure and gas saturation diagnostic tools. A knowledge of the evolving reservoir properties and conditions in real time allows the possibility of controlling and modifying steam injection and production strategies. Thus, non-invasive methods such as 3-D surface seismic monitoring has the potential of becoming a powerful tool for the efficient management of EOR projects.

### **1.3 RADAR IMAGING OF NUCLEAR WASTE REPOSITORIES**

All the countries producing nuclear generated electrical power encounter the problem of management and disposal of the nuclear waste. At present many of these countries are researching methods for underground disposal of high level nuclear waste. As part of the Canadian Nuclear Fuel Waste Management Program, Atomic Energy of Canada Limited (AECL) is studying the plutonic rock of the Canadian Shield as a medium for disposal of nuclear waste.

One of AECL's principal geoscience research sites is the Whiteshell research area which is located near Pinawa in southeastern Manitoba, Canada. In this site an underground research laboratory (URL) has been built that has a vertical shaft and two main working levels at 240 and 420 m depth. An extensive drilling program has been carried out in the granitic Lac du Bonnet Batholith near the western margin of the exposed Precambrian Shield. The main objectives of the research in this site are to apply and refine geophysical methods for characterization of potential disposal vault sites in igneous rocks of the Canadian Shield and to refine and calibrate the regional geosphere model for use in hypothetical disposal vault performance assessment calculations.

Geophysical techniques are used for site screening, evaluation and excavation-scale characterization. The techniques used for site screening and evaluation are airborne and surface magnetic and electromagnetic (EM), surface gravity and surface seismic reflection methods. The techniques used for site characterization, such as detecting, characterizing and mapping fractures zones within the plutonic rock mass are well logs, high resolution seismic reflection, crosshole seismic tomography and surface and borehole ground penetrating radar methods. The method studied in this thesis is ground penetrating radar (GPR).

Ground-Penetrating Radar (GPR) is being used to map the earth's shallow subsurface in engineering applications, groundwater detection, environmental and archaeological site assessment. The radar reflection method is based on backscattering from discontinuities in dielectric constants within a rock mass. Although the radar reflection method uses electromagnetic waves in the 10 to 1000 MHz frequency band, there are similarities to the seismic reflection method which uses viscoelastic waves in the 10 to 1000 Hz band. The kinematic similarities between the radar reflection and seismic reflection methods are explored in this thesis. Furthermore, both commercially available and our own seismic

processing algorithms such as the 2-D frequency-space depth migration are applied to GPR data from AECL's Whiteshell research area in Manitoba in order to detect and image fracture zones in the plutonic rock with a resolution never before achieved.

## 1.4 OUTLINE OF THE THESIS

This thesis consists of eight chapters and five appendices.

Chapter 1 introduces some of the concepts, problems and directions of this research work.

Chapter 2 presents the current supercomputer and workstation technology with emphasis given to parallel computers. It overviews existing experience, explores and suggests techniques for the utilization of the new powerful computers for seismic data processing and imaging.

Chapter 3 contains 2-D elastic and 3-D modeling algorithms. An existing 2-D elastic modeling algorithm is modified, parallelized and fine-tuned for realistic wave propagation simulations over steam injection sites. Also, a new 3-D acoustic modeling method is developed for simulating the evolution of a pressure field in complex geologic models. A fast vectorized algorithm was developed for this and was implemented on vector supercomputers and tested with synthetic and real examples.

Chapter 4 contains a number of 2-D and 3-D migration algorithms. Parallel computer algorithms are presented for the 2-D and one-pass 3-D poststack and prestack depth migrations in the space-frequency domain that use implicit finite differences. Also, a new reverse time migration method is developed that uses either a full and an one-way wave system and explicit finite differences. Based on this method four algorithms are presented for poststack and prestack depth migration in the time-space domain and they are tested with realistic synthetic 3-D seismic data. Also, a dispersion analysis of the 3-D migration algorithms is performed.

Chapter 5 discusses the geology, the reservoir and the thermally enhanced oil recovery of the Cold Lake oil sands. It reviews seismic wave attenuation and velocity dispersion in porous media. There is a discussion on the correlation between seismic character changes and reservoir conditions and properties during cyclic steam stimulation.

Chapter 6 involves seismic monitoring studies of EOR projects at the Cold Lake tar sands. In total four 3-D seismic surveys are migrated with the one-pass 3-D depth migration developed in this thesis. Extensive simulations of wave propagation through the reservoir during different cycles of the thermal process are performed. Also, an extensive

seismic attribute analysis is performed on the 3-D seismic data volumes in order to image the steam-heated zone and other petrophysical changes during the steaming process.

Chapter 7 discusses the processing and interpretation of ground penetrating radar data. These data were recorded over the plutonic rocks of the Canadian Shield by the Atomic Energy of Canada as part of the Canadian nuclear waste management program. The processing is performed using seismic processing algorithms and mainly the 2-D migration algorithm developed in this thesis.

Chapter 8 contains conclusions, discusses the original contribution of this thesis and suggests directions for future research.

## CHAPTER 2

### VECTOR AND PARALLEL COMPUTERS FOR SEISMIC DATA PROCESSING

#### 2.1 INTRODUCTION

In the 1970s, the design of high performance supercomputing evolved from scalar to vector architecture (e.g., CRAY-1, CDC STAR 100) that drove peak performance to few tens of Mflops (Mega,  $10^6$  floating points operations per second). In the 1980s, vector processing (e.g., Cyber 205, CRAY X-MP, CRAY-2, ETA-10) continued the upward surge in computing performance in the order of hundreds of Mflops to few Gflops (Giga,  $10^9$  floating point operations per second). In the 1990s, vector/parallel supercomputers (e.g., CRAY Y-MP C90) and massively parallel processors (e.g., CRAY T3D) are driving performance in hundreds of Gflops and approaching Tflops (Tera,  $10^{12}$  floating point operations per second). The different processing architectures as they evolved with time are illustrated in Figure 2.1.

Recent advances in computing based on the vector computation and the subdivision of the computational sequence into parallel components have allowed the development and implementation of more accurate and cost effective seismic imaging methods that were impossible in the past. In this thesis, 3-D seismic modeling and migration has become feasible, efficient and more accurate with the use of vector and parallel supercomputers. An overview of the computer technology used in this thesis and its importance in the seismic data processing will be presented in the following sections.

#### 2.2 VECTOR SUPERCOMPUTERS

The scalar computing on mainframes with the Von Newman design is essentially processing of one data point at a time. On the other hand, vector computing applies a small set of program instructions repeatedly to multiple data elements, which is essentially processing of data in an assembly line fashion. However, the computational process is performed in a certain sequence and it cannot be accelerated beyond a certain point.

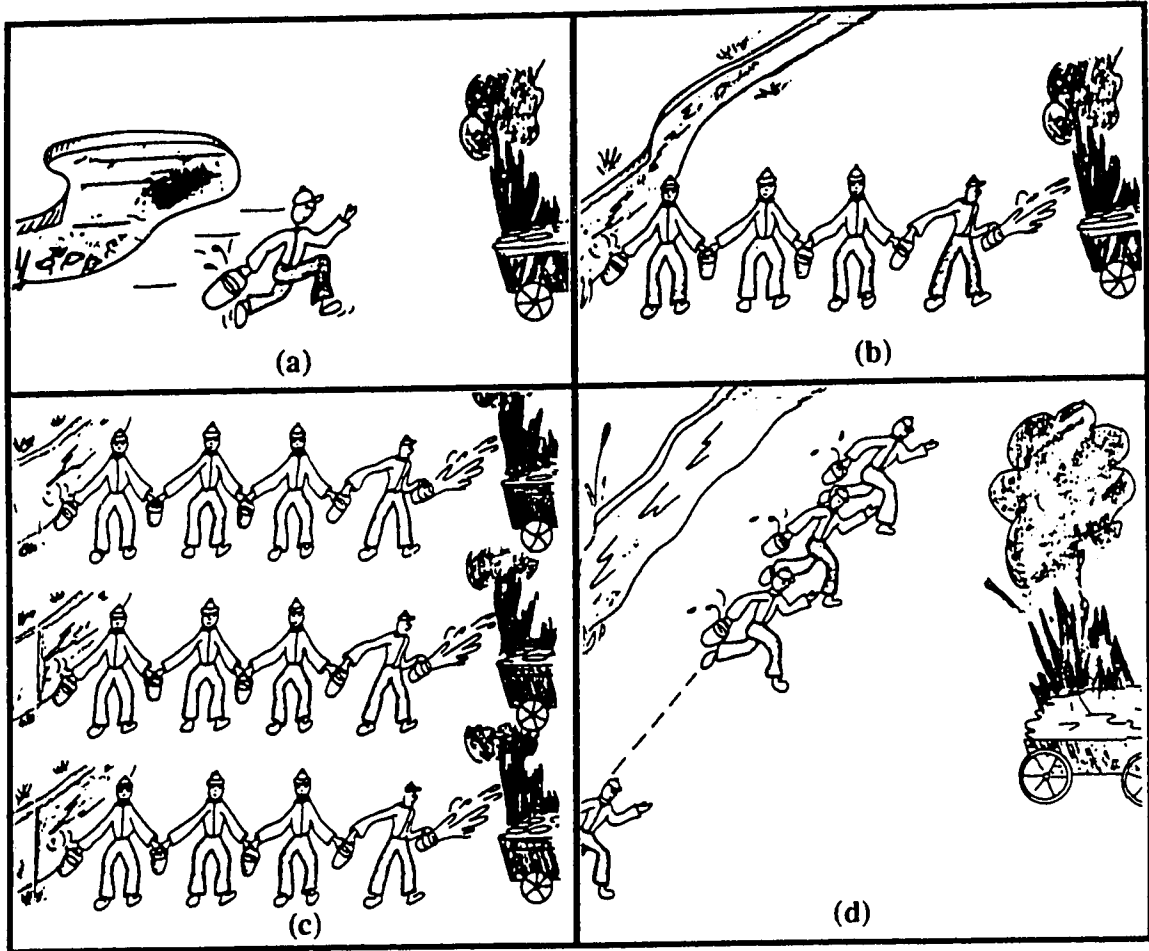


**Figure 2.1:** Cartoons illustrating the different processing architectures as they evolved with time: (a) scalar processing; (b) vector processing; (c) vector/parallel processing; and (d) parallel processing (modified after Moriarty, 1987).



Vector supercomputers involve the use of one or at most a few (CRAY C90, 16 CPUs with 1 Gflops peak performance per processor) fast processors with increased packing capacity, minimum switching times and pipelining. Pipelining of a code involves the breakup of an instruction to its components, such as instruction fetching, decoding, operand address calculation, operand fetching and execution; each of which can be executed independently with simultaneous computation on different data sets.

The process by which an application can utilize vector technology is called *vectorization*. Data structure is the key to effective vectorization. This means that data must be restructured in a global vectorization fashion. The data and computations must be separated into elements that do not depend on each other. Then, these elements can be processed in one vector instruction. Vector computer performance requires long vectors in order to minimize the costly effect of the vector startup. By Amdahl's law, speedup to percentage of vectorization of a code is not linear. That means, that in order to succeed an appreciable amount of performance, a code must be 80 to 90 percent vectorized.

Vector processing greatly improves the performance of applications that emphasize calculations involving arrays of data. It eliminates most of the testing and branching operations normally associated with loops. It minimizes the time spent waiting for operands to be loaded and results to be stored by referencing groups of memory locations and using multiple element (vector) registers. It performs identical arithmetic operations on groups (vectors) of operands. It also maximizes the use of the available arithmetic functional units. Furthermore, it reduces the number of machine language instructions that must be fetched, decoded and executed.

Generally, loops containing array references that use loop induction variables as subscripts are good candidates for vectorization. A loop induction variable is a variable that is incremented or decremented by a constant value on each iteration of the loop (e.g., the loop control variable).

Generally, when loops are nested, only the innermost loop can be vectorized. The compiler can sometimes distribute or interchange nested loops in order to improve vectorization performance. Some assignments into scalar values can be vectorized by the compiler using vector reduction operations (some loops can be vectorized even if the results of operations are not stored into arrays of data). Use of loop induction variables in calculations does not inhibit vectorization. Conditionals within loops can often be vectorized.

## 2.3 PARALLEL COMPUTERS

### 2.3.1 Parallel Computer Architectures

Multiple processor systems can be divided into *shared-memory* computers and *distributed-memory* computers depending on the relationship of CPUs to memory. In the distributed-memory (message-passing) systems, processors that need to share or swap data have to explicitly pass a message over the interconnection network. This approach is a high-latency interconnect and depends on the topology of the network, the switching method, the message length and the network traffic. On the other hand, in the shared-memory systems all processors have equal and unbiased access to a global memory. This approach is a low-latency interconnect. However, shared-memory computers need to retain synchronization in data access. But as the number of CPUs accessing the shared memory increases, access becomes a bottleneck.

There are two extreme types of parallel computers. One type is termed *coarse-grained*, it has few powerful processors, typically vector processors (e.g., CRAY Y-MP8 C90), that work large individual computational tasks within a given problem, and is associated with *coarse-grain parallelism*. Typically, coarse-grained systems have fewer than 20 processors and have shared memories and compilers which automatically can vectorize and parallelize parts of the code. Codes executed on these machines should have vectorizable inner loops and outer loops that can be spread across available processors. The other type is termed *fine-grained*, it has a large number (up to thousands) of less powerful processors (e.g., nCUBE, Myrias) or even small custom designed processors (e.g., CM2), that work on smaller computational tasks within a given problem, and it is associated with *fine-grain parallelism*. In the middle we can put *medium-grained* systems with fewer (<100) larger processors (e.g., workstation clusters) with slower interconnect. These systems have distributed memories, where each processor has its own distinct bank of memory, and processors share data by sending messages or emulating shared memory.

A traditional classification that relates to the programming model is the Flynn taxonomy (Flynn, 1966). It groups computers in four categories: SISD (Single Instruction stream / Single Data stream), SIMD (Single Instruction stream / Multiple Data stream), MISD ( Multiple Instruction stream / Single Data stream) and MIMD (Multiple Instruction stream / Multiple Data stream). Also, Duncan (1990) separates parallel computers into synchronous and asynchronous systems.

Serial computers such as mainframes and workstations are SISD class since they act in a single instruction at a time. In the MISD class there are not any commercial computers.

Synchronous architectures are SIMD systems and pipelined vector processors. SIMD computers consist of multiple processors that simultaneously execute the same instruction on separate streams of data that are fed to each processor. This kind of parallelism is called *data parallel*. Generally, SIMD parallel computers have a large number of processors each with relatively low computer power and memory. SIMD systems are distributed-memory computers. The Connection Machine (CM2) which can have up to 64,000 processors is an SIMD distributed-memory computer.

Some vector supercomputers have multiple pipelined processors that can operate concurrently. Although vector supercomputers do not have a large number of processors, they can also be considered SIMD because a single vector instruction causes multiple pieces of data (vectors) to be operated on. The Fujitsu VPX240/10 is a single processor, pipelined SIMD system.

MIMD class computers consist of multiple processors that can execute different sets of instructions simultaneously while working on independent data. Each processor of a MIMD computer is a complete computing resource with its own memory and works independently. MIMD machines have, in general, a smaller number of processors relative to the SIMD ones. MIMD systems are asynchronous based architectures that support higher level parallelism (subroutine and task levels). MIMD computers can be divided into distributed-memory systems and shared-memory systems. Some of today's distributed-memory MIMD are the Intel iPSC/860 Hypercube, the Myrias SPS3 and the Connection Machine CM5. On the other hand, computers such as the Convex C-series vector multiprocessors and the CRAY Y-MP C90 are shared-memory vector/parallel computers.

### **2.3.2 Massively Parallel Processors (MPPs)**

Serial computers use a single central processing unit (CPU) with a specified amount of memory. By using additional CPUs we can exploit any inherent parallelism within a given problem, and therefore, provide a faster solution. Parallelism, then, represents a way by which we can enhance computational performance.

According to Astfalk (1993a), peak performance for a single CPU has been leveling off since about 1986. The single CPUs machines can not meet computing demands because in the current design the physics limits the cycle time to a CPU to approximately 1 ns (Astfalk, 1993a). In current computer design there are a number of limitations such as the

electrical pulses that move through the computer's conductor paths are speed of light bound, heat generation per volume, lithography limitation and ballistic electrons. Therefore, in terms of communication, the rate of data transfer is ultimately bounded and the distance that information has to travel is essentially limited by physical constraints. The cycle time of today's fastest computers is 2-3 ns. But many users are seeking computing power increases by a factor of 10-100.

Another aspect of high performance is the cost per peak Mflops (million floating points operations per second). The highest performance supercomputer today, the CRAY C90, has 16 CPUs and costs \$25-30 million. It has peak performance 16,000 Mflops with a cost of \$1700 per peak Mflops. On the other hand, the 735 Hewlett-Packard workstation with a cost of about \$40,000, has a peak performance of 198 Mflops with a cost of \$200 per peak Mflops. The above comparison (Astfalk, 1993a) shows that supercomputers are poorer in price-performance than workstations.

In summary, current computer designs can not progress fast enough to meet computational demands; there are limitations in performance that can be achieved from single CPUs; and vector multiprocessor supercomputers are expensive. Therefore, high performance and cost effectiveness requires *Massively Parallel Processors (MPPs)* which can achieve greatly improved price-to-performance ratios. *Massively* means multiple processors within a machine that working in *parallel*, simultaneously, on a single problem. A MPP system is qualified as scalable if it can be expanded without introducing a fundamental bottleneck. Scalability relates the computational performance to the size of the machine. If a computer is scalable then an increase in the number of processors produces an analogous increase in its computational speed (Fox, 1989). The term massively parallel computer or MPP is often used synonymously for a fine-grain computer.

The general direction in MIMD massively parallel computers is globally shared distributed memory (Myrias SPS3). The computer has physically distributed memory but the hardware presents to the user a global address space. This makes programming easier since the user's logical view is that of a shared-memory machine. Currently, supercomputer vendors such as Convex and CRAY are following the above approach in the development of their MPP systems.

In late 1993, CRAY Research introduced an MIMD MPP system; the CRAY T3D. It uses the 64-bit DEC Alpha chip which is capable of 150 Mflops peak performance. This is a reduced instruction set computing (RISC) microprocessor which is cache-based and has pipelined functional units. In the CRAY T3D, processors communicate at rates of 300 Mbytes/sec in every direction, resulting in up to 76.8 Gbytes/sec of bisection bandwidth

for a 1024-processor system. The memory is physically distributed among the processors but is globally addressable. It is scalable in all aspects; from 32 to 2048 processors, from 512 Mbytes to 128 Gbytes of memory and from 4.2 Gflops to 300 Gflops peak performance. The CRAY T3D system can support high performance on applications with fine, medium and coarse-grain parallelism by taking advantage of the globally shared distributed memory, the high performance RISC microprocessors and the low latency interconnect technology.

MPPs with the use of RISC microprocessors are capable of utilizing coarse grain parallelism and distributed memory architecture. This allows the implementation of not only simple process level parallelism but also algorithmic parallelism for compute intensive applications such as seismic modeling and migration. However, MPPs are technology driven, their success depends on advances in the performance and functionality of commodity reduced-instruction-set-computing (RISC) microprocessors. According to Holling and Ketelsen (1991), MPPs are and will continue to be communications bound, not compute bound; memory will drive affordability; interconnect technology will drive efficiency; and I/O will drive accessibility.

In conclusion, MPP systems that closely integrate RISC microprocessors with the proven capabilities of current scalar/vector/parallel architectures will be truly powerful systems that can offer exciting new opportunities for geophysical supercomputing.

### **2.3.3 Workstation Clusters**

Workstation technology has provided users with very good price/performance ratios. Currently, it continues to do so with the reduced instruction set computing (RISC) microprocessors, such as the 64-bit DEC Alpha chip capable of 150 Mflops peak performance, which are cache-based and have pipelined functional units.

RISC technology provides the opportunity to succeed cost effectiveness in seismic data processing. However, RISC workstations do not provide the capacity required for solving large problems. But this limitation can be addressed by creating a parallel computer consisting of a network of many RISC processors. The IBM 9076 Scalable POWERparallel 1 (SP1) computer is an example of this type of parallel system. It consists of 8 to 64 RISC 6000 processor nodes in frames of 8 to 16 processors and with each node configured with 64 to 256 Mbytes of memory. In this system each processor can have its own local disc (0 to 2 Gbytes) that results to small interprocessor communications.

Many research facilities, universities and companies have a large investment in

workstations (e.g., the University of Alberta has 750 units) and due to hard economic times it is possible to capitalize on this investment before purchasing additional computing power. For example, at the University of Alberta the FDDI Campus Research Ring interconnects workstations located across campus and have them appear as a single computing facility (English, 1993). This FDDI network operates at 100 Mb/s for high speed data transfer and can operate at a total distance of up to 200 Km with a maximum of 1 Km distance between active workstations. Participation is voluntary and researchers wishing to devote the entire power of their workstation to their own computing can disable the shared usage of their machine by issuing a software command.

A network (cluster or farm) of workstations such as IBM RS/6000s configures a powerful MIMD parallel computer system. The main disadvantage of the workstation clusters over massively parallel computers is their slower interconnect. However, many of the features required to make massively parallel systems to perform and use efficiently, which were described earlier, are applicable to workstation clusters. For example, Myrias Computer Technologies has implemented its PAMS operating system to network workstations and provides all the features of the massively parallel versions plus additional support to better integrate into the workstation environment (Karpoff and Lake, 1993). Other available software platforms for managing interprocessor communication, scheduling and synchronization are the PVM (Parallel Virtual Machine from Oakridge National Laboratory), Network Linda, Express, DQS (Distributed Queuing System).

Applications with inherent coarse grain parallelism are well suited for workstation clusters since we can have a large number of independent high CPU intensive tasks requiring few synchronizations and inter-process communication.

#### **2.3.4 Problems and Solutions in Parallel Computers**

It is widely accepted that the next generation of high performance computers will be largely parallel in nature. Massive parallel computers have for a decade been presented as being the future of high performance computing. Today, massively parallel computers are only modestly used in non-research environments despite their considerable raw power and potential cost performance advantages. Some of the problems related to the acceptance of MPPs in mainstream computing today are: third-party software packages, porting effort, compilers, latencies and data decomposition (Astfalk, 1993b). The main problem that the move from one single CPU to many parallel CPUs is that there are billions and billions of lines of existing code that were written with the sequential machine in mind and a porting

effort is necessary in order to run existing code on parallel computers. For example, distributed memory parallel computers present to the user a programming model that requires explicit message passing.

Existing compilers are procedure-based compilers. This means that during optimization the compiler operates on a single procedure or subroutine at a time. But we need compilers that can perform interprocedural optimization so that the compiler can automatically parallelize procedures and procedure call trees. Also, the compiler must perform automatic data decomposition of arrays within the user code.

The time spent for the execution of an application program consists of two parts, the computation and the communication. In most parallel algorithms the time spent to communicate information among the processors of a parallel system is higher than the time spent for computation. The main goal when using a massively parallel computer is to succeed the highest possible ratio of computation to communication time.

The techniques for the parallelization of an application algorithm depend on the nature of the algorithm and the structure of the data. The user of a MIMD programming model needs to follow certain steps such as decomposition, mapping and fine-tuning when porting an algorithm. *Decomposition* is the division of the problem into a set of parallel processes and data. According to Grewal et al. (1993), there are three general decomposition methods: the perfectly parallel decomposition, the domain decomposition and the control decomposition. Mapping is the way that processes and data are distributed among the processors in order to have load balancing. Finally, fine-tuning is the last step, when the user makes changes to the working parallel algorithm in order to improve performance.

When our problem is “embarrassingly” parallel the code can be parallelized among the available processors and the concurrently executing parts require little or no communication (perfectly parallel decomposition). A seismic application of this kind is going to be presented in a later chapter where we parallelized and implemented the 3-D depth migration in the frequency-space domain on a Myrias SPS3 parallel computer. But in many applications, such as seismic modeling or migration in the time domain, there is need of inter-task or inter-processor communication over the course of parallel execution. Interconnect latency is defined as the time delay between a processor requesting a piece of data and actually receiving it. Naturally, in order to have high performance we need low latencies.

Domain decomposition is a technique that decomposes the domain of computation into segments each of which can be assigned to a processor. Different topologies such as

overlapping geometries, pipelining, gapped, triangular or pyramid shapes (Kapotas, 1991), can be used for different applications. Also, no single decomposition technique may be effective for large and complex problems.

If we want good performance from a distributed-memory MIMD parallel computer we need to parallelize the outer loops of a code since parallel inner loops result in high startup and synchronization/communication costs. This is opposite to the vectorization approach where the inner loops were vectorized and the whole computation was faster. Unfortunately, outer loops have more loop dependencies than inner loops. However, domain of dependence decomposition (Wilson and Karpoff, 1993), can be applied to an application code to change the order in which computations are performed without changing the computations themselves or the dependencies among them. This can dramatically reduce synchronizations necessary during computations, thus making it well suited for parallelization of codes implemented on MIMD distributed-memory computers.

Another way to minimize communication time is data decomposition. We can position the data in the correct place among the processors before computation begins so that certain amounts of computations can be done without requiring data transfers. The data decomposition is closely related to domain decomposition. Researchers at Rice University (Fox et al., 1990) have developed Fortran-D (“D” for “Data” or “distribution” or “decomposition”) which is a set of Fortran extensions for allowing a priori placement and alignment in the memory of distributed memory machines. Also, the High-Performance Fortran Forum (HPFF), a group of academia and industry representatives, has developed the so-called High-Performance Fortran (HPF) (it can be obtained via anonymous *ftp* on *titan.cs.rice.edu.*), (Astfalk, 1993c). Its minimal set of Fortran extensions can help the user to perform data decomposition and distribution across a multitude of parallel hardware platforms.

## 2.4 SUPERCOMPUTING AND SEISMIC DATA PROCESSING

Since the 1970s, the demand for more computer power has increased significantly among the geophysical community. Up to date this need has typically been met by mainframes and vector supercomputers. However, conventional supercomputer architecture as we discussed earlier is approaching physics limits in communication/computation imposed by signal propagation and heat dissipation. Thus, some form of massively parallel processing is required for successful implementation of computationally demanding algorithms such as 3-D modeling and migration.



In forward modeling, one starts with an assumed earth model and a time-varying source function to simulate the propagation of the wavefield forward in time. Synthetic seismograms are then created by recording the time histories of the wavefield at spatial locations of interest for any receiver-source geometry. In contrast, in seismic imaging one attempts to construct a possible earth model from the observed seismic wavefield. Conceptually, all depth migrations involve the transfer of time data volumes to depth data volumes. For example, post stack depth migration is performed by recursive downward continuation of the recorded at the surface wavefield  $(x,y,z=0,t)$  and then, by applying certain imaging principals at each depth step for the generation of the migrated wavefield  $(x,y,z,t=0)$ .

There are a number of problems associated with 3-D seismic processing. The first problem of 3-D seismic processing is reading the vast amount of data into the computer. For example, a 3-D survey with 300 receiver lines and 1000 shots per line. Each shot is recorded at 120 receivers for a total of 36 million traces (Eisner, 1989). If each trace has 1500 samples, then the total amount of the 3-D data need to be processed is 54 billion samples or words, or equivalently 216 Gbytes for 32-bit words. Furthermore, assuming that we have an efficient way of feeding input data into the computer, the second problem that arises is whether the entire data volume can reside within the disk farm of our computer system.

The third major problem in 3-D seismic is whether we have enough computational power for implementing sophisticated processing and modeling algorithms. Most problems in exploration seismology such as modeling and migration, can be reduced to time progression or depth extrapolation problems where the wavefield is recursively extrapolated in time or space by solving numerically some form of the wave equation. Today there is only one obstacle to the use of 3-D wave-equation numerical techniques and that is the availability of computational power. The recursive wavefield calculations are very computationally demanding. Conventional supercomputer architecture, as we discussed earlier, is approaching physical limits in communication/computation imposed by signal propagation and heat dissipation. However, massively parallel computers may be capable of offering a feasible solution to this problem by utilizing the inherent parallelism found in seismic processes. Parallelism is certainly not a new concept and in essence, it implies concurrency. Computational solutions of seismic problems can utilize parallelism in source, receiver, space, frequency, wave number and even time domain.

A large number of migration and modeling algorithms have already been implemented with varying degree of difficulty and success on SIMD and MIMD massively processors

(MPPs), on workstation clusters and on vector/parallel supercomputers. Next, we present some examples of seismic parallel implementations.

Integral or Kirchhoff migration methods in time or depth compute the integral solution of the wave equation. Since the algorithm requires a large amount of floating point operations in the traveltimes computations and a large number of data transfer in the diffraction summation, it is well suited for parallelization and implementation on massively parallel computers. Van Trier (1987) has implemented a constant-offset Kirchhoff depth migration algorithm on Connection Machine with 64K processors and achieved a 2 to 4 Gflops of sustained performance. In his approach data points from a large number of traces residing on different processors are summed into each migrated point, depending on the migration aperture. However, this can create problems in parallel environments, such as load inbalancing and high communication times, because of poor data locality. In systems like the Myrias SPS3, this can result in moving entire pages between processors when only a single data element is needed (Kapotas and Karpoff, 1993). Also, Charrette (1991) implemented a 2-D Kirchhoff prestack migration on a MIMD nCUBE parallel computer with 128 processing elements. He calculated travel-time maps using ray tracing on a single processor and he performed the imaging in parallel over shot points.

Finite difference schemes are discrete methods where a computational grid is superimposed over the earth model in question. The simplest way to parallelize a finite difference code is to use a fine-grain parallel computer and assign at each grid point of the finite difference mesh a processor. Fricke (1988) has successfully implemented reverse time migration on a SIMD Connection Machine (CM1) that has 64 K processors. Highman and Pieprzak (1991) implemented a 3-D poststack one-pass depth migration algorithm on a SIMD massively parallel computer (Connection Machine CM2). The algorithm is based on an explicit finite difference  $\omega$ -x-y scheme that uses McClellan transformations for building 2-D convolutional operators. Their parallel implementation achieved 6 Gflops sustained performance using 65,536 processing elements (PEs). Also, a group of researchers from Mobil Research and Thinking Machines developed and implemented an explicit finite difference 2-D acoustic modeling algorithm on a massively parallel Connection Machine (64 K CM2). This code achieved a sustained performance of 5.6 Gflops in 1989, giving the group the 1989 Gordon Bell Prize award, and 14.182 Gflops in 1991.

However, in algorithms such as the above ones where explicit finite difference schemes are used, each processor not only needs to reference its own local memory for previous and second previous values, but also needs to get values from its neighbours (the number of intertask communications depends on the order of the spatial and temporal

operator). This kind of implementation may be successful only on SIMD fine-grain machines with small processors. But on machines such as the MIMD (ones with more powerful processors) this kind of approach results to very low computation-to-communication ratios. This is because the amount of calculation at each grid point is not very computing intensive to benefit from the capabilities of a MIMD. Therefore, if one uses more powerful processors capable of performing a large number of floating point operations then one must assign tasks with equivalent number of floating operations. A coarse-grain parallelization approach can utilize parallelism that runs over one of the spatial coordinates such as depth allowing the other spatial domains to be calculated serially inside each task for the advanced time.

Kapotas (1991) has extensively parallelized and implemented a number of finite difference migration and modeling algorithms on a MIMD Myrias parallel computer. He utilized coarse-grain parallelism over depth for implementation of explicit finite difference algorithms such as 2-D reverse time migration and 3-D acoustic modeling. Also, he parallelized the reverse time migration algorithm combining parallelism over space (x-domain) and dependence decomposition that allows partial parallelism over time. Furthermore, he parallelized implicit finite difference 2-D and 3-D poststack and prestack depth migration algorithms over frequencies. Kao (1993) developed a preconditioned iterative 3-D implicit finite difference depth migration algorithm for parallel implementation on the massively parallel CRAY T3D system.

A number of 3-D seismic processing algorithms have been successfully implemented on vector/parallel supercomputers. Holling and Ketelsen (1991) performed interactively 3-D poststack time and depth migration on a large data set (800x400 CDPs, 1.5 Gbytes) and achieved high performance using a CRAY Y-MP system. Kao et al. (1992) presented parallel implementation of 3-D one-pass depth migration using synthetic data on a 16-processor GRAY Y-MP C90 computer. They used the split-step Fourier transform method for downward continuation and they parallelized the algorithm over frequencies and/or depth extrapolation steps. Also, Kao (1993) implemented a 3-D prestack Kirchhoff time migration on the same machine using multitasking. Most recently, Blanc et al. (1993) were able to migrate large data sets, in the order of 1.5 million traces, by implementing an accurate 3-D poststack migration algorithm on CRAY C90 with 16 processors. Their algorithm was based on the Remez-Soubaras method for calculating spatial convolutional filters for the wavefield extrapolation and utilized parallelism over frequencies.

On the other hand attempts for utilizing the capabilities and cost-performance of networked workstations are currently under way. Black et al. (1991, 1992) implemented a

3-D finite-difference depth migration algorithm on a cluster of RISC/6000 (IBM 530) workstations that was networked via Ethernet and used the Network Linda parallel operating system. He parallelized his algorithm over frequencies and groups of depth-slices. Also, Schleicher and Copeland (1993) parallelized an one-pass 3-D migration algorithm with a variety of options for downward continuation including finite difference, phase shift plus interpolation and split-step transform methods on a network of RISC processors. Furthermore, they show the advantage of the RISC network system over a mainframe in terms of cost and performance after benchmarking the migration algorithm. Chen (1993) and Liu (1993) discussed parallel implementation of 3-D phase-shift migration and 3-D prestack Kirchhoff migration, respectively, on a cluster of workstations. Furthermore, Koshy et al. (1991) have exploited the inherent parallelism found in 3-D seismic ray tracing using a network of workstations (SUNs).

In the later chapters of this thesis, a number of migration and modeling algorithms are developed and implemented (Kalantzis et al., 1993) successfully on massively parallel computers and vector supercomputers (see Appendix A for a description of the computers used). 2-D elastic finite difference modeling algorithms were highly vectorized by Vafidis et al. (1992), and fine-tuned and implemented in this thesis on a Convex C210 for realistic simulations of wave propagation in reservoirs during thermally enhanced oil recovery. Also, 3-D acoustic modeling and reverse time migration algorithms were developed. They are based on an explicit finite difference MacCormack splitting scheme and have been vectorized and implemented on a Fujitsu VPX/240 supercomputer (see for a description of the Fujitsu supercomputer in Appendix A). The 3-D migration algorithm for a problem of size  $97 \times 113 \times 260$  and 800 time steps required about 28 minutes CPU time and attained over 90 percent total code (including I/O) vectorization on the Fujitsu VPX/210 supercomputer. The explicit finite difference modeling and migration algorithms have also been parallelized using both coarse-grain parallelism over space and domain of dependence decomposition (partial parallelism over time) with significant improvements in performance. Furthermore, implicit finite difference 2-D and one-pass 3-D poststack and prestack depth migration algorithms in the frequency-space domain has been developed and parallelized over frequencies and space. All above parallel modeling and migration algorithms have been implemented on a 44-processor MIMD Myrias SPS3 parallel computer (see for a description of the Myrias parallel computer in Appendix A). The one-pass 3-D depth migration (including I/O and FFT) for a 3-D data set of size  $90 \times 73$  CDPs, 1500 depth steps and 250 frequencies required about 9 hours of CPU time on 40 processors of a Myrias SPS3 MIMD parallel computer.

## 2.5 CONCLUSION

The high resolution imaging of the earth's structure and the prediction of its properties has always been the seismologist's dream. Thanks to current advances in computer technology, theoretical and experimental developments in our knowledge of seismic wave phenomena in the rocks, expanded usage of 3-D seismic and integration of geological and reservoir engineering information, this dream is on the verge of becoming reality.

3-D seismic technology plays an important role in exploration and development of hydrocarbons resources. 3-D seismic data provide a more accurate image of the earth's complex subsurface than 2-D data. But this leads to large data volumes (e.g., a typical marine survey has 40 million traces) that need sophisticated analysis. Both the large amount of data and sophisticated processing algorithms need enormous amounts of computing resources. However, *utilizing the inherent parallelism of seismic processes we can use parallel computers for accurate and efficient 3-D seismic processing.*

Parallelization depends on the numerical technique used and the size and type of the particular problem, e.g., model/grid size for modeling or data volume for migration. Therefore, we should exploit carefully the parallelism of each individual application. We should always assign parallel tasks with equivalent number of floating operations as the ones that the corresponding processors are capable of.

Also, the new generation of workstations can be used in *visualization, image processing* (e.g., contrast stretching, artificial illumination, edge detection etc.) and *interpretation of all aspects of 3-D seismic data* such as traveltime, depth, reflection amplitude, frequency, phase, polarity, dip, azimuth. Because of the greater need to interact with 3-D seismic data during processing and interpretation and the need to integrate seismic with geological and reservoir engineering information, there has been a shift from mainframe to interactive workstation applications. However, this shift does not imply a reduced need for supercomputers. Workstations merely provide a new interactive window to visualize and integrate the available data.

In the above sections we discussed current vector and parallel computer technology. We presented some of the problems and solutions that this technology presents, especially in seismic applications. Also, we reviewed a number of parallel seismic applications already implemented on a number of parallel systems.

In conclusion, we can see a potentially powerful *exploration and production seismic*

*integration paradigm* where the utilization of current and future computer technology together with sophisticated algorithms will enable us to manage, interact and integrate all available data. In large seismic processing centers, *vector/parallel supercomputers and MPPs can be used as compute servers and superintegrators of vast amounts of information*. On the other hand, *workstations and/or workstation clusters can be used as visualization, interaction and integration servers*. Furthermore, in smaller centers workstation clusters, connected to a larger machine capable of managing the large data volumes, could be used as *cost-performance effective compute servers and information integrators*.

## REFERENCES

- Astfalk, G., 1993a, Fundamentals and practicalities of MPP: The Leading Edge, **12**, No.3, 839-843.
- Astfalk, G., 1993b, Fundamentals and practicalities of MPP: The Leading Edge, **12**, No.9, 907-911.
- Astfalk, G., 1993c, Fundamentals and practicalities of MPP: The Leading Edge, **12**, No.10, 992-998.
- Black, J.L., Su, C.B., and Bauske, W.S., 1991, Networked parallel 3-D depth migration: 61st SEG Annual International Meeting and Exposition, Houston, Expanded Abstracts, 353- 356.
- Black, J.L., Su, C.B., and Bauske, W.S., 1992, Performance of parallel downward continuation: 62nd SEG Annual International Meeting and Exposition, New Orleans, Expanded Abstracts, 326-329.
- Blanc, J.Y., Huard, I., and Gomez, A., 1993, Three-dimensional Remez-Soubarau poststack depth migration: CRAY CHANNELS, **15**, No.3, 18-21.
- Charrette, E.E., 1991, Ray equation-based Kirchhoff prestack depth migration on the nCUBE: 61st SEG Annual International Meeting and Exposition, Houston, Expanded Abstracts, 341-343.
- Chen, T., 1993, Network parallel 3-D phase-shift migration: 63rd SEG Annual International Meeting and Exposition, Washington D.C., Expanded Abstracts, 177-179.
- Duncan, R., 1990, A survey of parallel computer architectures: Computer IEEE, **2**, 5-16.
- Eisner, E., 1989, Supercomputers in seismic exploration: Handbook of Geophysical

Press.

- English, W., 1993, Sharing workstations and clusters across an FDDI Campus Research Ring, In: Proceedings of Supercomputing Symposium '93, Calgary, Alberta, 119-126.
- Flynn, M., 1966, Very high speed computing systems: Proc. IEEE, **54**, 1901-1909.
- Fox, G., 1989, Solving problems on concurrent processors: Volume I, Prentice Hall, N.J.
- Fox, G., Hirandandani, S., Kennedy, K., Koebel, C., Kremer, U., Tseng, C., and Wu, M., 1990, Fortran D language specification: Technical Report TR90-141, Dept. of Computer Science, Rice University, Texas.
- Grewal, K., Williams, D., Schuh, C., and Bauwens, L., 1993: Performance benchmarks for finite-difference CFD code on 320-node Myrias, In: Proceedings of Supercomputing Symposium '93, Calgary, Alberta, 189-193.
- Highnam, P.T., and Pieprzak, A., 1991, Implementation of a fast , accurate 3-D migration on a massively parallel computer: 61st SEG Annual International Meeting and Exposition, Houston, Expanded Abstracts, 338-340.
- Holling M., and Ketelsen, K., 1991, 3-D time and depth migration at gigaflops speed: CRAY CHANNELS, **13**, No. 2, 4-7.
- Kalantzis, F., Dai, N., Kanasewich, E.R., Phadke, S., and Vafidis, A., 1993, 2-D and 3-D seismic reflection modeling and imaging using vector and parallel supercomputers: In Proceedings of Supercomputing Symposium '93, Calgary, Alberta, 25-32.
- Kapotas, S., 1991, 3-D imaging of reflection seismic wavefields using parallel computers: Ph.D. Thesis, University of Alberta.
- Kapotas, S., and Karpoff, W., 1993, Seismic applications on parallel MIMD machines Lessons from experience: In Proceedings of Supercomputing Symposium '93, Calgary, Alberta, 33-40.
- Kao, J.C., 1992, Multitasked computation of 3-D prestack Kirchhoff time migration on the Cray Y-MP C90: 62nd SEG Annual International Meeting, New Orleans, Expanded Abstracts, 3011-313.
- Kao, J.C., and Stoffa, P.L., 1992, Parallel implementation of poststack 3-D split-step depth migration on the Cray Y-MP C90: 62nd SEG Annual International Meeting, New Orleans, Expanded Abstracts, 307-310.
- Kao, J.C., 1993, Preconditioned iterative 3-D finite-difference depth migration ore modeling on the CRAY T3D massively parallel processors: 63nd SEG Annual International Meeting, Washington D.C., Expanded Abstracts, 185-188.

- International Meeting, Washington D.C., Expanded Abstracts, 185-188.
- Karpoff, W, and Lake, B., 1993, PARDO - a deterministic, scalable programming paradigm for distributed memory parallel computer systems and workstation clusters, In: Proceedings of Supercomputing Symposium '93, Calgary, Alberta, 145-152.
- Koshy, M., Pereya, V., and Meza, J., 1991, Distributed computing applications in forward and inverse geophysical modeling: 62st SEG Annual International Meeting, Houston, Expanded Abstracts, 349-352.
- Liu, L.L., 1993, 3-D prestack Kirchhoff migration: parallel computation on workstations: 63nd SEG Annual International Meeting, Washington D.C., Expanded Abstracts, 181-184.
- Moriarty, K.J.M., 1987, Supercomputers a personal perspective, in: Proceedings of Supercomputing Symposium '87, Calgary, Alberta, 57-100.
- Schleicher, K., and Copeland, J., 1993, Parallel one-pass 3-D migration: 63nd SEG Annual International Meeting, Washington D.C., Expanded Abstracts, 174-176.
- Vafidis, A., Abramovici, F., and Kanasewich, E.R., 1992, Elastic wave propagation using fully vectorized high order finite differences: *Geophysics*, **57**, 218-232.
- Van Trier, J., 1991, Prestack Kirchhoff depth migration on the Connection Machine, Thinking Machine Corporation, Technical Report Series, TMC-210.
- Wilson, D.C., and Karpoff, W.T., 1993, Dependence decomposition: parallel execution of time steps, In: Proceedings of Supercomputing Symposium '93, Calgary, Alberta, 73-80.



## CHAPTER 3

### SEISMIC MODELING

#### 3.1 INTRODUCTION

In the last decades, several techniques have been developed for simulating the propagation of seismic wavefields in the earth. Because of the large amount of data and the complex theoretical format, the conventional modeling schemes produced limited results in many cases. However, recent advances in computing based on the vector computation and the subdivision of the computational sequence into parallel components can allow the development and implementation of more accurate and cost effective methods.

In forward modeling one starts with an assumed earth model to generate the wave field by using ray tracing or solving wave equations. In order to gain an acceptable geological model, comparisons are often made between the synthetic and observed seismograms. In contrast, in imaging one attempts to construct a possible model from the observed seismic wave field.

Prior to the availability of supercomputers, seismic modeling was essentially performed in 1-D and 2-D using ray tracing. Even today with supercomputers available ray trace modeling is still the most widely used seismic modeling method. The main reason for that is that ray tracing is usually faster than wave equation methods and it is close to the way that a geophysicist thinks about how a seismic section is formed. However, ray theory (Cerveny et al., 1977), a high frequency approximation, breaks down in many cases such as at caustics the predicted amplitude is infinite and in shadow zones the amplitude is zero. On the other hand, in cases of complex geology and/or complex wave phenomena wave-equation modeling has a number of advantages over ray tracing. Some of these advantages are (Baker, 1989): (a) automatic generation of diffractions, critical refractions and multiples; (b) more accurate amplitudes and waveforms in the presence of small structures and thin beds; (c) no missing of seismic events regardless of complexity.

One group of approaches to seismic wave-equation modeling are the discrete-coordinate methods such as the finite difference methods (Alterman and Karal, 1968;

Alford et al, 1974; Boore, 1972; Kelly et al., 1976; Mufti, 1985; Dablain, 1986; Vafidis et al., 1992), the finite element methods (Smith, 1975; Marfurt, 1984) and other methods that combine time advancing algorithms and integral transformations with respect to space variables such as Fourier transform method (Bracewell, 1965, Reshef et al., 1988) and the pseudo-spectral method (Gottlieb and Orszag, 1977; Gazdag, 1981; Kosloff and Baysal, 1982; Mikhailenko and Korneev, 1984, Kosloff et al., 1984, Dablain, 1986; Fornberg, 1987).

In finite difference solutions, the spatial and time variables are discretized by superimposing a rectangular grid on the model. We can follow two approaches in the forward modeling (Kelly et al., 1976). The *homogeneous approach* is where we solve the wave equation and impose boundary conditions explicitly at each interface between the layers of the model. Alternatively, there is the *heterogeneous approach*, where we solve the wave equation directly for the whole model.

The finite difference method, since its introduction into computational seismology in the late sixties, has proved to be particularly versatile in extending the scope of solvable problems. The finite difference method offers a direct solution to the problem expressed in terms of the basic equations, and the initial and boundary conditions. In the elastic case, the method automatically accounts not only for direct waves, primary and multiple reflection waves but also converted waves, head waves, diffraction waves and waves observed in ray-theoretical shadow zones.

The finite difference method generally requires a large computer memory with high performance speed in order to avoid some significant problems associated with the technique. The first problem arises from the need to use fine grid spacing to avoid dispersion of energy which degrades the quality of the resulting seismograms. The second problem is numerical stability. In order to keep the model numerically stable, the ratio of time sampling-to-grid spacing must be kept very small and this results in a prohibitive amount of CPU time. Also, truncation errors are introduced by replacing the wavefield derivatives with difference relations in finite difference solutions. Their magnitude depends on the size of the grid spacing and time sampling interval. But the resultant truncation errors are negligible and the computed seismograms are very accurate since we use a fine grid and temporal sampling to avoid dispersion and instability. Therefore, with the advent of supercomputer technology these problems can be overcome and finite difference methods can receive special attention because they are capable of producing a complete synthetic seismogram for a realistic earth model.

Finite difference schemes can generally be placed in two broad categories: *explicit* and *implicit*. In explicit schemes, the response is evaluated exclusively at one space location at an advanced time directly from the response on the neighboring grid points already determined at previous times. In implicit schemes, the response is evaluated simultaneously at all space locations at an advanced time from known values at previous times through a matrix inversion technique. The explicit operators are easier and more economical to implement but suffer from stability problems. For hyperbolic equations the explicit schemes are preferred because the stability conditions are not as severe as with parabolic equations.

One of the key factors in forward modeling is the implementation of the source. For the two dimensional problem, since an axial symmetry is implied, we use a line source. In three dimensions we use a point source. Convolution of the impulse response with the source excitation results in an integral which can be numerically evaluated (Romberg or Gauss integration). A Gaussian function whose frequency response is band limited with a known peak frequency is often used to describe the source excitation.

A basic problem in theoretical seismology is to determine the wave response of a given model to the excitation of an impulsive source by solving the wave equations under certain simplifications. In a scalar approximation, the acoustic wave equation may be solved to evaluate the waveform but only compressional waves (P-waves) are considered.

A more complete approach is to study the vector displacement field using the full elastic wave equation for modeling both P-waves and shear waves (S-waves). A more realistic simulation can be performed through the heterogeneous elastic wave equation in two dimensions since coupling between P and SV waves is considered. Methods which allow the modeling of seismic wave propagation in complex laterally and vertically varying structures, containing combinations of isotropic and anisotropic layers, are highly desirable. In order to calculate the elastic response of a model, two coupled second order differential equations must be solved simultaneously. Instead of solving this second order system, the equivalent first order system was solved numerically for isotropic media (Vafidis et al., 1992) and for transversely isotropic media (Tsingas et al., 1990). This system consists of the basic equations of motion in the x and z directions and the stress-strain relations.

However, important wave properties such as attenuation and dispersion require a more sophisticated set of equations, such as Biot's equations for porous media. Biot (1956) developed a theory from the view point of continuum mechanics for wave motion in

a porous elastic solid saturated with a viscous compressible fluid. This is an inertial flow model where attenuation of wave energy is due to the motion of the pore fluid relative to the rock frame. More recently de la Cruz and Spanos (1985) constructed macroscopic wave equations for elastic porous media filled with viscous fluid by using volume averaging techniques in conjunction with physical arguments. Wave dispersion and dissipation in these models are mainly due to the viscous fluid motion relative to the solid matrix. Numerical solution of Biot's acoustic wave equations is given by Hassanzadeh (1991) and a second order finite difference solution to Biot's poroelastic wave equations is proposed by Zhu and McMechan (1991). Dai (1993) reformulated Biot's and de la Cruz-Spanos equations into first order differential system which enable one to obtain the fluid and solid particle velocities and stress components and also the fluid pressure. For the two-dimensional problem of wave propagation in porous media, SH waves decouple from P and SV waves. The Biot's model predicts the existence of one shear and two compressional waves with a faster and a slower velocity. However, mathematical models based on this type of mechanism suffer many times from excessive free parameters that makes realistic wave simulations for exploration targets very difficult or impossible.

Considerable progress has been also made in seismic wave attenuation for single phase material. In this context, seismic attenuation is taken to describe any energy losses, other than those due to spherical divergence, reflections, transmissions and mode conversions, which a seismic wave experiences as it propagates through a medium. Emmerich and Korn (1987) used a generalized Maxwell body to approximate an arbitrary Q law yielding a second order differential equation system with extra intermediate variables for SH waves. A first order hyperbolic system has been derived for 2-D anelastic acoustic wave motion by Vafidis et al. (1993) based on the generalized Maxwell body approximation and solved with an explicit finite difference scheme. Furthermore, Blanch et al. (1993) used finite difference schemes to model wave propagation in 2-D and 3-D viscoelastic media. On the other hand, Carcione et al. (1988) used pseudo-spectral methods for simulation of viscoelastic wave propagation.

Despite the extensive theoretical and algorithmic developments described above, realistic and accurate wave propagation simulations in elastic, viscoelastic and porous media are possible only in two dimensions due to memory and computational limitations of current computer technology.

The advent of the new generation of supercomputers motivated this work towards realistic simulations of wave propagation with higher accuracy in two and three

dimensional inhomogeneous media. In this research we developed a 3-D acoustic modeling algorithm for simulating the evolution of a pressure field. Furthermore, existing algorithms such as 2-D elastic (P-SV and SH) modeling algorithms (Vafidis et al., 1992) have been modified and fine-tuned for realistic elastic wave simulations. Both 3-D acoustic and 2-D elastic algorithms have been vectorized, parallelized and implemented on vector and parallel supercomputers, such as the CONVEX 210 vector computer, the Fujitsu VPX 240/10 supercomputer and the Myrias SPS-3 MIMD parallel computer.

Computer simulations of seismic wave propagation were essential for the interpretation of the field data from enhanced oil recovery projects studied in this thesis. Using the above algorithms, finite difference modeling of seismic waves in acoustic and elastic media in two and three dimensions in the region over the steam-heated zone during cyclic steam stimulation of oil sands was performed, as it will be shown in later chapters. These modeling studies were undertaken in order to examine the relation between reservoir properties such as porosity, saturation and permeability with seismic characteristics such as velocity, amplitude and frequency modification with time.

## **3.2 ELASTIC MODELING IN TWO DIMENSIONS**

### **3.2.1 Introduction**

In forward seismic modeling the wave response of a given model to the excitation of an impulsive source is determined by solving the wave equations. When we use the acoustic wave equation to evaluate the waveform only compressional waves (P-waves) are considered. However, if we use the full elastic wave equation the vector displacement field can be evaluated since we consider both compressional (P) and shear (S) waves.

Vafidis et al. (1992) developed 2-D elastic wave modeling algorithms and implemented them on a Cyber 205 vector supercomputer. In this part, we modified his algorithms, applied more accurate absorbing boundaries, fine-tuned, and implemented them on vector/parallel supercomputers and massively parallel processors (MPPs). However, present computer limitations did not allow us to expand them into three dimensions. Nevertheless, accurate and realistic simulations of seismic wave propagation were performed in very detailed and sophisticated 2-D elastic reservoirs before and after steam injection in oil sands at Cold Lake, Alberta.

### 3.2.2 The Equations and the Numerical Method

For two dimensional SH-wave propagation in a heterogeneous medium the basic equation can be solved. This equation in a heterogeneous isotropic medium is:

$$\frac{\partial}{\partial x} \left( \mu(x,z) \frac{\partial u}{\partial x} \right) + \frac{\partial}{\partial z} \left( \mu(x,z) \frac{\partial u}{\partial z} \right) = \rho(x,z) \frac{\partial^2 u}{\partial t^2} \quad (3.2.1)$$

where  $u(x,z,t)$  is the displacement in the horizontal plane and in the y-direction,  $\mu(x,z)$  is the shear modulus,  $\rho(x,z)$  is the density and  $\partial$  denotes partial derivative. Body forces have been neglected. But instead of solving numerically this second order hyperbolic wave equation one can use an equivalent first order system (Virieux, 1984 and 1986) which can be derived from the equation of motion and the stress-strain relations for isotropic media (Vafidis et al., 1992) and transversely isotropic media (Tsingas et al., 1990). For heterogeneous isotropic media the equation of motion is

$$\frac{\partial v}{\partial t} = \frac{1}{\rho} \left( \frac{\partial \sigma_{xy}}{\partial x} + \frac{\partial \sigma_{zy}}{\partial z} \right) \quad (3.2.2)$$

and the stress-strain relations

$$\begin{aligned} \frac{\partial \sigma_{xy}}{\partial t} &= \mu \left( \frac{\partial v}{\partial x} \right) \\ \frac{\partial \sigma_{zy}}{\partial t} &= \mu \left( \frac{\partial v}{\partial z} \right) \end{aligned} \quad (3.2.3)$$

From the above equations (3.2.2, 3.2.3) one obtains the following equivalent first order system (Virieux, 1984, 1986, Bayliss et al., 1986; Vafidis et al., 1992) in matrix form

$$\frac{\partial}{\partial t} \begin{bmatrix} v \\ \sigma_{xy} \\ \sigma_{zy} \end{bmatrix} = \begin{bmatrix} 0 & \rho^{-1} & 0 \\ \mu & 0 & 0 \\ 0 & 0 & 0 \end{bmatrix} \frac{\partial}{\partial x} \begin{bmatrix} v \\ \sigma_{xy} \\ \sigma_{zy} \end{bmatrix} + \begin{bmatrix} 0 & 0 & \rho^{-1} \\ 0 & 0 & 0 \\ \mu & 0 & 0 \end{bmatrix} \frac{\partial}{\partial z} \begin{bmatrix} v \\ \sigma_{xy} \\ \sigma_{zy} \end{bmatrix} \quad (3.2.4)$$

$v(x,z,t)$  is the particle velocity in the y-direction and  $\sigma_{xy}(x,z,t)$  and  $\sigma_{zy}(x,z,t)$  are the stress components. The above equation can be written in a compact form as

$$\partial_t \mathbf{U} = \mathbf{A} \partial_x \mathbf{U} + \mathbf{B} \partial_z \mathbf{U} \quad (3.2.5)$$

Numerical solutions to the SH-wave equation do not describe converted phases. A more realistic simulation can be performed through the elastic wave equation in two dimensions since coupling between P and SV-waves is considered. Methods which allow the modeling of seismic wave propagation in complex laterally and vertically varying structures, containing combinations of isotropic and anisotropic layers, are highly desirable. In order to calculate the elastic response of a model two coupled second order differential equations must be solved simultaneously. Instead of solving this second order system, the equivalent first order system will be solved numerically. This system consists of the basic equations of motion in the x and z directions and the stress-strain relations after taking the first time derivative

$$\rho \frac{\partial \dot{u}}{\partial t} = \frac{\partial \sigma_{xx}}{\partial x} + \frac{\partial \sigma_{xz}}{\partial z} \quad (3.2.6)$$

$$\rho \frac{\partial \dot{w}}{\partial t} = \frac{\partial \sigma_{xz}}{\partial x} + \frac{\partial \sigma_{zz}}{\partial z}$$

and the stress-strain relations after taking the first time derivatives

$$\frac{\partial \sigma_{xx}}{\partial t} = (\lambda + 2\mu) \frac{\partial \dot{u}}{\partial x} + \lambda \frac{\partial \dot{w}}{\partial z}$$

$$\frac{\partial \sigma_{xz}}{\partial t} = \mu \left( \frac{\partial \dot{w}}{\partial x} + \frac{\partial \dot{u}}{\partial z} \right) \quad (3.2.7)$$

$$\frac{\partial \sigma_{zz}}{\partial t} = \lambda \frac{\partial \dot{u}}{\partial x} + (\lambda + 2\mu) \frac{\partial \dot{w}}{\partial z}$$

where  $u=u(x,z,t)$  and  $w=w(x,z,t)$  are the particle displacements in the x and z directions

respectively;  $\dot{u}$  and  $\dot{w}$  are particle velocities;  $\sigma_{xx}$ ,  $\sigma_{xz}$ ,  $\sigma_{zz}$ , are the stress components;  $\mu=\mu(x,z)$  and  $\lambda=\lambda(x,z)$  are the Lamé parameters;  $\rho=\rho(x,z)$  is the density;  $\partial$  denotes partial derivative; and dot denotes time derivative. In this formulation there are no space derivatives of the Lamé coefficients.

Equations (3.2.6) and (3.2.7) can be written in matrix form (Vafidis et al., 1992)

$$\frac{\partial}{\partial t} \begin{bmatrix} \dot{u} \\ \dot{w} \\ \sigma_{xx} \\ \sigma_{zz} \\ \sigma_{xz} \end{bmatrix} = \begin{bmatrix} 0 & 0 & \rho^{-1} & 0 & 0 \\ 0 & 0 & 0 & 0 & \rho^{-1} \\ \lambda+2\mu & 0 & 0 & 0 & 0 \\ \lambda & 0 & 0 & 0 & 0 \\ 0 & \mu & 0 & 0 & 0 \end{bmatrix} \frac{\partial}{\partial x} \begin{bmatrix} \dot{u} \\ \dot{w} \\ \sigma_{xx} \\ \sigma_{zz} \\ \sigma_{xz} \end{bmatrix} + \begin{bmatrix} 0 & 0 & 0 & 0 & \rho^{-1} \\ 0 & 0 & 0 & \rho^{-1} & 0 \\ 0 & \lambda & 0 & 0 & 0 \\ 0 & \lambda+2\mu & 0 & 0 & 0 \\ \mu & 0 & 0 & 0 & 0 \end{bmatrix} \frac{\partial}{\partial z} \begin{bmatrix} \dot{u} \\ \dot{w} \\ \sigma_{xx} \\ \sigma_{zz} \\ \sigma_{xz} \end{bmatrix} \quad (3.2.8)$$

or again in a compact form

$$\partial_t \mathbf{U} = \mathbf{A} \partial_x \mathbf{U} + \mathbf{B} \partial_z \mathbf{U} \quad (3.2.9)$$

Furthermore, Tsingas et al. (1990) formulated the P-SV and SH problem for transversely isotropic elastic inhomogeneous media.

Equations (3.2.5) and (3.2.9) describe first order hyperbolic systems that are solved numerically using an explicit finite difference method based on the MacCormack splitting scheme. Using a splitting in time approach (Strang, 1968), the solution  $\mathbf{U}$  of the equations (3.2.5, 3.2.9) can be approximated by

$$\mathbf{U}^{n+2} = \mathbf{F}_x \mathbf{F}_z \mathbf{F}_z^\dagger \mathbf{F}_x^\dagger \mathbf{U}^n \quad (3.2.10)$$

where  $\mathbf{F}_x$ ,  $\mathbf{F}_x^\dagger$  are one-dimensional difference operators approximating the solution of the one-dimensional equation



$$\partial_t U(x,z,t) = A \partial_x U(x,z,t) \quad (3.2.11)$$

while  $F_z$  and  $F_z^\dagger$  correspond to a similar partial differential equation with respect to  $z$  and  $x=x_0$ , a constant. The MacCormack scheme (Gottlieb and Turkel, 1976), applied to (3.2.11) consists of a predictor and a corrector (section 3.3.4). The MacCormack scheme for particle velocity and stress components in the  $x$ -direction for 2-D elastic (P-SV and SH) modeling is given by Vafidis (1988).

### 3.2.3 Absorbing Boundaries for 2-D Elastic Modeling

The size of the models used in wave propagation simulations is limited both laterally and vertically by the available computer memory. When implementing discrete methods such as finite difference for wave-equation modeling one major consideration is the generated artificial reflections from the model boundaries. Therefore, it is necessary to simulate infinite boundaries on the finite computational grid. Depending upon the problem and the strength of the artificial reflections different boundary conditions can be used, such as approximate-radiation conditions (for simulating an infinite medium), stress free conditions (Neuman condition or free surface condition) and the zero particle velocity condition which is equivalent to zero displacement condition (Dirichlet condition or rigid surface condition).

Lysmer and Kuhlemeyer (1969) imposed viscous behavior on the artificial boundaries so that much of the incident energy is absorbed mathematically. For first order systems this condition becomes a Dirichlet condition and can be implemented easily (Bayliss et al., 1986). This condition is exact for normal incident P and S- waves. However, it does not absorb Rayleigh waves since it is based on the one-dimensional characteristics. One way of solving this problem is by burying the source.

Clayton and Engquist (1977), Reynolds (1978) and Keys (1985) used the paraxial approximation of the wave equation for constructing absorbing boundary conditions. However, these conditions have limitations for large angle of incidence to the boundary.

Israeli and Orszag (1981) approximated radiation conditions at the numerical boundaries using one-dimensional transmissive sponge boundaries. They proposed an operator that can transmit waves in one direction and attenuate them in the opposite direction. Cerjina et al. (1985), Kosloff and Kosloff (1986) and Sochacki et al. (1987)

implemented on second order wave-equation modeling this sponge approach for boundary conditions. They enlarged the computational grid and used a damping mechanism on the additional part of the computational grid. However, this approach is computationally expensive, since the sponge must be applied smoothly over a transition zone three to five wavelengths long in order to avoid artificial scattering from the sponge itself.

More recently, Dai (1993) developed one-dimensional absorbing boundary conditions, based on the characteristic analysis of the first order hyperbolic systems, that absorb perpendicularly incident waves. For P-SV wave modeling the 1-D absorbing conditions for the bottom boundary can be described by the following equation (Dai, 1993):

$$\begin{bmatrix} u \\ w \\ \sigma_{xx} \\ \sigma_{zz} \\ \sigma_{xz} \end{bmatrix} = \frac{1}{2} \begin{bmatrix} 0 & 1 & 0 & 1 & 0 \\ 1 & 0 & 0 & 0 & 1 \\ \frac{-\lambda}{V_p} & 0 & 1 & 0 & \frac{\lambda}{V_p} \\ -V_p\rho & 0 & 0 & 0 & V_p\rho \\ 0 & -V_s\rho & 0 & V_s\rho & 0 \end{bmatrix} \begin{bmatrix} w^{(l)} - \frac{\sigma_{zz}^{(l)}}{V_p\rho} \\ u^{(l)} - \frac{\sigma_{xz}^{(l)}}{V_s\rho} \\ 0 \\ 0 \\ 0 \end{bmatrix} \quad (3.2.12)$$

where  $u^{(l)}$ ,  $w^{(l)}$ ,  $\sigma_{zz}^{(l)}$  and  $\sigma_{xz}^{(l)}$  are the values of  $u$ ,  $w$ ,  $\sigma_{zz}$  and  $\sigma_{xz}$  at the bottom boundary calculated by the finite difference scheme just prior to the transition zone. Furthermore, Dai (1993) implements the 1-D boundary conditions in combination with conditions that are imposed in a transition zone adjacent to the boundary region. In the transition zone, he uses a wave modification method that adjusts the propagating waves so that they reach the boundaries at normal angles, or a sponge filter that selectively dissipates the remaining incoming waves. For example, for the bottom boundary region, the modification method, basically, produces a the transition zone which is anisotropic and in which the velocities laterally change smoothly to zero. Therefore, the outgoing waves from the transition zone are perpendicular to the bottom boundary where thereafter the 1-D absorbing conditions can absorb them effectively.

In the sponge approach a dissipative factor is basically imposed on the waves as they

propagate through the transition zone by adding a damping term in the wave equation (Dablain, 1986; Dai, 1993).

Ideally, we would like an absorbing boundary condition that has maximum absorbing power and minimum amount of memory and computation requirements. However, here we are interested in a practical solution that is accurate enough but also computationally efficient in terms of CPU and memory requirements.

In the elastic wave simulations that we perform at the Cold Lake oil sands (Chapter 6) we use absorbing boundaries that combined three techniques. First, we include an absorbing boundary region (no more than 30 grid nodes in each direction). Second, we use the wave modification technique that modifies the outgoing waves so that the wavefront reaches the borders at normal angles. This is succeeded by imposing some kind of anisotropy in the medium's physical parameters in the border area. Third, we apply a mirror image technique at the edge of the boundary. This technique imposes values on all differential operators at every time step so that they are mirror images of the corresponding values inside the grid. This combined approach in the absorbing region enables us to generate synthetic seismograms free of artificial reflections from the finite boundaries of the models used.

### **3.3 ACOUSTIC MODELING IN THREE DIMENSIONS**

#### **3.3.1 Introduction**

Most seismic modeling is currently conducted in 2-D using both ray tracing and wave equation. Some ray tracing is performed in 3-D and there is a limited amount of 3-D wave-equation modeling. However, accurate and realistic 3-D wave-equation modeling is becoming increasingly important as we collect more 3-D data, search for smaller and complex reservoirs, and use enhanced oil recovery methods. A 3-D world requires a 3-D solution. 3-D modeling can help in the optimum selection of the acquisition parameters, in understanding amplitude variations as a function of offset, in the identification of lateral velocity variations and estimation of more accurate velocity models, and in more dependable interpretation of the real seismic data. However, because of its stringent computational demands it is still mostly a research tool and constitutes a challenge for today's most powerful computers (Mufti, 1989; Mora, 1988 and 1989; Fagin, 1991; Piau et al., 1991; Kapotas, 1991).

Pereyra et al. (1992) performed 3-D elastic wave simulations using the finite element method. In one of the largest up-to-date simulations using this approach, they simulate a single shot experiment over a recumbent fold geologic model. They solved this problem using a grid with  $234 \times 234 \times 240$  elements and about 13.3 million nodes, a 3 Hz pressure source, 1700 time steps and time increment of 0.6 ms, on a Fujitsu VP2400/10 in 4.5 CPU-hours with sustained rate of performance of about 0.5 Gflops.

The numerical solution of the 3-D acoustic wave equation provides a useful method for simulating the evolution of a pressure field which corresponds to the P type of body waves most frequently used.

Reshef et al. (1988) solved the acoustic wave equation using spatial derivatives in the Fourier domain on a GRAY X-MP supercomputer. However, among the existing methods for forward modeling, finite difference methods are the most popular. Mufti (1985) developed an implicit finite difference modeling algorithm in order to avoid numerical stability problems and he used higher order differences in order to use larger grid intervals and thus to overcome computational limitations. Also, Mufti (1989) implemented 3-D explicit finite difference modeling on a CRAY-2 supercomputer. In terms of parallelization, Mora (1988) performed 3-D acoustic modeling on a CM2 SIMD parallel computer. Also, Kapotas (1991) performed explicit finite difference 3-D acoustic modeling for a medium size problem (grid dimensions:  $80 \times 80 \times 80$ ) on a parallel MIMD computer.

Realistic large scale 3-D acoustic wave modeling for simulating 3-D seismic surveys is possible today with the availability of powerful vector and parallel supercomputers. The larger virtual memory of the todays supercomputers results in finer grids which dramatically minimize the dispersion effects even for the popular second order schemes.

Mufti (1989), after developing a fourth order finite difference modeling algorithm, asked the following question: "What else can be done to develop a modeling algorithm which yields more accurate results than the simple fourth-order algorithm?" Here, we have an answer to this question. We developed a very fast vectorized and parallelized accurate algorithm for modeling the acoustic wave propagation in a 3-D heterogeneous medium. However, due to the massive number of grid points in a 3-D model, we did not consider the use of implicit finite difference approach, but used an explicit method in the time domain. The acoustic wave equation after it is reduced into a first order hyperbolic system is solved with a particle velocity-stress finite difference method and the dimensional splitting technique. This method is a version of the MacCormack scheme that is second order accurate in time and fourth order accurate in space. The algorithm is highly vectorized

following the semantic vectorization approach and using the matrix times vector by diagonals technique. Also, the algorithm is parallelized utilizing grain parallelism over depth and using the domain of dependence decomposition technique that results in a partial parallelism over time. The algorithm is implemented on either vector and parallel supercomputers with results that are pronounced in both execution time and in handling quite large models. An original hyperbolic system is also formulated for one-way wave propagation in heterogeneous three dimensional media. This system is used in implementing absorbing boundaries.

In the following sections, we present the formulation of the system of first order partial differential equations (hyperbolic system) which is equivalent to the 3-D scalar wave equation. Also, we describe the computational aspects of the finite difference code and details for the absorbing boundaries. Simple numerical examples, such as a two layer 3-D model, illustrate the fundamental aspects of propagation in three dimensional media. 3-D synthetic seismograms and snap shots are generated for the French model (two domes and a fault). Furthermore, large scale 3-D acoustic wave propagation simulations are performed for realistic models at the Cold Lake oil sands.

### 3.3.2 Problem Formulation: Equations

In this development, we consider a 3-D medium with two horizontal axes,  $x$  and  $y$ , and a vertical axis pointing downward. The medium is assumed isotropic. The 3-D acoustic scalar wave equation (see Appendix B) is

$$\frac{\partial^2 P}{\partial x^2} + \frac{\partial^2 P}{\partial y^2} + \frac{\partial^2 P}{\partial z^2} = \frac{1}{V^2(x,y,z)} \frac{\partial^2 P}{\partial t^2} , \quad (3.3.1)$$

where  $P=P(x,y,z,t)$  is the pressure field; and  $V=V(x,y,z)=\sqrt{K(x,y,z)/\rho}$  is the seismic wave velocity in the medium where  $K(x,y,z)$  is the bulk modulus and  $\rho$  is the density independent of spatial coordinates. However, instead of using the above equation we consider the equations of motion

$$\rho \frac{\partial^2 u_x}{\partial t^2} = \frac{\partial P}{\partial x} , \quad (3.3.2)$$

$$\rho \frac{\partial^2 u_y}{\partial t^2} = \frac{\partial P}{\partial y}, \quad (3.3.3)$$

$$\rho \frac{\partial^2 u_z}{\partial t^2} = \frac{\partial P}{\partial z}, \quad (3.3.4)$$

and the pressure-strain relation

$$P = K \left( \frac{\partial u_x}{\partial x} + \frac{\partial u_y}{\partial y} + \frac{\partial u_z}{\partial z} \right). \quad (3.3.5)$$

In the above equations ( $u_x, u_y, u_z$ ) is the displacement vector,  $\rho = \rho(x, y, z)$  is the density and  $K = K(x, y, z)$  is the bulk modulus or incompressibility. By taking the time derivative of both sides in (3.3.5) and by replacing the displacement vector with the particle velocity vector ( $v_x, v_y, v_z$ ), we obtain the following first-order partial differential equations:

$$\frac{\partial P}{\partial t} = K \left( \frac{\partial v_x}{\partial x} + \frac{\partial v_y}{\partial y} + \frac{\partial v_z}{\partial z} \right), \quad (3.3.6)$$

$$\rho \frac{\partial v_x}{\partial t} = \frac{\partial P}{\partial x}, \quad (3.3.7)$$

$$\rho \frac{\partial v_y}{\partial t} = \frac{\partial P}{\partial y}, \quad (3.3.8)$$

and

$$\rho \frac{\partial v_z}{\partial t} = \frac{\partial P}{\partial z}. \quad (3.3.9)$$

In matrix form this system of equations can be written as :

$$\frac{\partial \mathbf{U}}{\partial t} = \mathbf{A} \frac{\partial \mathbf{U}}{\partial x} + \mathbf{B} \frac{\partial \mathbf{U}}{\partial y} + \mathbf{C} \frac{\partial \mathbf{U}}{\partial z} \quad (3.3.10)$$

where

$$\mathbf{U} = \begin{bmatrix} P \\ v_x \\ v_y \\ v_z \end{bmatrix} \quad (3.3.11)$$

$$\mathbf{A} = \begin{bmatrix} 0 & K & 0 & 0 \\ \rho^{-1} & 0 & 0 & 0 \\ 0 & 0 & 0 & 0 \\ 0 & 0 & 0 & 0 \end{bmatrix} \quad (3.3.12)$$

$$\mathbf{B} = \begin{bmatrix} 0 & 0 & K & 0 \\ 0 & 0 & 0 & 0 \\ \rho^{-1} & 0 & 0 & 0 \\ 0 & 0 & 0 & 0 \end{bmatrix} \quad (3.3.13)$$

$$\mathbf{C} = \begin{bmatrix} 0 & 0 & 0 & K \\ 0 & 0 & 0 & 0 \\ 0 & 0 & 0 & 0 \\ \rho^{-1} & 0 & 0 & 0 \end{bmatrix} \quad (3.3.14)$$

This system is hyperbolic since the eigenvalues of the matrices  $\mathbf{A}$ ,  $\mathbf{B}$  and  $\mathbf{C}$  are real and their eigenvectors are independent. The above system is solved in the next sections for 3-D acoustic modeling of seismic wave propagation in heterogeneous media.

### 3.3.3 Source Excitation

We use an explosive point source whose analytic solution can be evaluated from Green's function in a free infinite homogeneous space. For a point source located at  $(x_s, y_s, z_s)$ , the pressure is given by (Aki and Richards, 1980):

$$P(x, y, z, t) = \frac{1}{4\pi d} S\left(t - \frac{d}{V}\right), \quad (3.3.15)$$

where  $d = \sqrt{(x-x_s)^2 + (y-y_s)^2 + (z-z_s)^2}$ , the prime denotes derivative and the time variation of the source is taken as a Gaussian function  $S(t) = C e^{-\sigma(t-t_1)^2}$  with  $\sigma$  and  $C$  constants and  $t_1$  a positive time delay. The particle velocities are given by

$$v_x = \frac{1}{\rho} \left[ \frac{1}{d^2} S\left(t, \frac{d}{V}\right) - \frac{1}{Vd} S'\left(t, \frac{d}{V}\right) \right] \frac{x - x_s}{d} \quad (3.3.16)$$

$$v_y = \frac{1}{\rho} \left[ \frac{1}{d^2} S\left(t, \frac{d}{V}\right) - \frac{1}{Vd} S'\left(t, \frac{d}{V}\right) \right] \frac{y - y_s}{d} \quad (3.3.17)$$

$$v_z = \frac{1}{\rho} \left[ \frac{1}{d^2} S\left(t, \frac{d}{V}\right) - \frac{1}{Vd} S'\left(t, \frac{d}{V}\right) \right] \frac{z - z_s}{d} . \quad (3.3.18)$$

### 3.3.4 Numerical Solution

The finite difference numerical method is based on the concept of splitting in time (Strang, 1968). Equation (3.2.10) can be written in a linearized version as

$$\frac{\partial U}{\partial t} = \mathbf{A} \frac{\partial U}{\partial x} + \mathbf{B} \frac{\partial U}{\partial y} + \mathbf{C} \frac{\partial U}{\partial z} = (\mathbf{L}_x + \mathbf{L}_y + \mathbf{L}_z) \mathbf{U} . \quad (3.3.19)$$

From Taylor's theorem

$$\begin{aligned} U(x, y, z, t+\Delta t) &= \left( 1 + \Delta t \frac{\partial}{\partial t} + \frac{1}{2} \Delta t^2 \frac{\partial^2}{\partial t^2} + \dots \right) U(x, y, z, t) = \\ &= \exp\left(\Delta t \frac{\partial}{\partial t}\right) U(x, y, z, t) = \\ &= \exp\left[\Delta t (\mathbf{L}_x + \mathbf{L}_y + \mathbf{L}_z)\right] U(x, y, z, t) \end{aligned} \quad (3.3.20)$$

but

$$\exp(\Delta t (\mathbf{L}_x + \mathbf{L}_y + \mathbf{L}_z)) = \exp\left(\frac{\Delta t}{2} \mathbf{L}_x\right) \exp\left(\frac{\Delta t}{2} \mathbf{L}_y\right) \exp(\Delta t \mathbf{L}_z) \exp\left(\frac{\Delta t}{2} \mathbf{L}_y\right) \exp\left(\frac{\Delta t}{2} \mathbf{L}_x\right) \quad (3.3.21)$$

is accurate up to second order in time and the corresponding difference approximation is

$$U^{n+2} = F_x F_y F_z F_z^+ F_y^+ F_x^+ U^n \quad (3.3.22)$$



where  $F$  denotes 1-D difference operators,  $U^n$  represents the discrete vector of unknowns at time  $t=n \Delta t$ . One advantage of splitting methods is that stability is governed by the 1-D schemes. Also, splitting methods have smaller phase error than a wide class of unsplit schemes (Turkel, 1979).

The  $F_x$ ,  $F_x^+$  are one-dimensional difference operators approximating the solution of the one-dimensional equation

$$\partial_t U(x,y,z,t) = A \partial_x U(x,y,z,t) \quad (3.3.23)$$

Each operator advances the time step by 1/3 of a time interval so that the final output from the six operators is  $n+2$  time units.

For the finite difference solution, a grid mesh ( $I \times J \times K$ ) is superimposed on a 3-D model. The discrete points are defined as  $(x_i, y_j, z_k, t_n)$  and  $x_i = i \Delta x$  for  $i=0, 1, \dots, I$ ;  $y_j = j \Delta y$  for  $j=0, 1, \dots, J$ ;  $z_k = k \Delta z$  for  $k=0, 1, \dots, K$ ; and  $t_n = n \Delta t$  for  $n=0, 1, \dots, N$ ; where  $\Delta x$ ,  $\Delta y$  and  $\Delta z$  are the grid spacings in  $x$ ,  $y$  and  $z$ -directions and  $\Delta t$  is the time step. Consider a (2,4) version of the MacCormack scheme (Vafidis et al., 1992) which when applied to the one dimensional system (3.3.23) in the  $x$ -direction consists of the predictor:

$$U_{i,j,k}^{(1)} = U_{i,j,k}^n - \frac{\Delta t}{6 \Delta x} A_{i,j,k} (7U_{i,j,k}^n - 8U_{i+1,j,k}^n + U_{i+2,j,k}^n) \quad (3.3.24)$$

and the corrector:

$$U_{i,j,k}^{n+1/3} = \frac{1}{2} (U_{i,j,k}^{(1)} + U_{i,j,k}^n) + \frac{\Delta t}{12 \Delta x} A_{i,j,k} (7U_{i,j,k}^{(1)} - 8U_{i-1,j,k}^{(1)} + U_{i-2,j,k}^{(1)}) \quad (3.3.25)$$

where  $\Delta t$  is the time step (in seconds),  $\Delta x$  is the grid spacing (in meters) in the  $x$ -direction, the subscripts  $i, j, k$  correspond to  $x, y, z$  and the superscript (1) denotes the intermediate step. Equations (3.3.24) and (3.3.25) are used in alternate time steps with:

$$U_{i,j,k}^{(1)} = U_{i,j,k}^n + \frac{\Delta t}{6 \Delta x} A_{i,j,k} (7U_{i,j,k}^n - 8U_{i+1,j,k}^n + U_{i+2,j,k}^n) \quad (3.3.26)$$

and

$$U_{i,j,k}^{n+1/3} = \frac{1}{2} (U_{i,j,k}^{(1)} + U_{i,j,k}^n) - \frac{\Delta t}{12 \Delta x} A_{i,j,k} (7U_{i,j,k}^{(1)} - 8U_{i-1,j,k}^{(1)} + U_{i-2,j,k}^{(1)}) \quad (3.3.27)$$

A detailed description of the MacCormack scheme for the pressure and the particle velocity components is given in the Appendix C.

In terms of accuracy the MacCormack scheme is second order in time and fourth order in space. The splitting technique in one direction is described by equations (3.3.24 to 3.3.27). In three dimensions the MacCormack splitting scheme is performed in the following steps: (1) the pressure field and the particle velocity components are calculated at time step  $n+1/3$  taking into account wave propagation in the x-direction only, using equations (3.3.24, 25); (2) then, they are evaluated at time step  $n+2/3$  taking into account wave propagation in the y-direction only, using a similar set of equations as the (3.3.24, 25); (3) then the wave field is evaluated at time step  $n+1$  taking into account wave propagation in the z-direction only, using a similar set of equations as the (3.3.24, 25); (4) the alternate expressions similar to (3.3.26, 27) are applied at time  $n+4/3$  taking for propagation in the z-direction; (5) then, they are calculated for propagation in the y-direction at time  $n+5/3$  from alternate equations similar to (3.3.26, 27); and (6) finally, the pressure field and the particle velocity components are evaluated for propagation in the x-direction at time  $n+2$  using alternate equations (3.3.26,27).

Waves propagating on a discrete grid become progressively dispersed with time. This is called grid dispersion. The higher frequency waves are delayed relative to the ones of lower frequency. As a result, on the synthetic seismograms a substantial “tailing” of the signal is generated. Grid dispersion increases as the grid spacing becomes larger. Dispersion analysis indicates that the shortest wavelengths in the model need to be sampled at five grid points per wavelength. Thus, to avoid grid dispersion, the grid spacing must be

$$\Delta x < \frac{\lambda_{\min}}{6} \quad (3.3.28)$$

where the  $\lambda_{\min}$  is the minimum wavelength present in the computations and it relates to the minimum wave velocity. In general, the spatial resolution is based on the minimum seismic wave velocity and the stability condition is based on the maximum wave velocity present in the model. The stability condition of the method (Gottlieb and Turkel, 1976) is

$$\frac{\Delta t}{\Delta x} V_{\max} < \frac{2}{3} \quad (3.3.29)$$

where  $\Delta t$  is time step,  $\Delta x$  is the grid spacing and  $V_{\max}$  is the maximum seismic velocity present in the model. This yields the largest time steps for computational efficiency without losing temporal accuracy.

### 3.3.5 Absorbing Boundary Conditions for 3-D Acoustic Modeling

Internal interfaces are not treated by explicit boundary conditions because they are in a heterogeneous formulation (Kelly et al., 1976). They are represented naturally by changes of physical parameters of the model. However, difficulty arises in the boundary regions since both incoming and outgoing waves are present. A boundary condition is required to minimize the incoming waves from the artificial boundary reflections. Only six explicit boundary conditions have to be considered: the six sides of the finite-sized model. Here, we introduce a new set of absorbing boundaries for waves propagating in 3-D. We will derive the boundary condition for the bottom side of the model by applying characteristic analysis (Dai, 1993) to the 1-D wave system

$$\frac{\partial U}{\partial t} = \mathbf{C} \frac{\partial U}{\partial z} . \quad (3.3.30)$$

Assume that  $U(z,t)$  is a solution of the above equation in the computational region  $z \in (0,H)$ . Then, we can write

$$\mathbf{L}_C^{(i)} \mathbf{C} = \lambda_i \mathbf{L}_C^{(i)} \quad (3.3.31)$$

$$\mathbf{C} \mathbf{R}_C^{(i)} = \lambda_i \mathbf{R}_C^{(i)} \quad (3.3.32)$$

where  $\lambda_i$  is an eigenvalue of  $\mathbf{C}$  with the corresponding left eigenvectors  $\mathbf{L}_C^{(i)}$  (row vector) and the right eigenvectors  $\mathbf{R}_C^{(i)}$  (column vector) and because of the orthonormality of left and right eigenvectors

$$\mathbf{L}_C^{(i)} \mathbf{R}_C^{(j)} = \delta_{ij} \quad (3.3.33)$$

Then, from equations (3.3.31,32,33) it follows that

$$\mathbf{L}_C \mathbf{C} \mathbf{R}_C = \Lambda \quad (3.3.34)$$

and the one-dimensional equation (3.3.30) for the acoustic problem can be expressed as

$$\frac{\partial \mathbf{U}}{\partial t} = \mathbf{R}_C \Lambda \mathbf{L}_C \frac{\partial \mathbf{U}}{\partial z} \quad (3.3.35)$$

where  $\mathbf{L}_C$  consists of rows that are the normalized left eigenvectors of  $\mathbf{C}$

$$\mathbf{L}_C = \frac{1}{\sqrt{2}} \begin{bmatrix} 1 & 0 & 0 & -\sqrt{K\rho} \\ 0 & \sqrt{2} & 0 & 0 \\ 0 & 0 & \sqrt{2} & 0 \\ 1 & 0 & 0 & -\sqrt{K\rho} \end{bmatrix} \quad (3.3.36)$$

$\mathbf{R}_C$  consists of columns that are the normalized right eigenvectors of  $\mathbf{C}$

$$\mathbf{R}_C = \frac{1}{2} \begin{bmatrix} 1 & 0 & 0 & 1 \\ 0 & \sqrt{2} & 0 & 0 \\ 0 & 0 & \sqrt{2} & 0 \\ \frac{1}{-\sqrt{K\rho}} & 0 & 0 & \frac{1}{\sqrt{K\rho}} \end{bmatrix} \quad (3.3.37)$$

and  $\Lambda$  is diagonal with  $\Lambda_{ii} = \lambda_i$  ordered so that  $\lambda_1 < \lambda_2 < \lambda_3 < \lambda_4$ . For  $\lambda_i < 0$  we have downgoing waves and for  $\lambda_i > 0$  we have upcoming waves. The eigenvalues of  $\mathbf{C}$  for the acoustic case are  $(\lambda_1, \lambda_2, \lambda_3, \lambda_4) = (-\sqrt{\frac{K}{\rho}}, 0, 0, \sqrt{\frac{K}{\rho}}) = (-V, 0, 0, V)$ , where  $V = \sqrt{\frac{K}{\rho}}$  is the wave velocity in the medium. Thus,  $\Lambda$  can be written in matrix form as

$$\Lambda = \begin{bmatrix} -\sqrt{\frac{K}{\rho}} & 0 & 0 & 0 \\ 0 & 0 & 0 & 0 \\ 0 & 0 & 0 & 0 \\ 0 & 0 & 0 & \sqrt{\frac{K}{\rho}} \end{bmatrix} \quad (3.3.38)$$

Substituting equations (3.3.36, 37, 38) into equation (3.3.35) and allowing only downgoing wave propagation by letting  $\lambda_4 = 0$ , we obtain the one dimensional one-way system

$$\frac{\partial}{\partial t} \begin{bmatrix} P \\ v_x \\ v_y \\ v_z \end{bmatrix} = \frac{1}{2} \begin{bmatrix} -\sqrt{\frac{K}{\rho}} & 0 & 0 & K \\ 0 & 0 & 0 & 0 \\ 0 & 0 & 0 & 0 \\ \frac{1}{\rho} & 0 & 0 & -\sqrt{\frac{K}{\rho}} \end{bmatrix} \frac{\partial}{\partial z} \begin{bmatrix} P \\ v_x \\ v_y \\ v_z \end{bmatrix} \quad (3.3.39)$$

or in compact form

$$\frac{\partial U}{\partial t} = C_d \frac{\partial U}{\partial z} \quad (3.3.40)$$

Then, the 3-D one-way wave system in the bottom or top absorbing region taking into account only *downgoing* (+z) or *upgoing* (-z) waves, respectively, and setting no restriction for waves propagating in the x and y direction, becomes

$$\frac{\partial U}{\partial t} = \mathbf{A} \frac{\partial U}{\partial x} + \mathbf{B} \frac{\partial U}{\partial y} + C_{\pm} \frac{\partial U}{\partial z} \quad (3.3.41)$$

where **A** and **B** are the same as in the full 3-D system and are given by (3.3.12) and

(3.3.13), respectively, and  $C_{\pm}$  is given by

$$C_{\pm} = -\frac{1}{2} \begin{bmatrix} \pm\sqrt{\frac{K}{\rho}} & 0 & 0 & -K \\ 0 & 0 & 0 & 0 \\ 0 & 0 & 0 & 0 \\ -\frac{1}{\rho} & 0 & 0 & \pm\sqrt{\frac{K}{\rho}} \end{bmatrix} \quad (3.3.42)$$

Also, the 3-D one-way wave system in the left or right side absorbing regions taking into account only -x or +x outgoing waves, respectively, and setting no restriction for waves propagating in the y and z direction, becomes

$$\frac{\partial U}{\partial t} = A_{\pm} \frac{\partial U}{\partial x} + B \frac{\partial U}{\partial y} + C \frac{\partial U}{\partial z} \quad (3.3.43)$$

where  $A_{\pm}$  is given by

$$A_{\pm} = -\frac{1}{2} \begin{bmatrix} \pm\sqrt{\frac{K}{\rho}} & -K & 0 & 0 \\ -\frac{1}{\rho} & \pm\sqrt{\frac{K}{\rho}} & 0 & 0 \\ 0 & 0 & 0 & 0 \\ 0 & 0 & 0 & 0 \end{bmatrix} \quad (3.3.44)$$

and  $B$  and  $C$  are the same as in the full 3-D system (3.3.10) and are given by (3.3.13) and (3.3.14), respectively. Furthermore, the 3-D one-way wave system in the front or back side absorbing region taking into account only -y or +y outgoing waves, respectively, and setting no restriction for waves propagating in the x and z direction, becomes

$$\frac{\partial U}{\partial t} = A \frac{\partial U}{\partial x} + B_{\pm} \frac{\partial U}{\partial y} + C \frac{\partial U}{\partial z} \quad (3.3.45)$$

where  $B_{\pm}$  is given by

$$B_{\pm} = -\frac{1}{2} \begin{bmatrix} \pm \sqrt{\frac{K}{\rho}} & 0 & -K & 0 \\ 0 & 0 & 0 & 0 \\ -\frac{1}{\rho} & 0 & \pm \sqrt{\frac{K}{\rho}} & 0 \\ 0 & 0 & 0 & 0 \end{bmatrix} \quad (3.3.46)$$

and A and C are the same as in the full 3-D system (3.3.10) and are given by (3.3.12) and (3.3.14), respectively.

The *dispersion relation of the 3-D acoustic one-way wave system for downgoing waves* is

$$\frac{k_z^*}{k} = \frac{k^2 - k_x^2 - k_y^2}{k^2 - \frac{1}{2}k_x^2 - \frac{1}{2}k_y^2} \quad (3.3.47)$$

On the other hand the dispersion relation of the 3-D full scalar wave equation is

$$\frac{k_z}{k} = \sqrt{1 - \frac{k_x^2}{k^2} - \frac{k_y^2}{k^2}} \quad (3.3.48)$$

If we use two-way wave propagation in the model volume and one-way wave (downgoing) propagation in the absorbing region, the effective reflectivity at the bottom boundary is

$$r = \frac{k_z - k_z^*}{k_z + k_z^*} \quad (3.3.49)$$

Substituting (3.3.47) and (3.3.48) into (3.3.49) we have

$$r(\theta, \phi) = \frac{\cos\theta - (1 - \sin^2\theta \sin^2\phi - \sin^2\theta \cos^2\phi)(1 - 0.5 \sin^2\theta \sin^2\phi - 0.5 \sin^2\theta \cos^2\phi)^{-1}}{\cos\theta + (1 - \sin^2\theta \sin^2\phi - \sin^2\theta \cos^2\phi)(1 - 0.5 \sin^2\theta \sin^2\phi - 0.5 \sin^2\theta \cos^2\phi)^{-1}} \quad (3.3.50)$$

where

$$k = \frac{\omega}{V}, \quad k_x = \frac{\omega}{V} \sin\theta \sin\phi, \quad k_y = \frac{\omega}{V} \sin\theta \cos\phi \quad (3.3.51)$$

with  $\theta$  and  $\phi$  denoting the wave propagating angles measured from the z-axis to the x-y plane and from the y-axis to the x-axis. Figure 3.1 illustrates the reflectivity versus  $\theta$  and  $\phi$ . We observe that the reflectivity takes very small values. Thus, the one-way wave system is effective when used as an absorbing boundary condition.

### 3.3.6 Numerical Examples

In this section the method is tested with a simple wave propagation problem of two half spaces separated by an interface (Aki and Richards, 1980). In generating synthetic seismograms the following procedure is taken. First a P-wave velocity and a density value are assigned to each grid point. Also the model parameters like grid spacing, source and receiver locations, dimensions of the model etc. must be given. It should be noted that any receiver and source geometry can be handled by the 3-D modeling algorithm. Second, from the stability condition of the numerical scheme and the maximum P-wave velocity we calculate the maximum time step. Third, the source is inserted in the computational grid through the pressure. The numerical scheme described in the previous section is applied at every grid point in order to advance in time the four components of the propagation vector. Particle velocity or pressure synthetic seismograms are generated at all recording locations in the computational grid by extracting the particle velocity or pressure amplitude at those grid points for a sequence of time steps and then plotting these values as time series.

Figure 3.2 illustrates the model geometry where the receivers are located along two parallel lines and the source is located between the receiver lines. This two layer model was excited by point source whose time function is Gaussian with peak frequency at 30 Hz and the delay time  $t_1$  is 100 ms. Figure 3.3 illustrates the analytical and numerical solutions for



a source-receiver distance of 48 m. The numerical solution is calculated using grid spacing 5.5 m and time step 1 ms. Portion of the 3-D synthetic shot gather for the pressure field (Figure 3.4.a) show a very strong direct wave arriving at around 85 ms while the reflected waves are very weak (almost invisible). The particle velocity field (vertical component) is shown in Figure 3.4.b where we mainly observe the reflected waves at around 140 ms.

### **3.4 VECTORIZATION OF THE FINITE DIFFERENCE MODELING ALGORITHMS**

Matrices are viewed usually in terms of rows and columns, and in most of the scientific programming languages a row or column type storage is assumed. For band matrices however, a very efficient way of minimizing storage requirements is the storage by diagonals. In a vector computer every diagonal will be viewed as a vector. In addition to saving space, this type of storage has the advantage of allowing one to perform a number of matrix manipulations e.g., matrix transposition. There is however a price to pay for these advantages, namely the matrix algorithms are more difficult to describe and the whole picture is less intuitive. Besides, the diagonals have different lengths and their total number is larger than the number of rows or columns. Madsen et al. (1976) gave a description of the matrix multiplication by diagonals both for full and band matrices.

Since only vector operations are involved, the algorithm is suitable for vector computers. For narrow-band matrices the algorithm is more efficient than the row by column multiplication. Finite difference (FD) schemes consist of a number of simple vector operations (vector additions and vector multiplications) including matrix by vector multiplications. Matrix times vector by diagonals is a very efficient vectorized algorithm which helps in the complete vectorization of the FD scheme. The technique described above decreases the computational time of FD by a factor of about 50 (Vafidis et al. 1992).

The 2-D elastic modeling algorithms were implemented on a Convex C210 vector "mini"-supercomputer (see Appendix A for a description of the Convex C210). Elastic simulations on a model of grid size 400 x 800 nodes and 8000 time steps required about 2 hours of CPU time. On the other hand, the 3-D acoustic modeling algorithm due to its large CPU and memory requirements was implemented on a Fujitsu VPX/240 supercomputer (see Appendix A for a description of the Fujitsu) in order to handle large 3-D models.

*(Text continued on page 57)*

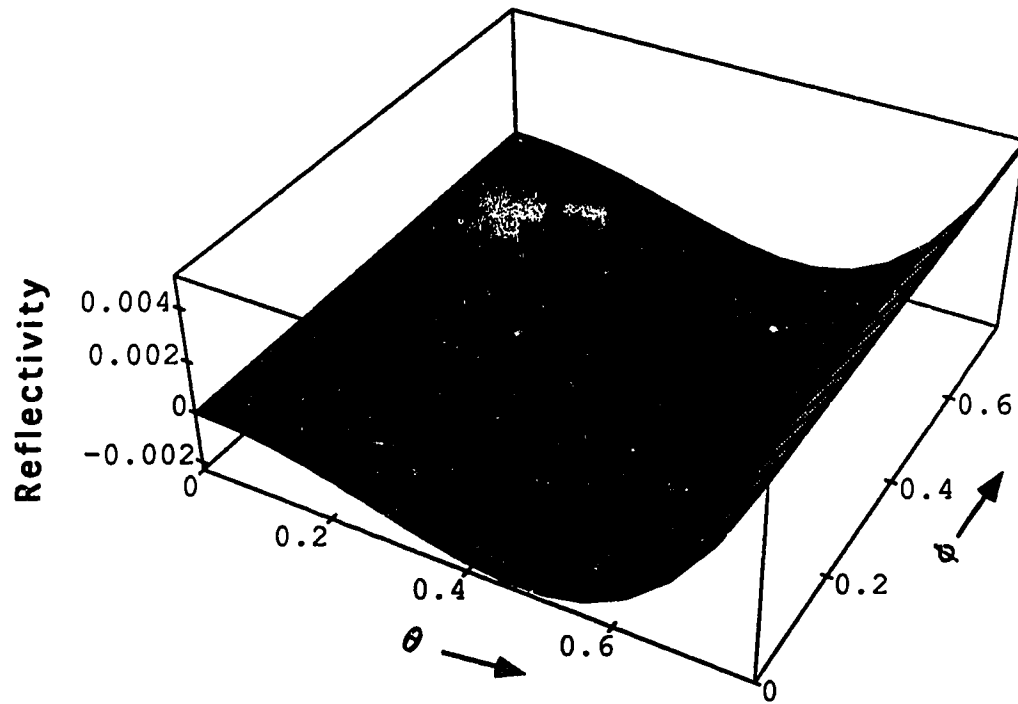


**Figure 3.1:** Reflectivity versus the wave propagating angles.

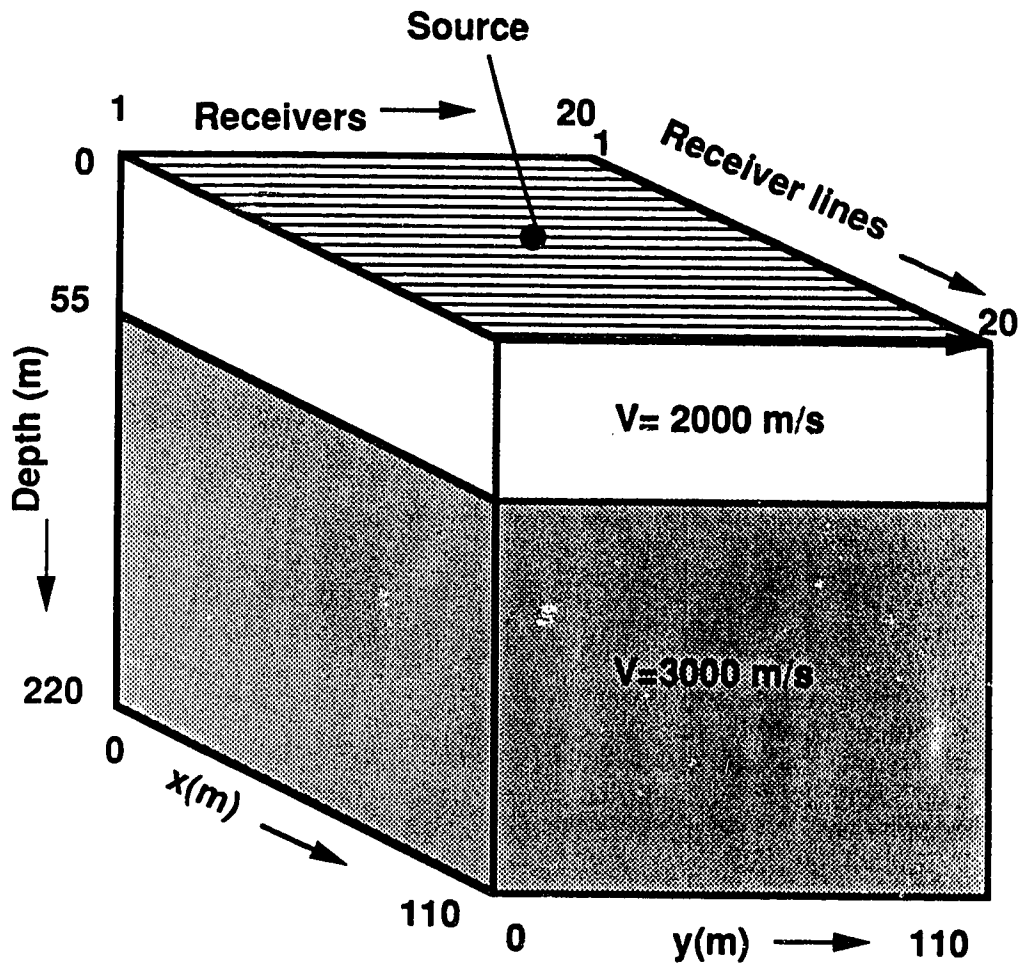
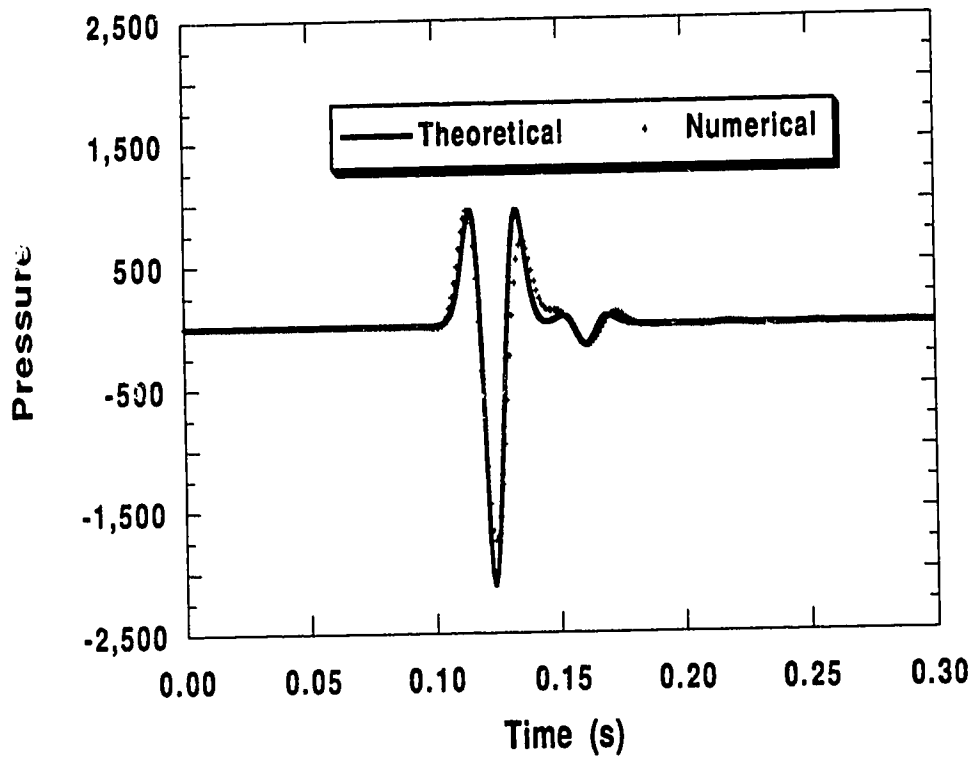
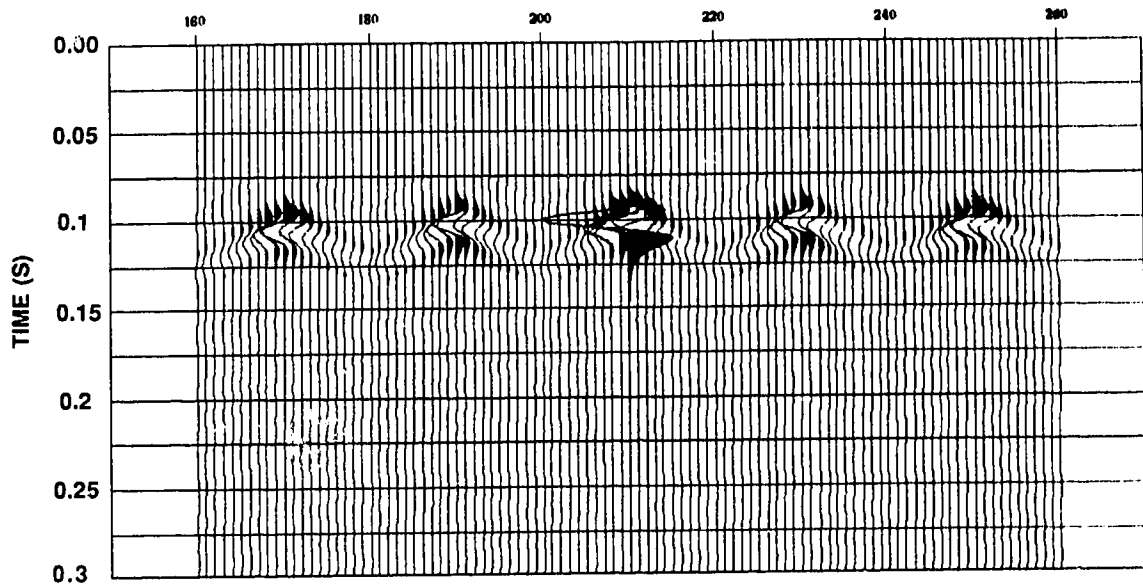


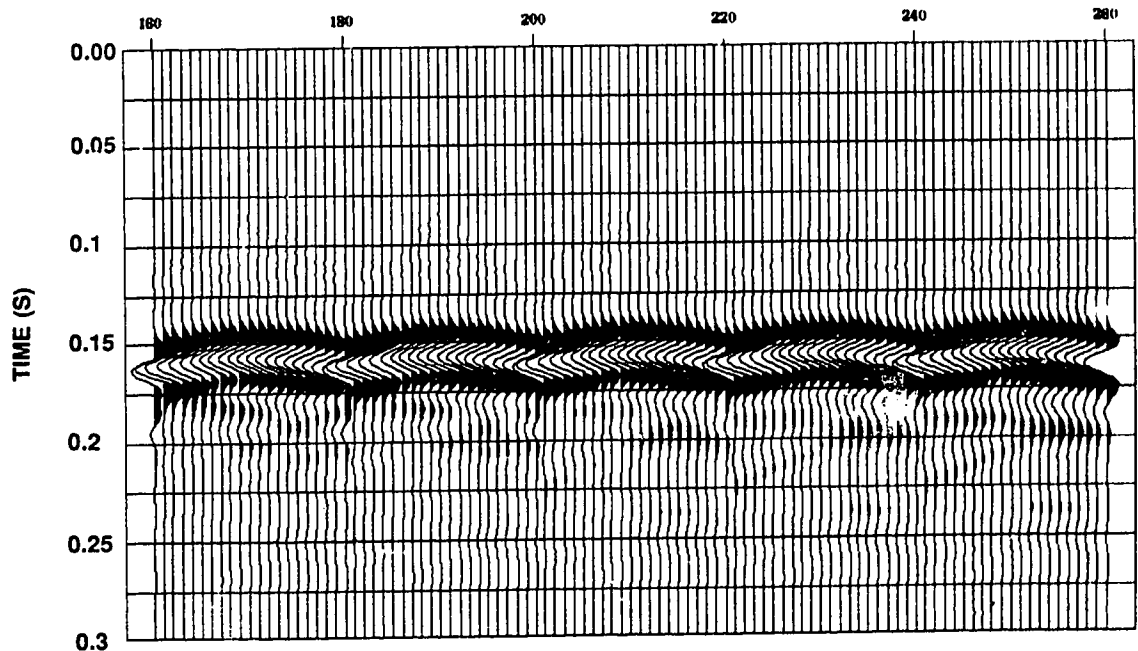
Figure 3.2 : The two-layer model used for testing the 3-D acoustic modeling method



**Figure 3.3 :** The analytical (theoretical) and numerical solutions at a source-receiver distance of 48 m for the two layer model that was excited by point source whose time function is Gaussian with peak frequency at 30 Hz and a time delay of 100 ms.



(a)



(b)

Figure 3.4 : Portion of the 3-D synthetic seismograms (shot gathers) for the pressure field (a) and for the particle velocity field (b) from 3-D acoustic modeling on the two-layer model.

The 3-D modeling algorithm is highly vectorized and is implemented without any tuning on the Fujitsu VPX/240. The code attained high vectorization (including I/O) during execution that varied between 90 and 98 percent for various applications of different I/O requirements. High temporal and spatial resolution simulations for a model of grid size 100 x 150 x 200 nodes and 8000 time steps required 130 minutes of CPU time with a total vectorization of 98 percent.

### 3.5 SEISMIC MODELING IN PARALLEL

From our experience with finite difference modeling on vector computers such as Cyber 205 and Convex 210, we believe that existing limitations in simulating wavefields in two and three dimensions are related to the limited memory and CPU capacity available on these computers. For example, a realistic acoustic wave simulation for a 2-D model of dimensions 2000 X 3000 m and grid spacing 1 m requires 240 MBytes of memory. Also, the splitting technique used requires 112 floating point operations (multiplications and additions) per grid point in order to advance the solution by one time step. For overcoming problems due to the large CPU time and memory requirements of the above algorithms, we have developed parallel algorithms for 2-D and 3-D finite difference modeling.

As shown above, the MacCormack splitting type finite difference scheme involves 1-D operators in x, z directions (and y if we are doing 3-D modeling). For the operator in x direction, the wavefield at grid point (i,k) at the next time level is calculated from the wavefield at grid points (i-2,k), (i-1,k), (i+1,k), (i+2,k) at the current time level; similarly for the operator in z direction. Therefore, only second order neighbours in every direction are required for calculations. Neighbours along diagonal directions are not needed. Figure 3.5 illustrates the computation of the wavefield in time and along only one direction (x). Based on the above observations one can introduce parallel task allocation into each grid point location. The ultimate goal would be to have as many processors as grid points. However, this *fine-grain parallelism* cannot be utilized on a MIMD parallel computer since the amount of computations at each grid point is not floating point intensive but rather it is communication intensive. Thus, intercommunication between the processors during the execution of parallel tasks is the key requirement for parallelizing finite difference in time domain.

The evolution of the wavefield with time is based on the above scheme which as we showed has local characteristics. This makes the algorithm suitable for implementation on a

parallel multiprocessor network. The outer most loop that can be parallelized is source loop. Each shot can be simulated independently on a every processor.

Furthermore, a *coarse grain-parallelism* over space can be utilized. Parallelism runs over one of the spatial coordinates allowing the other spatial domains to be computed serially inside each task for higher efficiency. If we have a 2-D model matrix ( $I \times K$ ), then depending upon the number of the available processors we divide the model matrix into submatrices. Our algorithm is flexible, we can partition the model in many ways or the algorithm itself can calculate the best way to partition the problem. Since second order neighbours (Figure 3.5) are involved in the calculations, to perform time marching on a submatrix we need two additional rows and columns on each of its sides. Each model submatrix ( $L \times M$ ) is assigned to a processor and requires  $[(L+4) \times (M+4)]$  memory space per task (Figure 3.6.a). However, the memory requirement on each node (processor or task) for SH and P-SV elastic wave simulation is  $[15 \times (L+4) \times (M+4)]$  and  $[25 \times (L+4) \times (M+4)]$ , respectively. The number of 15 and 25 represents the number submatrices (arrays) for the required physical parameters stored on each node, for the SH and P-SV problem, respectively. After all the physical parameters required by the individual nodes are distributed to the respective processors, the calculations begin. Using the intercommunication capability of the processors (Figure 3.6.b), after each time step the data along the boundaries of the submatrices (two rows and two columns) are exchanged with the immediate neighbours. For the submatrices along the boundaries of the whole model the immediate neighbours are less than four and therefore, lesser data exchange is involved. However, computations along the boundaries of the model are performed in a different manner since boundary conditions are implemented.

We have implemented this parallel algorithm on a 44-processor Myrias SPS<sup>2</sup> MIMD parallel computer. The implementation is based on the uncashed shared memory approach of the Myrias system (see Appendix A) for the intertask communication and on the creation of "semaphores" for the synchronization of tasks. There is a significant improvement in performance in comparison to the the serial version implemented on the Convex 210. However, we did not benchmark the parallel algorithm. Phadke (personal communication, 1993) has benchmarked the SH version of this parallel algorithm on a transputer based parallel computer. The processing nodes are T-800 transputers from INMOS Ltd. of UK with 4 MBytes of memory each. For SH wave simulation, the algorithm was implemented on 50 nodes: (1) for model size 250x250 and 1000 time steps, the required CPU time was 536 sec; (2) for model size 500x500 and 1500 time steps, the required CPU time was 1745

seconds.

Although computations within each time step can be parallelized as we have shown above, we recognized two problems: one, there is typically insufficient work to achieve high parallel efficiencies, and two, increased paging movement between the processors since at each time step intercommunication between the processors and synchronization of tasks is necessary. The explicit finite difference algorithms such as the one we parallelized above have an outer loop over time steps, which can not be parallelized because a given iteration depends on the results of the previous iteration. However, we can solve this problem by using an algorithmic technique called *domain of dependence decomposition* (Wilson and Karpoff, 1993) that provide us with a partial parallelism over time. Kapotas and Karpoff (1993) have applied this technique for the parallelization of explicit finite difference algorithms, based on the second order scalar wave equation, such as 2-D reverse time migration.

The dependence decomposition as it was implemented on the 2-D elastic modeling algorithm is described next. We subdivide the solution matrix into subregions based on one spatial dimensions (1-D decomposition). Then, we compute each one of these subregions in parallel but independently; no communication and synchronization between parallel tasks is required. This process is repeated for a number of time steps until further computations cannot be made; "building picks." Then, we merge the subregions, now synchronization and communication between processors is required, and divide the model matrix by shifting the division point by one half of the width of the subregions. The computations start again independently for each subregion; "filling valleys". This technique is a two-step process that can continue alternatively until the desired model matrix is computed (Figure 3.7.a). As a result, the propagation of the wavefield can be advanced several time steps with a number of global synchronizations that is less than the number of time steps.

We can apply two or three-dimensional decomposition by dividing the global model matrix into smaller regions in one, two or three (for 3-D models) spatial coordinates, respectively. However, decomposition in more than one-dimension is a more complicated technique. Because after the first step, that is the building of "pyramids", we need to repartition the computational grid in more than one direction in order to fill all the "valleys", thus resulting into a more than two step process. For example, in Figure 3.7.b a four-step 2-D decomposition technique is shown where we are building pyramids and filling valleys.

*(Text continued on page 63)*



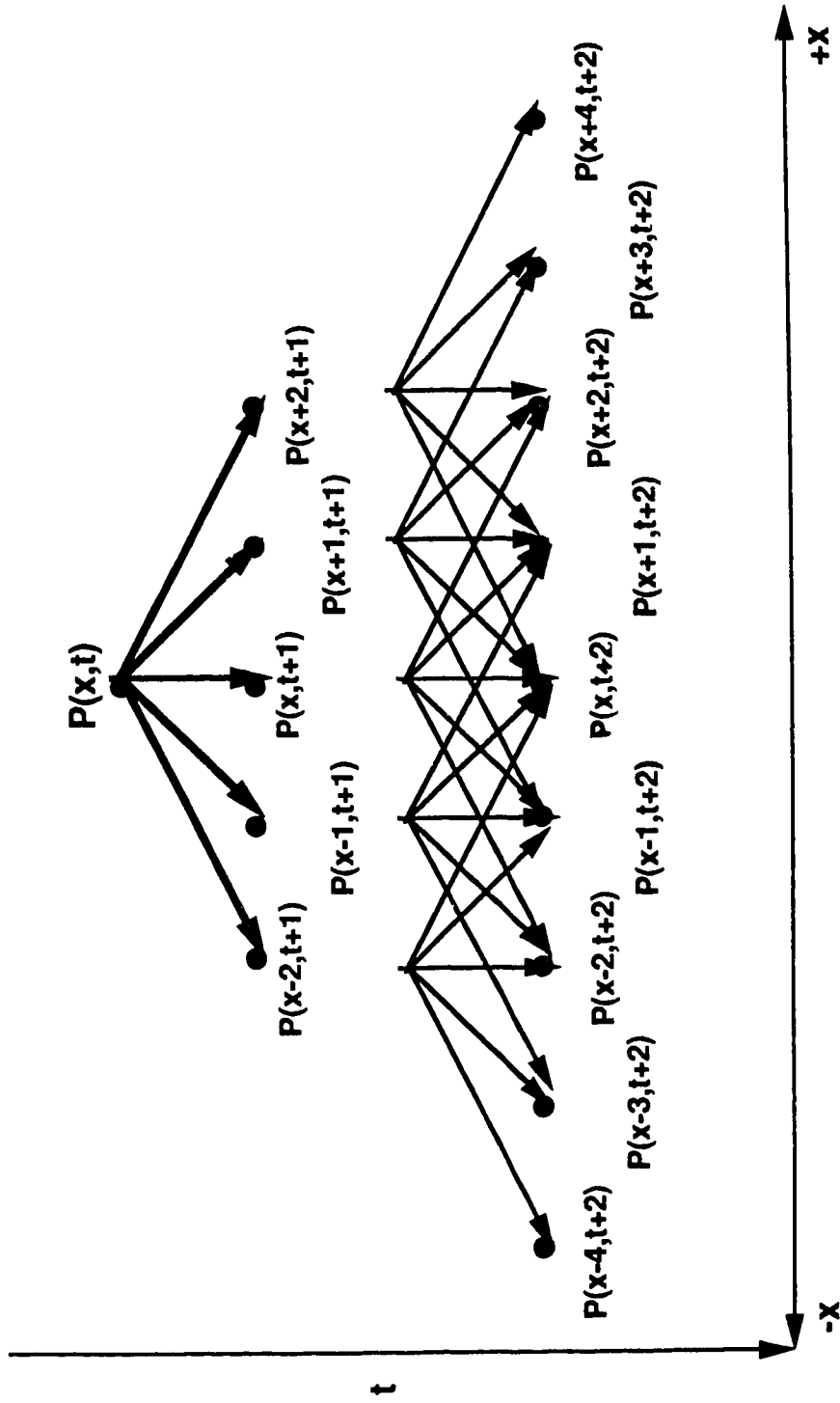
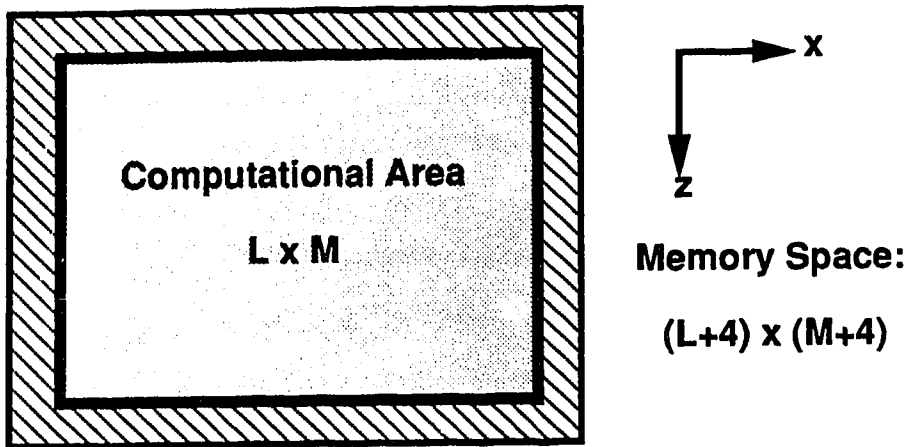


Figure 3.5 : Finite difference solution for the operator in the x-direction. Up to second order neighbours in every direction are required for calculations at each time step.

(a) DATA STRUCTURE FOR EACH TASK / PROCESSOR



(b) COMMUNICATION BETWEEN TASKS

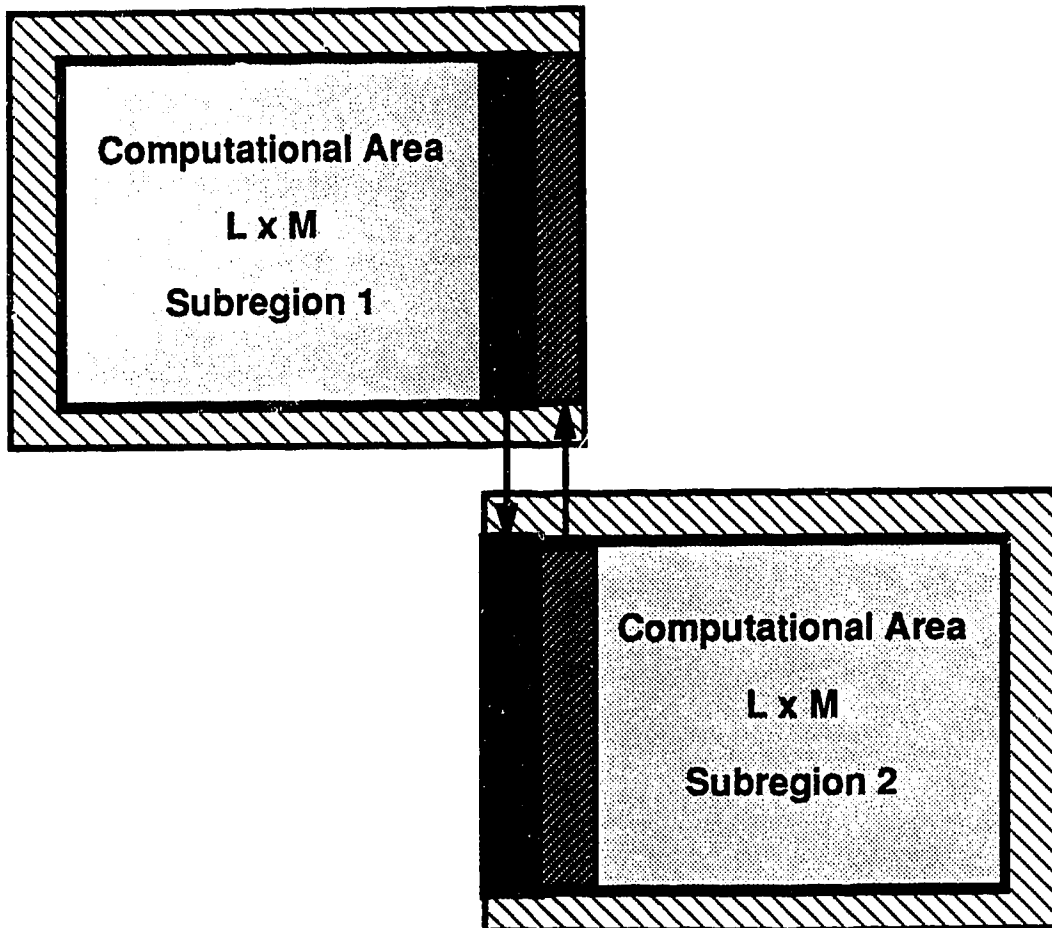
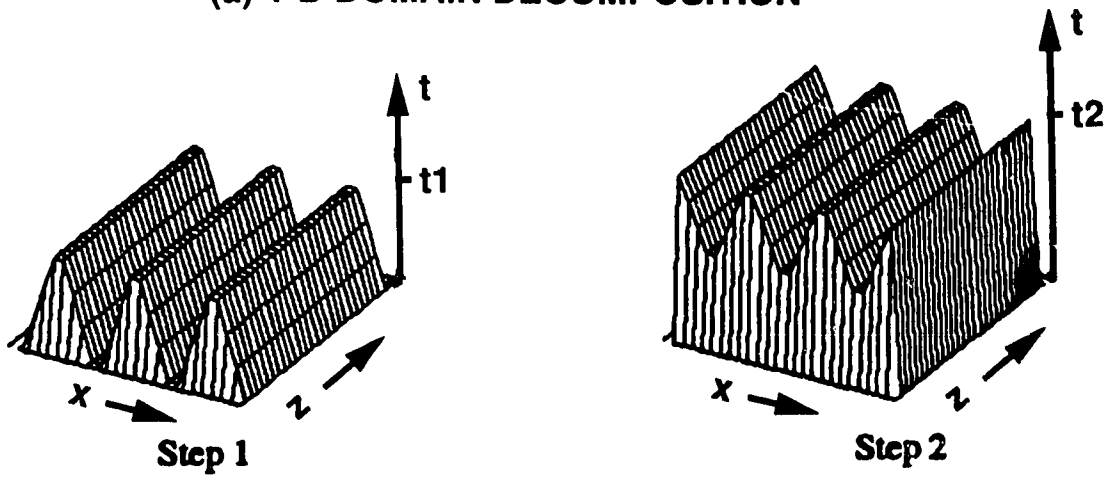
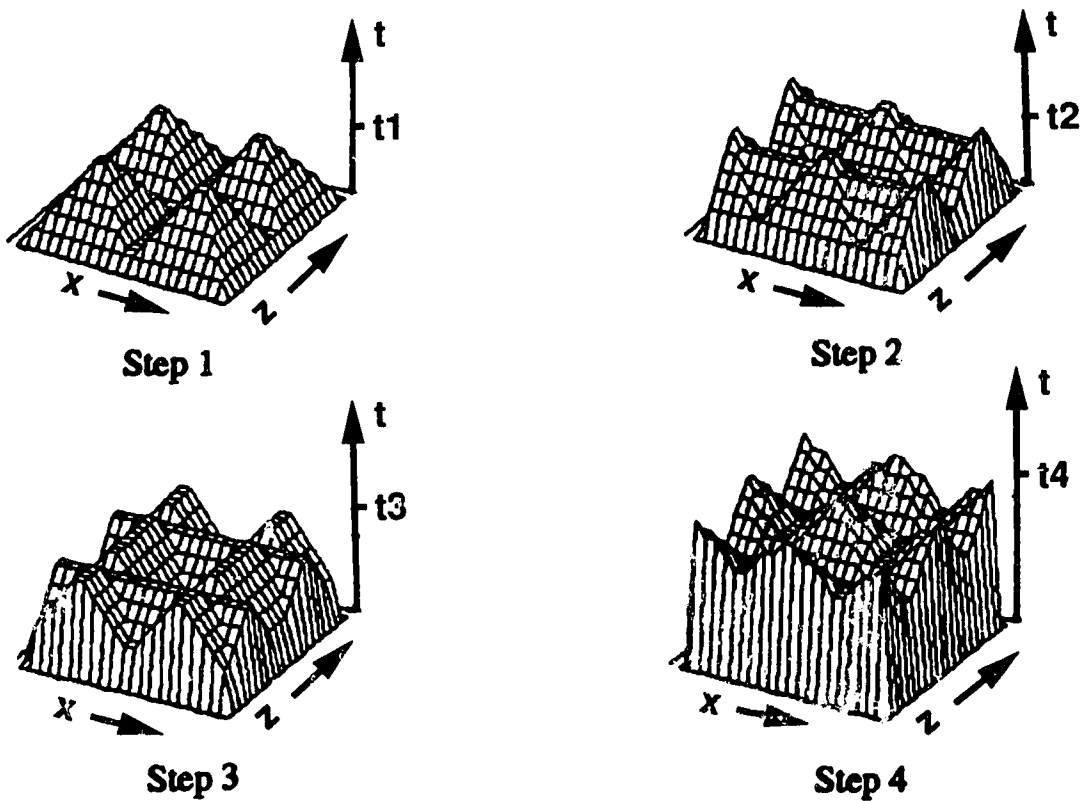


Figure 3.6 : Coarse grain parallelism for 2-D elastic modeling. (a) A model submatrix is assigned on each processor. (b) Communication between tasks / processors is required.

**(a) 1-D DOMAIN DECOMPOSITION**



**(b) 2-D DOMAIN DECOMPOSITION**



**Figure 3.7 :** Dependence decomposition for partial parallelism over time for 2-D elastic modeling. (a) 1-D domain decomposition and (b) 2-D domain decomposition.

There is a trade-off between creating more pyramids (increasing the maximum number of processors) and increasing the height of the pyramids (increasing the amount of work per parallel task). Currently, we are working towards an optimum solution that will make the model move a significant number of time steps between synchronizations. The domain decomposition technique can at least double the parallel efficiency of the code since the requirements for the system to support paging are dramatically reduced.

## **3.6 2-D ELASTIC AND 3-D ACOUSTIC MODELING APPLICATIONS**

### **3.6.1 Introduction**

With finite difference modeling one is computing synthetic shot records. For interpretation purposes we stack all shot records to get a stacked seismic section. However, when one moves from 2-D to 3-D the computational task increases by at least 2 or 3 orders of magnitude only in terms of calculating seismic sections along different orientations of the 3-D structure. One can avoid this by calculating zero-offset sections using the exploding reflector model (Loewenthal et al., 1976) where point sources are assigned at every grid point of the model in the subsurface and are exploding simultaneously at zero time resulting in only upcoming travelling waves with half the velocity of the medium. Mufti 1989 used this approach for 3-D modeling on a CRAY-2 for a dome model of 240x240x240 grid dimensions and spacing of 20 m, max freq of source=50 Hz, dt=2 ms (time sampling interval), number of time steps (nt)=500.

### **3.6.2 Simulations during Thermal EOR Processes at Cold Lake**

Computer simulations of seismic wave propagation were essential for the interpretation of field data from monitoring thermally enhanced oil recovery (EOR) projects at Cold Lake, Alberta. Finite difference modeling of seismic waves in 2-D elastic and 3-D acoustic media in the region over the steam-heated zone is performed in order to examine the relation between reservoir conditions such as pressure, temperature and saturation with seismic characteristics such as velocity, amplitude and frequency modification with time.

Computer simulations of 2-D elastic and 3-D acoustic wave propagation are carried out for very detailed multi-layer models before any steaming and during the steam and production cycles. P-wave line and point sources were used for the 2-D elastic and 3-D

acoustic modeling, respectively. A Gaussian function was used as a source of excitation with a dominant frequencies of 50 or 100 Hz. Synthetic zero offset sections and shot gathers were generated for all components of particle velocity or stress components and pressure field. The common shot gathers can directly be compared with field shot gathers or after sorting into CMP gathers, NMO and stacking, the resultant stacked section can be migrated and compared to a field inline or crossline. The shot gathers and the stacked sections after steam injection show reflections and diffractions from the steam zone. The amplitude of the reflector at the top of the steam zone is stronger since the bitumen has been replaced by steam or has been heated. Time delays are observed below the low velocity steam zone.

Extensive 2-D elastic modeling has been carried out for Mobil's and Esso's EOR projects (before, during and after steam injection). The results are presented and discussed in Chapter 6. The simulation of each shot gather, for a model of grid size 393 x 501 nodes and 8046 time steps, required 2.01 hours of CPU time on a Convex 210.

3-D acoustic modeling was performed on a large scale model from the oil sands in the Cold Lake area of Alberta. However, at this time only a limited amount of simulations were performed due to large storage and transfer requirements of the generated data. In particular, the 3-D acoustic simulations generate a large amount of synthetic data which require large disc space in order to be stored and analyzed. Also, the transfer of the generated data from the Fujitsu VPX/240 (located at the High Performance Computing Center in Calgary), where the simulations are performed, to our workstation (at the University of Alberta in Edmonton) is extremely time consuming task due to low data transfer rates (only 7.7 Kbytes/sec). A representative zero offset section is shown in Chapter 6 (Figure 6.10.a) that was generated over a realistic 3-D model from the Cold Lake oil sands. The discretization of this model resulted into a grid size of 97 x 113 x 260 nodes. The simulation of either 3-D zero offset sections or 3-D shot gathers for this model required 28 and 128 minutes of CPU time and attained 92 and 98 % vectorization on the Fujitsu VPX/240 using 801 (time step of 1 ms) and 8001 (time step of 0.1 ms), respectively.

### **3.6.3 Three-dimensional Acoustic Wave Simulations for the French Model**

Computer simulations of 3-D acoustic wave propagation were carried out for a more complicated model similar to that presented by French (1974). The main structures on this model are two domes and a fault. The dimensions of the model are shown in Figure 3.8

with one depth slice (~120 m) and a vertical cut (~inline 45) from the 3-D velocity model. Also, the location of some inlines and crosslines of the seismic grid are shown (Figure 3.8) with respect to the structures (domes and fault). A Gaussian function was used as a source of excitation with a dominant frequency of 30 Hz. The model was discretized ( $dx=dy=dz=5.5$  m) to a grid size of 156 x 156 x 120 nodes (including absorbing boundaries, only 7 grid points on each side). For one source location (shot 1, Figure 3.8) synthetic shot gathers were generated for all components of particle velocity components and pressure field (four in total). Also, seven snapshots of the evolving pressure field through the 3-D model were generated at no extra cost (except I/O). Furthermore, 3-D zero offset data can be generated by setting a source at every receiver location. The CPU time required for these simulations, using 500 finite difference time steps (time step=1 ms) and sampling rate also of 1 ms, was only 5 minutes on the Fujitsu VPX/240 and the total vectorization (including I/O, attained 92 percent).

Representative portions (along inline 45 and crossline 16) of the 3-D shot gather (vertical particle velocity component) are shown in Figure 3.9. These show the high quality of the data recorded and thus, the capabilities of our algorithm to model complicated structures. However, the data are extremely difficult to interpret due to diffractions and sideswipe events from the domes and the fault and due to reflections from the flat interfaces below. Of course, when one visualizes the model geometry and the location of the source it is possible to account for all the arrivals in the data. For example, it is easy to identify the diffractions from the domes. Furthermore, a depth slice (77 m) and a vertical profile (along inline 45) from the 3-D snapshot at time 150 ms is shown in Figure 3.10. These snapshots show the complex evolution of the pressure field at that particular time (as the two domes and the fault begin to affect the wavefield). However, snapshots at later times are far too complex and difficult to interpret.

*(Text continued on page 69)*

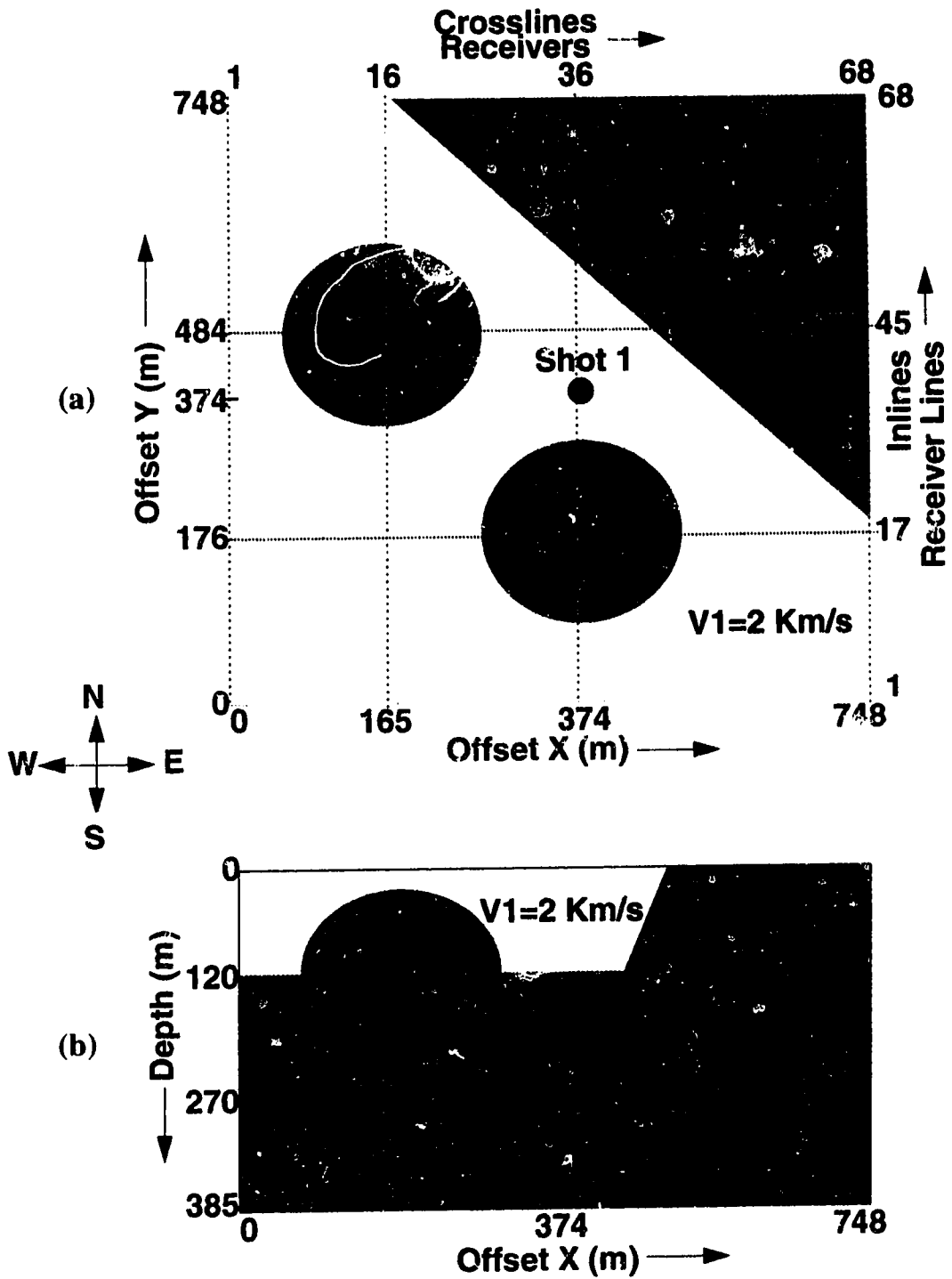
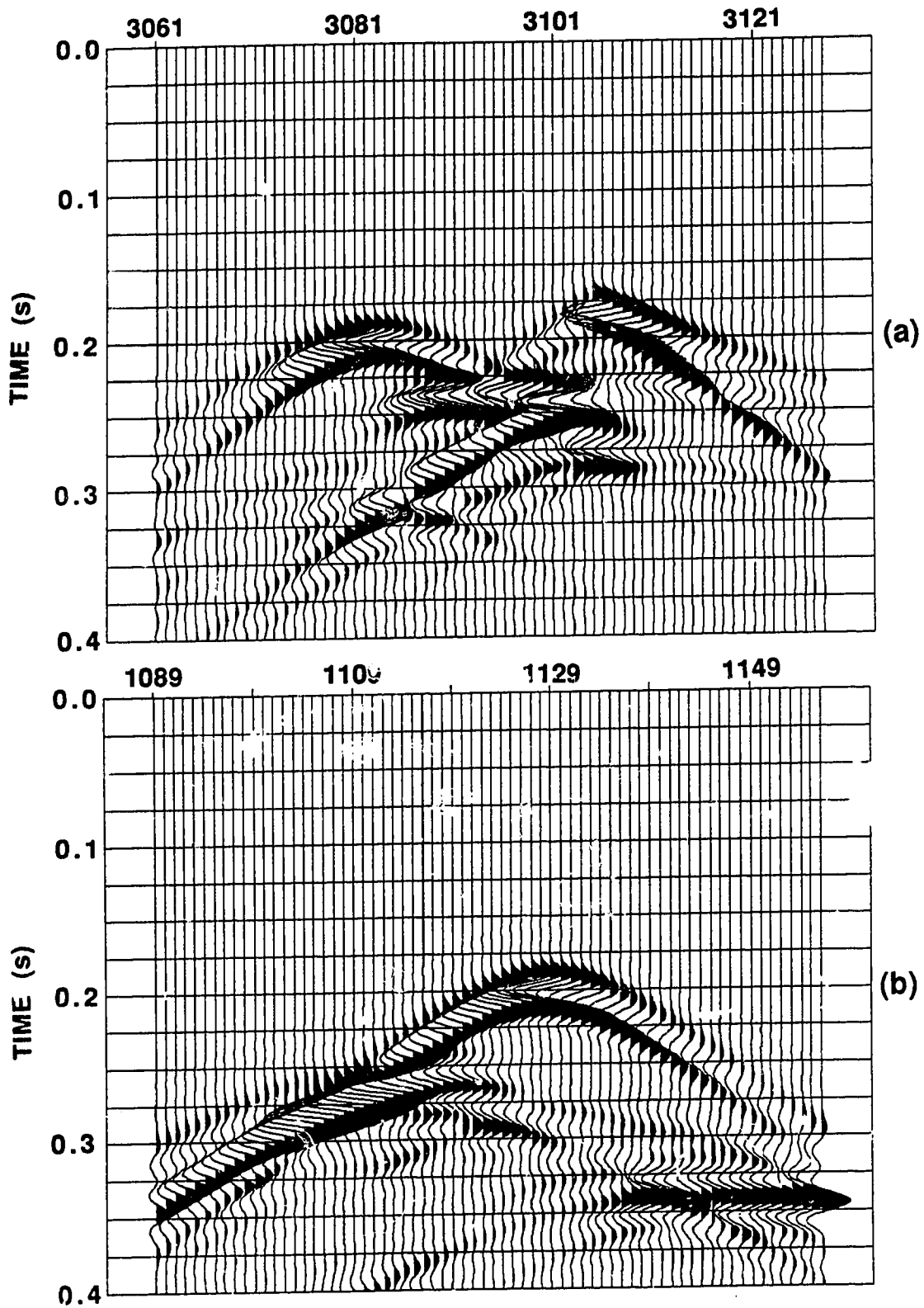
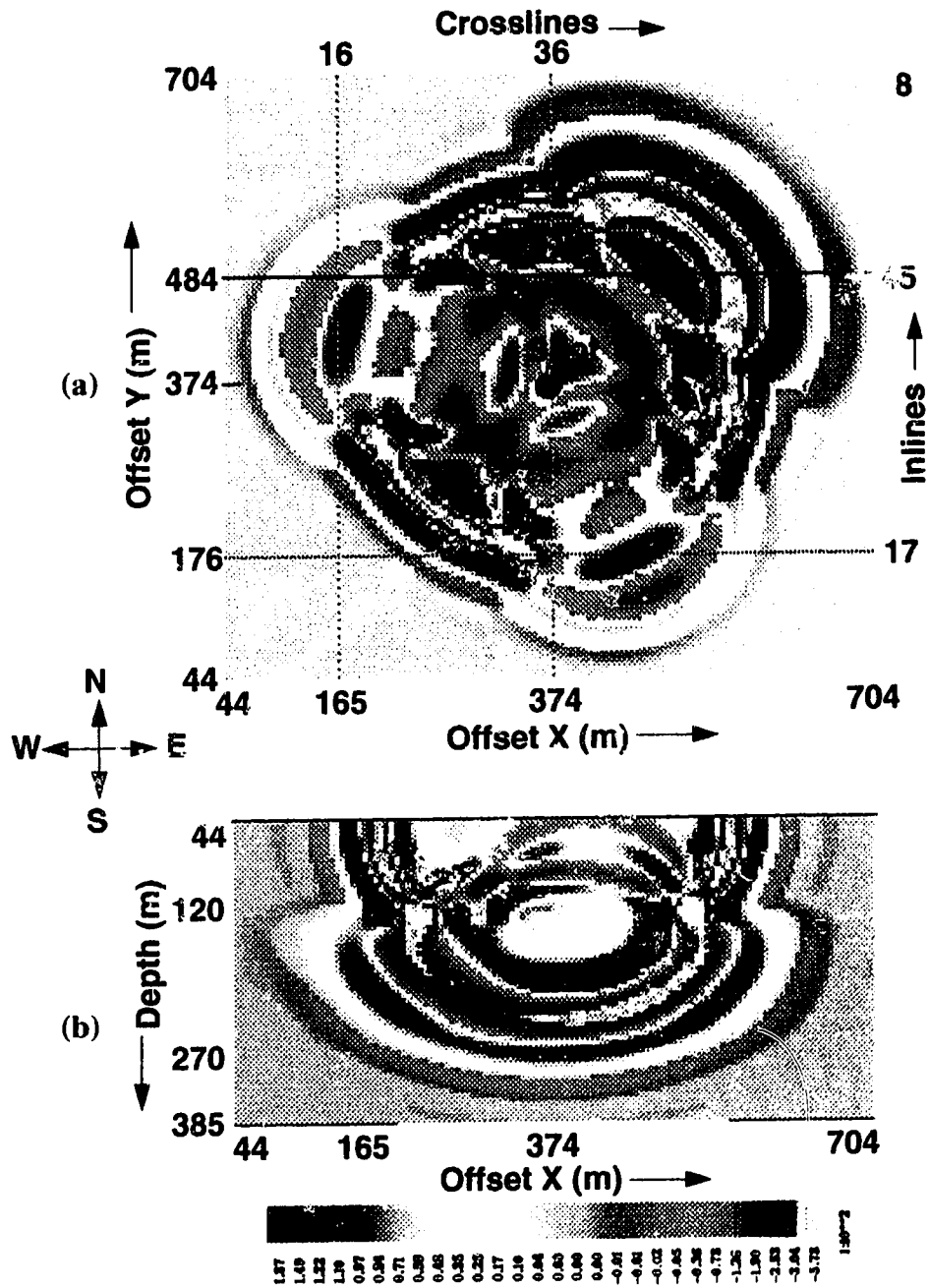


Figure 3.8 : A depth slice and a vertical cut of the French model (two domes and a fault) used for 3-D acoustic modeling.



**Figure 3.9:** Portions of the 3-D shot gather (vertical particle velocity component) from the 3-D acoustic wave simulation for the French model (Figure 3.8): (a) along inline 45 and (b) along crossline 16.





**Figure 3.10:** (a) A depth slice (77 m) and (b) a vertical cut (along inline 45) from the 3-D snapshot (150 ms) for the pressure field from the 3-D acoustic wave simulation for the French model (Figure 3.8).

### 3.10 CONCLUSION

The advent of the new generation of vector/parallel supercomputers and massively parallel processors (MPPs) motivated this work towards simulations of wave propagation with higher accuracy in two and three dimensional inhomogeneous media. We follow the semantic vectorization approach in which the numerical parts of the program are fully vectorized. The larger virtual memory of the supercomputers results in finer grids which dramatically minimize the dispersion effects. Furthermore, we utilized the inherent parallelism present in the problem over the space domain and applied a domain decomposition technique for additional parallel efficiency. The result is a pronounced decrease in execution time, ability to handle quite large models and an increase in accuracy and resolution. Particularly, the implementation of the 3-D acoustic modeling algorithm on the Fujitsu VPX/240 supercomputer resulted in pronounced CPU and vectorization performance thus opening the avenues for large scale realistic wave propagation simulations in 3-D complex structures.

Existing 2-D elastic modeling algorithms were modified to incorporate high resolution complex models and use very efficient absorbing boundary conditions. Furthermore, they were vectorized, parallelized and fine tuned resulting a five-fold increase in performance over the original ones.

The 3-D acoustic modeling algorithm was tested with a simple model and the French model. It was shown that the algorithm is capable of simulating the propagation of wavefields and generate synthetic seismograms of high quality and resolution in complex structures. Also, both 2-D elastic and 3-D acoustic modeling are used extensively (Chapter 6) for high resolution and large scale simulations in the Cold Lake oil sands before and during steam stimulation processes.

The numerical solution of the 3-D acoustic wave equation provides a useful method for simulating the evolution of a pressure field which corresponds to the P or compressional type of body waves which is most frequently recorded. In the 3-D acoustic modeling both lateral and vertical variations of the acoustic (P-wave) velocity and density are allowed. The method accounts for many important wave phenomena such as diffraction, interference and generation of multiple reflections. Although the use of the acoustic wave equation rules out the generation of shear and surface waves, it is still accurate enough for many important exploration and production problems. Another advantage of 3-D modeling is that time slices (snap shots) come at no extra cost and they

can enable us to examine the spatial configuration of the wavefield as it propagates through the 3-D earth model and reaches the surface at different times.

The 3-D modeling algorithm may easily be extended to simulate wave propagation in three dimensional anisotropic heterogeneous media. Furthermore, the computational performance of the algorithm suggests the possibility of large scale 3-D elastic wave simulations in realistic and complex media. However, both topics are beyond the scope of this thesis and are left for further research.

In conclusion, the 3-D finite difference modeling is a remarkably flexible method that can simulate fast and accurately the seismic response of geologically complex structures and stratigraphic areas. Indeed this choice of modeling allows computations to run as fast as the acquisition of 3-D field seismic data. We believe that employing the current vector and parallel supercomputer technology, the above algorithms can be powerful tools in all phases of exploration and reservoir geophysics including exploration and hydrocarbon reservoir predevelopment, development, operation and enhanced oil recovery phase.

## REFERENCES

- Aki, K., and Richards, P., 1980, *Quantitative seismology: Theory and methods*, V. I, W. H. Freeman and Co.
- Alford, R.M., Kelly, K.R., and Boore, D.M., 1974, Accuracy of finite-difference modelling of the acoustic wave equation: *Geophysics*, **39**, 834-842.
- Alterman, Z., and Karal, F.C., 1968, Propagation of elastic waves in layered media by finite-difference methods: *Bull., Seis. Soc. Am.*, **58**, 367-398.
- Baker, L.J., 1989, Is 3-D wave-equation modeling feasible in the next ten years?, in: *Supercomputers in seismic exploration, Handbook of Geophysical Exploration, Section I, Volume 21*, by E. Eisner (ed), Pergamon Press.
- Bayliss, A., Jordan, K.E., LeMesurier, B.J. and Turkel, E., 1986, A fourth order accurate finite-difference scheme for the computation of elastic waves: *Bull., Seis. Soc. Am.*, **76**, 1115-1132.
- Biot, M.A., 1956, Theory of propagation of elastic waves in saturated porous solid, I: Low frequency range: *J. Acoust. Soc. Am.*, **28**, 168.
- Blanch, J.O., Robertsson, J.O.A., and Symes, W.W., 1993, Viscoelastic finite-difference modeling: 63rd SEG Annual International Meeting and Exposition, Washington

- D.C., Expanded Abstracts, 990-993.
- Boore, D.M., 1972, Finite-difference methods for seismic wave propagation in heterogeneous materials, *in* Bolt B.A., Ed., *Methods in Computational Physics: V.11*, Academic Press Inc., 1-37.
- Bracewell, R., 1965, *The Fourier transform and its applications*: McGraw-Hill, p.117.
- Carcione, J.M., Kosloff, D., and Kosloff, R., 1988, Wave propagation simulation in a linear viscoacoustic medium: *Geophysical Journal*, **93**, 393-407.
- Cerveny, V., Molotkov, I.A., and Psencik V., 1977, *Ray method in seismology* : University of Karlova, Praha.
- Cerjan, C., Kosloff, D., Kosloff, R., and Reshef, M., 1985, A nonreflecting boundary condition for discrete acoustic and elastic wave equations: *Geophysics*, **53**, 769-777.
- Dablain, M.A., 1986, The application of high-order differencing to the scalar wave equation: *Geophysics*, **51**, 54-66.
- Dai, N., 1993, Finite difference simulation and imaging of seismic waves in complex media, Ph.D. Thesis, University of Alberta, Edmonton, Alberta.
- de la Cruz, V., and Spanos, T.J.T., 1985, Seismic wave propagation in a porous medium: *Geophysics*, **50**, 1556-1565.
- Emmerich, H., and Korn, M., 1987, Incorporation of attenuation into time domain computations of seismic wave fields: *Geophysics*, **52**, 1252-1264.
- Fagin, S.W., 1991, *Seismic modeling of geologic structures*: Geophysical Development Series, Society of Exploration Geophysicists.
- Fornberg, B., 1987, The pseudospectral method: Comparisons with finite difference for the elastic wave equation: *Geophysics*, **52**, 483-501.
- French, W.S., 1974, Two-dimensional and three-dimensional migration of model-experiment reflection profiles: *Geophysics*, **39**, 265-277.
- Gazdag, J., 1981, Modeling of the acoustic wave equation with transform methods, *Geophysics*, **46**, 854-859.
- Gottlieb, D., and Turkel, E., 1976, Dissipative two-four methods for time dependent problems: *Math. Comp.*, **30**, 703-723.
- Gottlieb, D., and Orszag, S.A., 1977, *A numerical analysis of spectral methods: Theory and applications*, Society of Industrial and Applied Mathematics.
- Hassanzadeh, S., 1991, Acoustic modeling in fluid saturated porous media: *Geophysics*, **56**, 424-435.
- Kapotas, S., 1991, 3-D imaging of reflection seismic wavefields using parallel computers:

- Ph.D. Thesis, University of Alberta.
- Kelly, K.R., Ward, R.W., Treitel, S., and Alford, R.M., 1976, Synthetic seismograms: A finite-difference approach: *Geophysics*, **41**, 2-27.
- Kosloff, D., and Baysal, E., 1982, Forward modeling by a Fourier method: *Geophysics*, **47**, 1402-1412.
- Kosloff, D., Koren, Z., and Lowewenthal, D., 1984, Discrete derivative operators for seismic forward modeling and migration: presented at the 54th SEG Annual International Meeting and Exposition.
- Kosloff, R., and Kosloff, D., 1986, Absorbing boundary for wave propagation problems: *J. Comp. Phys.*, **63**, 363-376.
- Loewenthal, D., Robersons, L., Lu, R., and Sherwood, J., 1976, The wave equation applied to migration: *Geophysical Prospecting*, **24**, 380-399.
- Lysmer, J., and Kuhlmeyer, R.L., 1969, Finite dynamic model for infinite media: *J. Eng. Mech. Div.*, **95**, 859-877.
- Madsen, N.K., Rodrigue, G.H., and Karush, J.I., 1976, Matrix multiplication by diagonals on a vector/parallel processor: *Inform. Proc. Lett.*, **5**, 41-45.
- Marfurt, K.J., 1984, Accuracy of finite difference and finite-element modeling of the scalar and elastic wave equations: *Geophysics*, **49**, 533-549.
- Mikhailenko, B.G., and Korneev, V.I., 1984, Calculation of synthetic seismograms for complex subsurface geometries by a combination of finite integral Fourier transforms and finite difference techniques, *J. Geophys.*, **54**, 195-206.
- Mitchell, A.R., and Griffiths, D.F., 1981, *The finite-difference method in partial differential equations*: Jon Wiley & Sons Inc.
- Mora, P., 1988, 3-D acoustic forward modeling in the CM2: 58th SEG Annual International Meeting and Exposition, Anaheim, California.
- Mora, P., 1989, Modeling three-dimensional seismic waves, in: *Proceedings of the workshop on "Geophysics and computers - A look at the future"*, Houston, 139-163.
- Moufti, I.R., 1985, Seismic modeling in the implicit mode: *Geoph. Prosp.*, **33**, 619-656.
- Moufti, I.R., 1989, Application of supercomputers in three dimensional seismic modeling, in: *Supercomputers in seismic exploration, Handbook of Geophysical Exploration, Section I, Volume 21*, by E.Eisner (ed), Pergamon Press.
- Mufti, I.R., 1990, Large-scale three-dimensional seismic models and their interpretive significance: *Geophysics*, **55**, No.9.
- Pereyra, V., Richardson, E., and Zarantonello, S., 1992, 3-D finite-element and ray

- tracing simulation of elastic wave propagation, 62nd SEG Annual International Meeting and Exposition, New Orleans, Expanded Abstracts, 1227-1231.
- Paul, E., A.Sei and P. Duclos, 1991, GigaFLOPS performance for 2D/3D heterogeneous acoustic modeling on a massively parallel computer: Proceedings of the First International Conference on Mathematical and Numerical Aspects of Wave Propagation Phenomena, G. Cohen, L. Harpen, and P. Joly (eds), SIAM, 136-144.
- Reshef, M. Kosloff, D., Edwards, M., Hsiung, C., 1988, Three-dimensional acoustic modeling by the Fourier method: *Geophysics*, **53**, 1175-1183.
- Smith, W.D., 1975, The application of finite-element analysis to body wave propagation problems: *Geophys. J. Roy. Astr. Soc.*, **42**, 747-768.
- Sochacki, J., Kubichek, R., George, J., Fletcher, W.R., and Smithson, S., 1987, Absorbing boundary condition and surface waves: *Geophysics*, **52**, 60-71.
- Strang, G., 1968, On the construction and comparison of difference schemes: *SIAM J. Num. Anal.*, **5**, 506-517.
- Tsingas, C., Vafidis, A., and Kanasewich, E.R, 1990, Elastic wave propagation in transversely isotropic media using finite differences: *Geophys. Prosp.*, **38**, 933-949.
- Turkel, E., 1980, On the practical use of high order methods for hyperbolic systems: *J. Comp. Phys.*, **35**, 319-340.
- Vafidis, A., 1988, Supercomputer finite-difference methods for seismic wave propagation: Ph.D. Thesis, University of Alberta, Edmonton, Canada
- Vafidis, A., Abramovici, F., and Kanasewich, E.R., 1992, Elastic wave propagation using fully vectorized high order finite differences: *Geophysics*, **57**, 218-232.
- Vafidis, A., Dai, N., and Kanasewich, E.R., 1993, Wave propagation in viscoacoustic heterogeneous media: A velocity-pressure finite-difference method: *Canadian Journal of Exploration Geophysics*, **29**, 402-410.
- Virieux, J., 1984, SH-wave propagation in heterogeneous media: Velocity-stress finite-difference method: *Geophysics*, **49**, 1933-1957.
- Virieux, J., 1986, PSV-wave propagation in heterogeneous media: Velocity-stress finite-difference method: *Geophysics*, **51**, 889-901.
- Wilson, D.C., and Karpoff, W.T., 1993, Dependence decomposition: parallel execution of time steps, In: Proceedings of Supercomputing Symposium '93, Calgary, 73-80.
- Zhu, X., and McMechan, G.A., 1991, Finite-difference modeling of the seismic response of fluid-saturated, porous, elastic media using Biot theory: *Geophysics*, **56**, 328-339.

## CHAPTER 4

### SEISMIC REFLECTION IMAGING

#### 4.1 INTRODUCTION

##### 4.1.1 Migration

The seismic reflection method seeks to image the structure of the Earth from seismic wavefields recorded at the surface. The seismic signal recorded by a geophone is a superposition of seismic waves originating from all possible directions in the subsurface. Thus, much of the recorded energy is not from reflectors directly below the receiver but from horizons far away from the point of recording.

In the last decades several processing techniques have been developed for seismic data. One of the most advanced methods is *migration*. The term migration refers to the redistribution of the recorded wavefields to their true spatial subsurface reflecting positions. The migration technique positions dipping and diffracted data to their true position resulting in an image which has greater spatial resolution. For example, a point scatterer that is buried in a constant velocity medium generates a zero offset seismic section that is a hyperbola in two dimensions. In this case, migration integrates the wave amplitudes along the diffraction hyperbola and then places the result at the apex of it.

Migration is an inverse process in which the recorded events are propagated back to the corresponding reflector locations. In the process of seismic data acquisition, the upward travelling waves are recorded at the surface. In the migration process these recorded waves are used either as initial conditions or boundary conditions for a wavefield governed by the wave equation.

##### 4.1.2 Migration: Extrapolation and Imaging

There are two distinct parts to migration, namely, *extrapolation* and *imaging*. Extrapolation means reconstruction of the wavefield at depth from the seismic data recorded at the earth's surface. Imaging is the process, based on some principle, that allows one to obtain the local reflection strength from the extrapolated data in depth and create an image

of the subsurface reflectors.

If the seismic wave is recorded in water, the pressure field at the earth's surface can be approximated by the scalar wave equation (Appendix B). If the recording wave is on a solid surface the scalar equation can be used as an approximation for the vertical component of motion. This scalar equation can be used to downward continue the recorded wavefield in depth. However, the scalar wave equation is not often used for migration because of a number of reasons: (1) The scalar wave equation generates unwanted internal multiple reflections that involve both upcoming and downgoing waves. (2) The scalar wave equation with space variable coefficients generates energy that does not contribute to the focused image. (3) The depth dependence of the physical solution is a growing or damped exponential; these solutions are the evanescent waves. (4) The scalar wave equation has a second order depth- $z$  derivative. Thus, we need two boundary conditions for the extrapolation, one will be the pressure  $P(x,y,z,t)$  at  $z=0$  and the other the first derivative of the pressure  $(\partial P/\partial z)$  at  $z=0$ . However,  $\partial P/\partial z$  is unknown since it is not recorded.

Because of the above problems with the scalar wave equation, most extrapolation operators in wave theory based migrations are constructed from an one-way wave equation. The one-way wave equation is commonly obtained by seeking a polynomial or rational approximation to the dispersion relation of a square root form.

We reconstruct the wavefield in depth using an *extrapolation operator*. However, in order to image the subsurface reflectors from seismic data, an *imaging principle* has to be invoked. This principle is just a prescription for constructing a picture of the subsurface from the data. Different imaging principles lead to different types of migration.

Frequently in exploration seismology, we use the *zero-offset model*. This is based on the assumption that the source and receiver are in identical locations on the surface and the waves are true echoes similar to that used with electromagnetic or radar waves. For a more accurate approximation we correct for the extra travel time for spatially separated shots and receivers and derive a new data trace located midway between source and receiver, called the common midpoint (CMP) or common depth point (CDP) trace. Therefore, a CMP or CDP section may be regarded as data obtained from coincident source and receivers. In the zero offset model, the energy travel path from source to reflector is identical to that from reflector to receiver. The assumption is that all sources are activated simultaneously, but each receiver records signals originating from only the same source-receiver point. Such zero offset data do not correspond to any wavefield resulting from a simple experiment. As a result it is helpful to create a hypothetical physical experiment to



provide an intuitive picture of zero offset migration. Such an experiment is known as the *Exploding Reflector Model*, (Loewenthal et al, 1976). According to the ERM the energy sources are not at the surface, but they are distributed along the reflecting surfaces. In other words, the reflectors are represented by buried sources, which are "exploded" at the same time,  $t=0$ . Therefore one needs to be concerned only with upward traveling waves. Thus, the recorded signal  $P(x,y,z=0,t)$  is the surface ( $z=0$ ) expression of the upcoming wavefield  $P(x,y,z,t)$  that was generated by an explosion at time  $t=0$ . Since the record section involves two-way travel time, it needs to be converted to one-way travel time. In practice the time scale of CMP sections is kept unchanged. Instead the velocity of the wave propagation is scaled down by a factor of two. Then, the recorded field is extrapolated in depth  $P(x,y,z,t)$  and is imaged at time zero,  $P(x,y,z,t=0)$ . This imaging concept naturally leads to *poststack migration*.

A different imaging principle is based on the idea that *a reflector exists at points in the Earth where an upgoing wave is time coincident with the first arrival of a downgoing wave* (The Claerbout concept). The recorded wavefield at the surface receivers is extrapolated downward and correlated with the downgoing wave from the sources. Where the correlation between upgoing and downgoing waves is finite a reflector exists with the reflectivity being proportional to the correlation (Berkhout, 1982; Wapenaar et al., 1987). This leads naturally to an algorithm which extrapolates both up and downgoing wavefields to points of intersection, to obtain a reflection coefficient by correlation. Data recorded at the Earth's surface are considered as upgoing waves which can be extrapolated down into the Earth and backwards in time. Sources are considered to generate downgoing waves, which can also be extrapolated down into Earth but forward in time. Comparison with the extrapolated upgoing wave of the first arrival of the extrapolated downgoing wave yields a reflection coefficient. This concept leads naturally to *prestack migration such as common shot gather or profile migration* (Claerbout, 1970, 1971; Snyder, 1979; Jacobs, 1982; Marfurt, 1978; Tsingas and Kanasewich, 1990; etc.)

Another imaging method used for prestack depth migration is the *double downward continuation* approach (Schultz and Sherwood, 1980; Thorson, 1980; Kapotas 1991) or survey sinking (Claerbout, 1985). Survey sinking, based on the causality concept, transforms the seismic data into results of a depth sequence of seismic experiments performed inside the earth. In this technique both sources and receivers are downward continued into the earth with images being formed at time zero at the reflector positions. The double downward continuation approach is based on the *principle of reciprocity* (Aki and Richards, 1980) which states that the wave is the same when source and receiver are

interchanged. In practice, shot gathers are downward continued by one depth step and then the data are reorganized into common receiver gathers which subsequently are downward continued by the same depth step. The migrated depth section is imaged at zero travelttime and zero offset for each depth level. This process is carried out until the maximum depth is reached. This approach although accurate is very expensive computationally and requires surveys with symmetric arrangement of shots and receivers which are not always possible in field.

#### **4.1.3 Poststack versus Prestack Migration**

In seismic sounding the measurements of a physical experiment consist of source (shot) gathers. A shot gather is the seismic recording of reflected energy from a source at a unique location to closely spaced receivers. A reverse configuration can give a receiver gather.

Stacking of recordings from many source-receiver combinations is essential to improve the signal to noise ratio of the weak subsurface echoes. The stacking of records not only improve the signal to noise quality but reduces the immense amount of data that must be handled by a computer array processor. The final stacked product displays a section in which the source and the receiver are spatially identical for reflecting surfaces with little dip.

Poststack migration attempts to correct a stacked section for the effect of dip. But in many cases, the obtained stack sections with dipping or discontinuous reflectors are distorted since the original field records were made with source receivers not in identical positions. However, poststack migration is an important component of conventional processing (CDP processing).

In geologic areas where the velocity does not vary or varies only with depth, the common depth point (CDP) assumption is valid and poststack migration is applicable. However, complex geologic structure causes raypaths and arrival times to deviate significantly from the hyperbolic, straight-ray assumptions on which stacking is based. Then, the CDP stack inadequately represents the true zero-offset data that poststack migration expects. Therefore, in complex areas where the seismic velocity varies strongly laterally, the common midpoint assumption breaks down, poststack migration is inadequate and only prestack depth migration can place energy in its true subsurface position.

Many researchers have suggested methods for prestack migration (Jain and Wren, 1980; Schultz and Sherwood, 1980; Yilmaz and Claerbout, 1980; Temme, 1984; Wapenaar

et al., 1987; Reshef and Kosloff, 1986; Chang and McMechan, 1986; Stolt and Benson, 1986; Muller and Temme, 1987; Berkhout, 1987; Tsingas and Kanasewich, 1990). Prestack migration is a computationally expensive alternative to common depth point (CDP) processing but it gives correct imaging, better dip preservation and amplitude information. However, poststack migration is the most common type of migration routinely used in most exploration surveys, since migration of stacked sections is about two orders of magnitude (2-D cases) less expensive than current prestack migration methods. In conclusion, migration can be performed before or after stacking the data in time or depth.

#### 4.1.4 Migration Methods

There are many ways to migrate 2-D seismic data. The numerical techniques employed can generally be separated in three broad categories, namely: summation or integral methods such as Kirchhoff migration (French, 1975; Schneider, 1978); difference methods such as finite difference migration (Claerbout, 1970, 1976, 1985); and transform methods such as f-k migration (Stolt, 1978; Gazdag, 1978). Also, Berkhout (1982) developed a migration that is a spatial convolution process in the space-frequency domain. Most of migration methods employ the one-way scalar wave equations or approximations of it. But there are schemes that employ the full scalar wave equation (Kosloff and Baysal, 1983; Reshef and Kosloff, 1986). Also, migration can be accomplished employing the full elastic wave equation (Wapenaar et al., 1987).

One can view the various migration methods in terms of the complexity of the velocity models that one can accommodate. There are a number of constant velocity migration algorithms that can be applied for the migration of stacked data using the zero-offset and the exploding reflector models. In the wavenumber ( $k$ ) - space domain we have the phase-shift migration (Gazdag, 1978) and the f-k migration (Stolt, 1978). In space-time ( $x-t$ ) domain we have the Kirchhoff migration (Schneider, 1978) which is a summation method. On the other hand, we have the differential wave equation migrations (Claerbout, 1976) that can be performed either in space-time ( $x-t$ ) or frequency-space ( $\omega-x$ ) using explicit or implicit finite difference schemes. The methods used for poststack migration can be utilized for shot gather and common offset migrations (Stolt and Benson, 1986) most often using the so-called double-square root (DSR) equation. Constant velocity prestack migration eliminates distortions found in the stacked data due to reflector dip.

When there are moderate velocity variations, poststack time migration is commonly used. The use of the rms velocities is straightforward for the space ( $x$ ) domain migration

algorithms such as the Kirchhoff and the differential wave equation migrations. The  $f$ - $k$  migration has problems when applied in depth variable velocity fields which are overcome with a time stretch (Stolt, 1978). The phase-shift migration can handle a depth variable velocity perfectly well. A number of other schemes can be applied in conjunction with time migration. Partial prestack migration (Yilmaz and Claerbout, 1980) can correct moveout for dip so as to validate more standard processing sequences. Furthermore, full prestack time migration can be employed.

Migration can be performed in time in order to obtain a subsurface image. But hydrocarbons are extracted in depth and not reflection traveltime. For this reason time-to-depth conversion is necessary to properly interpret seismic data. This is usually accomplished with vertical trace stretching or ray tracing of selected reflectors. However, a conventional time migrated section can not simply be stretched to depth. Conventional time migration techniques fail, even with accurate knowledge of subsurface velocities, mainly because Snell's law is ignored at dipping interfaces. Time migration does not position reflected energy in its true location and treats improperly diffracted energy when the velocity varies substantially laterally. Therefore, a time migrated section needs to have an image ray (Hubral, 1977) correction so the events can be approximately located in the true horizontal location and depth. The depth conversion can be accomplished by mapping the data along image raypaths rather than by simple vertical stretching.

On the other hand, depth migration compensates for ray bending, lateral velocity pull-ups and structure. It accommodates lateral velocity variations and positions the energy at the true subsurface location. Also, a natural advantage of the depth migration is that the output image is displayed in depth and can be used directly for geologic interpretation and well depth estimates. The essential difference between depth migration and time migration is that depth migration can make proper use of the detailed velocity structure in complex media where the time migration cannot. There are a number of depth migrations. The modified Kirchhoff migration, using perturbed ray tracing via the Fermat's principle (Carter and Frazer, 1984), can allow some lateral velocity variations. Gazdag and Squazzero (1984) proposed the phase-shift plus interpolation migration. Also, there are the space-frequency ( $f$ - $x$ ) domain wave equation migrations such as explicit recursive migration (Gazdag, 1980; Berkhout, 1981) and implicit finite difference migration that uses a paraxial approximation to the one-way wave equation (Claerbout, 1985). Another approach to depth migration is the reverse time migration (Kosloff et al., 1983; McMechan, 1983) where instead of extrapolating the wavefield downward in depth, is extrapolated backwards in time.

The main alternative to conventional migration processing is to migrate the unstacked data. Prestack depth migration best handles nonzero dips, nonzero offsets and strong velocity variations and it can properly image complex structures. A number of prestack depth migration algorithms have been presented such as the profile or shot gather migration (Claerbout, 1970; Snyder, 1979; Tsingas and Kanasevich, 1990), the plane wave migration (Temme, 1984), the double-downward continuation (S-G) migration (Jain and Wren, 1980; Schultz and Sherwood, 1980; Thorson, 1980; Kapotas, 1991) and the prestack reverse time migration (Chang and McMechan, 1986).

Most extrapolation operators in wave theory based migrations are constructed from an one-way wave equation due to the fact that the signal recorded by the seismic surface survey come from the upward traveling wave field only. The one-way wave equations commonly obtained by seeking a polynomial or rational approximation to the dispersion relation of a square root form. Although successful in many situations, the method is limited by the assumptions made inherently in deriving the one-way wave equations. In particular it is assumed that spatial derivatives of the velocity can be ignored (Claerbout, 1976; Stolt, 1978; Gazdag, 1978). Also, the existing one-way equations often fail in simulating the downgoing wavefield at large propagating angles. In order to overcome these shortcomings, full wave equations were employed for migration purpose (Kosloff and Baysal, 1983; Reshef and Kosloff, 1986). For strong lateral velocity variation and steep dips the two-way wave equation migration possesses certain advantages over the commonly used parabolic or paraxial wave equation but suffers from unwanted internal multiple reflections which are generated from strong velocity variations. However, Dai (1993) developed a first order hyperbolic system for one-way waves in heterogeneous media that is accurate in simulating downgoing waves at propagating angles up to 75°. They used it for 2-D poststack and prestack depth migration through a back-propagating procedure with a less expensive explicit finite difference scheme in the space-time domain and with no unwanted internal reflections being present.

#### **4.1.5 3-D Migration**

A 3-D world requires a 3-D solution. Subsurface geological features in hydrocarbon exploration are three dimensional in nature. Some of the classical 3-D problems are: salt diapirs, reefs, overthrust and folded belts, major unconformities and deltaic sands. The 2-D seismic section is only a cross section of the 3-D seismic wavefield which contains signals from all possible directions. The complex overburden problem has a three-dimensional

character; hence, on a conventional 2-D seismic section data are in the wrong place, some signals appear as noise and interpretation does not resolve structural ambiguities. Also, in the presence of steep dips and lateral velocity variations, we need 3-D seismic, since on 2-D seismic lines we are going to record sideswipe energy. Therefore, this sideswipe energy can only be handled by 3-D migration of 3-D data.

3-D surface seismic acquisition is a well accepted tool since it can provide an accurate and detailed picture of the subsurface. These days in many areas of the world, the 3-D method is routinely used during the exploration and predevelopment phase to delineate structural and stratigraphic features, to define continuity of pay zones of gas or oil, to reduce the risk of dry holes and to predict drilling hazards such as faults and overpressure. Also, 3-D surface seismic is used in the initial phase to determine reservoir areal distribution and continuity. In the operating phase of a hydrocarbon field 3-D high resolution surface seismic surveys begin to impact reservoir management since seismic monitoring can help to detect permeability barriers, estimate continuity and plan accurately infill wells. Furthermore, 3-D surface seismic is used during the enhanced oil recovery phase (EOR) for monitoring over time the reservoir in order to evaluate the EOR design and efficiency.

3-D seismic data need migration in order to image properly the subsurface. The 2-D migration method can be extended into three dimensions. If we consider a point scatterer that is buried in a constant velocity medium then the zero offset traveltime curve in two dimensions is a hyperbola. We can imagine that the response in three dimensions is a hyperboloid. Migration in two dimensions amounts to summing amplitudes along the diffraction hyperbola, then placing the result at the apex of it which is the image of the point scatterer. Thus 3-D migration amounts to summing amplitudes over the surface of the hyperboloid. However, for 2-D migration few hundreds traces are included in the summation for each output trace and this implies that for 3-D migration thousands to millions traces are necessary in the summation.

The success of a 3-D seismic program greatly depends upon the accuracy of the 3-D migrated data volume, since an accurate interpretation requires accurate data. Therefore, 3-D migration continues to be an important area of ongoing research.

Most of the 2-D migration techniques described above can be extended into three dimensions. Thus, there are a variety of 3-D techniques such as Kirchhoff migration based on the Kirchhoff integral approach (Ratcliff et al., 1992; Cabrera et al., 1992); explicit or implicit finite difference migration based on the recursive depth extrapolation approach (discussed in more detail later); phase shift migration based on Fourier transforms (Hale et

al., 1991); reverse time migration based on reverse time extrapolation of seismic wavefields (Reshef and Kessler, 1989; Blacquiere et al., 1989; Chang and McMechan, 1989); and Gaussian beam migration based on the beam forming approach (Hill, 1991).

The main problem in the application of 3-D migration is the handling of the sheer volume of the 3-D data. For this reason, until recently, 3-D migration was performed as two-passes of 2-D migration, a method that replaces the true 3-D case with an approximation that solves a series of 2-D migrations in orthogonal directions (Brown, 1983; Gibson et al., 1983; Dickinson, 1988; Yilmaz, 1987), for reasons of computer efficiency. In the first pass the data are migrated in the inline direction and in the second pass the data are migrated in the crossline (perpendicular) direction.

Although, two-pass 3-D migration images data very well in many cases, the method has limitations. The two-pass 3-D migration is strictly valid for a constant velocity medium. The method commits errors when the velocity is not constant. These errors are caused because the migration cannot be exactly partitioned into inline and crossline migrations. In cases where we have vertical velocity variation, it makes a difference which direction we first migrate because if, for example, we first migrate in the inline direction, we end up with over-migration in this direction. In many cases the inaccuracies in the velocity model used create greater positioning errors than those caused by partitioning. However, in cases with steeply dipping events that do not fall exactly inline or crossline, the errors can be significant in the presence of a large vertical velocity gradient. Finally, in practice the two-pass 3-D migration is adequate if we have small dips and small vertical velocity gradient.

Among the most popular migration methods are the ones based on the recursive depth extrapolation of the recorded wavefield. If the computational environment can accommodate the complete 3-D volume the so called one pass or *alternating direction implicit* (ADI) 3-D finite difference migration can be used. The one-pass 3-D migration has been analyzed by several researchers and applied to the solution of the 3-D seismic problem (Yilmaz, 1987; Gibson et al., 1983; Jacobowicz and Levin, 1983). The method follows the classical solution of the system of equations, where for each depth step (or extrapolation step) the field is downward continued alternatively along the x and then y-directions. The advantage of an one-pass approach is that it handles velocity variations correctly, in contrast to the two-pass technique. But although it is a good approximation to the true solution, it tends to introduce large errors in the azimuthal direction of the wavefield.

Various authors have attempted to improve this solution by the introduction of extra calculations or other operators in the solution of the system of equations. Ristow (1980)

and Cary (1990, 1993) used a symmetric approach to eliminate the anisotropic behaviour of the solution by migrating not only along  $x$  and  $y$  alternately but also along  $45^\circ$  to  $x$  and  $y$ . Black and Leong (1987) used a partitioning approach to the downward extrapolator which avoids the splitting of the operator. Brown (1983) discussed the limitations of the operator separation approach under different velocity variations.

On the other hand, a direct solution of the scalar wave equation for the implicit finite difference 3-D migration is prohibitively expensive since we need to solve a pentadiagonal or a enneadiagonal (nine-fold) system of equations for the  $15^\circ$  or  $45^\circ$  approximation respectively to the dispersion relation using complex sparse-matrix solver techniques. There are many methods for the solution of complex sparse matrices such as complex matrix inversion, conjugate gradient or conjugate direction methods and Gaussian elimination based solvers. However, due to the large system of equations involved in the migration of large 3-D seismic data sets, these methods become unrealizable. Kapotas (1991) used sparse Gaussian elimination but as he admitted this method has prohibitive computer time requirements. Also, he solved the pentadiagonal system of equations by mapping the solution into a tridiagonal system using an under-relaxation method. However, the under-relaxation approach although elegant, it has the potential of numerical instabilities and computational inefficiency in a production environment since it is so much problem dependent. More recently, Kao (1993) presented a preconditioned iterative 3-D finite difference migration method. He used a preconditioned conjugate gradient method to solve the large sparse system. Also, he converted the complex pentadiagonal system to a symmetric and positive definite form and used a hybrid method for its solution.

Lately, various attempts have taken place to bridge the existing gap between one-pass 3-D extrapolation and the full 3-D extrapolation. Hale (1991) has demonstrated an explicit finite difference approach using McClellan transformations which are circular symmetric filters to eliminate the non-symmetric effect of ADI. Furthermore, Blanc et al. (1993) described a poststack depth migration algorithm in which downward extrapolation of the wavefield is performed by spatial convolution with finite-length filters. These filters usually are computed with nonlinear least-squares-based methods or Taylor expansions. However, in this algorithm they are computed by variants of the Remez exchange algorithm (Soubaras, 1992).

Thus in recent years, we have seen an increase in the use of 3-D migration methods in the poststack domain by means of two-pass and one-pass or splitting methods. However, recent advances in computing based on the subdivision of the computational sequence into parallel components might make feasible the exact solution of the 3-D migration problem in



the poststack and prestack domain.

#### **4.1.7 Migration Methods and Algorithms Developed in this Thesis**

Implicit finite difference migrations in the frequency-space domain are based on the recursive depth extrapolation of the wavefield. They are very popular due to their numerical stability, their computational advantages e.g., highly parallelizable over frequencies, and their ability to handle arbitrary velocity variations. However, because of the use of approximations to the one-way wave equations such as the paraxial approximation (Claerbout, 1985) they have accuracy limitations. On the other hand, reverse time explicit finite difference migration methods are based on the reverse time extrapolation of the wavefield. They are not very popular because of their high computational demands. However, they are very accurate and they can handle lateral velocity variations, dips greater than  $90^\circ$ , turning waves, shear waves, and anisotropy.

In the next sections, a number of 2-D and 3-D poststack and prestack depth migration parallel algorithms are developed that are based on recursive depth extrapolation ( $\omega$ -space implicit finite difference migrations). Also, new 3-D reverse time migration methods and algorithms are developed based on the reverse time extrapolation of the recorded wavefield. Each of these algorithms, depending on the particular application, provides certain advantages and disadvantages.

2-D poststack and prestack depth migration parallel algorithms in the  $\omega$ -x domain are developed that are based on an implicit finite difference solution of the  $65^\circ$  parabolic approximation of the one-way wave equation. Also, one-pass 3-D poststack and prestack depth migration parallel algorithms in the frequency-space domain are developed employing an alternative direction implicit finite difference solution of the  $65^\circ$  double square root approximation of the one-way scalar wave equation. The one-pass 3-D migration algorithms generally provide a reasonable tradeoff between imaging accuracy and computational demand. The migration algorithms are parallelized and implemented on parallel computers by utilizing the inherent parallelism of the seismic problem in frequency, space and source domain.

On the other hand, new 3-D reverse time migration methods are developed. Both poststack and prestack depth migration algorithms employ either a full wave or a one-way hyperbolic system. The solution is performed in the time-space domain employing explicit finite differences via the MacCormack splitting scheme. The 3-D reverse time migrations provide high imaging accuracy and versatility but also have higher computational demands

in comparison to the one-pass 3-D migration. The migration algorithms are highly vectorized and parallelized in space and partially in the time domain for implementation on vector and parallel supercomputers.

Choosing the appropriate migration method for a particular set of seismic data requires a knowledge of the type of subsurface lateral velocity variation present, the degree of imaging accuracy versus the computational expense we are willing to pay and the capabilities of our computer resources. In a later section, we present modern migration velocity analysis techniques and we propose a 3-D processing flow using the migration and modeling algorithms developed in this thesis, for 3-D velocity model building, 3-D forward modeling and accurate 3-D poststack or prestack imaging.

## **4.2 2-D $\omega$ -x FINITE DIFFERENCE DEPTH MIGRATION**

### **4.2.1 Introduction**

2-D seismic is still used widely for exploration purposes due to smaller acquisition and processing costs in comparison with 3-D. Therefore, 2-D migration is a widely used technique. The migration algorithms developed here are based on depth extrapolation of the recorded wavefield. The seismic problem is formulated in the frequency domain in order to take advantage of its inherent parallelism over frequencies during computations. Furthermore, any laterally slowly varying velocity function can be used for the extrapolation. By using different imaging conditions, both prestack and poststack depth migration algorithms are developed.

The above algorithms were implemented for a variety of problems. In chapter 7, the 2-D finite difference poststack depth migration algorithm was modified for migrating ground-penetrating radar data for imaging and characterization of fractures in granite. Furthermore, the 2-D migration algorithm was used for migration of deep crustal seismic data from the Alberta LITHOPROBE transect for imaging the structure of the crust down to 50 Km depth.

### **4.2.2 Depth Extrapolation with a $65^\circ$ Approximation to the One-way Wave Equation**

The observed scalar wavefield amplitude,  $P(x,z,t)$  at  $z=0$  can be approximated in two dimensions by the *scalar wave equation*

$$\frac{\partial^2}{\partial x^2} P(x,z,t) + \frac{\partial^2}{\partial z^2} P(x,z,t) = \frac{1}{v^2(x,z)} \frac{\partial^2}{\partial t^2} P(x,z,t) \quad (4.2.1)$$

where  $v(x,z)$  is the velocity of the medium.

The Fourier transformed pressure field is given by:

$$P(k_x, z, \omega) = \int \int P(x, z, t) e^{(ik_x x - i\omega t)} dx dt$$

or inversely, (4.2.2)

$$P(x, z, t) = \int \int P(k_x, z, \omega) e^{(-ik_x x + i\omega t)} dk_x d\omega$$

Applying the operator in equation (4.2.2) to the scalar wave equation (4.2.1) we obtain

$$\frac{\partial^2 P}{\partial z^2} + \left( \frac{\omega^2}{v^2(x,z)} - k_x^2 \right) P = 0 \quad (4.2.3)$$

which has a solution of the form

$$P(k_x, z, \omega) = P(k_x, 0, \omega) \exp\left(-i \left[ \frac{\omega^2}{v^2} - k_x^2 \right]^{1/2} z\right) \quad (4.2.4)$$

This is also a solution of the *one-way scalar wave equation*

$$\frac{\partial P}{\partial z} = -i \frac{\omega}{v} \sqrt{1 - \frac{v^2(x,z)}{\omega^2} k_x^2} P \quad (4.2.5)$$

where the minus sign is for the upcoming waves recorded on the surface and needed migration.

Taking the Fourier transform of both spatial and temporal coordinates ( $\partial/\partial x \leftrightarrow ik_x$ ,  $\partial/\partial z \leftrightarrow ik_z$ ,  $\partial/\partial t \leftrightarrow -i\omega$ ) in equation (4.2.1) one obtains the *dispersion relation of the scalar wave equation*,

$$k_z = \pm \frac{\omega}{v} \sqrt{1 - \frac{v^2(x,z) k_x^2}{\omega^2}} \quad (4.2.6)$$

Using equation (4.2.6) with the choice of minus sign for migration, the solution (4.2.4) of the scalar wave equation becomes,

$$P(k_x, z, \omega) = P(k_x, 0, \omega) \exp\left(-i \int_0^z k_z(z) dz\right) \quad (4.2.7)$$

The exponential term is the depth extrapolation operator.

Because of the problems associated with the scalar wave equation, most extrapolation operators in wave theory based migrations are constructed from a one-way wave equation. However, if lateral velocity variations are present we need to move from the wavenumber to space domain. For an efficient and accurate calculation of the square root, we employ the recurrence relation for the continuous fraction expansion (Ma, 1981)

$$R_{2n} = 1 - \sum_{i=1}^n \frac{\alpha y^2}{1 - \beta y^2} \quad (4.2.8)$$

where  $R=(1-y^2)^{1/2}$ . For  $n=1$  the above equation becomes

$$R_2 = 1 - \frac{\alpha y^2}{1 - \beta y^2} \quad (4.2.9)$$

where for 45° accuracy  $\alpha=0.5$  and  $\beta=0.25$  and for 65° accuracy  $\alpha=0.478242060$  and  $\beta=0.376369527$  (Yilmaz, 1987). Then, we have the following 45° or 65° parabolic approximation of the one-way scalar wave equation

$$\frac{\partial P(x,z,\omega)}{\partial z} = -i \left( \frac{\omega}{v(x,z)} - \frac{k_x^2}{\frac{\omega}{\alpha v(x,z)} - \frac{\beta v(x,z) k_x^2}{\alpha \omega}} \right) P(x,z,\omega) \quad (4.2.10)$$

In the same way, we can apply a continuous fraction expansion to the dispersion relation, (4.2.6) or  $k_x^2 + k_z^2 = k^2$ . Then, the 65° parabolic approximation of the normalized dispersion relation,

$$\frac{k_z}{k} = \sqrt{1 - \frac{k_x^2}{k^2}} \quad (4.2.11)$$

can be written as

$$\frac{k_z}{k} = \frac{1 - (\alpha + \beta) \frac{k_x^2}{k^2}}{1 - \beta \frac{k_x^2}{k^2}} \quad (4.2.12)$$

Next, we employ a retarded coordinate transformation system (Claerbout, 1985) which removes the effect of vertical translation. The retarded coordinate system is related through the local velocity,  $v=v(z)$ , at each source location to the cartesian system by the following equations:

$$\begin{aligned} t' &= t'(x, z, t) = t + \int_0^z \frac{dz}{v(z)} \\ x' &= x'(x, z, t) = x \\ z' &= z'(x, z, t) = z \end{aligned} \quad (4.2.13)$$

The upcoming pressure wavefield can be written in terms of a stationary wave  $Q(x, z, \omega)$  in the frequency domain as:

$$P(x, z, \omega) = Q(x, z, \omega) e^{-i \omega \int_0^z \frac{dz}{v(z)}} \quad (4.2.14)$$

or

$$Q(x, z, \omega) = P(x, z, \omega) e^{i \omega \int_0^z \frac{dz}{v(z)}} \quad (4.2.15)$$

Since the retarded wavefield  $Q$  being more slowly variable with depth  $z$ , it may be sampled less densely, thereby, conserving computational effort. Differentiating (4.2.14) with respect to  $z$  gives:

$$\frac{\partial P(x, z, \omega)}{\partial z} = \left( \frac{\partial}{\partial z} - \frac{i\omega}{v(z)} \right) Q(x, z, \omega) e^{-i \omega \int_0^z \frac{dz}{v(z)}} \quad (4.2.16)$$

Substitute (4.2.14) and (4.2.16) into (4.2.10) so that we obtain the time shifted upcoming wavefield:

$$\frac{\partial Q(x,z,\omega)}{\partial z} = +i \left( \frac{k_x^2}{\alpha v(x,z)} - \frac{\beta v(x,z) k_x^2}{\alpha \omega} \right) Q(x,z,\omega) - i \omega \left( \frac{1}{v(x,z)} - \frac{1}{v(z)} \right) Q(x,z,\omega) \quad (4.2.17)$$

The first term on the right hand side represents the *diffraction term* and the second term on the right represents the *thin lens* term which is solved analytically. In the derivation above we assume that  $v(x,z)$  is a locally constant medium velocity and  $v(z)$  depends on depth below the source, only. Equation (4.2.17) may be rearranged by substituting for:  $-k_x^2 = \partial^2/\partial x^2$  and  $m(x,z) = \omega/v(x,z)$ . Then, the diffraction term becomes

$$-\frac{i m(x,z)}{\alpha} \frac{\partial Q(x,z,\omega)}{\partial z} - \frac{i \beta}{\alpha m(x,z)} \frac{\partial^3}{\partial x^2 \partial z} Q(x,z,\omega) + \frac{\partial^2}{\partial x^2} Q(x,z,\omega) = 0 \quad (4.2.18)$$

This equation is also called the *65° approximation to the scalar wave equation*, since this form of the square root approximation to the dispersion relation yields reliable results when the angles of incidence of the rays normal to the wavefront are less than about 65° or 70°. It is also called a *paraxial* equation and has all the properties of *parabolic* differential equations. It is the most important equation for 2-D  $\omega$ - $x$  migration. Equation (4.2.18) is evaluated step by step starting at the surface and moving to any depth.

The thin lens term honors Snell's law and properly accounts for curving horizons which act like lenses in optics. It has the solution

$$Q(x,z+\Delta z,\omega) = Q(x,z,\omega) \exp \left[ -i \omega \left( \frac{1}{v(x,z)} - \frac{1}{v(z)} \right) \Delta z \right] \quad (4.2.19)$$

The lens term is a phase-shift extrapolator (applies a time shift) and is incorporated as a correction within each depth step with the evaluation of the diffraction term. This term is very important in the correct imaging of events.

The diffraction term is solved numerically using finite difference. Thus, equation (4.2.18) can be written as

$$-\frac{i\beta}{\alpha m} \delta_{xx} \delta_z Q - \frac{i m}{\alpha} \delta_z Q + \delta_{xx} Q = 0 \quad (4.2.20)$$

where  $\delta_z = \partial/\partial z$ ,  $\delta_{xx} = \partial^2/\partial x^2$ , and  $m=m(x,z)=\omega/v(x,z)$ . A fourth order of accuracy for the approximation of the second order differential is used and an implicit Crank-Nicolson (Mitchell and Griffiths, 1980; Claerbout 1976,1985) finite difference algorithm scheme is employed to solve the resultant difference equation (Appendix D). Writing the problem in matrix form for each harmonic yields an independent set of tridiagonal solutions for each harmonic component,  $\omega_j$ .

The migration process consists of two parts, namely, extrapolation and imaging. During extrapolation the wavefield recorded at the surface is downward continued and reconstructed at depth. The extrapolation is performed via the above described diffraction term, which is evaluated step by step starting at the surface and moving to any depth, using an implicit finite difference scheme. The resulted algorithm is recursive where the result of the previous step is required as an input to the current extrapolation step.

The imaging is based on some principal that can be applied to obtain the reflection strength from the extrapolated data. Depending upon the principle used we can have poststack or prestack depth migration.

#### 4.2.2 Poststack 2-D $\omega$ -x Depth Migration

A common midpoint (CMP) section may be regarded as a zero offset section where the data have been obtained from coincident sources and receivers and travel paths from sources to reflectors are identical to those from reflectors to receivers. Therefore, assuming that the zero offset model is valid, the imaging condition can be based on the principle of the Exploding Reflector Model (ERM) (Loewenthal et al., 1976). According to this model the recorded wavefield  $P(x,z=0,t)$  at the surface receivers is due to the fact that the sources are aligned along reflectors and diffractors and are exploded at  $t=0$  and the resulted energy propagates upwards with one-half the actual velocity  $v(x,z)$ . If the migration uses the ERM model for imaging condition the migration is called poststack or zero-offset migration.

For the above described depth migration in poststack domain, the final migrated result is obtained by applying the imaging condition by summing the  $Q(x,z)$  field over

frequencies

$$M(x,z) = \frac{1}{N} \sum_{i=1}^N Q(x,z,\omega_i) \quad (4.2.21)$$

where N is the number of frequencies used.

In geologic areas where the seismic velocity does not vary or varies just in depth or varies smoothly laterally, the common midpoint assumption is valid and the above poststack depth migration is applicable. But in areas where the seismic velocity varies strongly in the lateral direction, the common midpoint assumption breaks down and we need to use prestack migration such as the one described next.

### 4.2.3 Prestack 2-D $\omega$ -x Depth Migration

Prestack migration uses unstacked data (e.g., common source gathers) which are not zero source-receiver offset. Thus, we cannot use the exploding reflector model to accomplish a simultaneous downward continuation of sources and receivers. Therefore, the main difference between poststack (zero-offset) migration and prestack migration is the imaging condition and the fact that in the prestack migration the true medium velocity is used instead of the half value as in the zero-offset migration.

Tsingas (1989) used a  $45^\circ$  approximation to obtain a prestack migration algorithm. On the other hand, the method developed here uses the  $65^\circ$  approximation to the scalar wave equation in the  $\omega$ -x domain. However, it basically uses the same imaging condition as the one of Tsingas and Kanasevich (1990).

We can assume that a reflector exists whenever the direct wave (downgoing,  $D(x,z,\omega)$ ) from the source and the reflected (upcoming,  $U(x,z,\omega)$ ) waves are coincident. Then, the migrated depth section consists of wave amplitudes at the given location at the time of the arrival of the direct wave. Thus, the resulting image for each monochromatic wave is

$$Image(x,z,\omega) = U(x,z,\omega) \cdot \tilde{D}(x,z,\omega) \quad (4.2.22)$$

The recorded wave (i.e., common shot gather)  $P(x,z=0,t)$  at the earth's surface is extrapolated downward from the receiver ( $z=0$ ) into the medium (depth  $z$ ) in order to reconstruct the upcoming wave,  $Q(x,z,\omega)$ . Also, the wave from the source is extrapolated



downward into the medium. This is the downgoing wave and it is an impulse whose direct traveltimes from the source location to the subsurface points are computed separately. The migrated image is achieved where the two waves meet. Thus, the imaging condition for the 65° prestack depth migration in the frequency domain is

$$\text{Im}(x,z,t_d) = \frac{1}{N} \sum_{n=1}^N Q(x,z,\omega_n) \exp(-i \omega_n t_d(x,z)) \quad (4.2.23)$$

where  $N$  is the number of frequencies used. Also,  $t_d(x,z)$  is the direct arrival time from the source to the depth point  $(x,z)$ .

For each grid point, the imaging condition needs the one-way travel time from the source to that point. Various approaches can be used such as ray tracing (Chang and McMechan, 1986), cross correlation (Whitmore and Lines, 1986), amplitude detection (Lowenthal and Hu, 1991) and finite difference solution of the eikonal equation (Vidale, 1987). Traveltimes are classically computed with ray tracing techniques. However, ray tracing has a number of limitations such as inability to cover shadow zones and the large number of rays involved in heterogeneous media from which only one has to be picked.

Reshef and Kosloff (1986), and Tsingas and Kanasevich (1990) used 2-D ray tracing for the computation of the direct time arrivals from a source to each point at the subsurface in unperturbed media. Using Fermat's principle ("the change in travel time with respect to the change of the ray path is zero"), they solved a set of first order ordinary differential equations by employing a fourth order Runge-Kutta integration method. However, the Runge-Kutta method is expensive and difficult to implement for large velocity variations. Conversely, graphical methods devoted to wavefront tracing have been proposed. Vidale (1987) proposed a general wavefront tracing technique based on the finite difference approximation of the eikonal equation. With this approach, wave fronts rather than rays are propagated in the model. Vidale's method was improved by Qin (1990). Van Trier and Symes (1991) solved the Hamiltonian representation of the eikonal equation. More recently, Podvin and Lecomte (1991) developed a finite difference method based on the systematic application of Huygen's principle for the estimation of direct arrival times.

In our implementation, we calculate the direct arrival times from 2-D forward elastic modeling. Computation of the excitation time imaging condition with forward modeling is described in detail in a later section (3-D reverse time migration). Since, in most cases we need to simulate wave propagation in aid of interpretation of the real data and validation of the velocity model, we compute the direct arrival times at the same time. Here, we used the

2-D elastic modeling algorithms discussed in chapter 3.

### 4.3 ONE-PASS 3-D FINITE DIFFERENCE DEPTH MIGRATION

#### 4.3.1 Introduction

In order to avoid the above described complexities, described above, numerical instabilities and high computational demands with the 3-D direct solution, we decided to follow the one-pass approach for the development of our own 3-D depth migration algorithm. We think that this method provides the right tradeoff between accuracy and computational efficiency. Thus, in the next sections we developed one-pass 3-D finite difference prestack and poststack depth migration algorithms in the frequency-space domain that are based on a 65<sup>o</sup> approximation to the dispersion relation. The algorithms are highly parallelizable in the space and frequency domain and are implemented on a 44-processor MIMD massively parallel computer.

The poststack depth migration algorithm is very fast and is used for the improved imaging of steam zones during thermal EOR processes. For the type of velocity complexities that we have in the Cold lake area where we apply the algorithm for the migration of 3-D seismic data, we believe that it is a very accurate and computationally efficient algorithm.

#### 4.3.2 Problem Formulation: Equations

The observed seismic wavefield at  $z=0$  can be approximated by the 3-D scalar wave equation:

$$\frac{\partial^2}{\partial x^2} P(x,y,z,t) + \frac{\partial^2}{\partial y^2} P(x,y,z,t) + \frac{\partial^2}{\partial z^2} P(x,y,z,t) = \frac{1}{v^2(x,y,z)} \frac{\partial^2}{\partial t^2} P(x,y,z,t) \quad (4.3.1)$$

The Fourier transformed field is given by:

$$P(k_x, k_y, z, \omega) = \iiint P(x,y,z,t) e^{(ik_x x + ik_y y - i\omega t)} dx dy dt \quad (4.3.2)$$

Applying the above operator to the scalar wave equation leads to:

$$\frac{\partial^2 P}{\partial z^2} + \left[ \frac{\omega^2}{v^2(x,y,z)} - k_x^2 - k_y^2 \right] P = 0 \quad (4.3.3)$$

The solution to this equation is also solution to the one-way scalar wave equation for upcoming waves:

$$\frac{\partial P}{\partial z} = -i \frac{\omega}{v} \sqrt{1 - \frac{v^2(x,y,z) k_x^2}{\omega^2} - \frac{v^2(x,y,z) k_y^2}{\omega^2}} P \quad (4.3.4)$$

Also, taking the Fourier transform of both spatial and temporal coordinates in equation (4.3.1) one obtains the well known dispersion relation for scalar wave equation:

$$k_z(z) = \pm \frac{\omega}{v} \sqrt{1 - \frac{v^2(x,y,z) k_x^2}{\omega^2} - \frac{v^2(x,y,z) k_y^2}{\omega^2}} \quad (4.3.5)$$

where  $k_x$ ,  $k_y$ ,  $k_z$  are the horizontal and vertical wavenumbers and  $\omega$  is the angular frequency. For upcoming waves (migration) we use the minus sign.

The square root in the one-way wave equation or in the dispersion relation is approximated using Muir's expansion (Claerbout, 1985). Then, equation (4.3.4) becomes

$$\frac{\partial P}{\partial z} = -i \frac{\omega}{v} \left( \sqrt{1 - \frac{v^2(x,y,z) k_x^2}{\omega^2}} + \sqrt{1 - \frac{v^2(x,y,z) k_y^2}{\omega^2}} - 1 \right) P \quad (4.3.6)$$

Next, the square root terms are approximated by employing the recurrence relation, equations (4.2.8 and 4.2.9) for the continuous fraction expansion (Ma, 1981). Also, the horizontal wavenumbers are substituted by  $(-ik_x^2) = \partial^2 / \partial x^2$  and  $(-ik_y^2) = \partial^2 / \partial y^2$ . Then, the one-way wave equation becomes:

$$\frac{\partial P}{\partial z} = -i \left( \frac{\omega}{v(x,y,z)} - \frac{k_x^2}{\frac{\omega}{\alpha v(x,y,z)} - \frac{\beta v(x,y,z) k_x^2}{\alpha \omega}} - \frac{k_y^2}{\frac{\omega}{\alpha v(x,y,z)} - \frac{\beta v(x,y,z) k_y^2}{\alpha \omega}} \right) P \quad (4.3.7)$$

where for 45° accuracy  $\alpha=0.5$  and  $\beta=0.25$  and for 65° accuracy  $\alpha=0.478242060$  and  $\beta=0.376369527$  (Yilmaz, 1987). This is now a parabolic equation representing upgoing waves from reflectors to receivers.

Then, we employ a retarded coordinate transformation system (Claerbout, 1985) which removes the effect of vertical translation. This retarded coordinate system is related through the local velocity,  $v=v(z)$ , at each source location to the cartesian system by the following equations:

$$\begin{aligned} t' &= t'(x,y,z,t) = t + \int_0^z dz/v(z) \\ x' &= x'(x,y,z,t) = x \\ y' &= y'(x,y,z,t) = y \\ z' &= z'(x,y,z,t) = z \end{aligned} \quad (4.3.8)$$

Employing the above retarded coordinate system, the pressure wavefield  $P(x,y,z,\omega)$  can be written in terms of a stationary wave  $Q(x,y,z,\omega)$  in the frequency domain as

$$P(x,y,z,\omega) = Q(x,y,z,\omega) e^{-i\omega \int_0^z \frac{dz}{v(z)}} \quad (4.3.9)$$

or

$$Q(x,y,z,\omega) = P(x,y,z,\omega) e^{i\omega \int_0^z \frac{dz}{v(z)}} \quad (4.3.10)$$

Then, after differentiating equation (4.3.9) with respect to  $z$ , we obtain:

$$\frac{\partial P(x,y,z,\omega)}{\partial z} = \left( \frac{\partial}{\partial z} - \frac{i\omega}{v(z)} \right) Q(x,y,z,\omega) e^{-i\omega \int_0^z \frac{dz}{v(z)}} \quad (4.3.11)$$

Substituting equations (4.3.9) and (4.3.11) into equation (4.3.7), we obtain for the time shifted upcoming wavefield a differential equation in the  $\omega$ - $x$ - $y$  domain of the form,

$$\begin{aligned}
\frac{\partial Q(x,y,z,\omega)}{\partial z} = & i \frac{k_x^2}{\frac{\omega}{\alpha v(x,y,z)} - \frac{\beta v(x,y,z) k_x^2}{\alpha \omega}} Q(x,y,z,\omega) + \\
& + i \frac{k_y^2}{\frac{\omega}{\alpha v(x,y,z)} - \frac{\beta v(x,y,z) k_y^2}{\alpha \omega}} Q(x,y,z,\omega) \\
& - i \omega \left( \frac{1}{v(x,y,z)} - \frac{1}{v(z)} \right) Q(x,y,z,\omega)
\end{aligned} \tag{4.3.12}$$

The first two terms on the right hand side represent the 3-D *diffraction term*. The third term on the right is called the *thin lens* term that is solved analytically as in equation (4.2.19).

The 3-D diffraction term involves an enneadiagonal (nine-fold) system of equations that can be solved using sparse matrix solvers such as matrix inversion, conjugate gradient and Gaussian elimination. However, this full 3-D approach is prohibitively expensive. On the other hand, a feasible computer implementation of the above method can be made by using the two-pass or the one-pass approach. In the two-pass approach we have full separation of the diffraction term, thus this is equivalent of two 2-D migrations, first in the  $x$  and then in the  $y$  direction. The full separation of the extrapolation operator is valid only when the velocity is slowly varying in depth. On the other hand, we can use the one-pass or splitting approach if we have a slowly laterally varying velocity field. This approach uses an alternating direction implicit (ADI) Crank-Nicolson scheme (Mitchell, 1969; Mitchell and Griffiths, 1980) and often is called the ADI method. For the one-pass or ADI method the field is downward continued alternatively along the  $x$  and then  $y$ -direction for each depth step (extrapolation step). However, when we have strong vertical or lateral velocity gradients the two terms within the diffraction term do not commute and therefore, are not separable.

Upon splitting the diffraction term, we get one diffraction term in the  $x$ -direction and one in the  $y$ -direction. Then, substituting for  $-k_x^2 = \partial^2/\partial x^2$ ,  $-k_y^2 = \partial^2/\partial y^2$ , and  $m(x,y,z)=\omega/v(x,y,z)$ , replacing the differentials of equation by their respective finite differences and changing the sign of the  $z$  differentials to evaluate upgoing waves one has for the  $x$ -direction diffraction term:

$$-\frac{i \beta}{\alpha m} \delta_{xx} \delta_z Q - \frac{i m}{\alpha} \delta_z Q + \delta_{xx} Q = 0 \tag{4.3.14}$$

where  $\delta_z = \partial/\partial z$ ,  $\delta_{xx} = \partial^2/\partial x^2$ , and  $m=m(x,z)$ ; and for the y-direction diffraction term:

$$-\frac{i\beta}{\alpha m} \delta_{yy} \delta_z Q - \frac{im}{\alpha} \delta_z Q + \delta_{yy} Q = 0 \quad (4.3.15)$$

where  $\delta_{yy} = \partial^2/\partial y^2$ . A fourth order of accuracy for the approximation of the second order differential is used and an implicit Crank-Nicolson (Mitchell and Griffiths, 1980; Claerbout 1976,1985) finite difference algorithm scheme is employed to solve each resultant difference equation (Appendix D). The thin lens term is solved analytically and is incorporated as a correction within each depth step with the evaluation of equations (4.3.14) and (4.3.15) and is given by:

$$\text{Thin lens} = -i\omega \left( \frac{1}{v(x,y,z)} - \frac{1}{v(z)} \right) Q(x,y,z,\omega) \quad (4.3.16)$$

Each downward continuation or extrapolation step proceeds along  $x$  and then  $y$  coordinates solving a tridiagonal system of equations. For each extrapolation the ADI method requires the solution of  $2N$  complex tridiagonal systems of dimension  $N$ , where  $N$  is the number of input/output  $x$  and  $y$  coordinates. The algorithm is recursive where the result of the previous extrapolation step is used as an input to the current extrapolation step. Any laterally slowly varying velocity function can be used for the extrapolation.

### 4.3.3 One-Pass 3-D Poststack Depth Migration

The migration process consists of two parts, namely, extrapolation and imaging. During extrapolation the wavefield recorded at the surface is downward continued and reconstructed at depth. The imaging is based on some principle that can be applied to obtain the reflection strength from the extrapolated data.

After stacking and binning of the 3-D seismic data we have a regular geometry with a number of inline and cross-line stacked sections. A stacked (CDP) section may be regarded as a zero offset section where the data have been obtained from coincident sources and receivers and travel paths from sources to reflectors are identical to those from reflectors to receivers. Therefore, assuming that the zero offset model is valid, the imaging condition for the poststack depth migration can be based on the principle of the Exploding Reflector Model (ERM) (Loewenthal et al., 1976). According to this model the recorded wavefield

$P(x,y,z=0,t)$  at the surface receivers is due to the fact that the sources are aligned along reflectors and diffractors in the inline and cross-line direction and they are exploded at  $t=0$  with the resultant energy propagating upwards with one-half the actual velocity  $v(x,y,z)$ . But because of the splitting of the diffraction term at each depth step, we need to double the velocity. Thus, the input velocity into the migration is the true velocity.

The migrated result is obtained by applying the imaging condition and summing the  $Q(x,y,z)$  field over the frequency spectrum used.

$$Q(x,y,z,t=0) = \frac{1}{N} \sum_{\omega} Q(x,y,z,\omega) \quad (4.2.14)$$

where  $N$  is the number of harmonic terms within the Nyquist bandpass.

Consequently, the input for the one-pass 3-D poststack migration consists of the stacked seismic volume (inlines and crosslines) in time and the velocity model. The migrated result is a seismic volume with inline/crossline geometry in depth. Having the migrated result in depth makes the interpretation easier and more accurate.

#### 4.3.4 One-Pass 3-D Prestack Depth migration

The main differences between prestack and poststack migration are the imaging condition, the geometry of the input data and the velocity model. For the 3-D prestack migration we use the same imaging principal as the one used for the 2-D case.

Assuming that a reflector exists whenever the direct wave from the source and the reflected are coincident, the depth section will consist of wave amplitudes at the given depth location at the time of the arrival of the direct wave. If  $P(x,y,z=0,t)$  represents the recorded common shot gather at the earth's surface, the migrated shot gather will be the cross-correlation between downgoing and upgoing wave. Thus, for the 3-D prestack depth migration the imaging condition is:

$$M(x,y,z,t_d) = \frac{1}{N} \sum_{\omega} Q(x,y,z,\omega) e^{-i\omega t_d(x,y,z)} \quad (4.2.15)$$

where  $t_d(x,y,z)$  is the arrival time of the direct wave.

Consequently, the input to the migration is the shot gathers recorded at the earth's surface, the medium velocity and the direct time arrivals. A number of methods have been developed for computing travel time maps in 2-D and 3-D media (Shah, 1973). However,

here we compute the direct arrival times with the 3-D acoustic forward modeling developed in chapter 3.

#### 4.4 FORWARD MODELING IN THE FREQUENCY DOMAIN AND OTHER APPLICATIONS

The 2-D and 3-D poststack migration algorithms described above can be used for forward modeling. Thus, we perform modeling of zero-offset sections with the parabolic approximation of the scalar wave equation in the frequency domain.

In the same way as for poststack migration, modeling of zero-offset sections makes use of the exploding reflector model. We start by setting the upgoing wavefield equal to zero below the depth of interest. Then, we use the parabolic approximation of the scalar wave equation to depth extrapolate the wavefield towards the surface. According to the exploding reflector model, the sources are exploded on the reflectors at time zero and the wave propagate upwards with half the medium's velocity.

The 65° parabolic approximations to the the 2-D and 3-D scalar wave equations are used for 2-D and 3-D zero-offset modeling, respectively. The corresponding 2-D poststack and 3-D one-pass migration algorithms developed in earlier sections essentially can be run in the reverse direction, from the bottom up and thus can be used to model a zero offset section according to the exploding reflector model. In a similar way, Tsingas (1989) used a 2-D 45° migration algorithm for forward modeling of zero-offset sections. However, he used a delta function at  $t=0$  which has a Fourier transform that is a constant, independent of frequency. Thus, he modeled the exploding reflectors at each depth step by adding the reflection coefficients to all frequency components of the upgoing wavefield at each depth step. In our implementation, a Ricker wavelet is convolved at each upward depth step with the local reflectivity. However, since we are in the frequency domain we multiply it with the local reflection coefficient and the product is added to the passing upgoing wavefield. When the wavefield is upward continued to the surface and the extrapolation is completed, the synthetic zero-offset time sections are obtained after inverse Fourier transform of the resultant wavefield at the surface.

Since we are using the same extrapolation algorithm as we did for migration, and taking into account that migration is the inverse process of forward modeling, we reverse the sign of the velocity values during implementation of the migration algorithm for modeling.

For the 2-D forward implementation the velocities must be halved since we simulate



an exploding reflector experiment. However, in the 3-D forward modeling there is no need for that since we use the one-pass migration algorithm where, on the one hand, the exploding reflector model halves the velocities and, on the other hand, the splitting of the diffraction term at each depth step and subsequent extrapolation in two orthogonal directions results in doubling the velocities.

Tsingas (1989) incorporated attenuation in his 45° paraxial approximation based on a 2-D zero-offset modeling algorithm using a frequency independent  $Q$ . The parabolic approximation of the wave equation in the frequency domain employs a decomposition of the wavefield into monochromatic plane waves. Thus, each frequency harmonic can be extrapolated in depth independently. This property allows the incorporation of velocity dispersion and a frequency independent  $Q$  (Chapter 5, equation 5.12) in the 2-D and 3-D forward modeling and migration algorithms developed above.

Both 65-degree  $\omega$ - $x$  poststack and prestack migration algorithms can be extended to include anisotropy using the scalar wave equation for elliptically anisotropic media in the same way that Phadke et al. (1994) developed a 45-degree poststack migration for transversely isotropic media. However, this development does not take place in this thesis and it has been left for future research.

#### **4.5 PARALLEL IMPLICIT FINITE DIFFERENCE DEPTH MIGRATION AND MODELING ALGORITHMS**

A typical 3-D marine survey after stacking and binning has 1000 inlines and 1000 crosslines (one million CDP's/traces) with 1000 time samples per trace but often surveys are much larger (30 million traces). It would be extremely time consuming to perform an one-pass 3-D depth migration of this survey on a powerful single CPU computer, assuming that we did not have memory limitations. Therefore, a parallel implementation is necessary.

The design, implementation and performance of a parallel algorithm depends on a number of features such as domains of dependence, declaration of parallel regions, task (computational unit within a multitasked algorithm) level parallelism, understanding of all subroutine calls used inside the parallel region in order to assure that all tasks are executing in parallel. The key to a successful implementation of a multitasked algorithm is to precisely define and protect the shared data and add the necessary communication and synchronization controls to the parallel tasks.

For the design, implementation and performance of the above depth migration

algorithms on parallel computers (Kalantzis et al., 1993a) we can exploit the inherent parallelism of the seismic problem over frequencies, traces, depth slices, inlines and crosslines and shots in a number of different ways.

The most important domain in terms of parallel algorithm performance is the frequency domain. The parabolic approximation of the wave equation in the frequency domain decomposes the wavefield into monochromatic plane waves. Thus, each frequency harmonic can be extrapolated in depth independently on each processor with no need of intertask communication. However, the wavefield at each depth step is calculated from the wavefield in the previous depth step. Therefore, the algorithm is recursive in depth and the computation is inherently serial over depth steps.

The frequency (parallel) and depth (serial) loops are interchangeable in all the above developed algorithms. This property allowed us to use three programming models (Figure 4.1). The first, "MODEL I", employs a parallel frequency outer-loop. This has the advantage of using parallelism at the top level of the algorithm, thus, declaring a larger computational region. However, this frequency outer-loop programming model requires a much larger memory space that is proportional to the number of depth steps. This memory requirement does not allow the use of this parallel algorithm for migration of large 3-D seismic surveys or large number of depth extrapolation steps. Assume that we have a volume of size  $NX*NY*NZ$ . Then, this implementation requires the declaration of the following arrays in the 3-D case: a complex array of  $[NX*NY]$  size for each input monochromatic plane wave  $P(x,y,\omega_i)$ ; a real array of size  $[NX*NY]$  for the velocity field  $v(x,y)$  at each depth-slice; and a real array of size  $[NX*NY*NZ]$  for the output depth migrated volume for each frequency. Thus, the total memory requirement is  $[(NX*NY*4)*(3+NZ)]$  bytes.

One way to overcome this problem, is the use of a number of depth regions as in "MODEL II". Thus, the downward extrapolation is performed within each depth region for all frequency components in parallel. Then, the migrated output of this region is saved in the I/O storage area and its bottom part is used as an input for the migration of the next zone. This continues recursively for all depth regions or zones (NR). This algorithmic structure uses the following arrays: a complex array of  $[NX*NY]$  size for the input frequency plane  $P(x,y,\omega_i)$ ; a real array of size  $[NX*NY]$  for the velocity field  $v(x,y)$  at each depth-slice; and a real array of size  $\{NX*NY*(NZ/NR)\}$  for the depth migrated in each depth zone. Thus, the total memory requirement is  $\{(NX*NY*4)*[3+(NZ/NR)]\}$  bytes.

The third model, "MODEL III", uses a serial depth outer-loop and the parallel region

is confined to the inner frequency loop. This approach does not have memory limitations, however, it is computationally slower than the other two models since the computational parallel region is smaller. This parallel algorithm has the following memory requirements: an array of  $[NX*NY*N\omega]$  size for the input 3-D volume in frequency domain ( $P(x,y,\omega)$ ); an array of size  $[NX*NY]$  for the velocity field  $v(x,y)$  at each depth-slice; and an array of size  $[NX*NY]$  for the output migrated depth-slice  $Q(x,y)$ . Thus, the total memory requirement is  $[(NX*NY*4)*(2+2N\omega)]$ .

From the above models, MODEL I is the most efficient in terms of total CPU requirements but the worst in terms of memory requirements. MODEL III is better than MODEL II in terms of memory requirements only if  $2N\omega$  is smaller than  $NZ/NR$ . For a model of size  $50 \times 50 \times 50$ , 500 time samples and 250 frequencies, programming "MODEL I" used 385 sec and "MODEL III" used 485 sec on 40 processors of the Myrias SPS3 computer. Thus, in terms of CPU time requirements, "MODEL I" is more efficient than "MODEL III".

For the poststack migration, all frequency components after extrapolation are summed up (imaging condition) to give the migrated depth section. On the other hand, for prestack migration, after each depth extrapolation step is completed, each frequency component constructs a partial image by cross correlating the extrapolated field with the downgoing wave from the source (imaging condition). Then, all frequency partial images, after extrapolation to the maximum depth, are summed up to give the migrated shot gathers. For prestack migration an additional parallel loop can be implemented over shots.

The 2-D and 3-D poststack and prestack depth migration and zero-offset forward modeling parallel algorithms were implemented on a 44-processor (8Mbytes memory per processor) Myrias SPS3 MIMD parallel computer. Their pseudocodes are shown in Figures 4.2 to 4.6. We used only two extensions to FORTRAN 77: one is the "pardo" which is a parallel do loop and the other is the "mergeby(sum)" for automatic merging of results from different processors. The one-pass 3-D poststack migration (I/O, parallel FFT, migration with "MODEL III") of a 3-D seismic volume of size  $\{[NX*NY*NT]=90*73*1501\}$  using 250 frequencies and 1501 depth steps required about 9.1 hours of CPU time on 40 processors of the Myrias parallel computer.

## PARALLEL PROGRAMMING MODELS

### MODEL I

```
PARALLEL DO 10 over number of FREQUENCIES ( $N\omega$ )
  DO 20 over DEPTH steps ( $NZ$ )
    Extrapolation of depth slice  $Q(NX,NY,\omega_i)$  of size:  $\{[NX*NY]*8\}$ 
20  END DO over number of DEPTH steps
    Automatic merging of all frequency components=
    migrated volume  $\{[NX*NY*NZ]*4\}$ 
10  END PARALLEL DO over number of FREQUENCIES
```

---

### MODEL II

```
DO 10 over number of DEPTH REGIONS ( $NR$ )
  PARALLEL 20 DO over number of FREQUENCIES ( $N\omega$ )
    DO 30 over DEPTH steps ( $NZ/NR$ )
      Extrapolation of depth slice of size:  $\{[NX*NY]*8\}$ 
30  END DO over number of DEPTH steps
      Automatic merging of all frequency components=
      migrated region  $\{[NX*NY*(NZ/NR)]*4\}$ 
20  END PARALLEL DO over number of FREQUENCIES
10  END DO over DEPTH REGIONS
```

---

### MODEL III

```
DO 10 over DEPTH steps ( $NZ$ )
  PARALLEL DO 20 over number of FREQUENCIES ( $N\omega$ )
    Extrapolation of depth slice of size:  $\{[NX*NY*N\omega]*8\}$ 
20  END PARALLEL DO over number of FREQUENCIES
    Automatic merging of each migrated depth slice of size:  $\{[NX*NY]*4\}$ 
10  END DO over number of DEPTH steps
```

---

### TOTAL MEMORY REQUIREMENTS (Bytes)

```
MODEL I =  $[NX*NY*4]*[3+NZ]$ 
MODEL II =  $[NX*NY*4]*[3+(NZ/NR)]$ 
MODEL III =  $[NX*NY*4]*[2+(2*N\omega)]$ 
```

---

**Figure 4.1:** The code structure models used for parallelization of the migration and modeling algorithms in the frequency domain.

## 2-D FINITE DIFFERENCE $\omega$ -x 65° DEPTH POSTSTACK MIGRATION PARALLEL PSEUDOCODE

---

**INPUT:** parameters; reference velocity  $v(z)$ ; velocity model  $v(x,z)$ \*\*

**INPUT:** stacked section  $P(x,z=0,t)$

**PARALLEL FFT:** Fourier transform :  $P(x,z=0,\omega)$

**C MAIN PART OF PARALLELISM: EXTRAPOLATION+IMAGING**  
**\* PARALLEL DO ("PARDO") 20: over number of FREQUENCIES**  
**\* DO 30 over number of DEPTH steps**

**A. CALCULATE the time retarded field:**

$$Q(x,z,\omega) = P(x,z,\omega) e^{i \frac{\omega}{v(z)} \Delta z}$$

**B. EXTRAPOLATE using the diffraction term:**

$$-\frac{i m}{\alpha} \frac{\partial Q(x,z,\omega)}{\partial z} - \frac{i \beta}{\alpha m} \frac{\partial^3 Q(x,z,\omega)}{\partial x^2 \partial z} + \frac{\partial^2 Q(x,z,\omega)}{\partial x^2} = 0$$

where  $m = \omega/v(x,z)$  \*\*

**C. CORRECT with the thin lens term:**

$$Q(x,z,\omega) = Q(x,z,\omega) e^{-i \omega \left( \frac{1}{v(x,z)} - \frac{1}{v(z)} \right) \Delta z}$$

**30 END DO over number of DEPTH steps**  
**AUTOMATIC MERGING ("merge(sum)") for**  
**Imaging Condition:  $Q(x,z) = \sum_{i=1}^N Q(x,z,\omega_i)$**   
**40 END PARDO over number of FREQUENCIES**

**OUTPUT:** migrated depth section:  $M(x,z) = \frac{1}{N} Q(x,z)$

*\* frequency and depth loops are interchangeable*

*\*\* for velocity dispersion ,  $v = v(x,z,\omega)$  from equation (5.12) and  $m = \omega/v(x,z,\omega)$*

**Figure 4.2:** Parallel pseudocode for 2-D  $\omega$ -x 65° poststack depth migration as was implemented on a Myrias SPS3 parallel computer.

**2-D FINITE DIFFERENCE  $\omega$ -x 65° DEPTH  
PRESTACK MIGRATION PARALLEL PSEUDOCODE**

---

**INPUT:** parameters; reference velocity  $v(z)$ ; velocity model  $v(x,z)**$   
**INPUT:** shot gathers,  $P(x,z=0,t)$ ; direct traveltimes  $t_d(x,z)$   
**PARALLEL FFT:** Fourier transform,  $P(x,z=0,\omega)$

**C MAIN PART OF PARALLELISM: EXTRAPOLATION+IMAGING**  
**\* PARALLEL DO (“PARDO”) 10: over number of SHOTS**  
**\* PARALLEL DO (“PARDO”) 20: over number of FREQUENCIES**  
**\* DO 30 over number of DEPTH steps**

**A. CALCULATE the time retarded field**  

$$Q(x,z,\omega) = P(x,z,\omega) e^{i \frac{\omega}{v(z)} \Delta z}$$

**B. EXTRAPOLATE using the diffraction term**  

$$-\frac{i m}{\alpha} \frac{\partial Q(x,z,\omega)}{\partial z} - \frac{i \beta}{\alpha m} \frac{\partial^3 Q(x,z,\omega)}{\partial x^2 \partial z} + \frac{\partial^2 Q(x,z,\omega)}{\partial x^2} = 0$$

**C. CORRECT with thin lens term**  

$$Q(x,z,\omega) = Q(x,z,\omega) e^{-i \omega \left( \frac{1}{v(x,z)} - \frac{1}{v(z)} \right) \Delta z}$$

**D. CONSTRUCT PARTIAL IMAGE:**  

$$im(x,z_i,\omega_i) = Q(x,z_i,\omega_i) \exp(-i\omega_i t_d(x,z))$$

**30 END DO over number of DEPTH steps**  
**AUTOMATIC MERGING (“merge(sum))**  
of all frequency components:  $IM(x,z) = \sum_{i=1}^N im(x,z,\omega_i)$

**20 END PARDO over FREQUENCIES**  
**OUTPUT: Migrated shot gather:  $M(x,z) = \frac{1}{N} IM(x,z)$**

**10 END PARDO over number of SHOTS**

*\* shot, frequency and depth loops are interchangeable*

*\*\* with velocity dispersion  $v=v(x,z,\omega)$  from equation (5.12) and  $m=\omega/v(x,z,\omega)$*

**Figure 4.3:** Parallel pseudocode for 2-D  $\omega$ -x 65° prestack depth migration.

**ONE-PASS 3-D FINITE DIFFERENCE  $\omega$ -x-y 65<sup>0</sup> DEPTH  
POSTSTACK MIGRATION PARALLEL PSEUDOCODE**

---

INPUT: parameters; reference velocity  $v(z)$ ; velocity model  $v(x,y,z)$ \*\*  
INPUT: binned stacked 3-D volume,  $P(x,y,z=0,t)$   
PARALLEL FFT: Fourier transform,  $P(x,y,z=0,\omega)$   
**C MAIN PART OF PARALLELISM: EXTRAPOLATION+IMAGING**  
\* **PARALLEL DO (“PARDO”) 20: over number of FREQUENCIES**  
\* **DO 30 over number of DEPTH steps**  
    **CALCULATE the time retarded field**  
        
$$Q(x,y,z,\omega) = P(x,y,z,\omega) e^{i \frac{\omega}{v(z)} \Delta z}$$
  
    **DO 40 over number of INLINES**  
        **EXTRAPOLATE along the inline x-direction**  
            
$$-\frac{i m}{\alpha} \frac{\partial Q(x,y,z,\omega)}{\partial z} - \frac{i \beta}{\alpha m} \frac{\partial^3 Q(x,y,z,\omega)}{\partial x^2 \partial z} + \frac{\partial^2 Q(x,y,z,\omega)}{\partial x^2} = 0$$
  
**40**    **END DO over number of INLINES**  
        **DO 50 over number of CROSSLINES**  
            **EXTRAPOLATE along the crossline y-direction**  
                
$$-\frac{i m}{\alpha} \frac{\partial Q(x,y,z,\omega)}{\partial z} - \frac{i \beta}{\alpha m} \frac{\partial^3 Q(x,y,z,\omega)}{\partial y^2 \partial z} + \frac{\partial^2 Q(x,y,z,\omega)}{\partial y^2} = 0$$
  
**50**    **END DO 50 over number of CROSSLINES**  
        **CORRECT with the thin lens term:**  
            
$$Q(x,y,z,\omega) = Q(x,y,z,\omega) e^{-i \omega \left( \frac{1}{v(x,y,z)} - \frac{1}{v(z)} \right) \Delta z}$$
  
**30**    **END DO over number of DEPTHS**  
        **AUTOMATIC MERGING (“merge(sum)):**  
        for Imaging Condition:  $Q(x,y,z) = \sum_{i=1}^N Q(x,y,z,\omega_i)$   
**20** **END PARDO over FREQUENCIES**  
    **OUTPUT: depth migrated depth 3-D volume:  $M(x,y,z) = \frac{1}{N} Q(x,y,z)$**   
\* *frequency and depth loops are interchangeable*  
\*\* *with velocity dispersion  $v=v(x,y,z,\omega)$  from equation (5.12) and  $m=\omega/v(x,y,z,\omega)$*

**Figure 4.4:** Parallel pseudocode for one-pass 3-D  $\omega$ -x-y 65<sup>0</sup> poststack depth migration.

**ONE-PASS 3-D FINITE DIFFERENCE  $\omega$ -x-y 65° DEPTH  
PRESTACK MIGRATION PARALLEL PSEUDOCODE**

---

INPUT: parameters; reference velocity  $v(z)$ ; velocity model  $v(x,y,z)$ \*\*  
INPUT: shot gathers  $P(x,y,z=0,t)$  and direct traveltimes  $t_d(x,y,z)$   
PARALLEL FFT: Fourier transform,  $P(x,y,z=0,\omega)$   
**C MAIN PART OF PARALLELISM: EXTRAPOLATION+IMAGING**  
\* **PARALLEL DO ("PARDO") 10: over number of SHOTS**  
\* **PARALLEL DO ("PARDO") 20: over number of FREQUENCIES**  
\* **DO 30 over DEPTH steps**  
**CALCULATE the time retarded field**  
**DO 40 over number of traces along X**  
**EXTRAPOLATE along the x-direction**  

$$-\frac{i m}{\alpha} \frac{\partial Q(x,y,z,\omega)}{\partial z} - \frac{i \beta}{\alpha m} \frac{\partial^3 Q(x,y,z,\omega)}{\partial x^2 \partial z} + \frac{\partial^2 Q(x,y,z,\omega)}{\partial x^2} = 0$$
**40 END DO over X**  
**DO 50 over number of traces in Y**  
**EXTRAPOLATE along the y-direction**  

$$-\frac{i m}{\alpha} \frac{\partial Q(x,y,z,\omega)}{\partial z} - \frac{i \beta}{\alpha m} \frac{\partial^3 Q(x,y,z,\omega)}{\partial y^2 \partial z} + \frac{\partial^2 Q(x,y,z,\omega)}{\partial y^2} = 0$$
**50 END DO 50 over Y**  
**CORRECT with the thin lens term:**  

$$Q(x,y,z,\omega) = Q(x,y,z,\omega) e^{-i \omega \left( \frac{1}{v(x,y,z)} - \frac{1}{v(z)} \right) \Delta z}$$
**CONSTRUCT PARTIAL IMAGE:**  

$$im(x,y,z_i,\omega_i) = Q(x,y,z_i,\omega_i) \exp(-i\omega_i t_d(x,y,z))$$
**30 END DO over number of DEPTH steps**  
**AUTOMATIC MERGING ("merge(sum))**  
of all frequency components:  $IM(x,y,z) = \sum_{i=1}^N im(x,y,z,\omega_i)$   
**20 END PARDO over number of FREQUENCIES**  
**OUTPUT: Migrated shot gather:  $M(x,y,z) = \frac{1}{N} IM(x,y,z)$**   
**5 END PARALLEL DO over number of SHOTS**  
\* *shot, frequency and depth loops are interchangeable*  
\*\* *with velocity dispersion  $v=v(x,y,z,\omega)$  from equation (5.12) and  $m=\omega/v(x,y,z,\omega)$*

Figure 4.5: Parallel pseudocode for one-pass 3-D  $\omega$ -x-y 65° prestack depth migration.



## 2-D AND 3-D FINITE DIFFERENCE $\omega$ -x-y 65° ZERO-OFFSET FORWARD MODELING PARALLEL PSEUDOCODE

---

**INPUT:** reference velocity  $v(z)$ ; velocity model  $v(x,y,z)$ \*\*  
**CALCULATE:** Reflectivity(x,y,z)  
**INPUT:** upgoing wavefield at the bottom,  $P(x,y,z=z_b,t)$   
           in frequency domain:  $P(x,y,z=z_b,\omega)=\text{complex}(0.,0.)$   
**INPUT:** parameters and source (Ricker wavelet)  
**FFT:** Fourier transform, Source( $\omega$ )

**C MAIN PART OF PARALLELISM: UPWARD EXTRAPOLATION +**  
**C SIMULATION OF THE EXPLODING REFLECTOR MODEL**  
**\* PARALLEL DO (“PARDO”) 10: over number of FREQUENCIES**  
**\* DO 20 over number of DEPTH steps from bottom up**  
     **A. CALCULATE the time retarded field**  
     **B. APPLY THE EXTRAPOLATION OPERATOR AND**  
        **THIN LENS CORRECTION:**  
        used in the 2-D or one-pass 3-D migration algorithms  
     **C. SIMULATE EXPLODING REFLECTOR EXPERIMENT**  
        at time zero and zero offset  
         $Q(x,y,z,\omega_i) = Q(x,y,z,\omega_i) + (\text{Source}(\omega_i) \cdot \text{Reflectivity}(x,y,z))$   
**20 END DO over number of DEPTHS**  
     **AUTOMATIC MERGING (“merge(sum)):**  
        wavefield on surface:  $Q(x,y,z=0,\omega) = \sum_{i=1}^N Q(x,y,z=0,\omega_i)$   
**10 END PARDO over FREQUENCIES**  
     **PARALLEL INVERSE FFT of  $Q(x,y,z=0,\omega)$**   
     **OUTPUT: zero-offset time sections,  $P(x,y,z=0,t)$**   
*\* frequency and depth loops are interchangeable*  
*\*\* with velocity dispersion  $v=v(x,y,z,\omega)$  from equation (5.12)*

**Figure 4.6:** Parallel pseudocode for 2-D or 3-D zero-offset forward modeling (for 2-D set everywhere  $y=0$ ).

#### 4.6 APPLICATION OF THE IMPLICIT FINITE DIFFERENCE MIGRATIONS FOR IMAGING SEISMIC AND RADAR DATA

Reservoir monitoring during an enhanced oil recovery (EOR) process is critical for efficient management of the project. 3-D high resolution surface seismic is used since time-lapse seismic images can monitor reservoir changes that are induced during the process. We migrate with the 3-D poststack depth migration algorithm described above two 3-D high resolution seismic data sets before steam-injection (base) and during steam-injection (monitor), respectively, from a thermal EOR pilot site that were given us by Mobil Oil Canada (Kalantzis et al., 1993b). Also, we migrate 3-D seismic data during production (6th cycle) and steam-injection (8th cycle) from Esso's Cold Lake EOR project (Kalantzis et al., 1994). The one-pass 3-D post stack depth migration in the space-frequency domain was implemented on a 44-processor SPS3 Myrias MIMD parallel computer. The migration includes lateral velocity variations and uses some of the detail models that we used in the modeling. The computational efficiency of this algorithm allows us to use very small depth steps for the extrapolation of the wavefield (1 m) in contrast to other more accurate but problematic and expensive migration schemes such as the ones developed by Kapotas (1992) in which he uses depth steps of 8 m. However, the migration of the 3-D seismic monitoring data are discussed further in Chapter 6.

The 2-D  $\omega$ -x  $65^\circ$  poststack depth migration was used for the migration of the Alberta LITHOPROBE seismic data (Rong et al., 1994). Further discussion of the LITHOPROBE data and their migration is presented in Appendix E.

Seismic migration algorithms can be applied to ground-penetrating radar data due to the kinematic similarities between radar reflection and seismic reflection methods. Thus, the paraxial approximation to the scalar wave equation can be used for the depth migration of radar data the same way as applied to seismic data. The 2-D  $\omega$ -x  $65^\circ$  poststack depth migration was applied with very few modifications for migration of ground-penetrating radar (Kalantzis et al., 1994) from AECL's (Atomic Energy of Canada Limited) Whiteshell research area located near Pinawa in southeastern Manitoba. The depth migrated sections successfully imaged fractures in the granitic Lac du Bonnet Batholith to distances of at least 100 m below outcrop surfaces (see Chapter 7).

## 4.7 3-D REVERSE TIME MIGRATION

### 4.7.1 Introduction

Among many wave equation migrations one is the reverse time migration. In this method the surface recorded wavefield is considered as a surface boundary condition and extrapolation is performed backwards in time. Poststack reverse time migration has been presented by many authors, including Whitmore (1983), McMechan (1983), Baysal et al., (1983), Loewenthal and Mufti (1983) and Levin (1984). Furthermore, Chang and McMechan (1986), and Sun and McMechan (1986) developed 2-D prestack reverse time migration for acoustic and elastic waves, respectively, and they applied to synthetic offset vertical seismic profiles.

Reverse time migration is a powerful technique because it can handle everything (Hale and Witte, 1992) such as strong lateral velocity variations, dips greater than  $90^\circ$ , turning waves, shear waves, anisotropy and it is very accurate particularly with respect to amplitudes. Another advantage of the method is its ability to image irregular source-receiver geometries with elevation changes. Also, it is easy to produce offset dependent images that are useful for post-migration velocity analysis. Furthermore, code is reasonably simple to develop. However, it is not very popular due to its high computational demands (Reshef and Kessler, 1989) since it is basically the same as finite difference forward wave-equation modeling except the time is running backwards.

McMechan (1983) developed reverse time migration solving the full scalar wave equation in 2-D, using a second order explicit finite difference scheme. Since no paraxial approximations are involved, even  $90^\circ$  dips are correctly migrated. Also, for strong lateral velocity variations the scalar wave equation is superior to the paraxial one-wave equation. However, this method suffers from unwanted internal multiple reflections generated from strong velocity changes. This unwanted energy is especially troublesome when it is coherent and migrates to a time when the primaries are weak. Baysal et al. (1983) and Whitmore (1983) take care of this problem by setting model density=1/velocity so that there no impedance contrasts.

Gazdag (1981) presented a 90-degree dip two-way wave equation and Kosloff et al. (1984) derived a two-way wave equation in which evanescent instabilities are avoided and strong velocity variations can be accommodated. Baysal et al. (1983) used Gazdag's 90-degree dip wave equation for reverse time migration.

In order to avoid some of the problems in migration associated with the use of the full

wave equation, the one-way wave equation is often used for migration. In recursive depth extrapolation based migrations (Claerbout, 1985) the one-way wave equation is commonly obtained by seeking a polynomial or rational approximation to the dispersion relation of a square root form. However, the one-way equation, although successful in many migration problems, is limited by the assumptions made in its derivation. Particularly, it is assumed that spatial derivatives of the velocity can be ignored. Also, the need of accuracy requires higher order approximations at the expense of computational effort. On the other hand, for reverse time extrapolation based migrations Dai (1993) used an one-way wave system that is accurate up to at least 75 degree propagation angles.

The reverse time migration has been extended into three dimensions (Chang and McMechan, 1989, 1990). Here, we developed two 3-D reverse time migration methods that address and solve some of the problems present with the use of the full or the one-way wave equation. The first method uses a full acoustic wave first order hyperbolic system in heterogeneous media. This system is also used for 3-D acoustic forward modeling and for the computation of the excitation-time imaging condition. On the other hand, the second method uses a one-way acoustic wave first order hyperbolic system and is associated with all the advantages of the one-way wave equation. For example, the unwanted energy related to internal reflections is not present because we use only downgoing propagating waves. Both full and one-way wave hyperbolic systems are solved with an explicit finite difference method based on the MacCormack splitting scheme that is fourth order accurate in space and second order accurate in time. We use explicit rather than costly implicit schemes since the instability of explicit schemes is less severe for first order hyperbolic systems in the time domain than for parabolic equations in the frequency domain. Furthermore, both migration methods avoid problems with evanescent energy since wavefield extrapolation is performed in time instead of depth (Kosloff and Baysal, 1982).

#### **4.7.2 Reverse time migration with a 3-D full acoustic wave first order hyperbolic system**

As in all wave equation migrations, reverse time migration consists of two parts, namely, extrapolation and imaging. For the extrapolation we use the 3-D acoustic modeling algorithm, including the absorbing boundaries developed in chapter 3, in which the full scalar wave equation is formulated as a first order hyperbolic system and solved with explicit finite differences via the MacCormack splitting scheme. This approach gives us all the advantages associated with the full wave equation so that waves that turn around due to

refraction (turning waves) can be followed beyond the turning point.

#### 4.7.3 Reverse time migration with a 3-D one-way acoustic wave first order hyperbolic system

In this approach, we use the 3-D one-way wave (downgoing) first order hyperbolic system that is developed by applying characteristic analysis to the 1-D hyperbolic system (see section 3.3.5). The *3-D one-way wave system* taking into account only *downgoing (+z) waves* and setting no restriction for waves propagating in the x and y direction can be written as

$$\frac{\partial \mathbf{U}}{\partial t} = \sqrt{\gamma} \mathbf{A} \frac{\partial \mathbf{U}}{\partial x} + \sqrt{\gamma} \mathbf{B} \frac{\partial \mathbf{U}}{\partial y} + \mathbf{C}_d \frac{\partial \mathbf{U}}{\partial z} \quad (4.7.1)$$

where  $\mathbf{U}$  is a vector containing the pressure field and the particle velocity components,

$$\mathbf{U} = \begin{bmatrix} P \\ v_x \\ v_y \\ v_z \end{bmatrix} \quad (4.7.2)$$

$\mathbf{A}$  and  $\mathbf{B}$  matrices are the same as in the full 3-D system (3.3.11) and (3.3.12). We multiply matrices  $\mathbf{A}$  and  $\mathbf{B}$  in the one-way system with  $\sqrt{\gamma}$ , where  $0 < \gamma < 1$ , in order to reduce slightly the characteristic velocity of the waves in x and y direction. From an optimization where least-square fitting was performed between the dispersion relation of equation (4.7.1) and the exact one, we found  $\gamma=0.923$ . Matrices  $\mathbf{A}$  and  $\mathbf{B}$  are given in terms of the input velocity  $V=V(x,y,z)$  and density  $\rho=\rho(x,y,z)$  by

$$\mathbf{A} = \begin{bmatrix} 0 & V^2 \rho & 0 & 0 \\ \rho^{-1} & 0 & 0 & 0 \\ 0 & 0 & 0 & 0 \\ 0 & 0 & 0 & 0 \end{bmatrix} \quad (4.7.3)$$

$$\mathbf{B} = \begin{bmatrix} 0 & 0 & v^2\rho & 0 \\ 0 & 0 & 0 & 0 \\ \rho^{-1} & 0 & 0 & 0 \\ 0 & 0 & 0 & 0 \end{bmatrix} \quad (4.7.4)$$

and  $\mathbf{C}_d$  is given by

$$\mathbf{C}_d = \frac{1}{2} \begin{bmatrix} -v & 0 & 0 & v^2\rho \\ 0 & 0 & 0 & 0 \\ 0 & 0 & 0 & 0 \\ \rho^{-1} & 0 & 0 & -v \end{bmatrix} \quad (4.7.5)$$

The above system is solved with explicit finite differences using the MacCormack splitting scheme (section 3.3.4). Also, the one-way wave absorbing boundaries used for 3-D acoustic modeling (section 3.3.5) can be used for migration with the downgoing wave system. If the recorded data are interpreted as pressure field, then the pressure output from the solution of the one-way system after extrapolation and imaging is the depth migrated data volume.

#### 4.7.4. Reverse-Time Extrapolation

The extrapolation process is carried out in reverse time starting with the last time sample ( $T_L$ ) on the stacked volume (for poststack migration) or shot gathers (for prestack migration), at time  $t=T_L$  and proceeding until  $t=0$ . The reverse-time extrapolation process consists of two parts at each time step. First, a time slice corresponding to that time is extracted from the time reverse 3-D data volume and is inserted at the corresponding geophone locations in the finite difference grid as sources. Then, these virtual sources are forward extrapolated with a 3-D acoustic modeling algorithm that uses the full wave system or with an algorithm that uses the 3-D downgoing wave system.

At a specific time step  $t_i$  during extrapolation of a set of data, the energy in the seismograms at times  $t > t_i$  has already been transferred to the finite difference  $x$ - $y$ - $z$  meshes and is propagating back toward the point at which the disturbance was generated. Then, once one finite-difference step is taken, the data from time-slice at  $t_{i-1}$  are added to the virtual sources and so forth. Thus, reverse time migration is an initial value problem

instead a boundary value problem as in McMechan's (1989, 1990) implementation. The reversed time seismograms are considered as a time variations of wave sources along the receiver lines instead as a surface boundaries. Also, with this approach, we do not need to assume that  $P(x,y,z,t)=0$  and  $\partial P(x,y,z,t) / \partial t = 0$  for  $t > T_L$  as required in McMechan's approach.

#### **4.7.5 3-D poststack reverse time migration**

The basic assumption for migration of stacked sections is the Exploding Reflector Model (Loewenthal et al., 1976). According to this model a zero-offset or stacked section can be approximated for the data recorded over the same area in a single experiment where the subsurface has half the actual velocities and sources are exploded at time zero on all reflecting boundaries. Thus, for poststack migration we assume the velocity field used is accurate and both the zero-offset model and the Exploding Reflector Model are valid. Then, after the time reverse extrapolation of the recorded wavefield ( $P(x,y,z=0,t)$ ) is completed, the result should coincide with the reflecting horizons in the medium at time zero ( $P(x,y,z,t=0)$ ). Thus, in the poststack domain, the velocity is halved and the image step is taken at time zero at all spatial locations (grid points). Limitations of the poststack reverse time migration are associated with the use of the Exploding Reflector Model. Thus, poststack migration does not handle nonsymmetric ray paths, such as with most interbed multiples, in velocity models with strong velocity variations. Also, it does not handle transmission losses. This method depends strongly on the accuracy of the stacked section. Hopefully interbed multiples have been attenuated by deconvolution and stacking.

#### **4.7.6 3-D prestack reverse time migration**

For prestack reverse-time migration, we can use an imaging condition which selects only the downgoing energy or time coincidence of up and downgoing energy to avoid imaging spurious multiples. The determination and application of the imaging condition for any point in the image space involves computing the direct time at which the diffracted energies become simultaneously focused at that point during reverse time extrapolation. The time of imaging of each point is the one-way wave traveltime from the primary source to that point.

Most of 2-D reverse time migration algorithms apply ray-tracing (Chang and McMechan, 1986) to achieve an excitation-time imaging condition at each spatial location.

Another imaging approach in reverse time migration (Kapotas, 1991) uses double-downward continuation as in the case of the  $\omega$ - $x$  domain double-downward continuation (S-G) prestack migration. In this method the determination and application of the imaging condition at each point in time requires double continuation of sources and receivers downwards at the same time-step. As time propagates backwards through the grid, at each time step the time-reverse source gathers are extrapolated by downward continuation of the receivers and then they are reordered into receiver gathers and the sources are downward continued using the principal of reciprocity. Using this concept amplitudes are correlated (constructive interference) on the difference grid along the image.

However, when we move into three dimensional complex structures ray tracing has a number of problems such as at caustics and shadow zones. On the other hand, the use of double downward continuation in 3-D reverse time migration is prohibitively expensive, and therefore, it is impractical. Thus, for complex geology with strongly varying velocity the most reliable method for computing the excitation-time imaging condition is finite difference forward modeling. Chang and McMechan (1990) computed the direct wave traveltimes from the source to all grid points by solving the forward problem with the 3-D scalar wave equation and they accessed them during migration in reverse time order. Since, for prestack migration we already have built a nearly accurate velocity model, we believe that the best way to compute the excitation times for imaging is 3-D forward modeling which will simultaneously generate realistic synthetic seismograms that can be used for validation of the velocity model and interpretation of real data. Here, we compute the direct traveltimes from forward source extrapolation using the 3-D acoustic modeling algorithm, developed in chapter 3, that solves a first order hyperbolic wave system.

Calculation of the direct arrival time with our forward modeling algorithm involves very few changes in the computer code for the implementation of the minimum time criterion. However, apart from the direct wave, the head waves have also minimum traveltimes. Thus, an amplitude threshold is needed to reject the selection of imaging time for head waves (Loewenthal and Hu, 1991). We start by declaring an array  $t_d(nx,ny,nz)$  where  $nx$ ,  $ny$ ,  $nz$  are the number of grid points of the finite difference mesh in  $x$ ,  $y$  and  $z$  directions, respectively. Initially, the time array is set to zero,  $t_d(x,y,z)=0$ , for all grid points. Then, at each time step  $k$  of the finite difference solution, the propagating wavefield, the pressure if the data are interpreted as the pressure field, is compared to the amplitude threshold. At the grid points where the pressure is smaller than the threshold, the time is unchanged. At the grid points where the pressure is larger or equal to the threshold,



the time is set equal to the corresponding time step,  $t_d(nx,ny,nz)=k$ , and hence, the imaging time is determined for these points. Furthermore, in order to avoid the check of the pressure field at all the grid points in the model at each time step, a check of the time is done. If the time is not zero, a comparison of the pressure at the corresponding locations is not performed, otherwise, it is and if the threshold condition is met the time is updated. Thus, the imaging time condition  $t_d(nx,ny,nz)$  is updated only the first time that the pressure is larger or equal to the threshold and in this way the minimum direct arrival time is ensured.

All points in the medium that are excited simultaneously by the arrival of the direct wavefront in the forward problem (point diffractors - secondary sources) form an image trajectory which is the imaging condition at that time for the migration. The excitation time imaging condition is applied at each finite difference time step during reverse-time extrapolation. At the grid points that satisfy the imaging condition at that time (if the imaging time is equal to the time step count) the corresponding pressure amplitudes are extracted from the propagating wavefield and saved at their corresponding spatial location in an array with size equal to the finite difference grid size as a partial image. At a new time step, additional spatial locations are filled out. Finally, the entire migrated image is completed at the last time step that corresponds to the zero time of the recorded data.

#### **4.7.7 Advantages and Disadvantages with the two Approaches - Implementation of reverse time migration**

Both reverse time migration methods developed above (using either the full or one-way system) are very accurate since they do not use any approximations to the one way equation such as the paraxial approximation used in earlier section for implicit finite difference migration in the frequency domain. Also, these migrations perform a direct solution of the wave system and hence they do not have limitations in contrast to the one-pass 3-D depth migration that has considerable limitations, since it introduces errors in the azimuthal direction associated with the splitting of the extrapolation operator. Furthermore, the reverse time migration does not suffer from the unwanted evanescent energy since extrapolation is performed in time and not in depth as in the case of the recursive depth extrapolation based migrations.

The use of the full wave equation for migration can result in imaging of dips beyond 90 degrees. Whitmore (1983) and Baysal et al. (1984) presented imaging of turning waves in synthetic seismograms using reverse time migration. Claerbout (1985) presented a

modified phase-shift migration for imaging turning waves. Hale et al. (1992) used an extension to Claerbout's approach for imaging of 3-D seismic data recorded over an overhanging salt dome. Thus, our method that uses the full wave system since it does not have dip restrictions, should be able to migrate 3-D seismic data that contain turning waves generated in complex structures such as overhanging salt domes and intrusions of salt into faults. On the other hand, since we have both upgoing and downgoing waves, the method suffers from generation of multiples which can be avoided by using a non reflecting wave equation (Baysal et al., 1984) or a velocity smoothing technique (Loewenthal et al., 1991). The advantage of the one-way wave (downgoing) system developed above is that does not generate multiple energy.

With the use of prestack reverse time migration there is no need for demultiplexing the data since migration uses the time slices recorded in the field for extrapolation. Also, there is no need for common mid-point gathering since the migration is performed in the prestack domain on the recorded shot gathers.

Since imaged energy is coincident with the direct wavefront (first break) from the primary source, the direct (first break) arrival will satisfy the imaging condition. According to Sun and McMechan (1986), in order to avoid masking the structural details by the relatively high amplitude direct arrival energy, this must be removed from the recorded data before reverse time extrapolation. McMechan and Sun (1991) filter out the first breaks by downward continuation of the recorded wavefield using reverse time extrapolation to a depth beneath which these waves propagate and subsequently upward continue to reconstruct the original recorded wavefield with the subhorizontally waves removed. With our method, we could apply 3-D prestack reverse migration on recorded seismic shot gathers without the need of muting the first breaks. However, in order to avoid imaging the direct waves, during the implementation of the excitation-time imaging condition we extract the amplitudes of the vertical particle velocity component that does not contain the direct waves, instead of extracting the amplitudes of the propagating pressure field. Furthermore, with the use of reverse time migration there is need of filtering the ground roll since the surface waves can travel horizontally out of the computational plane during extrapolation.

If we know the near-surface velocity distribution and incorporate it with the existing elevations into the velocity model used for prestack migration, then elevation and velocity statics corrections will be performed implicitly during the wavefield extrapolation in migration. Thus, reverse time migration eliminates the need for explicitly performing elevation and near-surface velocity static corrections.

The finite difference grid size is determined after considering the stability condition

and numerical dispersion requirements for the explicit finite difference method that uses the MacCormack splitting scheme for the solution of the full or the downgoing wave in a first order hyperbolic system. However, the data do not require interpolation to be evenly spaced with a trace spacing equal to the increment of the finite difference grid. The reverse time migration does not require symmetry in the recorded data, it can accommodate any arbitrary recording geometry, thus eliminating the need of binning the data into inline and crossline directions. As a result, there is no need for elevation corrections because processing is done in the field recording coordinates. Also, with the use of prestack reverse time migration no normal or dip moveout is necessary since the migration is in the prestack domain. Furthermore, after migration there is no need for time-to-depth conversion since the reverse time migration is a depth migration.

The reverse time migration algorithms developed here are highly vectorized and are implemented on the Fujitsu VPX240 supercomputer. Also, they can be parallelized in the same way that the modeling algorithms were parallelized in Chapter 3.

#### **4.7.8 Applications of the Reverse Time Migration**

The 3-D poststack reverse time migration algorithms described above were used for depth migration of a 3-D synthetic data set (zero offset) from large scale modeling in the oil sands of Cold Lake, Alberta. The resultant migrated data have high resolution and resolved all the structures existed in the model. The migrated results are shown in Chapter 6 which discusses seismic monitoring experiments at Cold Lake (Figure 6.3.10.b). The migration was performed on a Fujitsu VPX/240 supercomputer. The CPU time required for the migration of a data set with 68x68 traces and 801 samples/trace was about 23 minutes for 200 depth steps. Also, the algorithm attained a pronounced vectorization (including I/O) in the order of 92 percent.

However, at this time only a limited amount of migrations were performed due to large storage and transfer requirements of the generated data. In particular, the 3-D migrations generate a large amount of synthetic data which require large disc space in order to be stored and analyzed. Also, the transfer of the data between the Fujitsu VPX/240 (located at the High Performance Computing Center in Calgary), where the algorithms are implemented, and our workstation (at the University of Alberta in Edmonton) is an extremely time consuming task due to low data transfer rates (only 7.7 Kbytes/sec).

At this time we are testing the prestack reverse time migration with the synthetic shot gathers generated for the French model in Chapter 3. This is necessary in order to verify

the expected capabilities of our algorithms in complex structures and in the prestack domain. Also, these algorithms need to be tested with real data sets from complex geologic areas such as overhanging salt domes and intrusions of salt into faults. However, all this is left for research in the immediate future.

#### 4.8 DISPERSION ANALYSIS FOR 3-D MIGRATION

The normalized dispersion relation of the 3-D scalar wave equation (4.3.1) is

$$\frac{k_z}{k} = \sqrt{1 - \frac{k_x^2}{k^2} - \frac{k_y^2}{k^2}} \quad (4.8.1)$$

The square root can be approximated using Muir's expansion (Claerbout, 1985), thus the dispersion relation becomes

$$\frac{k_z}{k} = \sqrt{1 - \frac{k_x^2}{k^2}} + \sqrt{1 - \frac{k_y^2}{k^2}} - 1 \quad (4.8.2)$$

Next, the square root terms are approximated by employing continuous fraction expansion (Ma, 1981) and we have the parabolic approximation of the dispersion relation,

$$\frac{k_z^*}{k} = \frac{1 - (\alpha + \beta) \frac{k_x^2}{k^2}}{1 - \beta \frac{k_x^2}{k^2}} + \frac{1 - (\alpha + \beta) \frac{k_y^2}{k^2}}{1 - \beta \frac{k_y^2}{k^2}} - 1 \quad (4.8.3)$$

where for 45° accuracy  $\alpha=0.5$  and  $\beta=0.25$  and for 65° accuracy  $\alpha=0.478242060$  and  $\beta=0.376369527$  (Yilmaz, 1987). On the other hand, the normalized dispersion relation of the 3-D acoustic one-way wave system (4.7.1) is

$$\frac{k_z^*}{k} = \frac{1 - (\alpha + \beta) \frac{k_x^2}{k^2} - (\alpha + \beta) \frac{k_y^2}{k^2}}{1 - \beta \frac{k_x^2}{k^2} - \beta \frac{k_y^2}{k^2}} \quad (4.8.4)$$

where constants  $\alpha$  and  $\beta$  are  $\alpha=\beta= \gamma/2 = 0.923/2$ .

Substituting equations

$$k = \frac{\omega}{V} , k_x = \frac{\omega}{V} \sin\theta , k_y = \frac{\omega}{V} \sin\phi \quad (4.8.5)$$

into equations (4.7.8) and (4.7.9) we get the dispersion relations in the  $k_z$ - $\theta$ - $\phi$  domain where  $\theta$  and  $\phi$  denoting the wave propagating angles measured with respect to the z-x and z-y planes.

In order to examine the accuracy of the one-way wave system we need to compare its dispersion relation with the exact one. In this comparison we also consider the 65 degree dispersion relation which forms the basis for the one-pass 3-D depth migration. In order for the migrations to be accurate, their dispersion relations must approximate a hemisphere in the  $k_z$ - $\phi$ - $\theta$  domain. Selected slices are shown to better illustrate the shape of the dispersion relations. We first consider slices that are parallel to the  $\phi$ - $\theta$  plane and we present three slices for different values of  $k_z$  (Figure 4.7 ). We observe that at high  $k_z$  both the approximate dispersion relations are quite accurate (Figure 4.7.a). At intermediate  $k_z$ , the dispersion relation for the one-way system has a symmetric shape, while the 65 degree one does not appear to be symmetric with respect to the center midpoint and produces more accurate values in the inline and cross line directions (Figure 4.7.b). For waves propagating at the horizontal plane ( $k_z=0$ ) both the approximate dispersion relations give inaccurate results (Figure 4.7.c).

Another way of examining the accuracy of these dispersion relations is by taking slices parallel to the  $k_z$ - $\phi$  or  $k_z$ - $\theta$  planes. On these slices which correspond to the inline or crossline directions, the proposed one-way system has a better overall performance (Figure 4.8.a). Finally in the diagonal direction (Figure 4.8.b) the proposed method (one-way system) is by far better than the 65 degree approximation.

*(Text continued on page 123)*

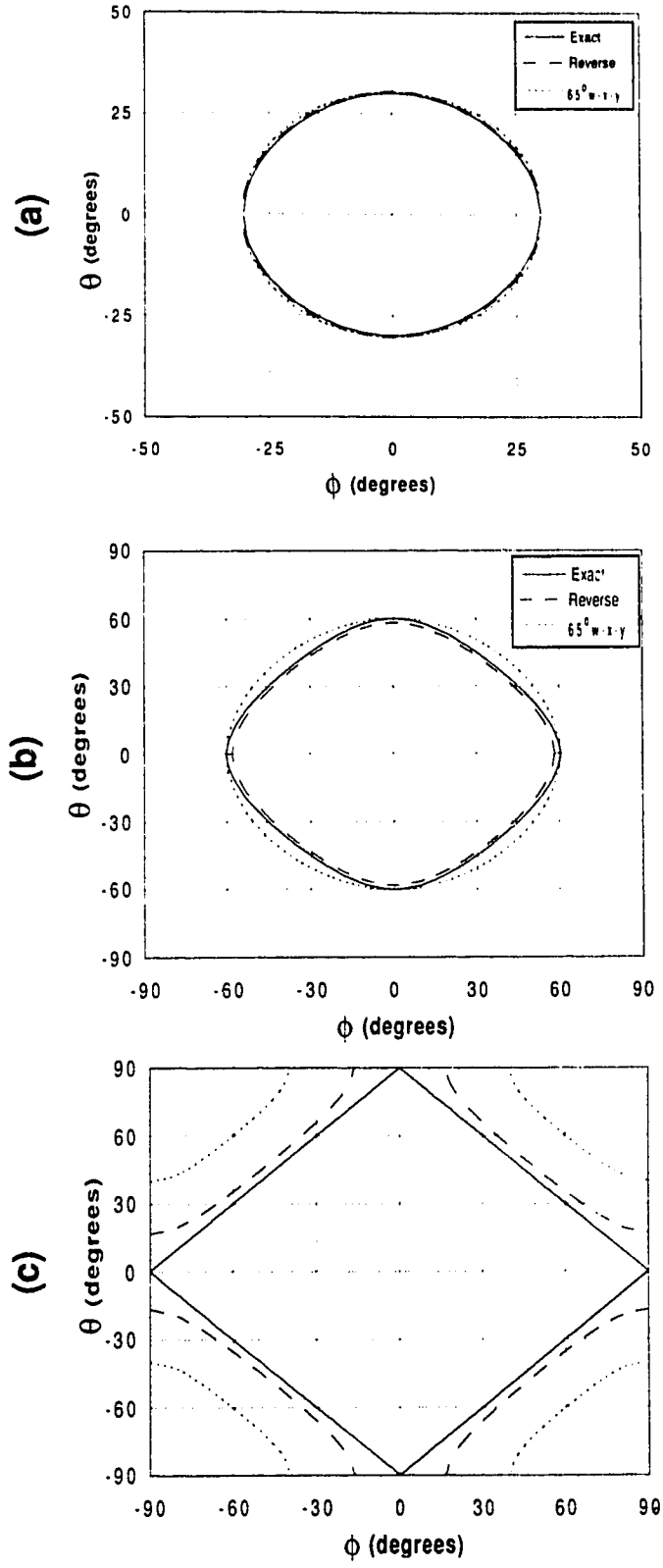
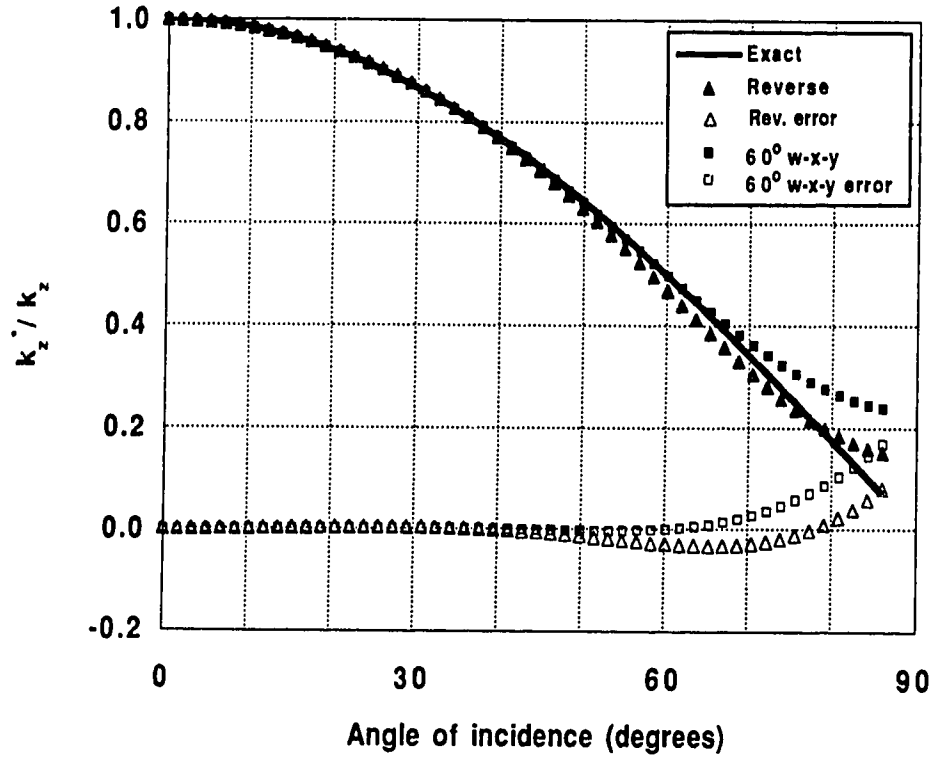
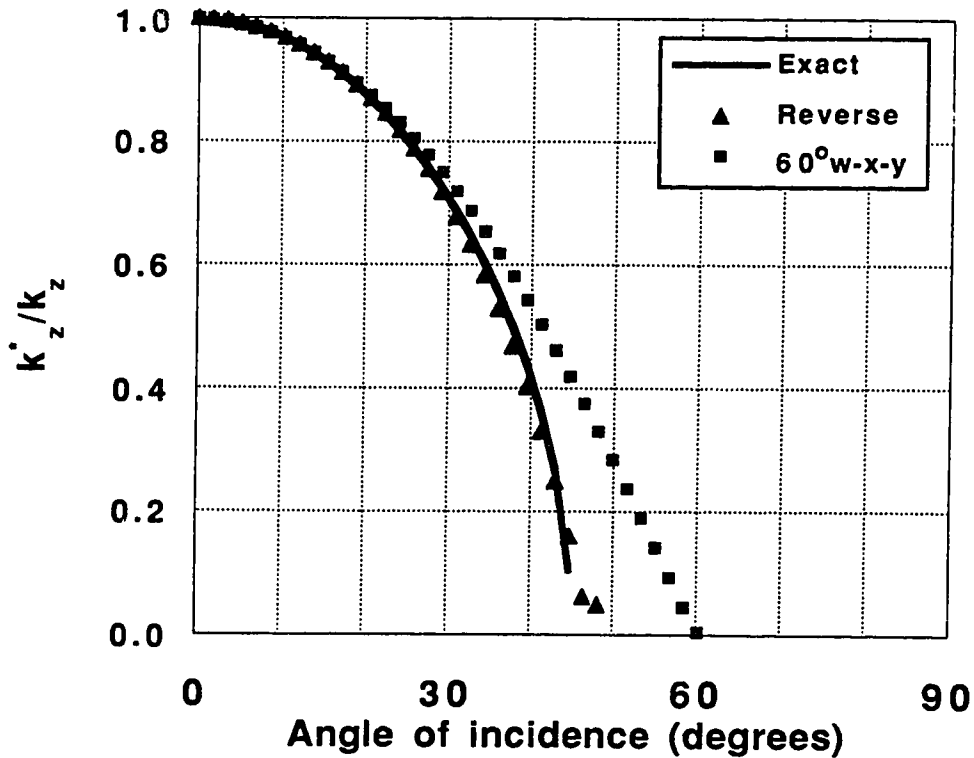


**Figure 4.7:** Slices parallel to the  $\phi$ - $\theta$  plane from the 3-D surfaces of the dispersion relations of the 3-D scalar wave equation, the proposed one-way system and the 65 degree approximation for different values of  $k_z$ : (a) high; (b) intermediate; and (c) zero.



(a)



(b)

Figure 4.8: Comparison of the dispersion relations of the 3-D scalar wave equation (hemisphere), the proposed one-way system and the 65 degree paraxial approximation in: (a) the inline or crossline direction and (b) in the diagonal direction.

## 4.9 MIGRATION VELOCITY ANALYSIS

As exploration moves into areas of more complicated geology, migration of seismic data becomes more important. High quality migrated data are most difficult to obtain where the earth's structure is complex. Thus, successful seismic imaging of complex geology requires accurate migration methods in order to collapse and position reflectors in their correct temporal and spatial locations. Current migration algorithms while in theory are able to image nearly vertical structures in practice the imaging result depends on velocity field used. Therefore, the quality of migrated seismic data depends on the accuracy of the migration method and on the accuracy of the migration velocity.

It is well known, that there is no distinct difference between migration velocity (wave equation approach) and stacking velocity (ray-theoretical approach) when the subsurface medium is horizontally layered. However, for dipping reflectors the two velocities differ; the stacking velocity is sensitive to the dip of the reflecting interface (Levin, 1971) and the migration velocity is independent of dip (Hubral and Krey, 1980). Therefore, it is essential to incorporate the dip information in the migration velocity (Yilmaz and Chambers, 1984).

All migration methods have the additional problem that it is necessary to have the wave velocities as a function of spatial coordinates before they can be applied accurately. Since the velocity is not known a priori, some iteration is necessary to remove migration artifacts such as overlapping or crossing reflectors, bow-tie patterns, etc. Velocity analysis (such as automatic stacking velocity analysis involving a coherency measure such as semblance) usually provides the RMS velocity at sparse times. However, most migrations require the interval velocity for each downward extrapolation step. Typically, the interval velocity is computed using Dix's formula which assumes constant interval velocity between RMS velocity data points. This assumption breaks down for migration of steep dips where high resolution velocity model is required.

It is generally accepted that prestack migration is the best tool for imaging complex earth structures. The problem with prestack depth migration is that finding a good velocity model from complex seismic data is very hard and that prestack depth migration needs a quite accurate velocity model to get good results.

The usual approach to obtaining an accurate velocity model is through multiple iterations of prestack depth migration. The first iteration solves for the velocity in the shallowest layer. Successive iterations solve for successively deeper velocity layers. However, this approach is prohibitively expensive and time consuming in comparison with the same approach used with poststack depth migration.



One approach of velocity model building uses inverse ray tracing for interval velocity estimation of the shallowest layer followed by map migration to estimate depth (Hadley, 1988). The sequence is repeated for subsequent layers which ensures an accurate overburden response. The main advantage of this approach is that the initial velocity model is built independently of the imaging algorithm without numerous iterations (Brzostowski et al., 1991).

Another velocity analysis method uses traveltimes tomography to match modeled traveltimes generated by ray tracing with interpreted travel times from prestack data. The tomography approach performs well when structure is relatively uncomplicated. However, it encounters difficulties when the structure is complicated for two main reasons (Lines et al., 1993): (1) it is difficult to identify traveltimes from prestack data, and (2) tomographic ray tracing may be a problem because reflected rays arrive from different paths of a curved reflector result large traveltimes residuals.

There are two main approaches for performing migration velocity analysis after prestack migration and before stack. One is depth-focusing analysis (Yilmaz and Chambers, 1984; Faye and Jeannot, 1986) and the other is residual wavefront curvature analysis. Hildebrand and MacKay (1992) give a comparison of the two methods.

Yilmaz and Chambers (1984) and Jeannot et al. (1986) used depth-focusing analysis with time migration and depth migration, respectively, for migration velocity estimation. In prestack migration we obtain the image at  $t=0$  and offset,  $h=0$  (imaging conditions). The depth-focusing method provides a measure of focusing accuracy by recognizing that when the migration velocity is incorrect the reflected energy does not collapse at the correct zero time and zero offset as predicted by the imaging condition but focuses best at non-zero times. This approach uses the build-up of energy at zero-offset and depth while relaxing the imaging condition to non-zero time. By outputting the continued wavefield in the time window (near zero) where the energy is best focused and taking the differences between the focusing and the migration depths, information is provided for updating the velocity model for another iteration of prestack migration.

Other prestack depth migration velocity analysis methods have been suggested by migrating common shot records (Taner et al, 1991; Al-Yahya, 1987) or common offset gathers (Gardner et al., 1974; Deregowski, 1990) with systematically varying velocity fields and observing the depth and spatial alignment of the resulting images. Data migrated with an incorrect velocity model exhibit residual moveout that degrades the resulting stack. The amount of residual moveout defines a correction to the velocity estimate (Schleicher et al., 1991). If the correct velocity is used, the earth's image at one location will be identical

on different migrated shot gathers. One of the most direct and robust tests (Blacquire, 1991) that indicate the correctness of the velocity model is the examination of migration coherency panels, known also as image gathers or common reflection point (CRP) gathers. If the migration velocity model was correct all events in an image gather or CRP gather would be flat. Coherency panels are used both for a final test on the quality of the velocity model (Blacquire and Duyndram, 1991; Marschall and Thiessen (1991) and as means to update the velocity model (Al-Yahya, 1897; Wang et al., 1991). If the migration velocity model was correct all events in an image gather or CRP gather would be flat.

Clearly the most difficult part of 3-D depth migration is the construction of an accurate velocity model. It is evident that the best velocity analysis technique in complex structures is the prestack migration velocity analysis. However, this procedure is very expensive since it is based on iterating on the 3-D prestack migrations. In an effort to simplify the model building process we utilized advanced visualization techniques and 3-D poststack depth migration. Visualization should not be thought of as an end result, but rather as a means to that end result. For example, it can be used as a tool to allow the user to visualize and interpret the migrated seismic data as well as to modify the depth model.

Next, we describe a practical and feasible approach that combines velocity analysis, 3-D migration and modeling and utilizes the modeling and migration algorithms developed in this thesis. We start with a velocity model by integrating all available information such as geologic data, sonic logs, velocity tomograms, and reservoir engineering data. Then, we use iterative one-pass 3-D poststack depth migration for velocity analysis. We use the one-pass approach because of its computational efficiency (implemented on a parallel computer). When a nearly accurate velocity model is obtained we stop the iterations and the one-pass 3-D poststack migration can be used for the final depth migrated data. Then, 3-D forward modeling is used for validation of the resulted velocity model, for interpretation of the 3-D seismic data and computation of the time excitation imaging condition (at no extra cost) for prestack migration imaging (if needed). If it is necessary we can apply more accurate migration methods such as the poststack reverse time migration developed in this thesis. Furthermore, 3-D prestack depth migration (e.g., the 3-D reverse time migration developed in this thesis) can be utilized, using the nearly accurate model derived from the poststack migration and the imaging condition determined from the forward modeling, in order to obtain the final depth migrated image. In Figure 4.9, the above described flow is shown. This method (parts of the flow) was used for migrating 3-D seismic monitoring data sets in a later chapter of this thesis.

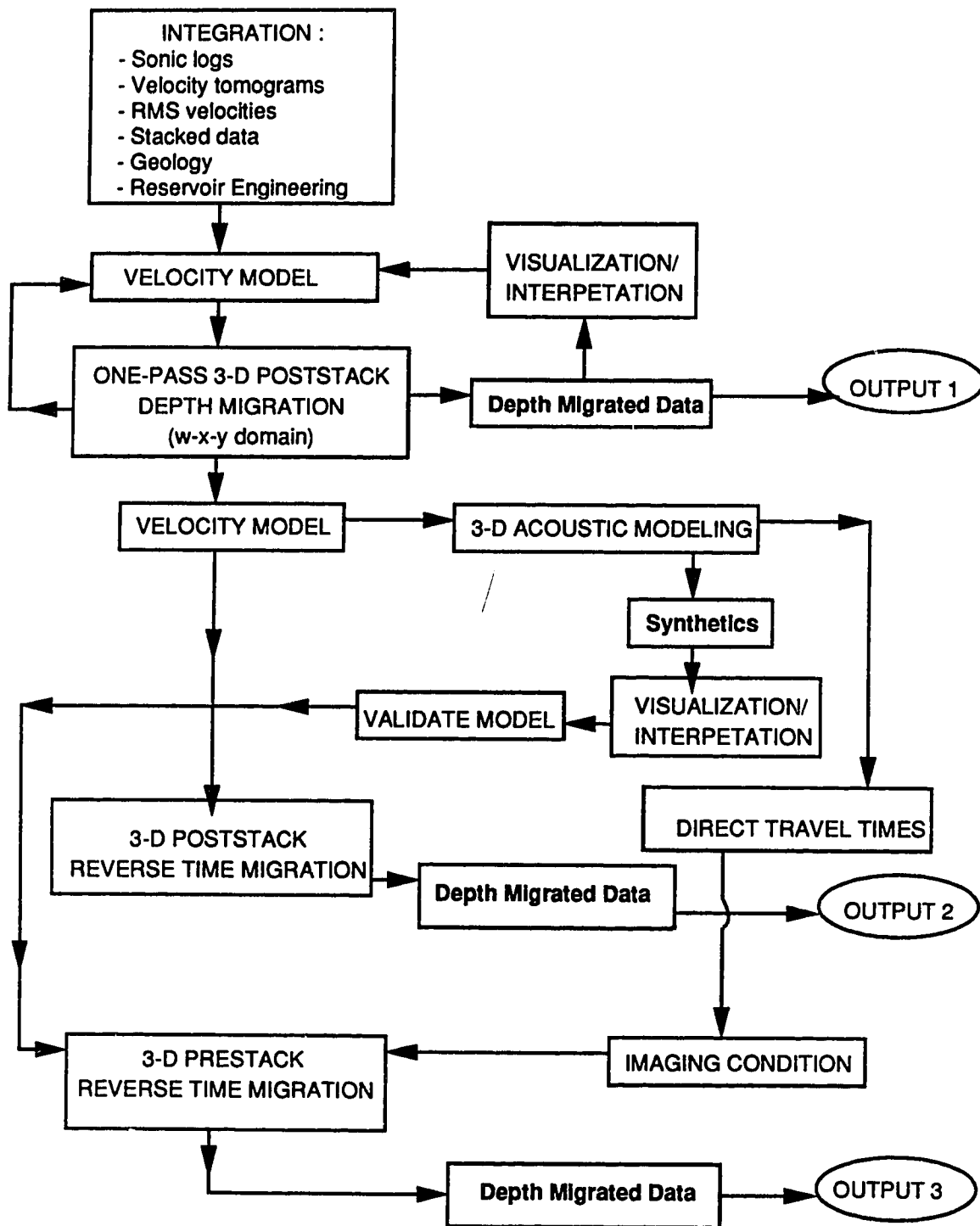


**Figure 4.9:** The algorithmic flow for velocity analysis, 3-D depth migration and modeling by utilizing the algorithms used in this thesis.

## 4.10 CONCLUSION

In this chapter a number of original 3-D migration methods and algorithms were developed. Also, existing methods were utilized for the development of a number of 2-D and 3-D depth migration parallel algorithms. The significant computational efficiency of these algorithms was demonstrated by implementing them on vector and parallel supercomputers.

2-D poststack and prestack depth migration algorithms in the frequency-space domain using implicit finite differences were developed and implemented on a parallel computer. These 2-D migration algorithms were adapted for applications that range from deep crustal imaging of seismic wavefields that involve 18 seconds long travel times (50 Km depth) and frequencies in the order of 1~ 100 Hz, to imaging of radar wavefields that involve 2000 nano-seconds (ns) long travel times and frequencies in the order of 50 MHz. Furthermore, a 3-D poststack and prestack depth migration parallel algorithm is developed in the frequency domain that uses a one-pass or alternative direction implicit (ADI) finite difference method. All implicit finite difference migration algorithms were highly parallelized by utilizing the inherent parallelism in the frequency and space domains that the seismic equations have and they were implemented on a 44-processor Myrias SPS3 MIMD parallel computer. In particular, the parallelization possibilities of the one-pass 3-D depth migration algorithm were fully explored. The one-pass 3-D poststack depth migration algorithm was extensively used for the imaging of seismic monitoring data from Cold Lake, Alberta. Our experience with this algorithm shows that it provides the right tradeoff between accuracy and computational efficiency.

An original formulation of the 3-D reverse time migration method was developed employing either a full or an one-way wave hyperbolic system that is solved with explicit finite differences using using the MacCormack scheme. This method is very accurate since it does not use any approximations to the one way equation such as the paraxial approximation used for implicit finite difference migration in the frequency domain. Also, it performs a direct solution of the wave system and hence does not have limitations in contrast to the the one-pass 3-D depth migration that has considerable limitations, since it introduces errors in the azimuthal direction associated with the splitting of the extrapolation operator. Furthermore, the reverse time migration does not suffer from unwanted evanescent energy since extrapolation is performed in time and not in depth, as in the case of the recursive depth extrapolation based migrations. The advantage of the full wave system for migration can result in imaging of dips beyond 90 degrees. On the other hand,

the advantage of the one-way system is that it does not generate multiple energy. Based on this method four new algorithms were developed for poststack and prestack depth migration of 3-D complex seismic data. All algorithms were highly vectorized using sophisticated approaches such as matrix multiplication by diagonals to take full advantage of the computational power of vector supercomputers. As a result, they were implemented on a Fujitsu VPX/240 supercomputer with pronounced CPU and vectorization performance.

The 3-D reverse time migration method, that uses the full wave system (since it does not have dip restrictions) should be able to migrate 3-D seismic data that contain turning waves generated in complex structures such as overhanging salt domes and intrusions of salt into faults. Also, the application of prestack reverse time migration can significantly simplify the processing of seismic data since there is no need for demultiplexing the data (data are input as time slices into the migration), sorting into common-midpoint gathers, elevation and near-surface static corrections, first break muting and removal of surface waves (ground roll), normal and dip moveout corrections (NMO and DMO) since these operations are eliminated or are performed automatically and implicitly with the reverse time migration. This eliminates the need for determination of separate velocities for statics, NMO and DMO corrections, stacking and migration. Thus, the entire seismic processing sequence can be reduced to determining an accurate velocity model with some kind of velocity analysis method and depth imaging of the 3-D seismic data with the reverse time migration. However, this extraordinary potential of our new 3-D reverse time migration has not fully tested and explored.

## REFERENCES

- Al-Yahya, K., 1987, Velocity analysis by iterative profile migration, Ph.D. Thesis, Stanford University.
- Aki, K. and Richards P. G, 1980, Quantitative Seismology, Theory and methods, W. H Freeman and Co., San Francisco.
- Baysal, E., Kosloff, D.D., Sherwood, J.W., 1983, Reverse time migration, *Geophysics*, **48**, 1514-1524.
- Baysal, E., Kosloff, D.D., Sherwood, J.W., 1984, A two-way nonreflecting wave equation: *Geophysics*, **49**, 132-141.

- Berkhout, A. J., 1987, Applied seismic wave theory, Elsevier Science Publishers, N.Y.
- Berkhout, A. J., 1982, Seismic Migration, Elsevier Science Publishers, Amsterdam.
- Berkhout, A. J., 1981, Wave field extrapolation techniques in seismic migration, a tutorial. *Geophysics*, **46**, 1638-1656.
- Blacquièrè, G. and Duynham, A., 1991, Prestack depth migration and macro velocity estimation: In Versteeg, R. and Grau, G. (eds) *The Marmousi Experience*, Zeist, EAEG.
- Blacquièrè, G., Debye, H., W.J., Wapenaar, C.P.A., and Berkhout, A.J., 1989, 3D table-driven migration: *Geophysical Prospecting*, **37**, 925-958.
- Black, J.L. and Leong, T.K., 1987, A flexible, accurate approach to 1-pass 3d Migration, 57th annual SEG Int. Meeting, New Orleans, October 1987.
- Blanc, J.V., Huard, I., and Gomez, A., 1993, Three-dimensional Remez-Soubaras poststack depth migration: *CRAY CHANNELS*, **15**, No.3, 18-21.
- Brown, D.L., 1983, Applications of operator separation in reflection seismology, *Geophysics*, **48**, 288-294.
- Brzostowski, M.A., Zakharov, P.V., Mills, G.F., and Schleicher, K.L., 1991, Comparative study of presalt imaging techniques in the Pre-Caspian Basin: Presented at the 61st SEG Annual International Meeting and Exposition, Houston, Expanded Abstracts, 195-196.
- Cabrera, J.J., Perkins, W.T., Ratcliff, D.w., and Lynn, W., 1992, 3D prestack depth migration on a massively parallel computer: implementation and case history: Presented at the 54th Ann. Mtg. Eur. Assoc. Expl. Geophys., Abstracts, 268-269.
- Carter, J.A. and Frazer, N.L., 1984, Accommodating lateral velocity changes in Kirchhoff migration by means of Fermat's principle, *Geophysics*, **49**, 46 - 53.
- Cary, P.W., 1990, Symmetric one-pass 3-D migration, *CSEG Recorder*, **10**, 3-15.
- Cary, P.W., 1993, 3-D migration with four-way splitting: 63rd SEG Annual International Meeting and Exposition, Washington D.C., Expanded Abstracts, 978-981.
- Chang, W. F., and McMechan G. A., 1986, Reverse - time migration of offset vertical seismic profiling data using the excitation time imaging condition, *Geophysics*, **51**, 67-84.
- Chang, W.F., and McMechan G. A., 1989, 3D acoustic reverse-time migration: *Geophysical Prospecting*, **37**, 243-256.
- Chang, W.F., and McMechan G. A., 1989, 3D acoustic prestack reverse-time migration: *Geophysical Prospecting*, **38**, 737-755.
- Claerbout, J.F., 1970, Coarse grid calculations of waves in inhomogeneous media with

- application to delineation of complicated seismic structure. *Geophysics*, **35**, 407-418.
- Claerbout, J.F., 1971, Toward a unified theory of reflector mapping: *Geophysics*, **36**, 467-481.
- Claerbout, J.F., 1976, *Fundamentals of Geophysical data Processing*, McGraw Hill Inc.
- Claerbout, J.F., 1985, *Imaging the Earth's Interior*, Blackwell Scientific Publications.
- Clayton R.W. and Engquist B., 1980, Absorbing boundary conditions for wave equation migration, *Geophysics*, **45**, 895-904.
- Clayton R.W. and Engquist B., 1977, Absorbing boundary conditions for acoustic and elastic wave equations, *Bull. Seism. Soc. Am.*, **67**, 1529 - 1540.
- Dai, N., 1993, *Finite difference simulation and imaging of seismic waves in complex media: Ph.D. Thesis, University of Alberta.*
- Deregowski, S.M., 1990, Common-offset migrations and velocity analysis: *First Break*, **8**, 225-234.
- Dickinson, J.A., 1988, Evaluation of two-pass three-dimensional migration, *Geophysics*, **53**, 32-49.
- French, W., 1975 Computer migration of oblique seismic reflection profiles, *Geophysics*, **40**, 961-980.
- Fricke, J.R., 1988, Reverse time migration in parallel: a tutorial. *Geophysics*, **53**, 1143-1150.
- Froidevaux, P., 1990, First results of a 3-D Prestack migration program, S.E.G. Expanded Abstracts, 60th Convention San Francisco, **II**, 1318-1321.
- Gardner, G.H.F., French, w.S., and Matzuk, T. 1974, Elements of migration and velocity analysis: *Geophysics*, **39**, 811-825.
- Gazdag, J., 1978, Wave equation migration with the phase-shift method. *Geophysics*, **43**, 1342-1351.
- Gazdag, J., 1980, Wave equation migration with the accurate space derivative method: *Geophysical Prospecting*, **28**, 60-70.
- Gazdag, J., and Squazzero, P., 1984, Migration of seismic data by phase-shift plus interpolation: *Geophysics*, **49**, 124-131.
- Gibson, B., Lerner, K., and Levin, S., 1983, Efficient 3-D migration in two steps, *Geophysical Prospecting*, **31**, 1-33.
- Hadley, D.M., Thorson, J., and Maher, S., 1988, Increasing interpretation accuracy: A new approach to interval velocity estimation: *The Leading Edge*, **7**, No. 9, 13-16.
- Hague, J. and Goloway, F., 1989 3-D omega-x migration on the IBM 3090/VF,

- Supercomputer, **33**, VI-5, 17-27.
- Hale, D., 1991, 3-D Depth migration via McClellan Transformations: *Geophysics*, **56**, 1778-1785.
- Hale, D., Hill, N.R., and Stefani, J.P., 1991, Imaging salt with turning seismic waves: 61st SEG Annual International Meeting and Exposition, Houston, Expanded Abstracts, 1171-1174.
- Hale, D., and Witte, D., 1992, Migration: progress and predictions: 62nd SEG Annual International Meeting and Exposition, New Orleans, Expanded Abstracts, 610-612.
- Hildebrand, F.B. 1974, Introduction to Numerical Analysis, New York, McGraw-Hill.
- Hildebrand, S., and MacKay, S., 1992, Depth migration velocity analysis: A comparison of two approaches: 54 th Mtg. and Tech. Exhibit., Europ. Assn. Expl. Geophys., Expanded Abstracts, 266-267.
- Hill, N.R., Watson, T.H., Hassler, M.H., and Sisemore, L.K., 1991, Salt-flank imaging using Gaussian beam migration: Presented at the 61st Ann. Internat. Mtg. Soc. Expl. Geophys., Expanded Abstracts, 1178-1180.
- Hubral, P., 1977, Time migration -- some ray theoretical aspects: *Geophysical Prospecting*, **25**, 738-745.
- Hubral, P., and Krey, T., 1980, Interval velocities from seismic reflection time measurements : SEG monograph.
- Jacobs, A., 1982, The prestack migration of profiles: Ph.D. Dissertation, Stanford University.
- Jain, S., and Wren, A. E., 1980, Migration before stack - Procedure and significance, *Geophysics*, **45**, 204 - 212.
- Jakubowicz, H. and Levin, S. 1983, A simple exact method of 3-D migration, *Geophysical Prospecting*, **31**, 34-56.
- Jeannot, J.P., Faye, J.P. and Denelle, E., 1986, Prestack migration velocities from focusing depth analysis: Presented at the 56th SEG Annual International Meeting and Exposition, Houston.
- Jonson, O., 1984 Three Dimensional Wave equation Computations on Vector Computers. *Proceeding of IEEE*, **72**, 90-95.
- Julien, P., 1990, 3-D Prestack Depth migration on Real Data, SEG Expanded Abstracts, 60th Int. Meeting San Francisco, **II**, 1329-1332.
- Kalantzis, F., Dai, N., Kanasewich, E.R., Phadke, S., and Vafidis, A., 1993a, 2-D and 3-D seismic reflection modeling and imaging using vector and parallel supercomputers: In Proceedings of Supercomputing Symposium '93, Calgary,



- Alberta, 25-32.
- Kalantzis, F., E. Kanasewich, N. Dai and N. Udey, 1993b, 3-D seismic monitoring of thermal EOR processes, case I: initial results: CSEG National Convention , Calgary, Expanded Abstracts, 66-67.
- Kalantzis, F., Kanasewich, E.R., Kostyukevich, A., and Udey, N., 1994: Integrated time-lapse reservoir monitoring: Modeling and Imaging: CSEG National Convention, Calgary, Expanded Abstracts, 122-123.
- Kalantzis, F., Stevens, K.M., Kanasewich, E.R., and Lodha, G.S., 1994, Depth migration of ground-penetrating radar data: CSEG National Convention, Calgary, Expanded Abstracts, 251-252.
- Kapotas, S., 1991, 3-D imaging of reflection seismic wavefields using parallel computers: Ph.D. Thesis, University of Alberta, Edmonton, Alberta.
- Kao, J.C., 1993, Preconditioned iterative 3-D finite-difference depth migration or modeling on the CRAY T3D Massively Parallel Processors: 63nd SEG Annual International Meeting and Exposition, Washington D.C., Expanded Abstracts, 185-188.
- Kosloff D.D. , and Baysal, E., 1983, Migration with the full wave equation, *Geophysics* **48**, 677 - 687.
- Kosloff D.D. , Baysal, E., and Sherwood, J.W.C., 1983, Reverse time migration: *Geophysics*, **48**, 1514-1524.
- Kosloff D.D. , Baysal, E., and Sherwood, J.W.C., 1984, A two-way nonreflecting wave equation: *Geophysics*, **49**, 132-141.
- Levin, F.K., 1971, Apparent velocity from dipping interface reflections: *Geophysics*, **36**, 510-516.
- Levin, S.A., 1984, Principles of reverse time migration: *Geophysics*, **49**, 581-583.
- Lines, L.R., Rahimian, F., and Kelly, K.R., 1993, A model-based comparison of modern velocity analysis methods: *The Leading Edge*, **12**, 750-754.
- Loewenthal, D., Roberson, L., Lu, R. and Sherwood, J., 1976, The wave equation applied to migration. *Geophysical Prospecting*, **24**, 380-399.
- Loewenthal, D., and Mufti, I.R., 1983, Reverse time migration in spatial frequency domain: *Geophysics*, **48**, 627-628.
- Loewenthal, D., and Hu, L.Z., 1991, Two methods for computing the imaging condition for common-shot prestack migration: *Geophysics*, **56**, 378-381.
- Ma, Z., 1981, Finite-difference migration with high-order approximation: Presented at Joint Meeting of Chinese Geophys. Soc. and Soc. Explor. Geophys.

- Marfurt, K.J., 1978, Elastic wave equation migration--inversion: Ph.D. Dissertation, Columbia University
- Marscall, R., and Thiessen, J., 1991, Marmousi-model data set: macro model verification and prestack depth migration: In Versteeg, R. and Grau, G. (eds) *The Marmousi Experience*, Zeist, EAEG.
- McMechan, G. A. 1983, Migration by extrapolation of time dependent boundary values, *Geophysical Prospecting*, **31**, 413-420.
- McMechan, G. A., Mooney, W. D., 1980, Asymptotic ray theory and synthetic seismograms for laterally varying structures: Theory and application to the Imperial Valley, California, *Bull. Seis. Soc. Am.* **70**, 2021-2035.
- McMechan, G.A., and Sun, R., 1991, Depth-filtering of first breaks and ground roll: *Geophysics*,
- Mitchell, A.R., 1969, *Computational methods in partial differential equations*: New York, John Wiley and Sons.
- Mitchell, A.R., Griffiths, D.F., 1980, *The finite difference method in Partial Differential Equations*, John Wiley & Sons.
- Mora, P. 1988, 3-D acoustic forward modeling in the CM2, Presented at the SEG Int. Meeting, Anaheim, Calif., Oct. 1988.
- Mufti, I. R., 1989, Application of supercomputers in three dimensional seismic modeling: In: *Supercomputers in Seismic Exploration*, Editors, Helbig and Treitel, Pergamon Press, N.Y.
- Muller, G, Temme, P., 1987, Fast frequency - wavenumber migration for depth dependent velocity, *Geophysics*, **52**, 1483 - 1491.
- Phadke, S., Kapotas, S., Dai, N., and Kanasewich E.R., 1994, Migration of P-wave reflection data in transversely isotropic media: *Geophysics*, **59**, 591-596.
- Podvin, P., and Lecomte, I., 1991, Finite difference computation of traveltimes in very contrasted velocity models: a massively parallel approach and its associated tools: *Geophys. J. Int.*, **105**, 271-284.
- Qin, F.H., Yi, L. and Schuster, G.T., 1990, Solution of the eikonal equation by finite difference method: Presented at the 60th SEG Annual International Meeting and Exposition, San Francisco.
- Ratcliff, D.w., Gray, S.H., and Whitmore, N.D., 1992, Seismic Imaging of salt structures in the Gulf of Mexico: *The Leading Edge*, **11**, no. 4, 15-31.
- Reshef, M., and Kosloff, D., 1986, Migration of common shot gathers, *Geophysics*, **51**, 324 - 331.

- Reshef, M., Kosloff, D., Edwards, M., Hsiung, C., 1988, Three-dimensional acoustic modeling by the Fourier method, *Geophysics*, **53**, 1175-1183.
- Reshef, M., and Kessler, D., 1989, Practical implementation of three-dimensional poststack depth migration : *Geophysics*, **54**, 309 - 318.
- Ristow, D. , 1980, 3-D finite difference migration, Ph.D. thesis, University of Utrecht, The Netherlands.
- Rong, L., Kanasevich, E.R., Kalantzis, F., and Burianyk, M., 1994, Basement reactivation and palaeozoic sedimentation from the Alberta Basement Transect line 9 and 10: Presented at the CGU Meeting, Banff, Alberta.
- Sattlegger, J.W., Stiller, P.K., 1974, Section migration, before stack, after stack, or in between. *Geophysical Prospecting*, **22**, 297-314.
- Schneider, W.A., 1978, Integral formulation for migration in two and three dimensions, *Geophysics*, **43**, 49-76.
- Schleicher, K.L., Grygier, D.J., and Brzostowski, M.A., 1991, Migration velocity analysis: a comparison of two approaches: 61st Annual International SEG Meeting, Houston, Expanded Abstracts, 1237-1238.
- Schultz, P.S., and Sherwood, J.W.C., 1980, Depth migration before stack, *Geophysics*, **45**, 376 - 393.
- Shah, P.M., 1973, Ray tracing in three dimensions: *Geophysics*, **38**, 600-604.
- Snyder, A., 1979, Common shot gather modeling and inversion: Stanford Exploration Project Report No 16.
- Soubaras, R., 1992, Explicit 3-D migration using equiripple polynomial expansion and laplacian synthesis: 62nd Annual International SEG Meeting, New Orleans, Expanded Abstracts,
- Stoffa, P., Fokkema, J., Freire, L.R., Kessinger, W.P., 1990, Split-step Fourier migration. *Geophysics*, **55**, 410-421.
- Stolt, R., 1978, Migration by fourier transform. *Geophysics*, **43**, 23-48.
- Stolt, R., and Benson, A.K., 1986, *Seismic migration - theory and practice*, Geophysical Press.
- Sun, R. and McMechan G., 1986, Pre-stack reverse time migration for elastic waves with application to VSP profiles. *Proc. IEEE*, vol. **74**, No.3, 457-465.
- Tanner, T., Postma, R., Lu, L., and Baysal, E., 1991, Depth-migration velocity analysis: 61st SEG Annual International Meeting and Exposition, Houston, Expanded Abstracts, 1218-1220.
- Temme, P., 1984, A comparison of common midpoint, single-shot and plane wave depth

- migration, *Geophysics*, **49**, 1896 - 1907.
- Thorson, J., 1980, Synthetic examples of prestack migration, Stanford Exploration Project Report No. 24, Stanford, California, p. 5-32.
- Tore, V., Poggio, T., 1986, On Edge Detection, *IEEE transactions on pattern analysis and machine intelligence*, PAMI-8, **2**, 147-163.
- Tsingas K., 1989, Seismic reflection imaging over a thermally enhanced oil recovery site: Ph.D. Thesis, University of Alberta, Edmonton.
- Tsingas K., and Kanasewich, E.R., 1990, Prestack shot gather migration and imaging a steam zone using a migrated omega-x stack: *Canadian Journal of Exploration Geophysics*, **26**, 17-32.
- Van Trier, J., and Symes, W.W., 1991, Upwind finite difference calculation of traveltimes: *Geophysics*, **56**, 812-821.
- Versteeg, R., 1991, Sensitivity of migration coherency panels to the velocity model: 61st SEG Annual International Meeting and Exposition, Houston, Expanded Abstracts, 1251-1254.
- Vidale, J., 1987, Finite-difference calculation of travel times: *Bull. Seism. Soc. Am.*, **78**, 2062-2076.
- Wang, S., Baumel, R., Hanson, D., Bell, D., Boyd, M., Cavanaugh, T., Cox, V., D'Onfro, P., Durrani, J., and Standlee, L., 1991, Common-offset depth migration as a velocity analysis tool: In Versteeg, R. and Grau, G. (eds) *The Marmousi Experience*, Zeist, EAEG.
- Wapenaar, C.P.A., Kinneging, N.A., and Berkhout, A.J., 1987, Principle of prestack migration based on the full elastic two-way wave equation, *Geophysics*, **52**, 151-173.
- Whitmore, D., 1983, Iterative depth migration by backward time propagation: 53rd SEG Annual International Meeting and Exposition, Expanded Abstracts, 382-385.
- Whitmore, N.D., and Lines, L.R., 1986, Vertical seismic profiling depth migration of a salt dome front: *Geophysics*, **51**, 1087-1109.
- Whitmore, N.D., and Garing, J.D., 1993, Interval velocity estimation using iterative prestack depth migration in the constant angle domain: *The Leading Edge*, **12**, 757-762.
- Yilmaz, O., 1987, *Seismic Data Processing*, Society of Exploration Geophysics, Tulsa OK.
- Yilmaz, O., and Claerbout, J. F., 1980, Prestack partial migration, *Geophysics*, **45**, 1753-1779.
- Yilmaz, O., and Chambers, R.E., 1984, Migration velocity analysis by wave-field extrapolation: *Geophysics*, **49**, 1664-1674.

## CHAPTER 5

### THERMALLY ENHANCED OIL RECOVERY OF THE COLD LAKE OIL SANDS AND WAVE PROPAGATION

#### 5.1. INTRODUCTION

Enormous reserves of bitumen or heavy oil (about 900 billion bbl oil or  $143 \times 10^9$  m<sup>3</sup>) are present in complex reservoirs in sands of Lower Cretaceous age in Alberta, Canada (ERCB, 1979). This heavy oil or bitumen is a low gravity high viscosity oil which under reservoir conditions is immobile. The terms *heavy oil* or *bitumen* imply a viscous crude hydrocarbon material not recoverable in its natural state by conventional production methods. Figure 2.1 outlines the major heavy oil accumulation regions of the lower Cretaceous deposits that occur in the western Canadian basin. These heavy oil deposits occur in the Peace River, Athabasca, Wabasca, Cold Lake, and Lloydminster areas. Also, we should add that huge reserves of bitumen are contained in the Palaeozoic carbonate rocks over a large area of north central Alberta.

Of all the bitumen reserves in place in Alberta's oil sands, only 7% lie close to the surface only in the Athabasca region and oil can be extracted from the reservoir by surface mining methods. The rest of the heavy oil will have to be extracted by *in situ* recovery processes that consist of increasing the mobility of the oil and then driving it into a production well.

In this research the area of study is the Cold Lake deposit that is located 300 km northeast of Edmonton and covers over 6500 km<sup>2</sup>. It is the second largest oil sands deposit in Canada and contains more than  $20 \times 10^9$  m<sup>3</sup> (125 billion barrels) of heavy oil in place. The minimum depth to the first oil sand at Cold Lake is 300 m and this dictates that production must be by some *in situ* processes. These are very costly and as such must be well planned and designed. Reservoir description plays a key role in the selection of the location for a scheme in the planning of a specific recovery process, and in the analysis and prediction of production performance. The bitumen from the oil sands of Alberta is normally recovered by an enhanced oil recovery (EOR) operation. Many of these involve steam injection to make the oil mobile. In the next sections, we discuss the geology of the oil sands in Alberta and we describe the reservoir types in the oil sands of Cold Lake area. Also, a brief description of the thermally enhanced oil recovery method used at Cold Lake is presented since in the next chapter we study two seismic monitoring experiments over EOR sites.

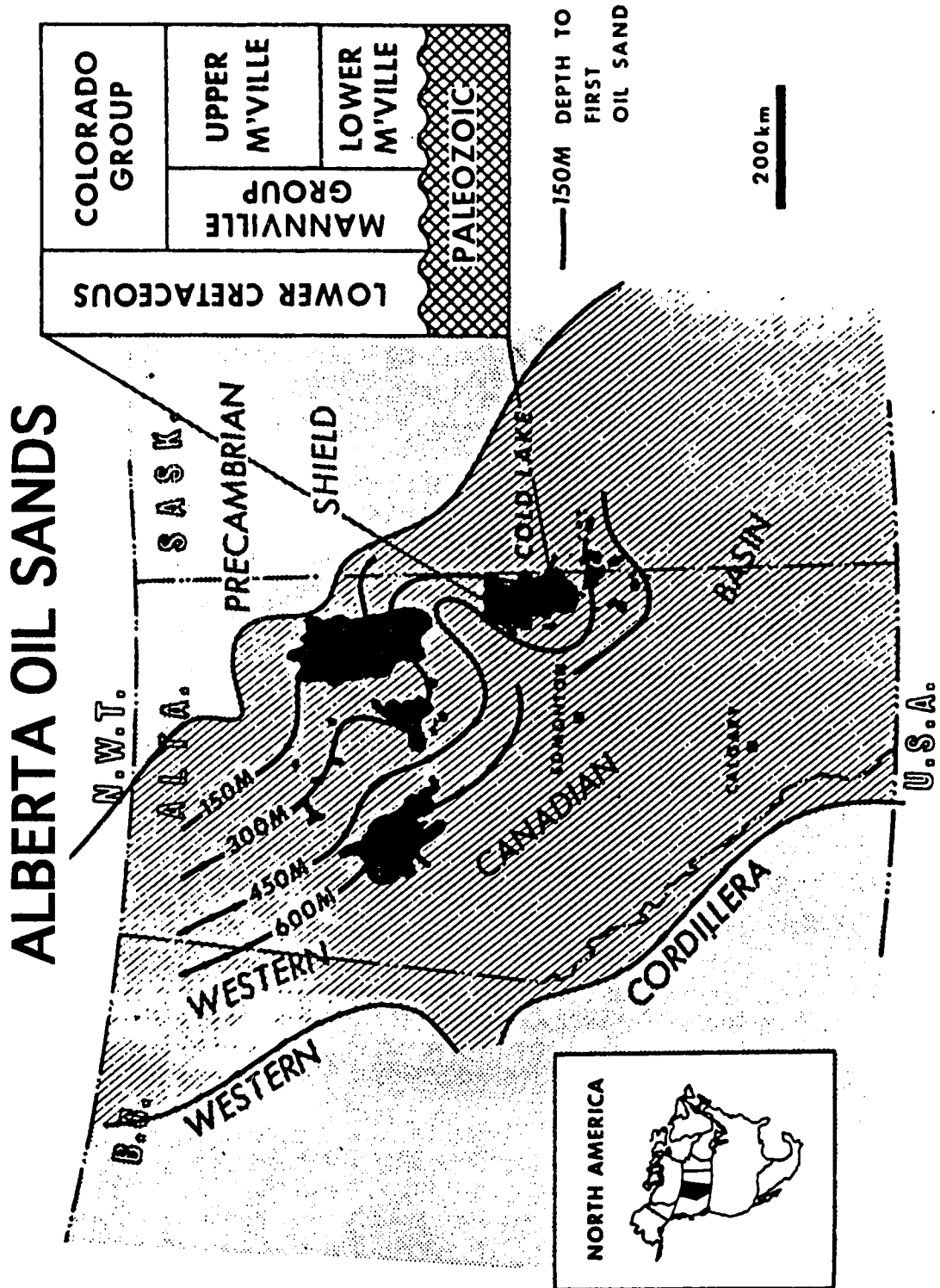


Figure 5.1: Map of the Alberta oil sands, outlining the major heavy oil accumulation regions of the Lower Cretaceous deposits that occur in the Western Canadian basin (modified after Harrison et al., 1979).

From the reservoir engineer's point of view it is important to monitor the growth of the steam fronts and to assess the changes occurring in the reservoir as a result of the steam stimulation. In particular, a knowledge of the size, position and physical state of the heated zone around the injection well is desired in the development of efficient heavy oil extraction techniques. Invasive techniques, such as drilling observation wells, are expensive and limited in spatial resolution. But petrophysical alterations in the heavy oil reservoirs during enhanced oil recovery (EOR), caused by pressure, temperature, the replacement of bitumen by steam or steam condensate, etc., contribute to velocity changes, attenuation and velocity dispersion of seismic waves in the affected reservoir. These changes on a seismic reflection record imply seismic attribute changes such as amplitude brightening of reflections from the top of the steam zone and travel time delays of reflectors within and below the steam invaded zone. Thus, non-invasive or remote sensing geophysical techniques, especially the surface seismic reflection method can be used to periodically monitor reservoirs during the EOR process and map the expanded steam-heated zone.

The goal of seismic monitoring of enhanced oil recovery processes is to positively impact the design and management of the oil recovery project. The seismic method can become a powerful technique for monitoring EOR processes if it can present to the reservoir engineers the zones where changes have occurred in temperature, pressure and saturation. In order to succeed, it is necessary to correlate qualitatively and quantitatively the seismic attributes and their changes in time with the reservoir conditions and properties.

Laboratory measurements at ultrasonic frequencies are used to establish correlations between seismic attributes and reservoir properties and conditions. But although laboratory experiments provide direct measurements of attenuation and velocity, they cannot quantitatively define the mechanisms that caused the resultant seismic changes. It is therefore necessary to compliment laboratory experiments with wave propagation theoretical models that can be tested against the experimental results and answer questions concerning the application of laboratory results obtained at ultrasonic frequencies to seismic attributes obtained at seismic frequencies. Then, it may be possible to define quantitatively in the seismic frequency range what mechanisms cause the observed seismic changes on the seismic monitoring data.

Since in thermal recovery most of the heavy oil is displaced from the pores of the porous medium and the seismic method is used for monitoring the recovery process, we need to have a good understanding of the seismic wave attenuation and velocity dispersion in fluid-saturated media. Hence, an overview of the most significant attenuation mechanisms and some important results from laboratory measurements of attenuation and velocity dispersion in fluid-saturated porous media is presented in a section of this chapter. Also, we discuss the petrophysical changes that take place in the reservoir and how they correlate to the observed changes of seismic attributes during an EOR process.

## **5.2. THE GEOLOGY OF THE ALBERTA OIL SANDS**

The heavy oil is contained in various sands of the Upper and Lower Mannville Group of Lower Cretaceous age (Harrison et al., 1979). The most important control on the distribution of the bitumen in the Cretaceous oil sands reservoirs relates to the facies patterns, as controlled by the depositional environments. Mannville Group sediments have undergone limited burial and minimal cementation. Primary porosity and permeability trends have been preserved and the bitumen saturation is mainly a function of the primary porosity and permeability characteristics (Mossop et al, 1979). Lower Mannville sediments are mainly non-marine sands, siltstones and shales and grade upward into interbedded marine shales, sands and siltstones of the Upper Mannville. The heavy oil is commonly associated with gas and water.

The largest heavy oil reserves occur in Lower Mannville sands of the McMurray Formation in the Athabasca area and lesser but still significant amounts in the Cold Lake and Wabasca area. At Cold Lake the Upper Mannville reservoirs contain oil in the Clearwater and Grand Rapids Formations and in their equivalents at Wabasca, Athabasca and Peace River areas. However, Cold Lake is unique in comparison with the other heavy oil areas in that oil is contained in all four formations of the Mannville Group.

At Cold Lake the Mannville Group was deposited near the eastern edge of the Western Canadian sedimentary basin on a Palaeozoic erosional surface as a nearshore - deltaic to offshore transition sand - shale complex. It is overlain by marine shales of the Colorado Group. These Mannville sands are noncemented and vary considerably in thickness, areal extent and reservoir quality. The Paleozoic unconformity occurs at a depth of around 500 to 600 m and the top of the Precambrian crystalline basement is at a depth of 1020 m. Both these horizons are prominent seismic reflection markers.

At Cold Lake the Mannville averages 210 m in thickness. The lower Mannville consists of the McMurray Formation, up to 60 m thick, and is characterized by a continuous basal sand section and an upper zone of thinner sand intersected with shales. The basal fluvial sands form good reservoirs but at Cold Lake are mainly water-bearing, however several well-developed oil-bearing sands are present in the upper McMurray where accumulations are localized by structural closure.

The Upper Mannville Group consists of the Clearwater Formation and the Lower and Upper Grand Rapids Formations. The Clearwater contains highly saturated sands having an aggregate thickness of about 50 m and it occurs at depths of 425 - 450 m. The Clearwater sands were deposited as nearshore deltaic sands with interbeds of siltstone and shale. When adequately structured the Clearwater can be entirely oil bearing, free of any underlying water. This formation contains the most significant oil reservoirs in the Cold Lake area, accounts for approximately one-half of the total bitumen in place at Cold Lake, and thus it has been the target of most pilot and production operations at Cold Lake to date.



The Upper and Lower Grand Rapids is up to 50 m thick each and primarily consist of thin sands associated with marine-shale interbeds. Depth to these sands is usually about 300 m. Reservoir sands in the Grand Rapids were deposited in nearshore deltaic environment as channel deposits and beaches interbedded with deeper-water shales. Oil accumulation is more variable than in the Clearwater and is generally associated with water and gas bearing sands.

In the Iron River region of the Cold Lake area (the Mobil area of study) the Mannville group consists of a sequence of sands and interbedded shales, containing the following formations: Colony, McLaren, Waseca, Sparky, G.P., Clearwater and McMurray. In the Lloydminster area the Mannville group consists of a sequence of nine different formations; the Upper Mannville group with Colony, McLaren, Waseca, Sparky, G.P., Rex, Lloydminster, and Cummings; and the Lower Mannville with the basal Dina Formation that is correlative with the McMurray Formation to the north. The best reservoirs are in the Sparky and Waseca formations.

### 5.3 RESERVOIR DESCRIPTION

The origin of the oil sands has long been a subject of speculation among geologists. Bailey et al (1973), suggested that tar accumulations were created by water washing and bacterial degradation of medium gravity crude oils. Water washing removes the more water soluble light hydrocarbons and normal paraffins, resulting in an increase in density and sulfur content which is tied to the more bacteria-resistant heavy and complex cyclic organic compounds.

Oil sands may be considered as a four - phase system: a dense interlocked skeleton of predominantly quartz sand grains, with pore spaces occupied by bitumen, water, gas and minor amounts of clay. Typical Alberta oil sand porosity is 32% with tar saturation 81% and water saturation 19%. The grain density is 2700 kg/m<sup>3</sup> and the bulk density is 2100 kg/m<sup>3</sup> (Harris and Sobkowicz, 1977; Dusseault, 1977). The viscosity of the Cold Lake bitumen is about 100,000 cp, under reservoir conditions (12<sup>0</sup>). This drops to less than 10 cp at a temperature of 220<sup>0</sup> C (Flock and Lee, 1977). In the Lloydminster area conventional and enhanced oil recovery processes produce a viscous 16<sup>0</sup> (965 kg/m<sup>3</sup>) to 24<sup>0</sup> (910 kg/m<sup>3</sup>) gravity oil. In most of the oil sands areas in Alberta the most common reservoir type is unconsolidated sand interbedded with nonreservoir silstones and shales.

Rock properties are some of factors that define reservoir quality. The size, shape and shorting of the grains are important factors that control porosity and permeability. Coarse, well-sorted and rounded sand grains result in good reservoirs with high porosity and permeability. In heavy-oil reservoirs the composition of the grains can affect reservoir quality because of the possible chemical reaction of some minerals in the presence of certain

fluids at high temperatures. Also, structural grain such as fractures and joints can create preferential flow which influences recovery efficiency. Another significant factor that can influence the recovery process is the continuity, horizontal and vertical, of the reservoir. Characteristics of sands such as grain-size distribution, silt and clay content can affect reservoir quality. The depositional environment helps to identify the sand type and its possible areal extent and continuity. Because the oil is so viscous it makes its distribution in the reservoir complex. In the Cold Lake oil sands the gas saturation is generally low but, in some cases of structural crests, gas caps exist.

Reservoir geometry such as the areal extent, thickness and structural attitudes is important in the recovery process. At Cold Lake structural attitudes are generally flat with some small dips which are possibly caused due to collapse of the underlying Devonian salts.

There are five distinct reservoir types at Cold Lake (Kendall, 1977):

Type I reservoirs are developed in the upper Grand Rapids when sediment distribution was under marine influence. They consist of lenticular, discontinuous, fine to medium grained sands with shale interbeds. This type of reservoir has an average thickness of 6 m, porosity less than 35% and generally poor permeability due to its high silt and clay content. Also, they are often characterized by gas, low oil in place and water.

Type II reservoirs are developed in the lower Grand Rapids when deposition was in deltaic and nearshore environment. They are thin but consist of more widespread sheet sands than type I and that makes good bed continuity. They have up to 35% porosity, good permeability and extensive oil saturation. Their fluid distribution consists of a thin oil zone underlain by water or shale. Stacking of sands can create a multizone recovery.

Type III reservoirs are also developed in the lower Grand Rapid formation. They are a thick sheet sand of deltaic environment with very good permeability and porosity up to 40%. They contain a thick, oil rich section (24 m) underlain by water bearing sands that can be up to 15 m thick.

Type IV reservoirs are developed in the Clearwater formation when there was a good sand supply with deposition in a deltaic complex of beach and offshore bars. The sands are clean, well sorted, fine-to-medium-grained. They are the most important reservoirs in Cold Lake with good permeability and average porosity up to 35%. They contain a thick oil section, up to 45 m thick, with no or partly underlying water.

Type V reservoirs are developed in the McMurray Formation and occur in sands that were deposited in a nearshore environment and interbedded with marine shales. They consist of thin beds that if stacked together can produce a reservoir of thickness up to 18 m. They have good permeability, average porosity of 35% and fairly good continuity. They contain oil and water and their areal extent is limited by structural closure.

## 5.4 ENHANCED OIL RECOVERY: CYCLIC STEAM STIMULATION

The surface mineable reserves are covered by less than about 40 m of overburden and are all located within the Athabasca deposit. The remaining bitumen, which has more than 150 m of overburden, must be recovered by *in situ* methods. The Cold Lake in place reserves are contained in four geological zones ranging in depth from 300 to 500 m. Bitumen at Cold Lake has a viscosity of 100,000 cp at a reservoir temperature of 120° C. Under these conditions the fluid is immobile and the reservoir impermeable.

The principle method of recovery used by Imperial Oil (Esso Resources) is cyclic steam stimulation (CSS), sometimes referred as "Huff and Puff", (Farouq Ali, 1974). According to this method steam is injected into a well at the highest possible rate (in order to minimize heat losses) at temperatures and pressures (310° C and 10 MPa) for several weeks (Fastwood, 1985). The injected steam heats the rock and the fluids around the wellbore. Vertical heterogeneities such as shale barriers, cause only partial vertical sweep while maintaining a radial advance of the fluids in the zone that is contacted. After injecting the desired volume of steam, the well may be shut in for about two weeks. This is called the *soak* period. Finally production takes place from the same wellbore. The Clearwater reservoir at Imperial Oil sites is an unconsolidated sand with porosity of 32 percent, permeability of 1 darcy and viscosity of about 150,000 cp. Twenty wells are directionally drilled from a single surface location or pad. Imperial Oil has more than 2000 wells that are spaced on regular 1.6 hectares grid and produce about 100,000 b/d.

Steamflooding or continuous steam injection involves a multiple well pattern consisting of a central steam injector and several corner producers. Steamflooding is recommended when reservoir pressure is low and steam injectivity is high, pointing to high permeability, small formations. The principal advantage of a steamflood is the large areal sweep efficiency which is unattainable in steam stimulation.

The steaming process substantially increases *in situ* temperature and decreases the effective stress, causes dilation and changes in gas - fluid saturation, density, P-wave velocity and Poisson's ratio of the porous rock. Zones with altered physical properties are detected by anomalous seismic amplitude responses due to the fact that an increase in gas-fluid saturation in the reservoir formation and changes in the compressibility of the rock and fluid matrix would produce measurable changes in seismic reflection amplitude.

Imperial Oil estimates to recover 20 percent of the bitumen over 10 years period and 10 CSS cycles. However, CSS becomes less efficient with time because larger steam volumes are required to access undepleted reservoir and mobilize bitumen. In order to properly manage the CSS process, increase recovery and reduce recovery costs, knowledge of the reservoir volume affected by the steam and the displacement efficiency is required. Time-lapse 3-D seismic monitoring might be used to map the steam-heated zones

in the reservoir. If we know the volume and shape of the reservoir affected by the steaming process we can determine the need of modifying EOR parameters such as steam cycle length, steam volumes and rates and well patterns. Furthermore, seismic monitoring over time can be used to evaluate reservoir conformance changes (conformance is the fraction of a swept area or volume relative to the total area or volume) that resulted from modifying the EOR process.

## **5.5 SEISMIC WAVE PROPAGATION IN FLUID SATURATED POROUS ROCKS**

In recent years, 3-D seismic reservoir imaging, seismic delineation of reservoir fluid saturations, seismic evaluation and characterization of hydrocarbon reservoirs, seismic monitoring of the reservoir during production and enhanced oil recovery over time have begun to emerge. However, seismic properties such as velocity and attenuation of the reservoir fluids and the host rocks must be understood and determined in order to use these methods and successfully interpret their results.

Furthermore, it has been realized that reservoirs are more complex and heterogeneous than assumed in the past. As a result of the heterogeneity of the reservoirs one has complexity of their recovery processes, problems such as the migration of gas caps in reservoirs with discontinuous shales, the existence of overpressure zones, and the difficulty of tracking steam or temperature in thermally enhanced oil recovery in reservoirs with large permeability variations. Thus, a major shift in the use of seismic methods is taking place that involves the need to correlate and establish relations between seismic parameters such as velocity anisotropy, bulk density and attenuation, and their representations on the seismic record by reflection travel times and other seismic attributes, and the production properties and conditions of the reservoir such as porosity, permeability, lithology, saturation, pressure, and temperature. To this end, wave propagation theories and laboratory measurements are used to establish correlations between seismic attributes and reservoir properties and conditions.

### **5.5.1 The quality factor $Q$ and velocity dispersion**

There are two types of attenuation: the *apparent* attenuation and the *intrinsic* attenuation. Apparent attenuation is caused by interference effects and scattering from velocity or density discontinuities. Seismic attenuation due to layering alone arises from a combination of the transmission losses through the interfaces of a layered subsurface structure and the generation of intrabed multiple reflections (O'Doherty and Anstey, 1971). Transmission losses decrease amplitudes uniformly at all frequencies. Also, intrabed multiples tend to increase amplitudes at lower frequencies of the spectrum and decrease

those at higher frequencies (Schoenberger and Levin, 1974). However, here we are going to discuss the *intrinsic* attenuation which is due to the rock anelasticity.

Seismic wave energy propagating through the earth is attenuated by conversion to heat. It is important to understand the attenuation process for two main reasons. First, seismic waves propagating through an anelastic medium suffer a generally frequency dependent decrease in amplitude and modification of the frequency and phase content. Second, attenuation properties of the medium can reveal information regarding lithology, permeability and saturation of the rocks. Attenuation is an anelastic process and is far more complex than the elastic aspects of seismic wave propagation.

The most common measure of attenuation is the quality factor  $Q$  or its inverse  $Q^{-1}$  which is also called internal friction or the dissipation factor and is defined in terms of the maximum energy stored during a cycle divided by the energy lost during the cycle. Also, it is defined in terms of the mean stored energy  $W$  and the energy loss  $\Delta W$ , during the cycle of a sinusoidal deformation (O'Connell and Budyanskiy, 1978):

$$Q = \frac{4\pi W}{\Delta W} \quad (5.1)$$

The quality factor  $Q$  is related to the phase angle ( $\phi$ ) between stress and strain (Aki and Richards, 1980),  $1/Q = \tan\phi$ . Equivalently, the  $Q$  is the ratio of the imaginary part to the real part of the complex modulus  $M(\omega)$ .

When the stress-strain relations are combined with the equilibrium equation, the resulting one-dimensional wave equation has a solution of the form

$$U(x,t) = e^{i(\omega t - kx)} \quad (5.2)$$

where  $k$  is the complex wavenumber

$$k(\omega) = \left( \frac{M(\omega)}{\omega^2 \rho} \right)^{-1/2} \quad (5.3)$$

and  $\rho$  is the density of the material. Then, the phase velocity is defined through the real part of the complex wavenumber  $k(\omega)$  as follows,

$$v(\omega) = \frac{\omega}{\text{Re}(k(\omega))} \quad (5.4)$$

and attenuation coefficient is defined as imaginary part of the complex wavenumber,

$$\alpha(\omega) = -\text{Im}(k(\omega)) \quad (5.5)$$

The common measures of attenuation are defined and related to one another as follows (Johnston and Toksoz, 1981):

$$\frac{1}{Q} = \frac{M_I}{M_R} = \frac{\Delta f}{f} = \frac{\delta}{\pi} = \frac{\alpha v}{\pi f} = \frac{\alpha \text{ (dB } / \lambda \text{)}}{8.686\pi} \quad (5.6)$$

where  $Q$  is the quality factor,  $\alpha$  is the attenuation coefficient,  $\delta$  is the logarithmic decrement,  $\Delta f$  is the resonance width,  $M_R$  and  $M_I$  are the real and imaginary parts, respectively, of complex modulus  $M$ ,  $v$  is the velocity,  $f$  is the frequency,  $\lambda$  is the wavelength, and dB is decibel (a unit used in expressing power or intensity ratios).

Kjartansson (1979), suggested a linear model for attenuation of waves where  $Q$  is frequency independent. This means that the loss per cycle is independent of the time scale of oscillations at least for seismic reflection prospecting. Kjartansson (1979) used a creep function which is a straight line in a log-log plot given of the following equation for  $t > 0$

$$\psi(t) = \frac{1}{M_0 \Gamma(1 + 2\gamma)} \left(\frac{t}{t_0}\right)^{2\gamma} \quad (5.7)$$

where  $\Gamma$  is the gamma function,  $t_0$  is an arbitrary reference time introduced so that  $t$  has the dimension of time, and  $M_0$  has the dimension of modulus and defines the nondispersive behavior of the modulus  $M$ . The time derivative of the creep function can be considered as representation of the compliance function for the case where strain results from a unit step stress excitation function. Thus, taking the time derivative of the equation (5.3) (Kjartansson, 1979), we have for  $t > 0$ :

$$s(t) = \frac{2\gamma}{M_0 \Gamma(1 + 2\gamma)} \left(\frac{t}{t_0}\right)^{2\gamma} \frac{1}{t} \quad (5.8)$$

If we take the Fourier transform of equation (5.8) and then, substitute with the Fourier transform of the modulus  $M(\omega)$  through the relation,  $M(\omega) = 1/S(\omega)$ , we have:

$$M(\omega) = M_0 \left(\frac{i\omega}{\omega_0}\right)^{2\gamma} = M_0 \left|\frac{\omega}{\omega_0}\right|^{2\gamma} e^{i\pi\gamma \text{sgn}(\omega)} \quad (5.9)$$

where  $\text{sgn}(\omega) = +1$  for  $\omega > 0$  and  $\text{sgn}(\omega) = -1$  for  $\omega < 0$  and  $\omega_0 = 1/t_0$ .

Using the definition of Q as the ratio of the imaginary part to the real part of the modulus  $M(\omega)$ , equation (5.6), and substituting equation (5.9), we have:

$$\frac{1}{Q} = \frac{M_I(\omega)}{M_R(\omega)} = \frac{\sin(\pi\gamma)}{\cos(\pi\gamma)} = \tan(\pi\gamma) \quad (5.10)$$

or

$$\gamma = \frac{1}{\pi} \tan^{-1}\left(\frac{1}{Q}\right) \quad (5.11)$$

Then, using equation (5.9), the velocity (5.4) can be written as

$$v(\omega) = \left(\frac{M_R(\omega)}{\rho}\right)^{1/2} = \sqrt{\frac{M_0}{\rho}} \frac{1}{\cos\left(\frac{\pi\gamma}{2}\right)} \left|\frac{\omega}{\omega_0}\right|^\gamma \quad (5.12)$$

and using (5.11) and setting  $v_0 = \sqrt{\frac{M_0}{\rho}}$  as the reference velocity at the reference frequency  $\omega_0$  ( $v_0$  being the nondispersive limit of the phase velocity) we have

$$v(\omega) = v_0 \frac{1}{\cos\left(\frac{1}{2} \tan^{-1}\left(\frac{1}{Q}\right)\right)} \left|\frac{\omega}{\omega_0}\right|^{\frac{1}{\pi} \tan^{-1}\left(\frac{1}{Q}\right)} \quad (5.12)$$

The attenuation coefficient (5.5) using (5.9) and (5.12) can be written as

$$\alpha(\omega) = \frac{\omega}{v(\omega) \tan\left(\frac{1}{2} \tan^{-1}\left(\frac{1}{Q}\right)\right)} \quad (5.13)$$

Thus, in a medium where wave propagation is linear and causal the presence of absorption requires the phase velocity to be a function of frequency. The relationship of frequency dependent phase velocity to frequency dependent absorption is known as the dispersion relation and also, as the Kramers-Kronig integrals (Aki and Richards, 1980).

For a linear theory (i.e., obeys the principle of superposition), the existence of absorption implies dispersion and determines its form unambiguously up to certain constants characteristic of the medium. It is the presence of this phase shift in the wave, due to absorption, which guarantees a causal arrival of the signal. In terms of the shape of the pulse in the time domain a low Q clearly demonstrates the result of the presence of both the dispersion and attenuation of the wavenumber components for measurements made at

not very large distances from the source (Futterman, 1962).

### 5.5.2 Attenuation mechanisms

The attenuation is a complex phenomenon. There are two approaches in understanding the behavior of  $Q$  in the rocks. The first is based on the generalized equation of linear elasticity (Hooke's law) or modified equations allowing certain nonlinearities. The second uses the physical and mathematical description of possible attenuation mechanisms such as friction, fluid flow, viscous relaxation.

One of the earliest proposed attenuation mechanism is *matrix anelasticity*, including frictional dissipation due to relative motions at grain boundaries and across crack surfaces (Walsh, 1966). This mechanism provides a constant  $Q$  with frequency, that is observed for many dry rocks. However, Winkler et al. (1979) found that at the low strain amplitudes encountered in exploration seismology, friction is not important.

Another mechanism proposed by Savage (1966) is *thermoelastic attenuation* in rocks containing cracks. This model predicts a decrease in attenuation with increasing pressure. Also, it provides an explanation to the increase of  $Q$  as frequency decreases at frequencies about 10 Hz. Kjartansson (1979) uses the thermoelastic model for partially fluid filled cracks in rock for which large changes in attenuation are predicted for small gas saturations. However, the thermoelastic theory would imply a rapid decrease in  $Q$  as temperature increases. Unfortunately, up-to-date there are not enough laboratory experiments on the effect of temperature on attenuation.

Another attenuation mechanism is due to *relaxation* caused by a phase change. Attenuation could change rapidly with temperature near phase changes. High attenuation has been observed at critical points in multicomponent systems (Spetzler and Anderson, 1968; Wang and Meltzen, 1972). Energy is absorbed by a medium whose equilibrium is disturbed by a stress wave.

Also, another loss mechanism is the *effective attenuation due to scattering* by inclusions in the rock. Although this is geometrical effect, it can, in some cases, affect the observed attenuation. Attenuation due to scattering is strongly dependent on frequency and it can be important at high ultrasonic frequencies but at seismic frequencies scattering due to pores is negligible.

The most important attenuation mechanisms are the *Biot's type mechanisms* and the *local flow mechanism*.

#### THE BIOT'S TYPE ATTENUATION MECHANISMS

Biot (1956, 1962) and Gærttsma and Smit (1961) developed a theory for the dynamic response of a linear porous elastic solid containing a viscous compressible fluid.



Attenuation results from the viscous motion of the pore saturating fluid relative to the solid matrix; *inertial flow model*. Biot's theory predicts three kinds of body waves: two dilatational and one shear. One of the dilatational waves (the first kind P-wave) and the shear wave are similar to the waves in elastic media. The other dilatational wave (the second kind P-wave) is highly attenuated and resembles a diffusion wave. Biot obtained his equations by ignoring the microscopic level, and assuming that the concepts and principles of continuum mechanics can be applied to measurable macroscopic variables.

The viscous resistance to fluid flow is frequency dependent for oscillating motion. But below a certain frequency this resistance is given by the ratio of the fluid viscosity to permeability which if considered constant describes a Poiseuille flow (pressure gradient). In order to incorporate the frequency dependence of viscous resistance, Biot derived a complex correction factor to the fluid viscosity. This factor is valid only for frequencies where the wavelength is large compared to the pore size. Therefore, the *Biot's type attenuation mechanisms are the pressure gradient flow and the viscous drag*. The viscous drag at the pore-fluid interface results in greater loss than flow induced by pressure gradients. Thus, the model predicts that the attenuation of S-waves is greater than for the P-waves in case of the fluid flow mechanism, since shear wave attenuation involves only the moving frame dragging the viscous fluid with it.

Velocity dispersion in the Biot theory are caused by the inertial drag of the pore fluid; i.e., when an acoustic wave passes through a fluid saturated porous medium, the pore fluid moves under the differential pressure generated by the passing wave behind the solid frame. At low frequencies, the pore fluid is locked on the frame so there is no relative dispersion. At high frequencies, the effect of inertia caused by the density difference causes the motion of the pore fluid to lag behind that of the solid frame, which in turn leads to higher velocities.

Stoll (1974) proposed a model that is based on Biot's theory but incorporates complex moduli to describe frame and fluid losses. He also considers the inelastic nature of the frame. He concludes that attenuation is attributed to two fundamentally different type of energy loss, one resulting from the *inelasticity of the skeletal frame that dominates at low frequencies* and the other due to the *motion of the pore viscous fluid relative to the frame that is predominant at higher frequencies*. Although it is generally concluded (White, 1965) that Biot's type of attenuation mechanism is negligible at low frequencies in consolidated rocks, it may be important at ultrasonic frequencies (Johnston et al., 1979) or in permeable, unconsolidated sediments at intermediate frequencies. White (1975) extended the *bulk-flow model* to include the effects of spherical gas pockets in fluid-saturated porous rocks. Also, White et al. (1976) showed that pressure differences in fluid-gas interface may greatly enhance fluid flow, resulting in a substantial attenuation even at seismic frequencies. The pressure dependence of attenuation due to fluid flow depends on

the change in permeability in the rock due to compaction and pore collapse. Permeability decreases with increasing pressure, but the rate of decrease depends on the total porosity and fraction of crack porosity.

More recently, de la Cruz and Spanos (1985) developed a wave propagation theory that has many similar elements found in Biot's theory as well some significant differences. First, this theory does not presuppose that during dilation porosity is constant as the Biot's does. Also, in contrast to Biot's approach, de la Cruz and Spanos constructed macroscopic wave equations for elastic porous media saturated with viscous fluid by using volume averaging techniques in conjunction with physical arguments. The microscopic equations, the continuum equations at the pore scale for the elastic solid and the viscous fluid, are spatially averaged over an elementary sphere. This sphere is sufficiently small and large so that both macroscopic and microscopic inhomogeneities do not affect the averaging. Then the solid and fluid movements are coupled through microscopic boundary conditions on the interfaces of the constituent phases of the materials. Wave dispersion and attenuation in this model is due to the viscous fluid motion relative to the solid matrix. Further developments of this theory include thermomechanical coupling (de la Cruz and Spanos, 1989) and viscous dissipation within fluid, including both shear viscosity and bulk viscosity dissipation mechanisms (Hickey et al., 1991).

#### THE LOCAL FLOW ATTENUATION MECHANISM

While Biot's type mechanisms treat bulk fluid flow in porous media, they ignore intercrack flow (local flow) which may dissipate seismic energy. The elimination of local flow and the condition of complete liquid saturation treated by Biot, severely limit the amount of flow and dissipation that can occur under wave excitation. *Intercrack fluid flow or local flow*, known also as "*squirt*" flow, was proposed as an attenuation mechanism by Mavko and Nur (1975). This mechanism results from the stress-induced flow of fluid between cracks at different orientation to the applied stress field. The effective elastic moduli of a fluid saturated solid containing thin cracks depend on the degree of interconnection between the cracks and the frequency of the applied stress field. O'Connell and Budiansky (1977) proposed a model which is based on the a fluid-filled solid containing a distribution of thin cracks and predicts four types of viscoelastic behavior including shear relaxation and squirt flow. There are two characteristic frequencies near which dissipation is largest and the elastic moduli change rapidly with frequency. The first corresponds to fluid flow between cracks and depends on the crack geometry and permeability. The second corresponds to the relaxation of shear stress in an isolated viscous fluid inclusion. Fluid flow between cracks accounts for attenuation of seismic waves in water saturated rocks. Energy dissipation due to intercrack flow is shown to be largest at frequencies ranging from 100 Hz to 1 MHz, depending upon the distribution of

crack shapes. The local flow mechanism is controlled by the local fluctuations of the compressibility of the pore spaces and predicts that attenuation and velocity dispersion depend upon the frequency and pore fluid viscosity, (Jones and Nur, 1983).

The local flow mechanism is based on the assumption that some parts of the pore space are more compliant than other parts. A wave as it propagates through the rock deforms the pore space and hence causes the pore fluid in the more compliant parts to tend to flow to the less compliant parts. Furthermore, the local flow mechanism assumes crack-crack and crack-pore connections in order to explain the dispersion results. In partially-saturated rocks, the pore fluid tends to flow to the empty regions of the pore space. The local flow mechanism is apparently related to the viscosity of the pore fluid, the permeability of the rock, the closure pressure of thin cracks, their aspect ratios, and the connectivity of the thin cracks to the round pores (high aspect ratio). Low permeability rock usually contain cracks of small aspect ratios. For low permeability rocks in which the cracks are still connected, the apparent dispersion of the acoustic velocities should be higher than that for high permeability rocks since the local flow takes longer to get to equilibrium in low permeability rocks.

All results regarding attenuation in rocks have to be correlated to rock properties such as permeability, grain size, porosity and rigidity. In a most general way, differences in attenuation between rocks under physical conditions are related to seismic velocities through the shear modulus (Hamilton, 1972a) which is related to the degree of consolidation and cementation. Rocks with higher velocity generally have higher  $Q$ . For unconsolidated sands, attenuation can be correlated with grain size and porosity (Hamilton, 1972b). However, in consolidated rocks, the microstructure and in particular the pore geometry may be critical in defining differences in attenuation. Mechanisms involving intercrack flow are very sensitive to microstructure. As a result, correlations between attenuation and bulk rock permeability may be difficult to establish.

In partial saturation, the presence of the gaseous phase allows fluid within a pore or crack to flow freely under pure compression (Mavko and Nur, 1979). The resulting attenuation is much higher than with complete saturation as treated by Biot. In general, the attenuation increases with increasing fluid concentration, but is much more sensitive to the aspect ratios of the pores and the liquid droplets occupying the pores, with flatter pores resulting in higher attenuation. Also, gas bubbles have several effects. First, the pore fluid bulk modulus is reduced, facilitating flow even under very small pressure gradients. In this case, as Stoll (1977) suggested, conversion to Biot diffusion type waves at an interface can result in substantial energy loss. Squirting flow would also be enhanced. Second, bubble squeezing and moving in particular may contribute to a decreased  $Q$ . Thus, in partially saturated rocks, the attenuation may be greater than in the fully saturated case. Therefore, attenuation may provide information independently of velocity for the saturation condition of porous rocks.

### 5.5.3 Laboratory measurements of attenuation and velocities

Laboratory measurements of attenuation and wave velocities in fluid saturated porous rocks under varying pressure, temperature, strain amplitudes, frequencies and saturation have been carried out by a number of investigators and are outlined in this section. However, theoretical and experimental studies of velocities and attenuation in heavy oils and tar sands are discussed in the next section which deals in details with the petrophysical and seismic changes occurring during thermally enhanced oil recovery in the Cold Lake oil sands.

#### PRESSURE DEPENDENCE OF ATTENUATION AND VELOCITY

Among the main factors that control compressional and shear velocities and attenuation in porous rocks saturated with fluids are confining pressure, pore pressure and saturation. The effect of the pore pressure counteracts the one of the overburden pressure. In brine saturated rock compressional and shear velocities are lower when pore pressure ( $P_p$ ) is equal to overburden pressure ( $P_c$ ) than when it is equal to atmospheric pressure ( $P_p=0$ ). However, because P-wave velocity in saturated rocks is relatively high the relative change in it due to pore pressure is smaller than the corresponding change in shear velocity. Extensive data analysis by Christensen and Wang (1985) show that to a first approximation, velocities are governed by the effective pressure,  $P_{eff} = P_c - \alpha P_p$ , where  $\alpha$  is a constant for a given rock.

Attenuation depends strongly on pressure. For all frequencies and saturation conditions laboratory experiments have shown that attenuation decreases (Q increases) with increasing pressure and levels off at constant value at a high pressure (Gardner et al., 1964; Toksoz et al 1979; Winkler and Nur, 1979). Also, Toksoz et al. (1979) performed laboratory measurements at ultrasonic frequencies (0.1-1 MHz) of the attenuation of seismic waves in rocks under pressure and different saturation conditions. He showed that the rate of attenuation decrease with pressure depends on saturation, rock type, and crack porosity and distribution. The attenuation coefficients increase linearly with frequency (constant Q) for both P- and S-waves in both dry and saturated rocks. Attenuation in brine and water saturated rock is greater than in dry or methane saturated rocks. Also, attenuation decreases (Q increases) with increasing differential pressure for both P- and S-waves in all cases of saturation. In water saturated rocks Q is higher for the P-waves than for the S-waves. However, in dry or methane saturated rocks Q is slightly higher for S than for P-waves.

Also, compressional wave velocity depends strongly on pressure. Generally, the

compressional and shear velocities in dry and saturated rocks depend very differently on the saturation of the samples, on confining pressure, and pore pressure (Nur and Simmons, 1969b). The compressional and shear velocities in dry rock increase with overburden pressure. However, when the rock is fully saturated at room pressure, a large increase in compressional velocity is obtained, whereas a small or no change is observed in the shear velocity.

Domenico (1976) performed velocity measurements of brine and gas saturated specimens and observed increase of velocity with increasing differential pressure. Dynamic frame compressibility (determined from velocity measurements) is decreasing nonlinearly with increasing differential pressure. Static frame compressibility (determined from volume reduction measurements) decreases almost linearly with increasing differential pressure. The shear modulus (derived from shear velocity measurements) increased nonlinearly with differential pressure. Also, Poisson's ratio for brine-saturated rocks decreases with differential pressure (increase from 400 to 500 psi) from 0.5 to 0.4. Although compressional velocity is primarily a function of differential pressure rather than of confining or pore fluid pressure separately, variations of pore fluid compressibility with pore pressure does modify velocity slightly.

The  $V_p/V_s$  ratios of gas saturated rocks often increase strongly with increasing effective pressure and decrease slightly with increasing temperature (Wang, 1988). In contrast when the rocks are saturated with fluids the ratios are usually decrease as effective pressure increases in low pressure ranges due to closures of the thin pores and cracks of the rocks and the ratios are insensitive to temperature changes. However in rocks with round pores the ratios are also insensitive to pressure changes.

## ATTENUATION AND VELOCITY ANISOTROPY

Velocity anisotropy is another important aspect of seismic wave propagation in rocks. It is generally caused by the preferential alignment of grains and cracks in rocks. A number of investigators such as King (1966), Nur and Simmons (1969c), Lo et al. (1986), and Rai and Hanson (1988) have measured velocity anisotropy in rocks. Also, they found that velocity anisotropy depends on the magnitude and nature of the applied stress and the lithology of the rock.

When cracks in a rock are randomly distributed and the rock is subject to equal stress in all directions, velocity increases are isotropic. However, rocks with a nonrandom distribution of cracks exhibit elastic wave anisotropy (Nur and Simmons, 1969c; Nur, 1971). Velocities in cracked rocks are sensitive to overburden pressure or stress. In cracked rocks, large increases in the velocities are caused by the closure of the cracks and the thin gaps at grain contacts under pressure. In general rocks become acoustically anisotropic under general triaxial stress conditions. Compressional waves travel faster in

the direction of the applied stress and the two shear waves travel generally with different velocities in any direction. The influence of stress on velocity can be described in terms of the anisotropy elements of an elastic crystal (Nur, 1971).

In most cases the changes of attenuation are due to the closure of microcracks in the rock. These cracks are open when the rock is unloaded. The effect of pressure on attenuation is determined from the difference between the overburden pressure and the pore fluid or reservoir pressure. While this behavior is commonly observed for velocity, it is not necessarily the case for flow properties such as permeability. As Walsh et al. (1970) observed attenuation appears to be anisotropic for an applied differential stress. Furthermore, Lockner et al. (1977) measured P, SV, and SH relative attenuation in a triaxially stressed rock and observed that crack orientation strongly affects attenuation. Shear waves polarized normal to the axis of maximum compression suffered the least attenuation as a result of the closure of cracks with faces in that plane. On the other hand, at high differential stresses, the onset of dilatancy, which causes the cracks to open, results in increased attenuation.

#### PORE FLUID AND SATURATION DEPENDENCE OF ATTENUATION AND VELOCITY

Attenuation for fully or partially fluid saturated rocks is higher than for dry rocks and depends on the degree of saturation, the fluid and the frequency. Attenuation in vacuum dry rocks is negligible,  $Q$  is hundred of thousands, compared with typical  $Q$  values in crustal rocks. For ultrasonic frequencies, Toksoz et al. (1979) found that attenuation in brine and water saturated rocks is greater than in dry or methane saturated rocks. Also,  $Q$  is higher for P-waves than for S-waves for water saturated rocks. However, for dry or methane saturated rocks  $Q$  for S-waves is slightly higher than  $Q$  for P-waves.

Winkler and Nur (1979) found for partially saturated Massilon sandstone that the compressional energy loss is larger than the shear energy attenuation ( $Q_p < Q_s$ ) and increases with degree of saturation. However, for fully water saturated rocks  $Q_p$  is larger than  $Q_s$ . Attenuation strongly depends on fluid saturation in rocks containing free fluid phase (Winkler and Nur, 1982; Murphy, 1983). This suggests that the absorption mechanism is due to the interaction of the pore fluid within the rock rather than absorption within the rock frame. Most of the laboratory results concerning wave propagation in fluid-saturated rocks are best interpreted using the local flow or squirt flow attenuation mechanism. The attenuation dependence on saturation may be used as a diagnostic for gas saturated reservoirs using relative attenuation measurements between compressional and shear waves.

A number of investigators such as King (1966), Bacri and Salin (1986) and Wang et

al. (1988) have shown that acoustic wave velocities in fluid-saturated rocks are related to pore fluid type (the bulk modulus of the the pore fluid). Furthermore, the viscosity and the chemical effect of the fluid on the surface of the rock grains can also influence the wave velocities (Murphy, 1984; Wang and Nur, 1985).

As far as the dependence of velocities on the degree of saturation, both velocities do not show much sensitivity to saturation except when it becomes close to 1 where the compressional velocity increases markedly (Murphy, 1982). This unfortunately suggests that velocity measurements cannot yield information regarding the degree of partial saturation in reservoir rocks. However, Murhpy (1984) showed that compressional velocities in tight gas sandstones at 600-6000 Hz band are more sensitive to partial saturation than in the ultrasonic frequency range. At low frequencies the increase of the P-wave velocity is sharp when saturation rises from 90 to 100 % and is gradual with saturation from 50 to 90 % at higher frequency range.

On the other hand, Domenico (1976) showed that compressional velocity decreases gradually with increasing brine saturation becoming minimum at 90% brine saturation and then increases abruptly and substantially to the highest value at full saturation. This variation is non-linear, thus the variation of the compressional reflection amplitude is not an accurate indication of gas quantity.

Agreement of velocity measurements in fluid-saturated rocks with Biot's theory depends on the microstructure and porosity of the rock, the viscosity of the pore fluid, and the interactions between the rock and the pore fluid. King (1966) reported on velocities of sandstones samples with his results being predicted by Biot's theory at high effective pressures. On the other hand, Nur and Simmons (1969b) showed that the measured velocities in low porosity rocks do not obey Biot's theory at low effective pressures Also, Gregory (1976) points out that agreement between measured velocities and Biot's theory depends on pressure, porosity, fluid-mineral interactions and the presence of microcracks in the rocks.

#### TEMPERATURE DEPENDENCE OF ATTENUATION AND VELOCITY

There are not many laboratory data on temperature dependence of attenuation. Gordon and Davis (1968) showed that  $Q$  is generally temperature independent at temperatures less than 150° C in dry rocks, and that attenuation increases at greater temperatures may be due to thermal cracking. Also, Spencer (1981) found a small shift in the attenuation peak to higher frequencies as a function of temperature for a water saturated Navajo sandstone. Furthermore, laboratory experiments on the effect of temperature on attenuation have been performed on samples of tar sands. However, these are discussed in the next section that deals with changes occurring in the oil sands during thermally enhanced oil recovery.

In fluid saturated rocks, saturation enhances the temperature dependence of both compressional and shear wave velocities. Furthermore, the effect of phase transition on the velocities is very large.

Timur (1968) studied velocities in rocks at permafrost condition and concluded that compressional wave velocity in water saturated rocks increases as the temperature decreases, and is nearly independent of temperature in dry rocks. Also, he showed that velocity increases (8 to 20 %) as the water in the pores of the rock transforms to ice and this increase depends on the lithology, pore structure and the nature of fluids in the rock. The liquid-solid transition has a large effect in rocks with pores of high aspect ratio.

Another phase transition in the pore fluid that affects velocities is the liquid-gas transition. Ito et al. (1979), conducted ultrasonic laboratory measurements on Berea sandstone samples at geothermal temperatures (145 °C, and 195 °C). They concluded that in the steam filled rock the compressional and shear wave velocity is lower and higher, respectively, than in the water filled rock. As a result the Poisson's ratio in steam saturated pores proved to be around 0.20 - 0.22 at 145 °C and 195 °C and 0.28 - 0.30 in water-saturated pores at the same range of temperatures. Thus, Poisson's ratio may be a useful tool of discrimination between steam and hot water in the pore space. They also found that the compressional wave velocity decreases where the shear wave velocity increases as the water in the pores transforms from water into vapor. The decrease in P-wave velocity is mainly caused by the increase of pore fluid compressibility where the S-wave increase is mainly due to the pore fluid density decrease. Furthermore, the P-wave velocity has a minimum at the transition point from liquid to vapor where the S-wave velocity has not. Thus, regions with both steam and hot water should exhibit anomalously low velocity and high attenuation of P-waves but not S-waves. The compressional velocity minimum may be caused due to the combined effect of increasing density as more and more steam transforms into water (close to the density of water-saturated rocks) and the low fluid bulk modulus remains low (close to that of steam) as long as any steam is present (the bulk modulus in the steam-saturated rock is lower than in a water-saturated rock). On the other hand, shear velocity is barely influenced since it is insensitive to the bulk modulus of the fluid. Although laboratory measurements were made over a frequency range that is  $10^3$ - $10^5$  order higher than the typical *in situ* studies, these results provide important physical insight into the effects of steam on wave propagation in porous rocks and suggest that high-resolution seismic methods may be able to recognize in-situ interfaces between steam-saturated and hot water-saturated rocks.

## STRAIN AMPLITUDE DEPENDENCE OF ATTENUATION

It is assumed that attenuation is independent of strain amplitude at least for the low



strains associated with seismic waves. However, laboratory data from a number of investigators (Peselnick and Outerbridge, 1961; Winkler et al, 1979; Johnston and Toksoz, 1980) show that for strains greater than  $10^{-6}$  amplitude depends on strain. Winkler et al (1979) showed that at 1 KHz, moderated effective pressures may reduce or eliminate amplitude dependence. They also found that in water saturated rocks the amplitude dependence is enhanced. Johnston and Toksoz (1980) found that for low heating pressures, where differential thermal expansion may tend to open preexisting cracks, the transition from constant Q to amplitude dependent Q migrates to lower strain amplitudes as a function of the maximum temperature achieved during cycling.

### FREQUENCY DEPENDENCE OF ATTENUATION

In terms of frequency, the common assumption is that Q is independent of frequency. For at least dry rocks, as Peselnick and Outerbridge (1961) have shown for dry limestone, Q is indeed independent of frequency. In most cases, attenuation values obtained by ultrasonic methods are higher than those obtained by lower frequency resonance techniques. In fluid saturated rocks, attenuation may be a result of flow type mechanism and is generally frequency dependent. Cur and Winkler (1980) observed an apparent peak in  $Q^{-1}$  for saturated Massillon sandstone at 4 KHz but a constant  $Q^{-1}$  for the dry case. Also, they observed for Spergen limestone a peak at frequency of 10 to 20 Hz. The peaks shift to higher frequencies with increasing pressure. Also, Nur and Simmons (1969) have shown a peak in attenuation of shear waves for glyserol-saturated granite. Wyllie et al. (1962) presented data for alundum that shown large variations in attenuation from 5 to 12 KHz.

### VELOCITY DISPERSION

Quantitative knowledge of velocity dispersion is difficult since there are no reliable methods by which one can measure the velocities as a continuous function of frequency over a broad band either in the field or in the laboratory. However, velocity dispersion has been documented within three nonoverlapping frequency bands (seismic, 10-150 Hz; sonic, 1000 -10000 Hz and ultrasonic, 0.1-1 MHz) by a number of authors such as Wuenchel (1965), Jones and Nur (1983) and Winkler (1983, 1986).

Spencer (1981) observed significant modulus dispersion in liquid saturated rocks and suggested that this dispersion is caused by stress relaxation which involves the movement of fluid molecules at the rock's pore surfaces, reducing surface energy and thus generating the observed frequency dependent softening in rocks.

Winkler (1983) observed decreases in compressional velocity as the wave frequency increases (negative dispersion) in dry rocks. On the other hand, the compressional velocity

in brine-saturated samples increases with increasing frequency (positive velocity dispersion). He also observed that the velocity dispersion in brine saturated rocks diminishes as the effective pressure increases, due to the closure of the thin pores or cracks in the rock.

Murphy (1984) measured velocity dispersion in a granite sample and fitted his results at low frequencies with Biot's theory and Gassmann's (1951) equation and at high frequencies with the self-consistent scattering theory (O'Connell and Budiansky, 1974). Also, Winkler (1985) developed a method for estimating velocity dispersion in rocks using Biot's theory and Gassmann's equation for low and high frequencies.

However, most of the laboratory data concerning velocity dispersion in fluid saturated porous media are best interpreted in terms of the local flow model (Winkler, 1985, 1986; Han, 1987; Wang, 1988). When the rock is saturated with a fluid of high viscosity, the time for the local flow to stop (or the pore pressure to equilibrate) is much longer due to the low mobility of the pore fluid. As a result the apparent dispersion of the velocity is larger. The opposite occurs when the rock is saturated with a fluid of low viscosity. The apparent dispersion of the velocities explained in terms of the local flow mechanism depend not only on the viscosity of the pore fluid but also on the thin crack presence and their aspect ratios. If the pore space of a rock is only composed of round pores (high aspect ratio), the velocity will basically have no dispersion since in this case all the parts of the pore space have the same compliance and hence there is no local flow to occur. As the effective pressure increases the crack tips connecting to the pores or other cracks will close, hence, the local flow activity of the pore fluid is limited and greatly decreased, with results in less apparent dispersion of the acoustic velocities.

Laboratory results (Spencer, 1981; Winkler, 1983; Murphy, 1984; Winkler, 1985; Jones, 1986) show that acoustic waves in fluid-saturated rocks are intrinsically dispersive (the velocities are a function of frequencies). However, it is important to know the difference in the magnitude of the velocity dispersion between seismic and laboratory ultrasonic frequencies in order to use laboratory obtained results for seismic and log interpretations.

Furthermore, discrepancies between seismic and sonic velocities were interpreted in terms of velocity dispersion (Stewart et al., 1984). These results indicate that the frequency content, phase spectrum and velocity may be strong indicators of the type of pore fluid in a formation. Alternatively, if the type of the pore fluid is known, these attributes could be used to monitor temperature changes of a formation. Thus, measurements of velocity dispersion and attenuation can be used as lithology and temperature indicators and/or microstructure indicators (Nyland, 1985; Tosaya et al., 1984).

#### 5.5.4 Summary on attenuation and velocity

In terms of frequency, strain amplitude, saturation, pressure and temperature dependence of attenuation and velocity, the following conclusions can be drawn:

- 1) Attenuation decreases with increasing confining pressure primarily due to the closing of cracks in the rock matrix. Also, the compressional wave velocity strongly depends on pressure and increases with increasing effective pressure. For applied nonhydrodynamic stress, both attenuation and velocity appear to be anisotropic.
- 2) Both attenuation and velocity depend on the degree of saturation and the fluid type. Attenuation for fluid saturated rocks is higher than for dry rocks. Compressional wave velocity decreases with increasing saturation and increases abruptly and substantially at full saturation.
- 3)  $Q$  generally is independent of temperature at low temperatures relative to the melting point. However, near the boiling temperatures of pore fluids, attenuation may be affected strongly by temperature. Also, compressional wave velocity strongly depends on temperature and decreases with increasing temperature.
- 4) Attenuation appears to be independent of strain amplitude for low strains that are associated with seismic waves.
- 5) Generally, the quality factor  $Q$  is frequency independent. However, in some highly porous and permeable rocks the total  $Q$  may contain a frequency dependent component.
- 6) Generally, acoustic waves in fluid-saturated rocks are intrinsically dispersive (the velocity is a function of frequency) and in particular, compressional wave velocity increases with increasing frequency.

Attenuation can be explained by a number of mechanisms, that are summarized next.

- 1) The primary mechanism for attenuation is friction on grain boundaries and thin cracks.
- 2) Increasing the differential pressure decreases the number of cracks contributing to attenuation by friction. Therefore, attenuation decreases with increasing pressure and eventually approaches a limiting value called intrinsic aggregate anelasticity.
- 3) In totally dry rocks, the attenuation is less than in wet or saturated rocks. With the introduction of fluid crack lubrication results to frictional sliding and attenuation increases.
- 4) In saturated porous rocks attenuation due to fluid flow plays a secondary but important role relative to friction. At low frequencies, squirting flow may be a viable mechanism, especial in partial saturation, case. At ultrasonic frequencies, the Biot type mechanism fluid flow, play an important role in the overall attenuation at high pressures.

In conclusion, the attenuation and velocity changes observed in porous rocks can be caused by a number of different mechanisms as discussed above. The relative importance of each mechanism depends on the physical conditions imposed upon the rock. Each mechanism depends on rock type, saturation conditions, pressure, frequency and amplitude of the wave. At present, no one mechanism is responsible for the bulk of attenuation and

no particular mechanism can be eliminated from consideration.

## **5.6 RESERVOIR CONDITIONS AND SEISMIC CHANGES DURING EOR PROCESSES**

It has been realized that reservoirs are more complex and heterogeneous than assumed in the past. The results of the heterogeneity of the reservoirs are the complexity of their recovery processes, problems such as the migration of gas caps in reservoirs with discontinuous shales, the existence of overpressure zones, and the difficulty of tracking steam or temperature during thermally enhanced oil recovery in reservoirs with large permeability variations. Thus, a major shift in the use of seismic methods is taking place that involves the need to correlate and establish relations between seismic parameters such as velocity, bulk density and attenuation, and their representations on the seismic record by reflection travel times and seismic attributes, and the production properties and conditions of the reservoir such as porosity, permeability, lithology, saturation, pressure, and temperature.

In the following, we discuss the changes in conditions and properties occurring in the Cold Lake oil sands during steam enhanced oil recovery and their effects on seismic wave propagation.

### **5.6.1 Effects of Pressure**

The effect of confining pressure on rock is to deform the most compliant part of the pore space (microcracks and loose grain contacts) and increase the stiffness of the rock i.e., the effective bulk and shear moduli (Nur and Wang, 1989). The effect of high pore pressure due to the steam injection is to mechanically oppose the closing of cracks and grain contacts resulting from the confining pressure, thus leading to low effective moduli and velocities. When these two processes counteract each other they do not influence as much the variations of compressional and shear velocities.

Based on an analysis of the reservoir conditions using reservoir simulations and observation wells (Eastwood et al., 1993) the effective stress is low (nearly 0 MPa and 2 MPa at 5 and 50 m distance from the wellbore, respectively) during the steam injection phase while it is high (nearly 9.5 MPa and 8 MPa at 5 m and 50 m distance from the wellbore, respectively) during the production cycle. Furthermore, the dilation is increased (6% to 3% at 5 m and 50 m distance from the well, respectively) during steam injection and decreased (2% to 0% at 5 m and 50 m distance from the well, respectively).

Siewert (1993) presented rock and fluid effects of a steam stimulation process under frac pressures which were observed on seismic monitoring data and confirmed in triaxial core tests. Also, he showed that reflection amplitude changes track reservoir pressure, with

frac anomalies emanating from known well locations. According to Siewert (1993) the dilation is the result of shear stresses acting in association with open fractures. Furthermore, the shear failure or unloading results in a reduction in the frame strength of the rock.

Therefore, low effective stress and high dilation during steam injection results in higher rock frame compressibility. Subsequently, this results in lower compressional velocity and higher seismic amplitude events. Thus, since both seismic and reservoir drive mechanisms are related to compressibility, seismic monitoring can provide valuable insight into the enhanced oil recovery process of the reservoir.

### 5.6.2 Effects of Temperature

Tosaya (1984) observed large velocities decreases with temperature in cores of heavy oil and tar sands from Venezuela, California and Alberta. In some cases, he observed 40% velocity decrease with temperature increase from 20 to 150 °C. In addition, he observed large decreases in the normalized P-wave amplitude with increasing temperature in the samples that contain oil, due to attenuation.

Wang and Nur (1986, 1987, 1988c), employing ultrasonic frequencies, demonstrated the effects of temperature on seismic velocities in sandstones and unconsolidated sands saturated with heavy hydrocarbons at confining pressures. They observed that the compressional and shear seismic wave velocities decrease by increasing the temperature from 20 to 120 °C. Particularly, the compressional velocity decreases by 10% to 15% in well consolidated sandstones saturated with heavy oil and by 15% to 40%, even 60%, in unconsolidated heavy oil and tar sands. The temperature dependence of the velocities is interpreted in terms of a phase transition of the heavy hydrocarbons and high pore pressure generated by the thermal expansion of the hydrocarbons. As temperature increases, the increase of compressibility and decrease in viscosity of the crude and tar, thermal cracking of the heavy hydrocarbons, and the melting of the solid or semi-solid hydrocarbon fractions all contribute to velocity decreases. On the contrary, in a heated zone where most of the oil has been replaced by steam (e.g., during the production cycle), we expect temperature effects to play a secondary role in the variation of both compressional and shear velocities of the reservoir.

Also, Wang's (1988) results show that according to both Biot's and local flow models, the temperature dependence of the compressional velocity in heavy oil saturated rocks in the seismic frequency band (10-200 Hz) should be about the same as that observed in the laboratory at about 1 MHz. This suggests that the large velocity decrease with increasing temperature in heavy oils reservoirs should also occur in-situ. Therefore, seismic methods can be used in-situ to monitor thermally enhanced oil recovery processes.

Eastwood (1992) showed results of ultrasonic experiments performed on Cold Lake tar sand samples. The compressional velocity, density, viscosity, bulk modulus of the Cold Lake oil sands decrease with increasing temperature and decreasing effective stress due to significant changes in fluid properties and the undrained bulk modulus. On the other hand, Eastwood (1992) constructed theoretical models to account only for temperature dependent fluid properties and to predict temperature dependence for velocity based on correlations independent of the ultrasonic experiments. These seismic wave propagation models utilized the Gassmann (1951) equation and the de la Cruz-Spanos (1985) theory with modifications presented in Hickey et al. (1991). The models predicted both P-wave velocity as a function of temperature for the Cold Lake bitumen close to the experimentally measured values. Furthermore, the de la Cruz-Spanos model showed that attenuation exhibits a strong frequency dependence and drops dramatically as temperature is increased. At lower temperatures (20~130 °C) the decrease occurred due to the viscous dissipation within the high viscosity fluid (viscosity of the fluid is a strong function of temperature). However, at higher temperatures attenuation increases because of temperature related momentum loss due to relative motion between the solid frame and the fluid continuum (Darcian resistance).

At Cold Lake during the steam cycle of the Esso's EOR process, steam at 315 °C is injected into the oil sands. Although steam is present in the vicinity of the wellbore, at 50 m distance from the wellbore the temperature is only 30 °C resulting in a steam zone that is smaller than the gas zone during production. The viscosity of the bitumen decreases as its temperature increases. Consequently, the bitumen's bulk modulus decreases. Thus, compressional wave velocity decreases significantly and attenuation increases during steam injection.

On the other hand, during the production cycle of the EOR process the temperature in the vicinity of the wellbore (5 m distance) is about 150 °C and at 50 m away is about 15 °C. However, steam effects during production are not separable from the evolving gas anomalies.

### 5.6.3 Effects of Gas

In the oil sand reservoirs at Cold Lake there are small free gas saturations e.g., 0~3 % in the Sparky sands. The presence of this gas indicates that the oil is at nearly the bubble point and exists in equilibrium in the form of micro-bubbles in pits and surfaces with high contact angles (Siewert, 1993, personal communication).

During steam injection because of the high pore pressure the free gas present in the oil sand reservoir is forced back into solution. The gas saturation during the steam injection was observed at Esso's Cold Lake project to be between 2% to 0% at 5 m and 50 m distances from the wellbore, respectively (Eastwood, 1993). The free gas reduction will cause a decrease in the fluid compressibility and thus, a velocity increase and a decrease in

the corresponding seismic amplitude.

On the other hand, during production as the heavy oil is produced the pores are filled with steam or steam condensate mixed with liberated gas. The gas saturation at Esso's Cold Lake oil sands reservoir during production is about 5% to 2% at 5 m and 50 m distance from the wellbores, respectively. The evolution of gas causes a decrease in the compressional wave velocity and a seismic amplitude increase.

#### **5.6.4 Effects of pore fluid type and saturation**

According to Wang and Nur (1988a) fluid saturation increases the P-wave velocity in the rock as predicted by both Gasmann's (1951) relation and Biot's theory (Biot, 1956a,b) due to the increase of the bulk modulus of the rock-fluid aggregate. However, the effect of heavy oil is much larger than expected from both theoretical models. This may be due to velocity dispersion, chemical or surface effects and the contribution of the increased shear modulus due to the viscous relaxation of the pore fluid.

Velocity dispersion is common in fluid-saturated rocks. Wave velocities increase with increasing frequency of the wave, due to the in-situ drag of the pore fluid or pore pressure gradient caused by the compliance heterogeneity of the pores. However, according to Wang and Nur (1988a), using either Biot's theory or the local (squirt) flow mechanism the compressional velocity in rocks saturated with heavy oil at 1 MHz is about the same as in the seismic band, due to oils high viscosity. An important consequence is that seismic wave reflections may occur at the interfaces between light and heavy oil saturated rocks.

Also, Wang (1988) analyzed the effects of pressure, temperature, viscosity and type of pore fluid, porosity, permeability, and pore geometry on the attenuation and apparent velocity dispersions in rocks. He concluded that pore fluid viscosity, permeability, and pore geometry are the major factors which affect velocity dispersion. His results show that in rocks saturated with low viscosity pore fluids, the apparent velocity dispersion is small, whereas in the same rock saturated with heavy oil with very high viscosity dispersion is much greater. This behavior is consistent with the local flow mechanism.

The influence of the pore fluid type on the acoustic velocities, separately from its pressure, depends on its compressibility. When pore fluid is relatively incompressible (brine), the effective bulk modulus of the rock is high. In contrast, the shear modulus is barely altered by the variation in fluid compressibility since there is only a volumetric change. In general, pore fluids tend to increase the compressional wave velocity because of their bulk modulus, but slightly decrease the shear wave velocity because of their density. When the pore fluid changes to steam or vapor the compressional velocity drops sharply in comparison with the same rock fully saturated with water, whereas the shear velocity does not change much, in fact it may increase slightly due to the overall density decrease of the

rock.

Tsingas (1989) used Geertsma's (1961) equation at zero frequency to predict the effect on the compressional seismic velocity when steam is injected into the oil sand reservoir, bitumen is replaced by steam or steam condensate and temperature effects are neglected assuming a mature steam zone. The fact that shear stresses are responsible for shear distortions the presence of fluid makes no difference to the shear modulus and therefore, the shear modulus of the saturated rock is the same as of that of the rock frame. Hence, the shear velocity is not affected by the steam replacing the bitumen. Therefore, Poisson's ratio will be affected through the compressional velocity changes and can be a good discriminator between steam and hot water in the pore space. When the ratio of the compressional to the shear wave velocities changes, a variation of the Poisson's ratio occurs.

A change in the Poisson's ratio, produces a variation of seismic acoustic reflected amplitude at normal and nonnormal angles of incidence, (Ostrander, 1984; Domenico, 1976). Poisson's ratio has been found to be as low as 0.16 in steam dominated geothermal fields (Majer and McEvilly, 1979), between 0.20 to 0.22 in steam saturated rocks at temperatures of 145 to 195 °C (Ito et al., 1979), and between 0.20 to 0.23 in *in-situ* combustion processes (Justice et al. 1989). Zones with low Poisson's ratio in the order of 0.15 to 0.23 (predominantly steam or gas saturated zones) can cause an increase of reflected amplitude with angle, whereas, zones with high Poisson's ratio in the order of 0.35 to 0.4 (predominantly brine or water saturated) cause a decrease in the reflected amplitude with angle.

Thus, during cyclic steam stimulation (CSS) in the oil sands, the injected steam displaces the pore fluid (oil) resulting in an increase of the overall compressibility of the reservoir rock and as result the compressional velocity decreases.

### 5.6.5 Utilizing seismic attributes

Since the same petrophysical effects described earlier are anticipated to occur also *in-situ*, we can use seismic methods, particularly 3-D high resolution surface seismic surveys, to monitor the thermal enhanced oil recovery process. Ideally, we would like to continuously monitor reservoirs throughout their volume using seismic methods in order to map the direction of propagation, the shape, the rate of movement, and the spatial heterogeneity of the steam fronts, and determine changes in the reservoir properties and conditions. For example, if the seismic images show that the injected steam flows with different speed in different directions, this may suggest permeability heterogeneities of the reservoirs rocks.

During steam injection the reservoir conditions are the local maximum in terms of temperature and fluid pressure (315 °C, 10 MPa). The high dilation in association with the



low effective stresses cause an increase of the rock compressibility. When steam is injected into oil bearing reservoir, it is trapped by shales barrier located above the perforation levels, it heats the rock and fluids, and it displaces a certain fraction of the in-place oil. The high temperature decreases the viscosity of the bitumen, thus the bitumen has lower bulk modulus and higher compressibility. Attenuation increases with the high temperature alteration of the reservoir rocks. Also, since some of the oil is displaced by the injected steam and the rock is partially altered, both the compressibility of the reservoir rock and attenuation increase. On the other hand, the gas saturation drops and this reduction decreases the fluid compressibility. However, in some cases there is an increased gas saturation along the top of the reservoir boundary. Therefore, overall the rock frame and fluid compressibility increases. This results in a decrease of the compressional wave velocity and an increase in wave attenuation in the steam effected reservoir.

On the other hand, during the production cycle of the EOR process the reservoir conditions are at a local minimum in terms of pressure and temperature but the gas saturation is high (~5%). Thus, the main seismic anomalies during production cycle are associated with the increased gas saturation. The evolution of gas during production and the remaining steam or steam condensate cause an increase in the compressibility of the fluid. The high compressibility results in a decrease of the compressional wave velocity.

The velocity decrease, the increase in attenuation and the variable fluid saturation imply that time delays (pushdowns or velocity sags), amplitude and spectral anomalies of seismic reflections from subsurface zones invaded by the steam zone can be observed on seismic sections.

The reflector at the top of the reservoir, usually the boundary between the shale above and hot fluid saturated oil sands below, has an increased reflection amplitude ("bright spot"). On the other hand, reflectors below the steam affected reservoir are time delayed and are decreased in reflection amplitude ("dim spots"). The bright spot seismic method has been used in monitoring the forming, growing, moving and shrinking processes of gas caps. Hence, it could be used here where bright spots are occurring due to the velocity decrease and variable fluid saturation during both steam and production cycles.

Amplitude anomalies on the monitoring seismic images can be used to indicate gas saturation changes in the reservoirs, to monitor the contacts, mobility, phase and temperature change of reservoir fluids, to determine distribution and continuity of the reservoirs as they are produced over time, to map reservoir heterogeneities and changes in pressure. Seismic attribute analysis, such as pushdown, amplitude and spectral differencing between the seismic images from different phases of an EOR process are used to track the steam fronts and map their spatial heterogeneity (Kalantzis et al., 1993.a, 1993.b, 1994; Eastwood et al., 1993, 1994)

Changes in the Poisson's ratio occurred during the EOR process, from 0.33~0.44 for brine or water saturated rock to 0.16~0.23 for steam or gas saturated rock, produce a

variation of seismic acoustic reflected amplitude at normal and nonnormal angles of incidence. Such changes in the Poisson's ratio have been studied by Tsingas and Kanasewich (1991) over a steam injection site. Their amplitude-versus-angle (AVA) analysis strongly suggests the application of seismic reflection methods in delineation and mapping of the steam-heated zones generated during a thermal EOR process.

The large volume, and high temperature and pressure steam that is injected into the reservoir during an EOR process may cause fracturing of shales (tight streaks) within the reservoir. These, shales act as permeability barriers and their continuity between the injection and production wells is important for planning the steaming and production strategies. Thus, fracture detection and stress determination is desirable during an EOR process. Velocity anisotropy (variation in velocity as a function of direction of wave propagation) results from fracturing or bedding alignment of rocks. Also, a secondary effect of anisotropy is the splitting of S-waves into polarized components which propagate at different velocities. Crampin (1985) infers crack densities and orientation from seismic data. Also, Lynn and Thomsen (1986) successfully applied shear-wave polarization to in-situ fracture detection. The stress and crack induced velocity anisotropy suggests the possibility of detecting the orientation and density of natural or induced fractures and determining the in-situ state of stress from seismic measurements (Martin and Davis, 1987). Therefore, 3-D multicomponent seismic monitoring of fracturing and stress conditions in the reservoir during an EOR process may be possible. Furthermore, since fractures provide high permeability paths for fluid movement, inferring the fracture orientation and density might result in mapping permeability changes.

Observation wells are used to monitor reservoir pressure, temperature and gas saturation during a thermal EOR process. However, observation wells are expensive and measure parameters at only one location. It is desirable to extend information about the reservoir away from the observation wells analysing seismic data from non-invasive methods such as surface seismic surveys.

In order to obtain reservoir information such as properties and volumetrics from seismic data, we need to qualitatively and quantitatively correlate the changes observed on the seismic attributes to changes in conditions of the reservoir during the thermally enhanced oil recovery process. This may be possible with integration and calibration of seismic data with geological and reservoir engineering data, such as geological models, well logs, and petrophysical models, through realistic seismic modeling studies, reservoir simulations and application of geostatistical methods. In the next chapter, seismic attribute images are generated from multiple monitoring surface 3-D seismic surveys at Cold Lake during EOR processes (Kalantzis et al., 1994). These seismic images are integrated with crosswell seismic velocity tomograms, geostatistical velocity models from sonic wells, geological models and engineering data. Also, Eastwood et al. (1994) are integrating data

geological models and engineering data. Also, Eastwood et al. (1994) are integrating data from 3-D surface seismic monitoring, cross-well tomography, well logs and reservoir simulations for Esso's Cold Lake steam stimulation project.

Determination of the spatial distribution of porosity, permeability and saturation is the most desirable application of the seismic method (Robertson, 1987). Geostatistical estimation methods have been proposed (Doyen et al., 1988) for mapping porosity from seismic data using the spatial cross-correlation between porosity measurements from a well and the seismic interval velocity. Seismic guided log property estimates can be done using geostatistical methods such as kriging. Hwang and McCorkindale (1994) used kriging with an external drift, incorporating both well and seismic travel times, combined with conditional simulations, to predict velocities and depths. An alternative approach, (Schultz et al., 1994a, 1994b) uses a seismic-guided log property estimation method to establish relations, via calibration and residual correction steps, between some seismic attributes and reservoir properties such as porosity and water saturation measured on well logs, and to estimate the spatial distribution of these properties. Also, Makland et al. (1993) used a pattern recognition technique to integrate three seismic attribute images (time, amplitude and frequency) obtained from differencing two monitor seismic data over an EOR site and the results delineated the areal extent of the steam-heated zones. Therefore, it may be possible to estimate porosity, saturation and permeability changes in the reservoir during enhanced recovery from monitoring by integration of seismic data with well and other data.

## 5.7 CONCLUSION

Enormous reserves of heavy oil are present in the complex reservoirs in sands of Lower Cretaceous age in Cold Lake area of Alberta, Canada. This heavy oil is immobile under reservoir conditions because of its high viscosity. Enhanced oil recovery methods such as steam stimulation are used to reduce the viscosity of the bitumen and produce it by pumping it to the surface. However, during the steaming process, the movement of fluids away from the heated sources at the perforation level is controlled by permeability heterogeneities and even small heterogeneities or anisotropy, caused from fracturing due to high pressure injected steam, can play an important factor in the efficiency of the EOR process. Therefore, it is important to image the shape and areal extent of the steam-heated zone and determine the direction and rate of movement of the thermal front.

Petrophysical alterations in the heavy oil reservoirs during enhanced oil recovery (EOR), as caused by pressure, temperature, the replacement of bitumen by steam or steam condensate, etc., contribute to velocity changes, attenuation and velocity dispersion of seismic waves in the effected reservoir. These changes on a seismic reflection record imply seismic attribute changes such as amplitude brightening of reflections from the top of the steam zone and travel time delays of reflectors within and below the steam invaded zone.

seismic reflection method can be used to continuously monitor reservoirs during the EOR process and map the expanded steam-heated zone.

In conclusion, the goal of seismic monitoring of an enhanced oil recovery process is to positively impact the design and management of the oil recovery project. However, in order for the seismic method to become a powerful technique for monitoring EOR processes, it must be able to present to the reservoir engineers the desired results in terms of temperature, pressure and saturation. In order to succeed in this, it is necessary to correlate qualitatively and quantitatively the seismic attributes and their changes over time with the reservoir conditions and properties as they change during the EOR process.

## REFERENCES

- Bacri, J., and Salin, D., 1986, Sound velocity of a sandstone saturated with oil and brine at different concentrations: *Geophys. Res. Lett.*, **13**, 326-328.
- Bailey, N.J.L., Jobson, A.M., and Rogers, M.A., 1973, Bacterial degradation of crude oil: Comparison of field and experimental data: *Chemical Geology*, **11**, 202 - 220.
- Biot, M.A., 1956a, Theory of elastic waves in a fluid-saturated porous solid. I. Low-frequency range: *J. Acoust. Soc. Am.*, **28**, 168-178.
- Biot, M.A., 1956b, Theory of elastic waves in a fluid-saturated porous solid. I. Higher frequency range: *J. Acoust. Soc. Am.*, **28**, 179-191.
- Biot, M.A., 1962a, Mechanics of deformation and acoustic propagation in porous media: *J. Appl. Phys.*, **33**, 1482-1498.
- Biot, M.A., 1962b, Generalized theory of acoustic propagation in porous dissipative media: *J. Acoust. Soc. Am.*, **34**, 1254-1264.
- Christensen, N.I., and Wang, H.F., 1985, The influence of pore pressure and confining pressure on dynamic elastic properties of Berea sandstone: *Geophysics*, **50**, 207-213.
- Crampin, S., Evaluation of anisotropy by shear wave splitting: *Geophysics*, **50**, 142-148.
- Dusseault, M.B., 1977, The geotechnical characteristics of the Athabasca oil sands, Ph.D. Thesis, University of Alberta, Edmonton, Alberta, Canada.
- de la Cruz, V., and Spanos, T.J.T., 1985, Seismic wave propagation in a porous medium: *Geophysics*, **50**, 1556-1565.
- de la Cruz, V., and Spanos, T.J.T., 1989, Thermomechanical coupling during seismic wave propagation in a porous medium: *J. Geophys. Res.*, **94**, B1, 637-642.
- Doyen, P., Journel, A., and Nur, A., 1988, Porosity from seismic data: a geostatistical approach: *Geophysics*, **53**, 1263-1275.
- Domenico, S.N., 1976, Elastic properties of unconsolidated porous sands reservoirs: *Geophysics*, **42**, 1339-1368.

- ERCB (Energy Resources Conservation Board), 1979, The Cold Lake project, ERCB 79-E, Alberta.
- Eastwood, J., 1992, Temperature dependent propagation of P and S waves in Cold Lake sands: comparison of theory and experiment: Internal Report, Imperial Oil, Calgary.
- Eastwood, J., Dilay, A., and Makland, M., 1993, Spectral analysis applied to monitoring of thermal recovery: 3rd Annual Intern. Meeting, Washington D.C., Soc. Expl. Geophys., Expanded Abstracts, 331- 334.
- Eastwood, J., Lebel, P., Dilay, A., and Blakeslee, S. 1994, Seismic monitoring of steam-based recovery of bitumen: *The Leading Edge*, **13**, No. 4, 242 - 251.
- Farouq Ali, S.M., 1974, Current status of steam injection as a heavy oil recovery method: *Journal of Canadian Petroleum Technology*, **13**, 54 - 68.
- Flock, D.L., and Lee, J., 1977, An experimental investigation of steam displacement of a medium gravity crude oil: The oil sands of Canada - Venezuela, CIM special volume, **17**, 386 - 394.
- Futterman, W.I., 1962, Dispersive body waves: *J. Geophys. Res.*, **67**, 5279-5291.
- Gardner, G.H.F., Wyllie, M.R.J., and Droschak, D., 1964, Effects of pressure and fluid saturation on the attenuation of elastic waves in sands: *Journal of Petroleum Technology*, **16**, 189-198.
- Gassmann, F., 1951, Elastic waves through a packing of spheres: *Geophysics*, **16**, 673-685.
- Geertsma, J., and Smit, D.C., 1961, Some aspects of elastic wave propagation in fluid-saturated porous solids: *Geophysics*, **26**, 169-181.
- Gordon, R.B., and Davis, L.A., 1968, Velocity and attenuation of seismic waves in imperfectly elastic rock: *J. Geophys. Res.*, **73**, 3917-3935.
- Hamilton, E.L., 1972a, A correlation between  $Q_s$  of shear waves and rigidity: *Mar. Geol.*, **13**, M27-M30.
- Hamilton, E.L., 1972b, Compressional wave attenuation in marine sediments: *Geophysics*, **37**, 620-646.
- Harrison, D.B., Glaister, R.P., and Nelson, H.W., 1979, Reservoir description of the Clearwater oil sand Cold Lake, Alberta, Canada, in: R.F. Meyer and C.T. Steele (eds): *The future of heavy crude oil and tar sands*, 264 - 279, McGraw-Hill.
- Harris, M.C. and Sobkowicz, J.C., 1977, Engineering behavior of oil sand: *The Oil sands of Canada - Venezuela*, CIM special volume, **17**, 270 - 280.
- Hickey, C., Eastwood, J., and Spanos, T.J.T., 1991, Seismic wave propagation in oil sands: *AOSTRA Journal of Research*, **7**, 67-81.
- Hwang, L.F., and McCorkindale, D., 1994, Troll field depth conversion using geostatistically derived average velocities: *The Leading Edge*, **13**, 262-269.
- Itto, H., DeVilbiss, J., and Nur, A., 1979, Compressional and shear waves in saturated

- rock during water-steam transition: *J. Geophys. Res.*, **84**, 4731-4735.
- Johnston, D.H., Toksoz, M.N., and Timur, A., 1979, Attenuation of seismic waves in dry and saturated rocks, Part II. Theoretical models and mechanisms: *Geophysics*, **44**, 691-711.
- Johnston, D.H., and Toksoz, M.N., 1980, Thermal cracking and amplitude dependent attenuation: *J. Geophys. Res.*, **85**, 937-942.
- Johnston, D.H., and Toksoz, M.N., 1980, Ultrasonic P and S wave attenuation in dry and saturated rocks under pressure: *J. Geophys. Res.*, **85**, 925-936.
- Johnston, D.H., and Toksoz, M.N., 1981, Seismic Wave Attenuation: Geophysics reprint series, No.2, Society of Exploration Geophysics.
- Jones, T.D., and Nur, A., 1983, Velocity and attenuation in sandstone at elevated temperatures and pressures: *Geophys. Res. Lett.*, **10**, 140-143.
- Justice, J.H., Vassiliou, A.A., Singh, S., Logel, J.D., Hall, B.R., Hutt, P.R., and Solanki, J.J., 1989, Acoustic tomography for monitoring enhanced oil recovery: *The Leading Edge*, **8**, 12-19.
- Kalantzis, F., Kanasewich, E.R., and Udey, N., 1993.a, 3-D seismic monitoring of thermal EOR processes, case study I: Initial results: presented at the CSEG National Convention, Calgary.
- Kalantzis, F., Kanasewich, E.R., Dai N., Kostykevich, A., and Udey, N., 1993.b, Imaging of reflection seismic wavefields in thermally enhanced oil recovery projects: 63rd Annual Intern. Meeting, Washington D.C., Soc. Expl. Geophys., Expanded Abstracts, 335- 338.
- Kalantzis, F., Kanasewich, E.R., Kostykevich, A., and Udey, N., 1994, Integrated time-lapse reservoir monitoring: Modeling and imaging: CSEG National Convention, Calgary, Expanded Abstracts, p. 122-123.
- Kendall, G.H., 1977, Importance of reservoir in evaluating in situ recovery methods for Cold Lake Heavy oil part I, Reservoir Description: *Journal of Canadian Petroleum Geology*, **16**, 41-47.
- King, M.S., 1966, Wave velocities in rocks as a function of changes in overburden pressure and pore fluid saturation: *Geophysics*, **31**, 50-73.
- Kjartansson, E., 1979, Constant Q-wave propagation and attenuation: *Journal of Geophysical Research*, **84**, 4737-4748.
- Lockner, D., Walsh, J.B., and Byerlee, J., 1977, Changes in seismic velocity and attenuation during deformation of granite: *J. Geophys. Res.*, **82**, 5374-5378.
- Lo, T.W., Coyner, K.B., and Toksoz, M.N., 1986, Experimental determination of elastic anisotropy of Berea sandstone, Chicopee shale, and Chelmsford granite: *Geophysics*, **51**, 164-171.
- Lynn, H.P., and Thomsen, L.A., 1986, Shear wave exploration along the principal axis: 56th Annual Intern. Meeting, Soc. Explor. Geophys., Expanded Abstracts, 473-476.

- Majer, E.L., and McEvilly, T.V., 1979, Seismological investigations at the Geysers geothermal field: *Geophysics*, **44**, 246-249.
- Makland, M., O'Regan, R., Dilay, A., and Eastwood, J., 1993, Pattern recognition: Theory and application to reservoir identification: 3rd Annual Intern. Meeting, Washington D.C., Soc. Expl. Geophys., Expanded Abstracts, 230-233.
- Martin, M.A., and Davis, T.L., 1987, Shear-wave birefringence: A new tool for evaluating fractured reservoirs: *The Leading Edge*, **6**, No. 10, 22-28.
- Mavko, G.M., and Nur, A., 1975, Melt squirt in the aesthenosphere: *J. Geophys. Res.*, **80**, 1444-1448.
- Mossop, G.D., Kramers, J.W., Flach, P.D., and Rottenfusser, B.A., 1979, Geology of Alberta's oil sands and heavy oil deposits, in: R.F. Meyer and C.T. Steele (eds): *The future of heavy crude oil and tar sands*, 197 - 207, McGraw-Hill.
- Murphy, W.F., III, 1982, Effect of microstructure and pore fluids on the acoustic properties of granular sedimentary materials: Ph.D. Thesis, Stanford University.
- Murphy, W.F., III, 1984, Acoustic measures of partial gas saturation in tight sandstones: *J. Geophys. Res.*, **89**, 11459-11559.
- Murphy, W.F., III, 1984, Sonic and ultrasonic velocities: theory versus experiment: *Geophysical Research Letters*, **12**, No.2, 85-88.
- Nur, A., and Simmons, G., 1969a, The effect of viscosity of a fluid phase on velocity in low porosity rocks: *Earth Planet. Sci. Lett.*, **7**, 99-108.
- Nur, A., and Simmons, G., 1969b, The effect of saturation on velocity in low porosity rocks: *Earth Planet. Sci. Lett.*, **7**, 183-193.
- Nur, A., and Simmons, G., 1969c, Stress-induced velocity anisotropy in rock: an experimental study: *J. Geophys. Res.*, **74**, 6667-6674.
- Nur, A., 1971, Effect of stress on velocity anisotropy in rocks with cracks: *J. Geophys. Res.*, **76**, 2022-2034.
- Nur, A., and Winkler, K., 1980, The role of friction and fluid flow in wave attenuation in rocks: *Geophysics*, **45**, 591-592.
- Nur, A., and Wang, Z., 1989, Seismic and acoustic velocities in reservoir rocks: Volume 1, Experimental Studies: *Geophysics* reprint series No.10, Society of Exploration Geophysicists.
- Nyland, E., and Dusseault, M.B., 1983, Fireflood microseismic monitoring; Results and potential for EOR process control, *Journal Canadian Petroleum Technol.*, **22**, 62-68.
- O'Connell, R.J., and Budiansky, B., 1974, Seismic velocities in dry and saturated cracked solids: *J. Geophys. Res.*, **79**, 5412-5426.
- O'Connell, R.J., and Budiansky, B., 1977, Viscoelastic properties of fluid saturated cracked solids: *J. Geophys. Res.*, **82**, 5719-5736.
- O'Connell, R.J., and Budiansky, B., 1978, Measures of dissipation in viscoelastic media: *Geophys. Res. Lett.*, **8**, 5-8.

- Ostrander, W.J., 1984, Plane wave reflection coefficients at gas sands at nonnormal angle of incidence: *Geophysics*, **49**, 1637-1648.
- O'Doherty, R.F., and Anstey, N.A., 1971, Reflections on amplitudes: *Geophys. Prosp.*, **19**, 430-458.
- Peselnick, L., and Outerbridge, W.F., 1961, Internal friction in shear and shear modulus of Solenhofen limestone over a frequency range of  $10^7$  cycles per second: *J. Geophys. Res.*, **66**, 581-588.
- Rai, C.S., and Hanson, K.E., 1988, Shear-wave velocity anisotropy in sedimentary rocks: A laboratory study: *Geophysics*, **53**, 800-806.
- Robertson, J.D., 1987, Carbonate porosity from S/P traveltimes ratios: *Geophysics*, **52**, 1346-1354.
- Savage, J., 1966, Thermoelastic attenuation of seismic waves by cracks: *J. Geophys. Res.*, **71**, 3929-3938.
- Schoenberger, M., and Levin, F.K., 1974, Apparent attenuation due to intrabed multiples: *Geophysics*, **39**, 278-291.
- Schultz, P.S., Ronen, S., Hattori, and Corbett, C., 1994a, Seismic-guided estimation of log properties, Part 1: A data-driven interpretation methodology: *The Leading Edge*, **13**, 305-310.
- Schultz, P.S., Ronen, S., Hattori, M., Mantran, P., and Corbett, C., 1994b, Seismic-guided estimation of log properties, Part 3: A controlled study: *The Leading Edge*, **13**, 770-776.
- Siewert, A.W., 1993, 3-D seismic monitoring of a steam stimulation process under frac pressures at the Iron River vertical well pilot, Cold Lake, Alberta: CSEG National Convention, Expanded Abstracts, 64-65.
- Spencer, J.W.Jr., 1981, Stress relaxations at low frequencies in fluid saturated rocks: attenuation and modulus dispersion: *J. Geophys. Res.*, **86**, 1803-1812.
- Spetzler, H., and Anderson, D.L., 1968, The effect of temperature and partial melting on velocity and attenuation in a simple binary system: *J. Geophys. Res.*, **73**, 6051-6060.
- Stewart, R.R., Huddleston, P.D., and Kan, T.K., 1984, Seismic versus sonic velocities: a vertical seismic profiling study, *Geophysics*, **49**, 1153-1168.
- Stoll, K.D., 1974, Acoustic waves in saturated sediments, in *Physics of sound in marine sediments*: L. Hampton, ed., New York, Lenum Press.
- Stoll, R.D., 1977, Acoustic waves in ocean sediments: *Geophysics*, **42**, 715-725.
- Timur, A., 1968, Velocity of compressional waves in porous media at permafrost temperatures: *Geophysics*, **33**, 584-595.
- Toksoz, M.N., Johnston, D.H., and Timur, A., 1979, Attenuation of seismic waves in dry and saturated rocks: I. Laboratory measurements: *Geophysics*, **44**, 681-690.

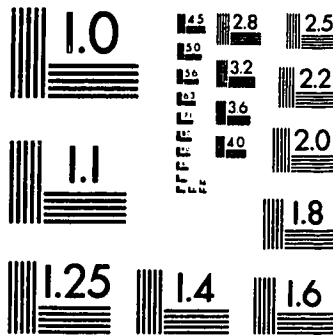


- Tosaya, C., Nur, A., Aronstam, P., and Da Prat, G., 1984, Monitoring of thermal EOR fronts by seismic methods: Presented at the 1984 Soc. Petr. Eng., Calif. Reg. Mtg.
- Tsingas, C., 1989, Seismic reflection imaging over a thermally enhanced oil recovery site: Ph.D. Thesis, University of Alberta.
- Tsingas, C., and Kanasevich, E.R., 1991, Seismic reflection amplitude versus angle variations over a thermally enhanced oil recovery site: *Geophysics*, **56**, 292-301.
- Walsh, J.B., 1966, Seismic wave attenuation in partially melted rock: *J. Geophys. Res.*, **71**, 2591-2599.
- Walsh, J.B., Brace, W.F., and Wawersik, W.R., 1970, Attenuation of stress waves in Cedar City quartz diorite: Air Force Weapons Lab. Tech. rep. No. AFWL-TR-70-8.
- Wang, Z., and Nur, A., 1985, Effects of pore fluid viscosity on the acoustical velocities in porous rocks: *J. Acoust. Soc. Am.*, **78** (S1), 32-33.
- Wang, Z., and Nur, A., 1986, Effect of temperature on wave velocities in sands and sandstones with heavy hydrocarbons: 56th Ann. Internat. Mtg., Soc. Explor. Geophys., Expanded Abstracts, 3-5.
- Wang, Z., and Nur, A., 1987, Wave velocities in hydrocarbons and hydrocarbon saturated rocks: 6th Ann. Internat. Mtg., Soc. Explor. Geophys., Expanded Abstracts, 1-5.
- Wang, Z., and Nur, A., 1988a, Velocity dispersion and the "local flow" mechanism in rocks: 58th Ann. Internat. Mtg., Soc. Explor. Geophys., Expanded Abstracts, 548-550.
- Wang, Z., and Nur, A., 1988b, Effect of different pore fluids on velocities in rocks: 58th Ann. Internat. Mtg., Soc. Explor. Geophys., Expanded Abstracts, 928-930.
- Wang, Z., and Nur, A., 1988c, Effect of temperature on wave velocities in rocks saturated with hydrocarbons: *SPE Reservoir Engineering*, **3**, 158-164.
- Wang, Z., and Nur, A., 1988d, Seismic wave velocities in tar sands: The basis for in-situ recovery monitoring: Proc. of the 4th Internat. Conf. on Heavy Crude and Tar Sands.
- Wang, Z., 1988, Wave velocities in hydrocarbons and hydrocarbon saturated rocks - with applications to EOR monitoring: Ph.D. Thesis, Stanford University.
- White, J.E., 1965, *Seismic waves: Radiation, transmission, and attenuation*: New York, McGraw-Hill Book Co. Inc.
- White, J.E., 1975, Computed seismic speeds and attenuation in rocks with partial gas saturation: *Geophysics*, **40**, 224-232.
- White, J.E., Mikhaylova, N.G., and Lyakhovitskiy, F.M., 1976, Low frequency seismic waves in fluid saturated layered rocks: *Phys. Solid Earth, Trans. Izv.*, **11**, 654-659.
- White, J.E., Martineau-Nicoletis, L., and Monash, C., 1983, Measured anisotropy in Pierre Shale: *Geophysical Prospecting*, **31**, 709-725.
- Winkler, K., and Nur, A., 1979, Pore fluids and seismic attenuation in rocks: *Geophys. Res. Lett.*, **6**, 1-4.

- Winkler, K., Nur, A., and Gladwin, M., 1979, Friction and seismic attenuation in rocks: *Nature*, **277**, 528-531.
- Winkler, K.W., 1983, Frequency dependent ultrasonic properties of high-porosity sandstones: *Journal of Geophysical Research*, **88**, No.B11, 9493-9499
- Winkler, K.W., 1985, Dispersion analysis of velocity and attenuation in berea sandstone: *Journal of Geophysical Research*, **90**, No. B8, 6793-6800.
- Winkler, K.W., 1986, Estimates of velocity dispersion between seismic and ultrasonic frequencies: *Geophysics*, **51**, 183-189.
- Wyllie, M.R.J., Gardner, G.H.F., and Gregory, A.R., 1962, Studies of elastic wave attenuation in porous media: *Geophysics*, **27**, 569-589.

3

PM-1 3½"x4" PHOTOGRAPHIC MICROCOPY TARGET  
NBS 1010a ANSI/ISO #2 EQUIVALENT



## CHAPTER 6

### SEISMIC MONITORING OF THERMALLY ENHANCED OIL RECOVERY PROCESSES AT COLD LAKE

#### 6.1 INTRODUCTION

Enormous reserves of bitumen or heavy oil are present in complex reservoirs in sands of Lower Cretaceous age in Alberta, Canada. This heavy oil or bitumen is a low gravity high viscosity oil, which under reservoir conditions, is immobile. Since only 7% of these deposits are accessible to surface mining, pilot studies are being carried out and production fields are being developed to recover the oil through *in-situ* methods. Most of these involve steam injection or fire flood methods to reduce the viscosity of the bitumen so it may be pumped to the surface. The movement of fluids away from the heated sources at the perforation level is controlled by permeability heterogeneities and even small heterogeneities or fracturing and the induced anisotropy can play an important role in the efficiency of the EOR process. Therefore, it is useful to image the shape, areal extent of the heated zone and determine the rate of movement of the thermal front.

In the enhanced recovery phase a number of processes such steam stimulation, steam drive, combustion (fire-flooding), CO<sub>2</sub> stimulation, can be used to initiate recovery in the case of heavy oil sands or increase recovery efficiency. Reservoir characterization is very important before starting an Enhanced Oil Recovery (EOR) project because of the possibility of failure due to reservoir heterogeneities and anisotropy. Also, reservoir surveillance during an EOR process is critical for the evaluation of the EOR efficiency. 3-D high resolution surface seismic and cross-well seismic data can be used for defining and monitoring EOR processes. Time-lapse seismic images can monitor reservoir changes that are induced during EOR processes when the observed seismic attribute changes are correlated to the reservoir conditions and properties. 3-D seismic surveys repeated over specified time intervals can be used to generate 4-D images (3-D plus calendar time) that can give valuable information regarding the management of EOR projects. With time-lapse seismic monitoring surveys the 3-D seismic data volume evolves continuously and as a result seismic interpretation and reservoir model become more detailed and sophisticated.

As Britton et al. (1983) reported, using a conventional seismic survey over a steam-flooded area, the seismic section clearly shows travel time delays and changes in wavelet shape around the steam injection well. Macrides et al. (1988), using seismic measurements before and after steam injection, showed that the waves that traveled through the steam zone are clearly delayed due to lower velocities and have significant changes in their seismic signature.

Greaves and Fulp (1987) used 3-D to monitor an *in-situ* combustion EOR process. The 3-D differential volumes that they produced between the three surveys (preburn, midburn and postburn), clearly, showed anomalies in association with the development of *bright spots* in the reflection from the reservoir and *dim spots* in the reflection just below the reservoir. Tsingas and Kanasewich (1991) performed amplitude versus angle analysis and using their ARPA displays showed the limits of a steam zone at Cold Lake.

Matthews (1992) used multiple 3-D seismic surveys to monitor a steam injection processes in tar sand reservoir. He performed pushdown analysis and velocity differencing and reported that the decrease in the seismic velocity exceeds 30 percent in some areas of the heated zone.

Paulson et al. (1992) used time-lapsed crosswell tomographic surveys to characterize a steamed oil reservoir in California. They concluded that seismic velocity depends on both reservoir temperature and the presence of gas. Also, they suggested that their resultant velocity tomograms could qualitatively represent cross-sections of oil saturation since the heat affects the amount of oil produced and the seismic velocities. Recently, Paulson et al. (1994) used again crosswell seismology to characterize an heavy oil reservoir in Alberta and evaluate the steamflood technology used for its recovery. They were able only to define the geology and detect the movement of heat. However, the velocity tomograms cannot be used for estimating actual temperatures since the velocity reduction does not depend only on temperature but also on other factors such as gas saturation.

Siewert (1993) has interpreted seismic monitoring data (base and steam-monitor) for changes in seismic travel times, attenuation and reflectivity. Also, he discussed rock and fluid effects of the steam stimulation process under frac pressures, at Mobil's pilot project at Cold Lake, which were observed on the seismic data and confirmed in triaxial core tests. Furthermore, he showed that reflection amplitude changes track reservoir pressure, with frac anomalies emanating from known well locations.

Recently, Eastwood et al. (1994) have analyzed and integrated data from two monitor 3-D seismic surface surveys obtained during production and steam cycles, crosswell data during production cycle, well log data (temperature and pressure), and data from thermal

reservoir simulations at Imperial Oil's Cold Lake oil sands. Similar anomalies (areal and volumetric conformance) associated with the thermal process were predicted from both seismic monitoring and reservoir simulations. Also, the spatial distribution of the anomalies on the seismic images were verified with the data from the observation wells. The crosswell tomograms on the other hand showed conclusively the presence of calcified tight streaks which impede vertical conformance growth from steam stimulation.

In the following, we are going to study two thermal EOR projects (Mobil Oil and Imperial Oil) in the oil sands at Cold Lake, Alberta, Canada. Some results of these studies were presented in a number of geophysical meetings by the author (Kalantzis et al., 1993a, 1993b, 1993c, 1994). These studies include 2-D and 3-D wave propagation simulations before and during the steam stimulation processes, and some processing and seismic attribute analysis of the 3-D seismic monitoring data. An extensive wave simulation is carried out in order to model wave propagation through the reservoir prior to any EOR process and during the steam injection and production cycles of the process. Both 2-D elastic and 3-D acoustic wave simulations are performed with the algorithms developed in Chapter 3. On both projects an analysis based of seismic differencing between surveys during different EOR cycles is carried out. In addition to analysing the data with the existing processing sequence as given to us by the oil companies, the data are normalized and migrated with the 3-D one pass poststack depth migration developed in Chapter 4. Then an extensive seismic attribute analysis is performed on the depth migrated data. Both the wave simulations and the seismic monitoring analysis are essential in order to understand the relation between reservoir changes such as pressure, temperature and saturation to seismic changes such as amplitude, time and frequency content. The resultant time-lapse seismic images may map the steam-heated zone, image changes in porosity and permeability, detect fractures and monitor gas caps.

## **6.2 U OF A PROCESSING AND ANALYSIS OF THE 3-D SEISMIC MONITORING SURVEYS**

### **6.2.1 Simulations of Seismic Wave Propagation at Cold Lake Oil Sands**

Computer simulations of seismic wave propagation were essential for the interpretation of field data. 2-D and 3-D finite difference modeling of seismic waves in acoustic and elastic media in the region over the steam-heated zone was performed in order to examine the relation between rock properties such as porosity, permeability and

saturation with seismic characteristics such as velocity, amplitude and frequency modification with time. The models used in these simulations were modified until a reasonable match was obtained between the field and synthetic data.

2-D elastic (P-SV) and 3-D acoustic wave simulations were carried out for very detailed multi-layer models. For the 2-D case, a P-wave line source with a Gaussian function as source of excitation with pick frequencies of 50, 65 and 100 Hz, was used to generate P-SV seismograms for vertical or horizontal components of particle velocity or stress components for multiple shot locations. Also, 3-D acoustic synthetic seismograms were generated using a point source of 100 Hz pick frequency. Synthetic shot gathers and zero offset sections for the pressure field or the particle velocity components are generated. Furthermore, snap shots of the propagating wavefield can be generated at no extra cost. For all simulations, the finite difference grid spacing was usually 1/4 of the bin size of the corresponding seismic grid. The sampling interval was 1 ms, however, the finite difference time step was 0.1 ms.

The common shot gathers can directly be compared with field shot gathers or after sorting into CMP gathers, NMO and stacking, the resultant stacked section can be migrated and compared to a field inline or crossline. Furthermore, zero offset sections were generated for computational efficiency which can directly compared to the real stacked sections since the layer structure of the velocity model in Cold Lake is relatively flat.

### **6.2.2 Energy Balancing**

The analysis of the 3-D seismic monitoring data is based on attribute differencing between the baseline (base: before any steam injection) and production and steam surveys (monitors: during production or steam injection) in order to image the anomalies associated with the changing conditions in the reservoir. Therefore, we would like the resultant time-lapse seismic images (attribute differences) to be associated with effects that are caused only by the EOR process. Although the surveys were recorded and processed in the same way, effects due to a number of factors other than the recovery process such as source conditions, changes in the weathering layer and water table may cause differences in the seismic character of the two surveys. In order to eliminate such effects the base and monitor surveys were energy balanced with respect to a specified time band.

A global trace balancing is applied on all 3-D monitor seismic data sets available as follows. One of the 3-D data volumes, the base or the first recorded monitor if no base is available, is used as a reference data set. On this data volume a time window about 100 ms

wide is selected. In this time window the reflections are consistent and continuous and are located well above the steam-heated reservoir. Then, the mean amplitude squared is computed from all traces in this data volume (base or first monitor) within the above window and from that the average per trace energy in this time band was defined. The result is a *global factor* calculated from the base (or first monitor if no base was recorded) 3-D data. Next for each trace in all data volumes (base and monitors), the sum of amplitudes squared within the same window was computed resulting in a *trace factor*. The ratio between the “global factor” and each “trace factor” results in a balancing factor (scaling factor) for that trace. This balancing factor is applied to all samples in the trace for all data sets. Consequently, both data sets have been normalized to a uniform amplitude energy. Therefore, differences between the base and the seismic monitors that may be due to differences in the source, water-table or any other effect not related to the EOR process should not be present anymore.

### 6.2.3 One-pass 3-D Depth Migration

Next, we depth migrate the energy balanced stacked base and monitor (production and/or steam) data volumes. For this we use the one-pass 3-D depth migration algorithm which was developed in Chapter 4. This is an one-pass depth migration algorithm in the frequency-space domain that solves a 65 degree approximation to the 3-D scalar wave equation. For the solution of the resulting differential equation we employ an implicit Crank-Nicolson finite difference scheme. Computer implementation of the one-pass 3-D depth migration uses an alternating direction implicit (ADI) method. The wave field is downward continued alternatively along the x and then y-direction for each depth step (extrapolation step). The algorithm is recursive where the result of the previous extrapolation step is input to the current extrapolation step. The migration result is obtained by applying the imaging condition summing the wave field over frequencies.

For the 3-D migration of all 3-D seismic monitoring data sets studied in this thesis we use a small extrapolation step of 1 m which yields images of high vertical resolution. Also, this algorithm can accommodate lateral velocity variations. Therefore, we can use high resolution velocity models that are generated from sonic logs, crosswell data and time-migrated sections. Furthermore, we can apply the depth migration in an iterative fashion, updating the velocity model until the required imaging quality is reached. All data sets from the same EOR project are migrated with the same velocity model in order to preserve the differences in amplitude and time/depth of reflectors within and below the steam-heated



reservoir. The migration was performed on 44 processors of a Myrias SPS3 parallel computer. The CPU time required for the migration (including I/O and FFT) of a data volume with 89 x 73 CDPs and 1501 time samples using 1500 depth steps and 500 frequencies was 14.3 hours.

#### **6.2.4 Seismic Attribute Analysis**

With time-lapse monitoring 3-D seismic surveys performed during the EOR process, the 3-D seismic information evolves continuously since the changing reservoir conditions are correlated to the seismic reflections recorded. Therefore, seismic interpretation and reservoir characterization can become more detailed and sophisticated with time. In order to do that we need to analyze all seismic attributes that correlate to changes occurring in the reservoir during the thermal process. A detailed analysis of the potential changes on these attributes and their correlations to the reservoir conditions and properties was presented in Chapter 5.

The seismic attributes can be analyzed separately for each seismic data volume (base or monitor). Also, they can correlate to corresponding attributes from other seismic surveys during the thermal process by differencing or taking the ratios of the resultant seismic images.

The 3-D seismic volume can be sliced into three orthogonal planes: the inlines and crosslines that are vertical sections and in time slices that are horizontal sections. Also, it can be sliced into any arbitrary orientation of the plane. A vertical profile shows all the seismic events as they occur in time or depth. On the other hand, a time or depth slice shows all seismic events for a particular travel time or depth. When a horizon is interpreted, the times or depths generated can provide the time or depth structure map and the amplitudes can provide the horizon slice. Differences between different horizons can provide isochrone or isopach maps. Also, differences between the time or depth structure maps of the same horizon from different monitor surveys can show time delays or apparent depth changes (pushdown) of the horizon that are caused due the velocity reduction in the steam heated zones of the reservoir during the thermal process.

When a velocity (acoustic impedance) interface is interpreted the amplitudes can provide a horizon slice. A horizon slice is a powerful product for studying reservoir properties. If colour is used it can show trends and patterns in the spatially varying amplitude. Hydrocarbon fluids and the presence of gas or steam reduce the acoustic impedance of the reservoir rocks and may produce a “bright spot” or an anomalously high

amplitude reflection. Also, reflections below the steam zone may have a reduced amplitude or “dim spot”. When the reservoir reflections have been identified, an attempt can be made to correlate them to reservoir properties. Also, a horizon slice within or below the steam heated reservoir can be differenced with the corresponding one from a later or prior monitor 3-D seismic survey over the same EOR site. The resulting difference map may show amplitude anomalies that are correlated to the reservoir changes occurring over the calendar time difference of the two surveys.

Reservoir reflections may show a “polarity reversal” (for example between a hydrocarbon zone and the water zone). Instantaneous frequency maps can also provide additional information about the changes occurring during the thermal process since spectral changes are observed during different phases of the recovery process (steam and production). Furthermore, other seismic attributes such as phase may provide information about the nature of seismically reflective horizons.

After processing the different data volumes with identical processing flows and the best available algorithms, colour is used to show trends and patterns (seismic anomalies) in the spatially varying seismic attribute. Ultimately, four dimensional high resolution seismic images may be generated when attributes are analysed in the three spatial dimensions and the calendar time of the continuing seismic monitoring.

In a interactive interpretation system such as the GeoQuest that we used in these studies, the selected seismic data display can be presented on a colour screen and the progressive results of our interpretation can be returned to the digital database.

### **6.3 SEISMIC MONITORING STUDIES AT IMPERIAL OIL'S D3 PAD**

#### **6.3.1 Cyclic Steam Stimulation recovery of the Cold Lake bitumen.**

The method of recovery at the Cold Lake oil sands used by Esso Resources (Imperial Oil) is cyclic steam stimulation. Since 1985, Imperial oil commercially has produced bitumen from the Clearwater oil sands reservoir at Cold Lake, Alberta, Canada. Currently, there are more than 2000 wells that are spaced on a regular 1.6 hectares grid that produce over 100,000 b/d of bitumen.

The Clearwater is the best reservoir unit at Cold Lake with high oil saturations and thick, relatively homogeneous sections. The entire Clearwater section is oil-bearing and free of underlying water when favorably structured. This unit contains more than 50% of the Cold Lake area bitumen and the areas where no underlying water is present are of

current interest. The Clearwater reservoir consists of unconsolidated sands with an average porosity of 32 % and permeability of about 1 darcy. The sands are saturated with bitumen that has a very high viscosity (about 150,000 cp). Fluid distributions are structurally controlled. On high trends, the oil leg can attain a thickness of 45 m, with no underlying water. Although there is no underlying water section on the crest of fractures, there may be an aquifer present on the flanks. Generally, the Clearwater reservoir has an excellent horizontal continuity. However, the vertical continuity is occasionally interrupted by discontinuous shale barriers, tight cemented siltstones and calcified tight streaks that can affect the vertical conformance of the steam stimulation.

According to the Cyclic Steam Stimulation (CSS) method, steam is injected into a well at high temperature (310 °C) and pressure (10 MPa) and at the highest possible rate (up to 240 m<sup>3</sup>/d), in order to minimize heat losses, for several weeks (for 40 to 90 days). The injected steam heats the rock and the fluids around the wellbore. Vertical inhomogeneities such as shale barriers, cause only partial vertical sweep while maintaining a radial advance of the fluids in the zone that is contacted. After injecting the desired volume of steam, the well may be shut in for about two weeks. This is called the *soak* period. Finally production takes place from the same wellbore. Twenty wells are directionally drilled from a single surface area or pad. Figure 6.3.1 shows the bottom hole locations at the reservoir level of 15 wells from the D-3 pad. The wells are then produced back at total fluid rates of approximately 90m<sup>3</sup>/d. In the present study the steam was injected at a depth of approximately 450 m in the Clearwater formation near Cold Lake, Alberta. It is a mature steam zone since steam injection started in 1985, and continued since then with on and off injection periods. Continued cyclic steam stimulation in this manner for 9 to 12 cycles is predicted to result in 20% recovery.

### 6.3.2 3-D Seismic Monitoring Reflection Surveys

In 1990, Esso initiated a 3-D high resolution seismic reflection program over a D3 pad undergoing CSS (Cyclic Steam Stimulation) in Cold Lake area of Alberta, Canada. The first survey was carried out in April of 1990 during the 6th production cycle and the second survey was carried out in January of 1992 during the 8th steam injection cycle. During the production cycle, reservoir conditions are at the local minimum in terms of temperature and pressure and there is high gas saturation in the vicinity of the wellbore. On the other hand, during the steam cycle, reservoir conditions are the local maximum in terms of temperature and pressure and there is small gas saturation in the vicinity of the wellbore.

Both surveys were centered on well D3-08 and included 15 from the total 20 injector/producer wells on the pad and 5 observation wells (Figure 6.3.1). The near well spacing (E-W) is 96 m and the far well spacing (N-S) is 167 m. For both experiments the field acquisition geometry was identical.

Each survey consisted of 296 geophones, buried 10 m below the surface in effort to improve the frequency content of the seismic signal, minimize statistical noise variations due to the weathering layer and eliminate subsequent survey difference caused by seasonal variations. Also, each survey consisted of 215 shot points buried at 18 m depth below the surface. The type of energy source was dynamite with 125 g per shot. The field data sample rate was 1 ms. After stacking the data, each survey consisted of 89 inlines and 73 crosslines with bin size of 8x8 m. However, in our analysis we used an area (504 x 504 m) centered around the central D3-8 well that included 64 inlines (from inline 15 to inline 78) and 64 crosslines (from CDP 6 to CDP 69). The average fold of the data in the area of study is about 20. Unfortunately, a base survey (prior any steam injection) that could provide us with a reference data set does not exist since the D3-pad is undergoing cyclic steam stimulation from 1985.

Also, crosswell seismic experiments were performed during the 6th production cycle (1990) between the observation wells. However, in this study we do not analyze the crosswell data, we just use the velocity tomograms generated by Imperial Oil for elastic wave modeling purposes. In the Clearwater reservoir area (about 450 m depth) the tomograms have a vertical resolution of 5 m and a horizontal resolution of 15 m.

Imperial Oil provided us digital copies of the field data, the stacked data and their migrated data, paper copies of the migrated data, digital copies of the velocity tomograms, sonic and density logs, and a 3-D geostatistical slowness model generated from sonic logs prior to the cyclic steam stimulation.

### **6.3.3 Seismic Wave Simulations during Thermal EOR Processes**

2-D and 3-D realistic simulations of seismic wave propagation were performed over the D3-pad in order to understand the changes in the seismic signature during the EOR process. A density model was generated from density logs. Also, a number of velocity models were used that were generated from sonic logs, a 3-D GEOSSET model, crosswell data, and depth migrated seismic data. Furthermore, velocity models were used that included steam zones. An attempt was made to generate synthetic data that resemble seismic monitoring data before and during the EOR process (base, steam, production).

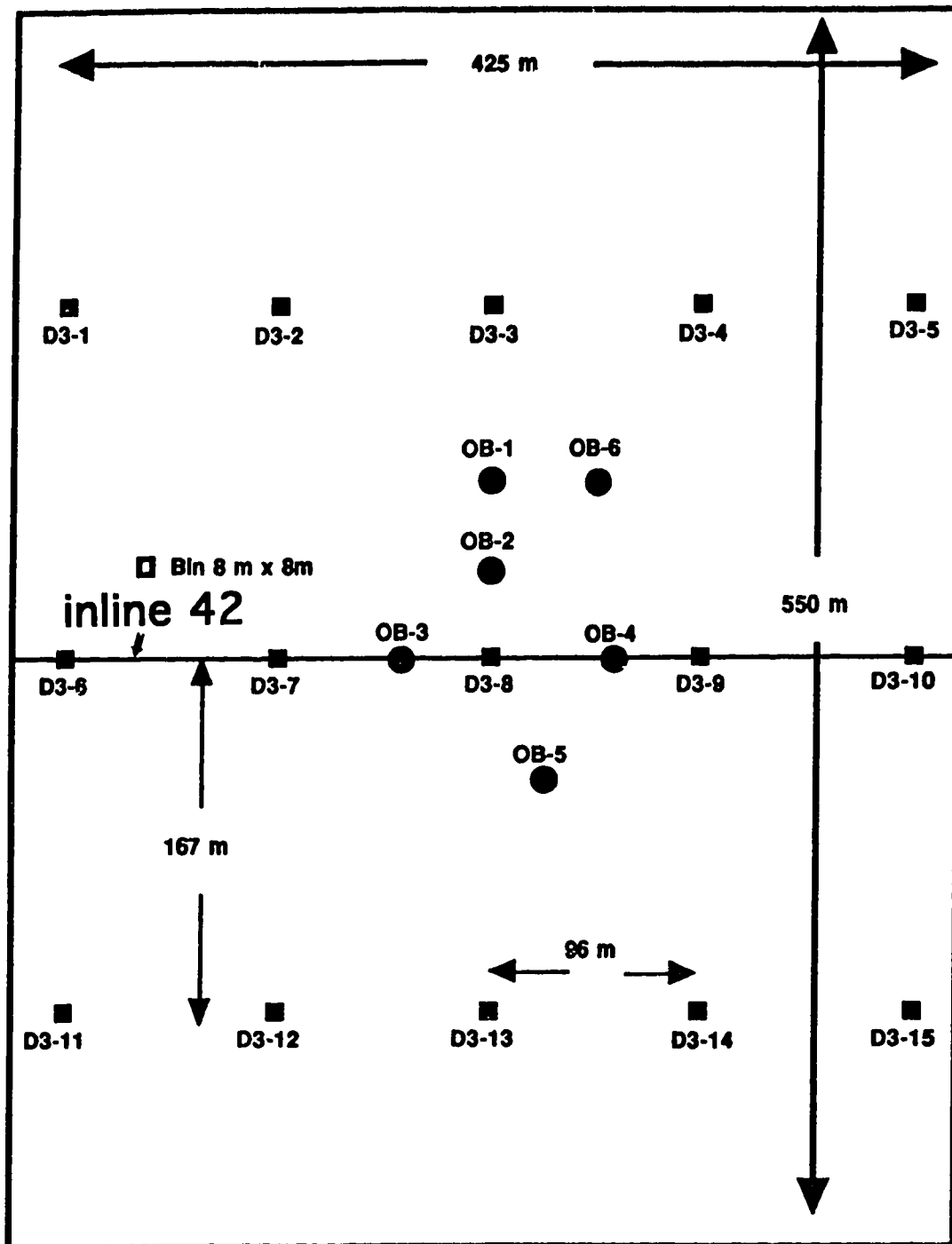


Figure 6.3.1: The site map of the Imperial Oil's D-3 pad (under CSS) at Cold Lake, shows the location of the producer/injection wells (D3-1 to D3-15) at reservoir depth level, the observation wells (OB-1 to OB-6) and the inline 42 of the seismic grid (8x8 m bins).

## ELASTIC WAVE SIMULATIONS WITH THE BASIC ESSO VELOCITY MODEL

A 3-D basic velocity model for the Esso D3 pad was generated using all the available sonic logs (velocity reduced by 10 %) and some depth migrated lines. This model was used for simulations prior to any steaming (base). In this model, we also incorporated steam zones in the location of each injection well. The steam zone was set 70 m wide and 25 m thick with 400 m/s velocity reduction. A vertical profile along inline 42 of the seismic grid from the basic model including a steam zone at the central well of the pad (D3-8) is shown in Figure 6.3.2.

2-D elastic modeling was performed along inline 42 using the basic model with and without steam zone. Using a Gaussian line source with a central frequency of 100 Hz, P-SV seismograms for the vertical component of the particle velocity were generated. In this study all generated synthetic shot gathers, zero-offset sections and stack sections have a trace spacing of 8 m. The synthetic zero-offset sections for the models with and without the steam zone are shown in Figure 6.3.3. The synthetic shot gathers for the models without and with steam zone are shown in Figure 6.3.4. The shot gather after steam injection shows reflections and diffractions from the steam zone. The amplitude of the reflector at the top of the steam zone is stronger since the bitumen has been replaced by steam. The amplitude of the Devonian reflector below the steam zone (at about 500 ms) is dimmed. Also, time delays are observed below the low velocity steam zone.

The amplitude spectrums of the shot gathers with and without steam zone were generated for various time windows. The spectrums are identical only for the time window 0 to 400 ms which is above the steam zone, but for the time window 400 to 500 ms and below are different for the two shot gathers. The spectral analysis of the synthetic shot gathers shows that the velocity changes due the steam injection cause frequency modification in the steam effected area and below.

## ACOUSTIC AND ELASTIC WAVE SIMULATIONS WITH THE 3-D GEOSSET MODEL

The GEOSSET model contains detailed 3-D slowness for the Clearwater formation and is referenced to an easting/northing coordinate system. The coordinates of the model were translated to the coordinates of the centre of the seismic grid. Also, they were rotated to align with the seismic grid (inline/crossline direction). Furthermore, the slowness was inverted to velocity. The depth of this model extends from 357 m to 526 m and is shown in Figure 6.3.5, notice the high velocity tight streaks cutting through the Clearwater reservoir.

For modeling purposes the velocity values were reduced by 10% (the model was generated from sonic velocities prior to CSS) and all velocities above 3000 m/s were filtered out. Then, the resultant velocity model was superimposed on the 3-D basic model developed earlier in order to have a velocity model that extends from the surface to depth of 1400 m.

From the 3-D modified GEOSET model (including above and below the basic model) we extracted a 2-D velocity model along the inline 42 direction (Figure 6.3.6.a). Elastic wave simulations were performed using this model, thus simulating a seismic base (no steam) shooting. A P-SV (vertical particle velocity) synthetic shot gather is shown in Figure 6.3.7.a. The source (65 Hz) is located at 288 m along the inline 42. We generated five synthetic common-shot gathers which after NMO and stacking resulted to the stack section. This section after applying AGC is a very realistic section (Figure 6.3.7.b) and comparable to the real data. Also, the synthetic seismograms show that tight streaks within Clearwater are detectable.

In order to simulate wave propagation during steaming, a steam zone with 70 x 25 m dimensions and 400 m/s velocity reduction was incorporated in the geoset velocity model (Figure 6.3.6.b). Then, elastic modeling was performed on the geoset model, with and without the steam zone, using a source of 100 Hz pick frequency. Portions of the zero offset sections in the vicinity of the the D3-8 well are shown in Figure 6.3.8. Both sections are the same above the reservoir but differ within and below the reservoir. For example, the positive event at about 0.44 s has higher amplitude in the monitor-steam section. Thus, indicating an amplitude increase (“bright spot”) at top of the steam zone. Also, the events within the reservoir (0.45 to 0.5 s) are different: in the two sections. Furthermore, the amplitude of the positive event at 0.52 s (top of the Devonian) is decreased (“dim spot”) on the monitor-steam section in comparison to the one on the base section.

Furthermore, a first attempt of 3-D acoustic modeling was undertaken using the 3-D modified GEOSET velocity model and a point source with central frequency of 100 Hz. A 224 x 288 m area of the model was used that was centered around the D3-8 well (Figure 6.3.1) and corresponded to 29 x 37 bins on the seismic grid (crossline 23 to 51, inline 28 to 64). Figure 6.9.a shows a vertical profile of the 3-D zero offset seismogram (vertical particle velocity component) which is along the inline 42 of the seismic grid (Figure 6.3.1). The trace spacing is 8 m and the positions of the traces correspond to the CDPs of the inline 42. The sampling interval of the data is 1 ms.

Also, the generated 3-D zero offset data set was depth migrated using 3-D reverse time migration developed in Chapter 4. The same portion of the depth migrated data as for the time section is shown in Figure 6.3.9.b. The sampling interval is 2 m. We can easily

observe the Grand rapids tight streak (at about 400 m), the top of the Clearwater formation (at about 420 m), two major calcified tight streaks in the Clearwater (at about 435 m and 450 m), the bottom of the Clearwater (at about 480 m), and the top of the Devonian (at about 550 m).

Both the 3-D acoustic modeling and migration images were generated with high resolution. This suggests that the potential of the 3-D acoustic modeling and migration algorithms developed in this thesis is high, since they can generate high quality seismic images before and during the cyclic steam stimulation which can help in the characterization of the reservoir as it evolves with time during the thermal process.

### ELASTIC WAVE SIMULATIONS WITH CROSSWELL VELOCITY TOMOGRAMS

The crosswell velocity tomogram generated from the crosswell experiment between OB3 and OB4 observation wells during the 6th production cycle was used for elastic modeling. A portion of the velocity tomogram corresponding to depths of 356 to 525 m was superimposed on the basic model in order to have a whole model that extends from the surface to 1400 m. This “basic + tomogram” velocity model (Figure 6.3.10.a) was used for elastic modeling of wave propagation during production since the tomogram was obtained from the crosswell experiment during the 6th production cycle.

In Figure 6.3.10.a we can observe a small velocity zone between 450 and 475 m which is associated with the steam-heated area around well D3-8. However, crosswell experiments were not performed during the steam cycle. Thus, in order to simulate steam injection during the 8th steam cycle, in this model (Figure 6.3.10.a) a wider steam zone was incorporated with dimensions of 75 x 25 m and velocity reduction of 400 m/s. The resultant velocity model for the steam cycle is shown in Figure 6.3.10.b.

Elastic modeling was performed using both velocity models (Figure 6.3.10). Synthetic zero offset sections are shown in Figure 6.3.11. The positive reflection event at about 0.44 s has an increased amplitude (bright spot) during the steam cycle and is associated with the top of the steam zone. On the other hand, the reflection character between 0.45 and 0.5 s is different in the two sections (Figure 6.3.11.a - production cycle and Figure 6.3.11.b - steam cycle). Also, the positive reflection event from the top of the Devonian at 0.52 s is reduced in amplitude (dim spot) during steam cycle.

*(Text continued on page 197)*



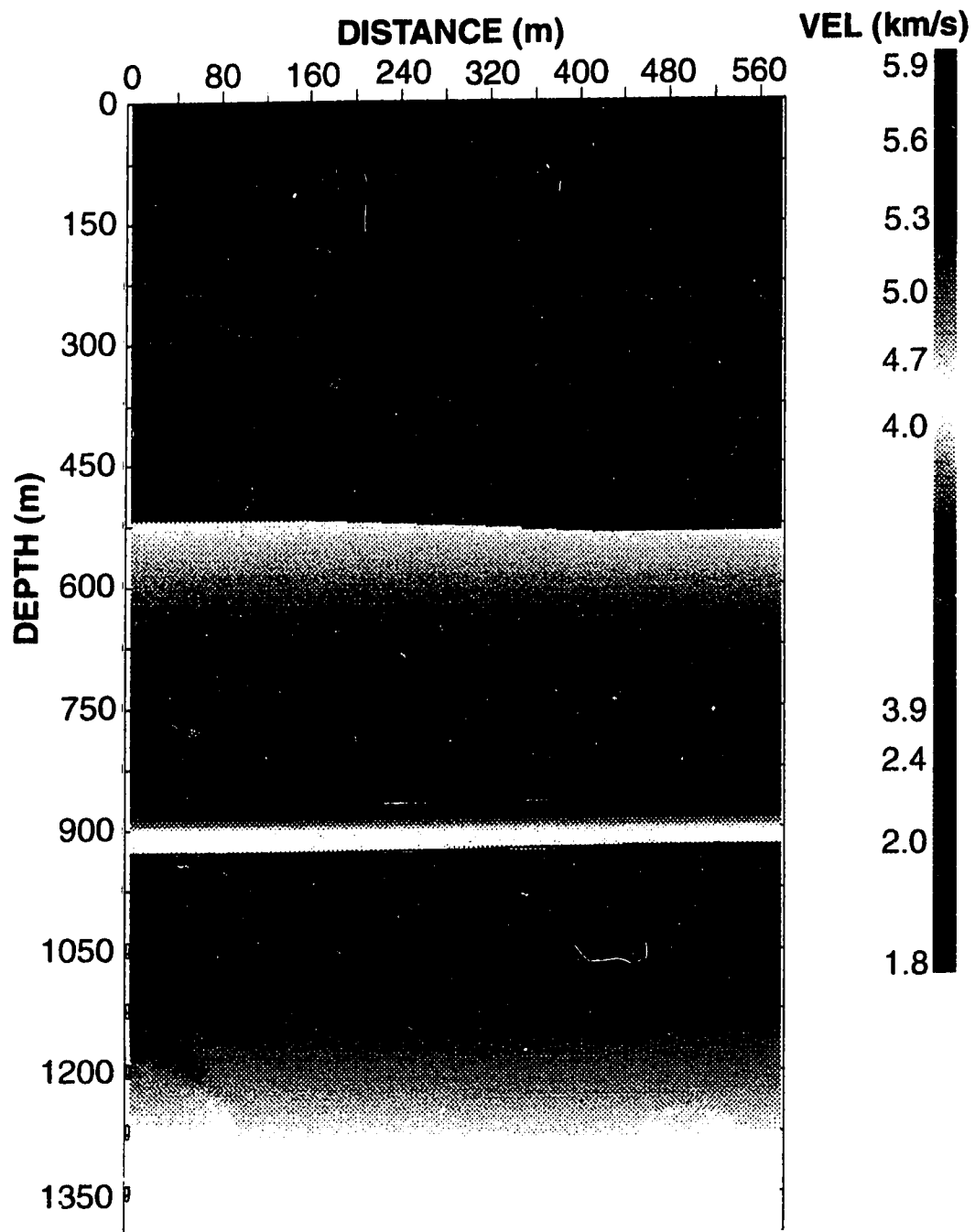


Figure 6.3.2: The basic velocity model used for 2-D elastic wave propagation simulations before steaming (no steam zone) and during steaming (with the steam zone) at Imperial Oil's D3-pad at Cold Lake, Alberta.

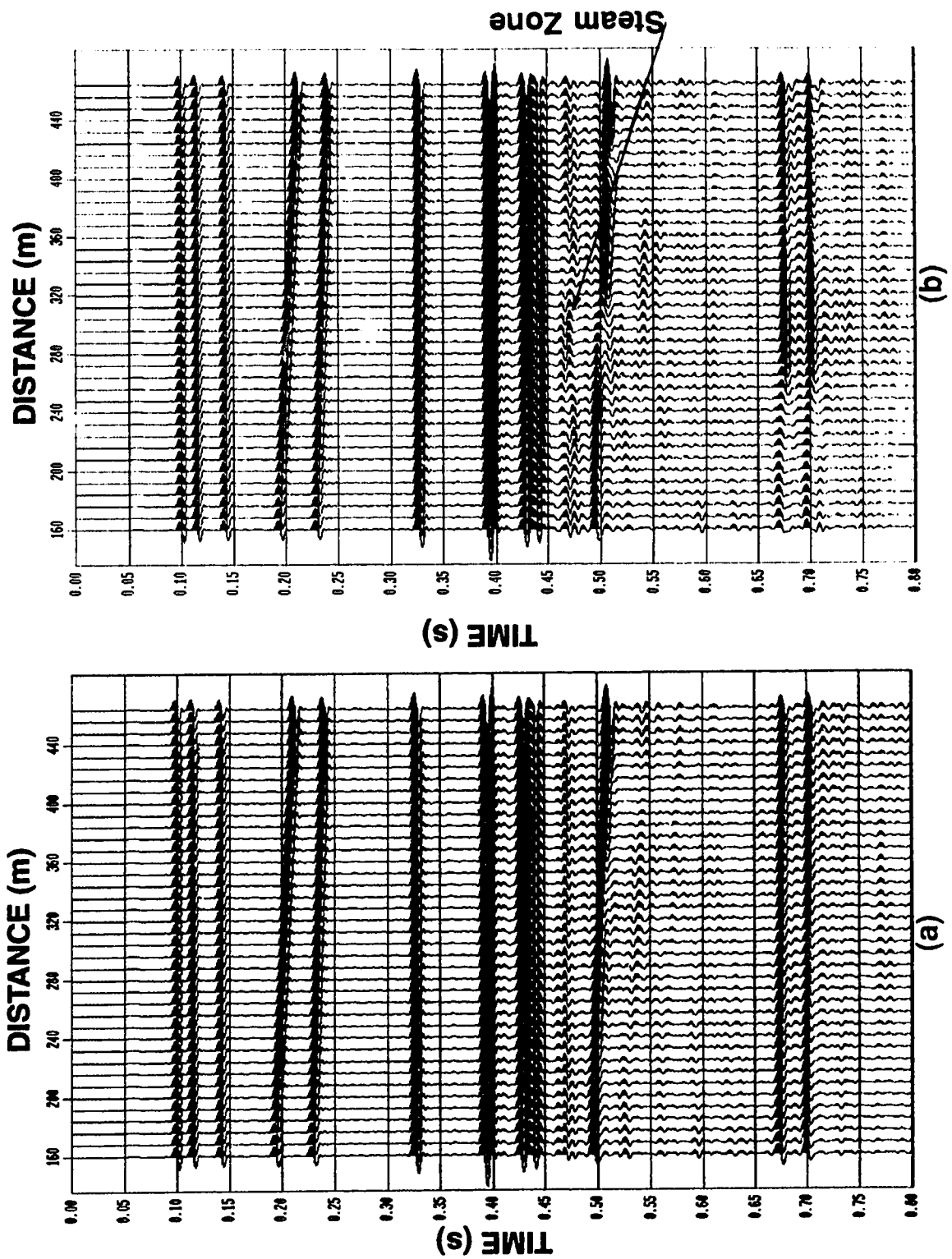


Figure 6.3.3: Synthetic zero offset sections (vertical particle velocity component) from 2-D elastic wave propagation simulations for the model (Figure 6.3.2) without (a) and with (b) the steam zone.

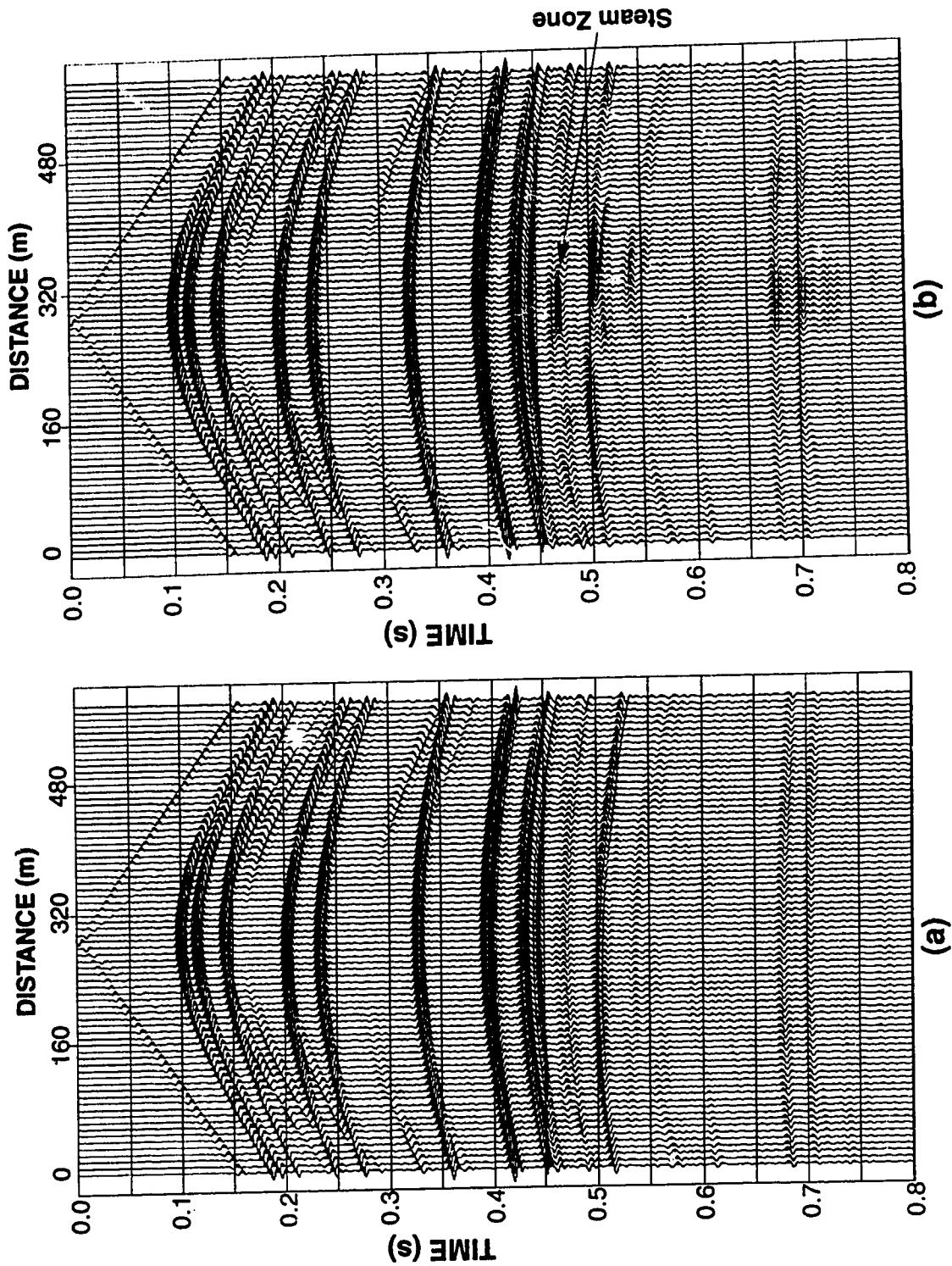


Figure 6.3.4: Synthetic shot gathers (vertical particle velocity component) from 2-D elastic wave propagation simulations for the model (Figure 6.3.2) without (a) and with (b) the steam zone.

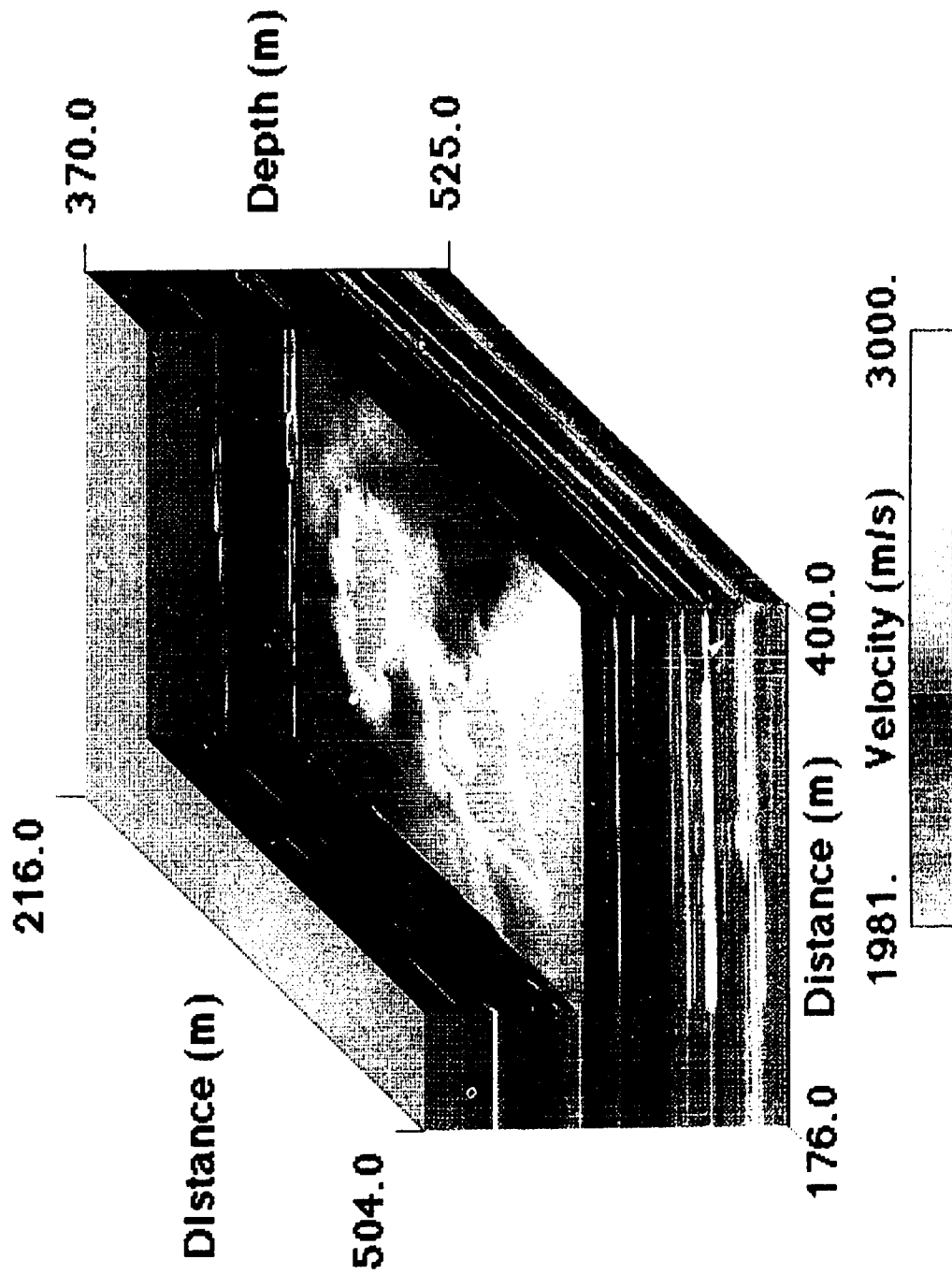


Figure 6.3.5: The 3-D GEOSSET model from Imperial Oil's D3-pad at Cold Lake, Alberta.

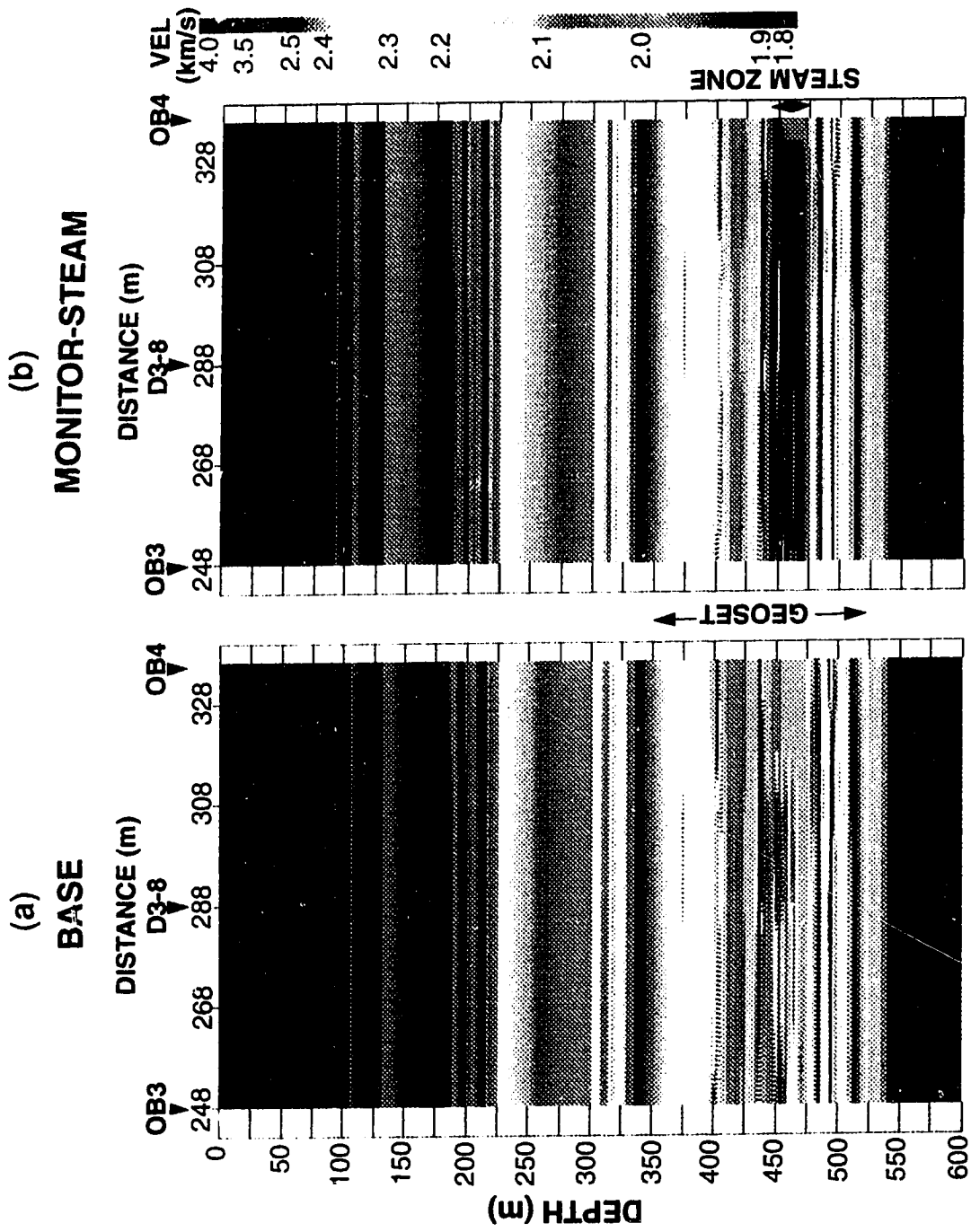
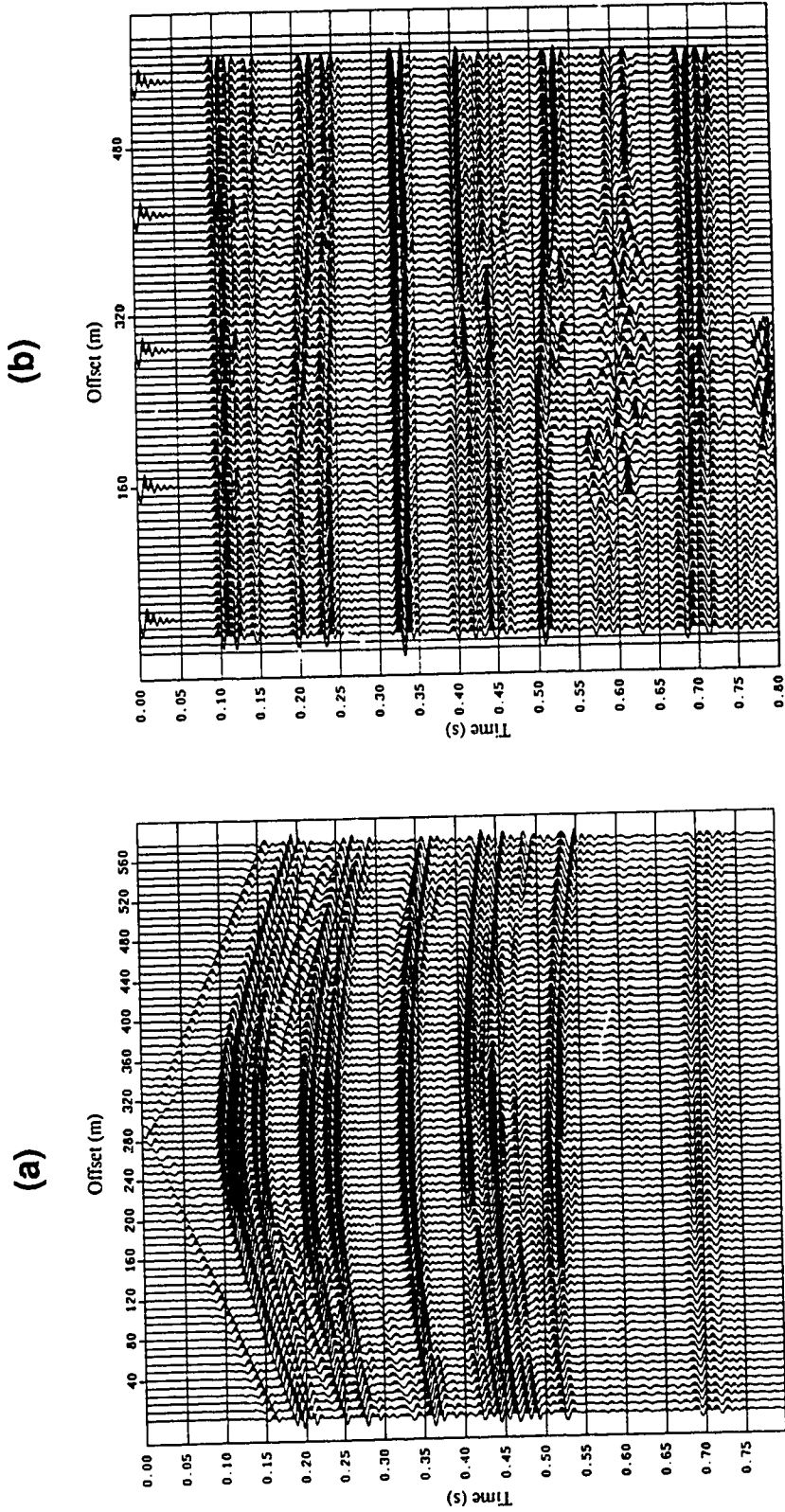
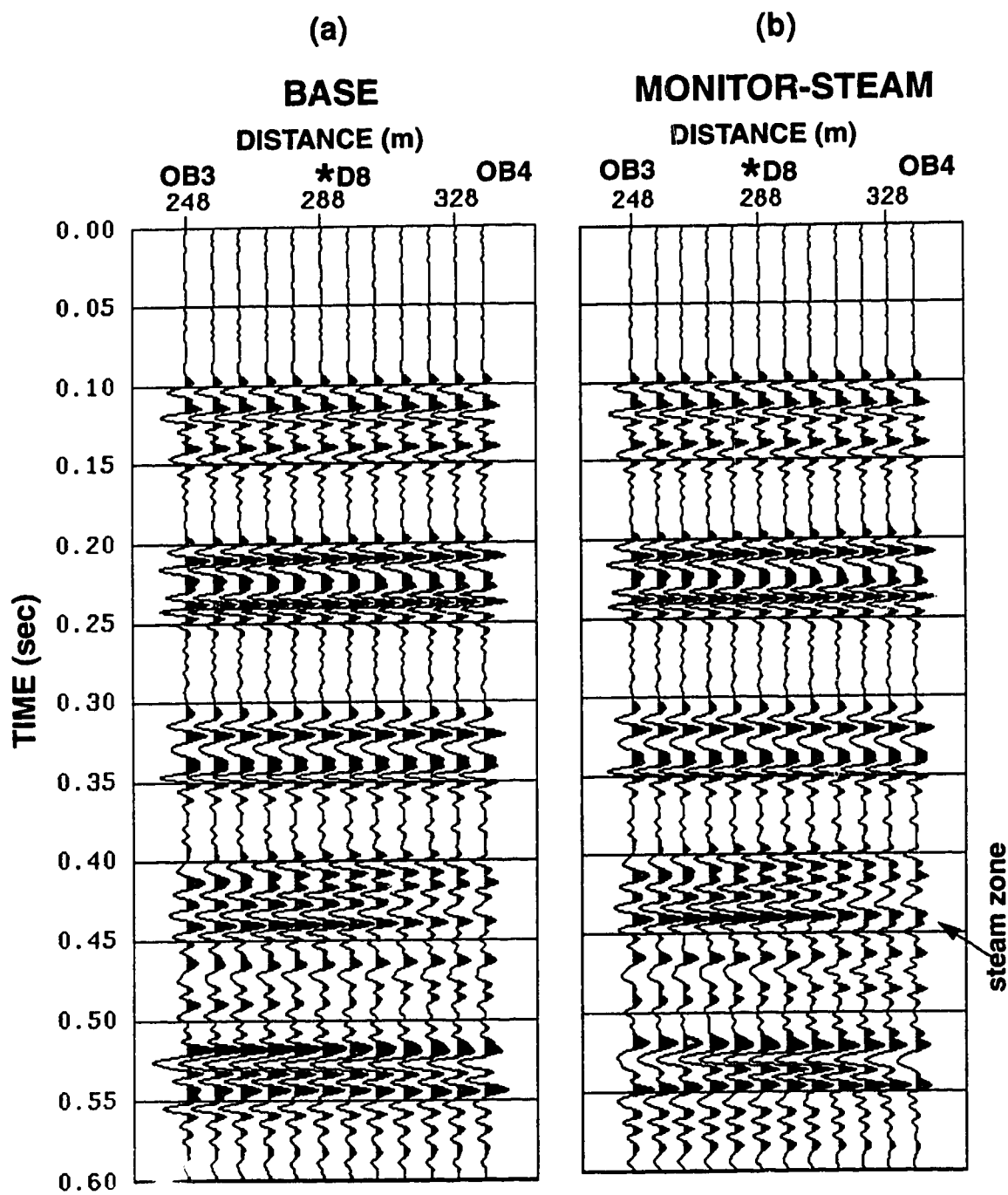


Figure 6.3.6: 2-D velocity models based on the basic model (Figure 6.3.2 with no steam zone) and the GEOSET model (Figure 6.3.5): (a) without steam zone (base model) and (b) with a steam zone (monitor-steam model).



**Figure 6.3.7:** 2-D elastic wave simulations for the base model (Figure 6.3.6.a): (a) shot gather and (b) stacked section.



**Figure 6.3.8:** Zero offset sections from elastic wave simulations for the models in Figure 6.3.6: (a) without a steam zone (base) and (b) with a steam zone (monitor-steam).

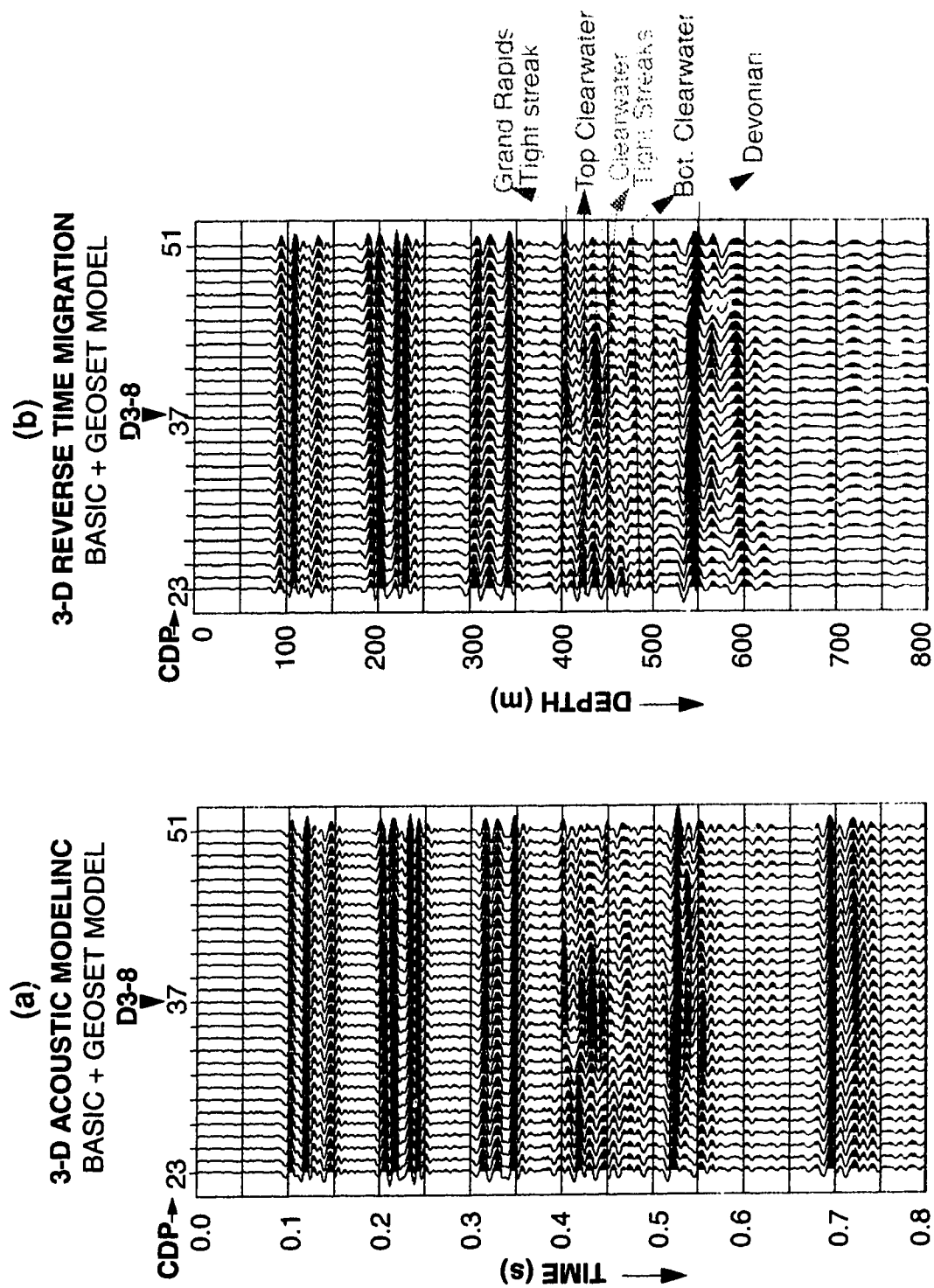


**Figure 6.3.9:** (a) Inline 42 of the 3-D synthetic zero offset section from 3-D acoustic wave propagation simulations for the modified 3-D GEOSET model; (b) the depth migrated section (inline 42) after 3-D poststack reverse time migration.



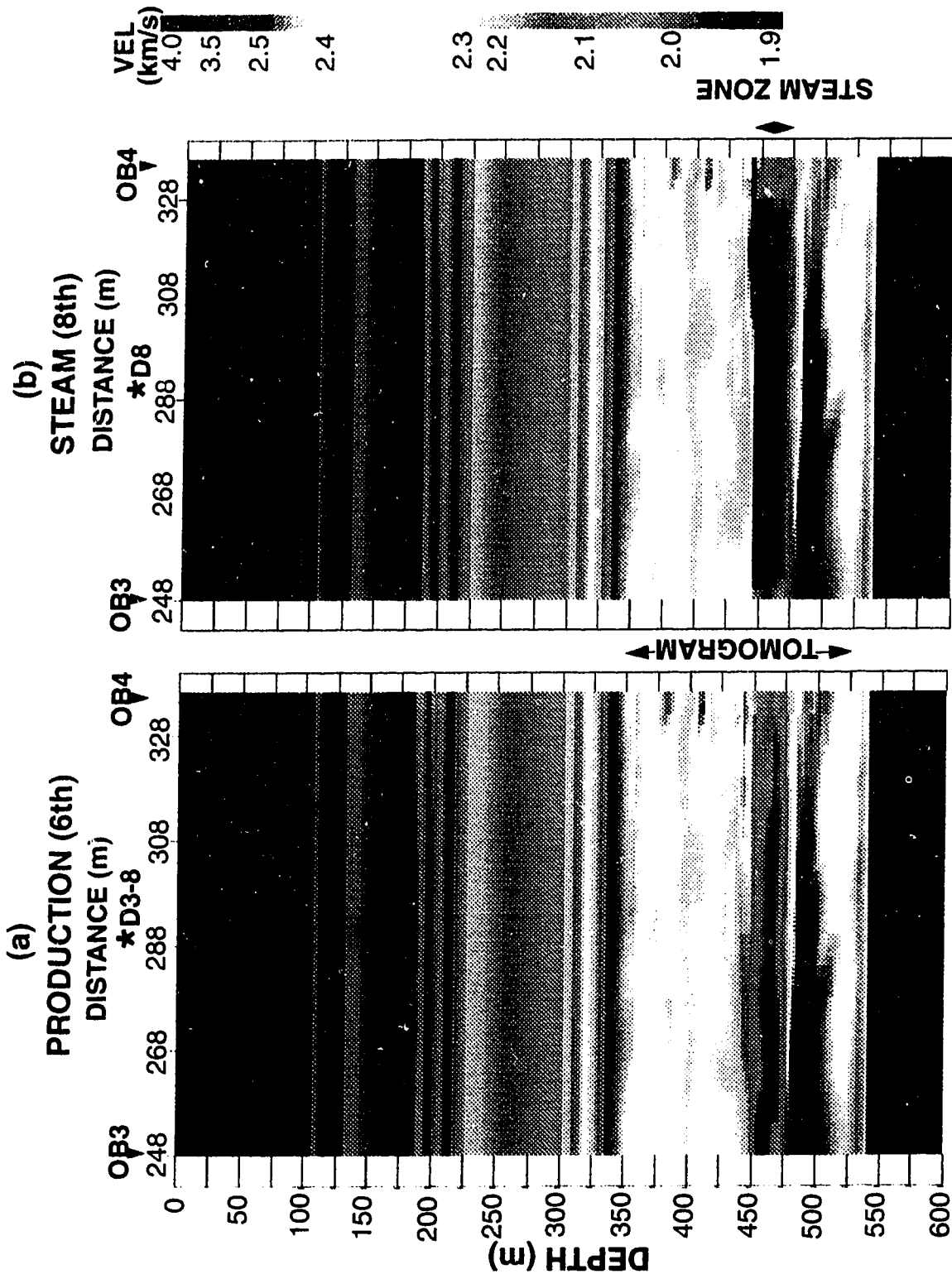
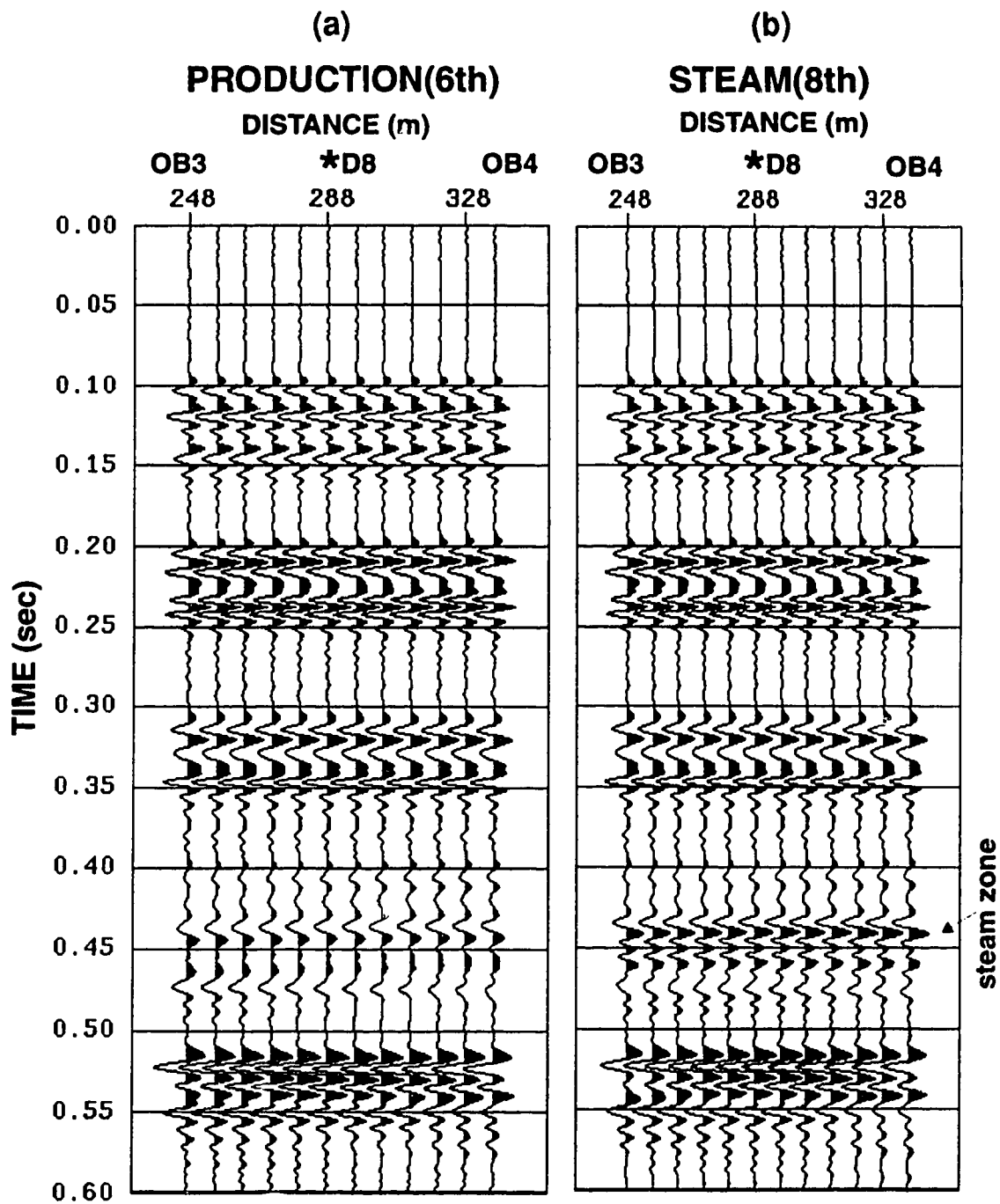


Figure 6.3.10: Velocity models based on (a) a crosswell velocity tomogram and (b) additionally a steam zone, and used for 2-D elastic wave simulations during production (1990) and steam (1992) cycles.



**Figure 6.3.11:** Synthetic zero offset sections (vertical particle velocity component) from 2-D elastic wave simulations for the models in Figure 6.3.10 during the 6th production cycle (a) and the 8th steam cycle (b).

### 6.3.4 Processing of the 3-D Reflection Surface Seismic Monitoring Data

Both seismic data volumes were processed by Imperial Oil with same processing flow which consisted of geometric spreading correction, first break mute, Q compensation, surface consistent deconvolution, CDP sort, velocity and statics analysis, 3-D NMO, residual statics, stack, f-k 3-D migration (single pass), and zero phase filtering (Figure 6.3.12).

On the other hand, our own processing involved energy balancing and one-pass 3-D depth migration of both production and steam data volumes (Figure 6.3.12). The stacked and time migrated data volumes were energy balanced. Furthermore, 3-D depth migration of both energy balanced stacked data volumes was performed in order to generate seismic images with higher spatial and vertical resolution. Also, since we depth migrate the data the resultant seismic sections are in depth thus avoiding time to depth conversions and making easier the interpretation process.

#### ENERGY BALANCING OF THE STACK AND TIME MIGRATED DATA

A global trace balancing was applied on both stacked and time migrated data sets (1990 and 1992) and was calculated as described in section 6.2.2. From the 3-D data volume (stacked or migrated) during the production cycle (1990) a time window between 230 sec and 360 sec was selected. The reason for the selection of this time window is that within this interval the reflections are consistent and continuous and are located well above the steam-heated zone in the Clearwater formation. A *global factor* was calculated from the production (1990) data. Next for each trace in both data volumes (1990 and 1992), a *trace factor* was computed. The ratio between the “global factor” and each “trace factor” results in a balancing factor (scaling factor) for that trace. This balancing factor was applied to all samples in the trace for both data sets. Consequently, both data sets (stacked or time migrated) have been normalized to a uniform amplitude energy. After the above process we have energy balanced stacked and time migrated data volumes for both production and steam surveys.

#### 3-D DEPTH MIGRATION OF THE ENERGY BALANCED STACKED DATA

Next, we depth migrated the energy balanced stacked data volumes (production 1990 and steam 1992). For this we used the one-pass 3-D depth migration algorithm which was

developed in Chapter 4. For the 3-D depth migration of both data sets (1990 and 1992) we used a small extrapolation step of 1 m that results migrated images of high vertical resolution. Also, we used high resolution velocity models by integrating sonic logs, time migrated sections and the 3-D GEOSSET model. Both data sets were migrated using the same velocity model in order to preserve the differences in amplitude and time/depth of reflectors within and below the steam-heated reservoir. The migration was performed on 44 processors of a Myrias SPS3 parallel computer. The CPU time required for the migration (including I/O and FFT) of each data volume (89x73 CDPs and 1501 time samples) using 1500 depth steps and 250 frequencies was 7.4 hours.

### **6.3.5 Seismic Attribute Analysis of the Time and Depth Migrated Data**

We performed seismic attribute analysis after applying additional processing in two different ways. In the first, we normalized (energy balanced) the two monitors after Esso's time migration. In the second, we normalized both stacked monitor data volumes and then applied our own 3-D depth migration. Therefore, we can generate a set of images after time migration and normalization, and another set of images after stacking, normalization and 3-D depth migration.

#### **ATTRIBUTE ANALYSIS OF THE NORMALIZED TIME MIGRATED DATA**

We performed seismic attribute analysis on both normalized time migrated data sets in a 64 x 64 bin area that is defined from inline 15 to inline 78 (inline[15,78]) and CDP 6 to CDP 69 (crossline[6,69]).

Figures 6.3.13 shows inlines 42 (vertical profiles) from both data volumes (1990 and 1992). Significant changes can be observed between the 1990 (production) and 1992 (steam) profiles in the amplitude and travel-time of the reflectors within and below the steam-heated zone in the Clearwater formation (about 450 m depth). Also, significant differences in the amplitude of the seismic reflection events are observed between time slices from both data volumes cutting through the reservoir.

The positive reflection event which corresponds to the top of the Devonian was picked for both data volumes. From the interpreted Devonian horizon the amplitude difference between the two surveys was taken. Figure 6.3.14.a shows the amplitude difference of the Devonian horizon between production (1990) and steam (1992). The amplitude of the Devonian is significantly decreased during the steam cycle. Again, the

main amplitude decrease (“dim spot”) is located in the area between the two upper rows of wells. Furthermore, the ratio of the Devonian amplitude maps between production’90 and steam’92 was taken. Again, the main amplitude anomaly, where the Devonian amplitude is larger for the production data and dimmed during the 1992 steaming, is located between the two upper rows of wells.

Isochrone maps were generated for the Devonian (production and steam) with respect to the Grand Rapids tight streak at about 400 ms which is nearly identical for both surveys. Then, the above isochrone maps were differenced. Figure 6.14.b shows the time delay (pushdown) of the Devonian horizon during the steam cycle (1992) with respect to the same horizon during the production cycle (1990). The main time anomaly is located between the two upper rows of wells (D3-1 to D3-4 and D3-6 to D3-9) shown on the same figure.

#### ATTRIBUTE ANALYSIS OF THE DEPTH MIGRATED DATA

The analysis of both depth migrated data sets is performed over a 64 x 64 bin area that extends between inline 15 to 78 and cross-line 6 to 69.

Figures 6.3.15 shows inline 42 (depth profile) from both production (1990) and steam (1992) depth migrated data volumes (compare with the time migrated data of Figure 6.14). On the other hand, Figure 6.3.16 shows the crossline 37 from both depth migrated surveys. On all profiles, the reflectors in the area of the steam-heated reservoir (Clearwater) are highly resolved and significant seismic changes can be observed between the two data sets on either inlines or crosslines. Also, the Devonian is pushed down during the steam cycle due to the velocity reduction in the steam-heated area above. Furthermore, some of the profiles may image fracturing that occurs during the steaming process (e.g., inline 62; crosslines 13, 25, 37).

Seismic attributes, using the Hilbert transform, were generated for inline 42. Figure 6.3.17 shows the cosine of the phase in degrees for inline 42 during production (1990) and steam (1992) cycles. We can observe the high resolution, sharpness and continuation of the reflectors attained with the depth migration. Figure 6.3.18 shows the instantaneous frequency for inline 42 from both 1990 and 1992 depth migrated data volumes. We can observe significant differences in the frequency content between production and steam cycle at the reservoir depths (about 400 to 500 m). The larger attenuation of the high frequencies during production may be associated with the higher gas saturation present in the vicinity of the wellbores during production.

We can look at the data by cutting through the volumes vertically (depth profiles) as in the figures above or horizontally (depth slices) as in the figures that follow next. The vertical extent of the steam-heated zone is about 30 m between 450 m to 480 m in the Clearwater formation. If we study the differences between depth-slices through the steam-heated zone from the 1990 and 1992 data volumes, we might be able to observe lateral changes in the steam zone and may track the steam front. However, amplitude differences between single depth-slices (at 1 m intervals) may not provide us with enough and accurate information since we are looking at only one sample of the seismic wavelet at each spatial location. However, we can look at depth-slices that are summed over 5 m intervals (5 samples per trace) such as the sum in the interval 450-455 m (Figure 6.3.19) and the sum in the interval 470-475 m (Figure 6.3.20) from the upper and bottom part of the steam-heated reservoir, respectively. On both Figures (6.3.19 and 6.3.20) during steaming (1992), we can observe hyperbolic shaped amplitude anomalies that are located above and below the upper row of wells (D3-1 to D3-4), respectively. These anomalies most likely are associated with the movement of the expanding steam front. Also, Figure 6.3.21.a shows the amplitude difference between production (1990) and steam (1992) data over 5 m depth interval between 450 and 455 m. This depth corresponds to the top of the steam-heated zone. We can observe a large amplitude anomaly between the two upper rows of wells (D3-1 to D3-10). Figure 6.3.21.b shows the amplitude difference between the 1990 and 1992 for the sum of depth-slices from 470 to 475 m (5 m interval) in the production and steam data volumes. On both amplitude difference maps in Figure 6.3.21 we can clearly observe a hyperbolic or semicircular anomaly near the top row of wells (D3-1 to D3-5) that propagates upwards (from the 470-475 m depth level to 450-455 m depth level) and that is expanding in a northeast direction. This moving anomaly probably indicates the movement of steam (steam front). Also, it is in agreement with the temperature measurements on the observation wells during steaming (1992) which show increased temperature between the two upper rows of wells (D3-1 to D3-10). Also, during steaming the two lower rows of wells (D3-6 to D3-15) were steaming with an 11 MPa pressure whereas the upper row of wells (D3-1 to D3-5) were steaming with about 5 MPa pressure, thus creating a differential pressure which is expected to result in a preferential movement of steam towards the area of the reservoir located in the vicinity of the upper row of wells (D3-1 to D3-5). The amplitude anomalies on Figure 6.3.21 may correlate the areal conformance at those depths. Furthermore, they suggest that the vertical conformance is about 25 m. However, a definite estimate of vertical conformance require a seismic data set from a base survey.

The major positive reflection event below the reservoir is the top of the Devonian (at about 550 m, see Figure 6.3.15). This horizon was picked from both depth migrated volumes. Figure 6.3.22 shows the apparent depth structure of the Devonian horizon in a 3-D perspective during production and steam injection cycles. The ridge observed on the 1990 (production) Devonian depth map between the two upper rows of wells (D3-1 to D3-10) has an apparent delay (pushdown) on the 1992 (steam) map. These depth maps were converted into isopach maps with respect to the depth of the Grand-Rapids tight streak (at about 400 m depth, see Figure 6.3.15). Next, the isopach maps from production and steam were differenced. The resultant apparent depth difference for the Devonian between the two surveys is shown in Figure 6.3.23.a. We can observe clearly that the main depth anomaly (pushdown) is located between the row of wells between D3-1 to D3-4 and D3-6 to D3-9. This anomaly is also in a good agreement spatially with the one on the time delay map generated from the analysis of the energy balanced time migrated data (Figure 6.3.14.b). Since we have both the depth pushdown map (Figure 6.3.23.a) and the time delay map of the Devonian (Figure 6.3.14.b), we can easily generate the corresponding velocity reduction map (Figure 6.3.23.b). This velocity reduction is caused in the steam-heated reservoir above the Devonian and is responsible for the apparent pushdown of the Devonian reflector below. This map may not give very accurate velocity reduction values since the time delay map was generated from the time migrated data and the depth pushdown map was generated from the depth migrated, thus the data underwent different processing. However, the largest velocity reduction values are spatially located near the wellbores of the steam injecting wells as expected.

Figure 6.3.24.a shows the amplitude difference between the 1990 (production) and 1992 (steam) Devonian horizon interpreted from the depth migrated data. Also, Figure 6.3.24.b shows the amplitude ratio between the 1990 and 1992 Devonian horizon. On both amplitude difference and ratio maps we can clearly observe a large amplitude anomaly between the two upper rows of wells (D3-1 to D3-4 and D3-6 to D3-9), (compare with the corresponding anomaly generated from the time migrated data in Figure 6.3.14.a). This amplitude anomaly indicates that the Devonian horizon is dimmed in this area due to a large steam-heated zone in the reservoir above.

*(Text continued on page 215)*

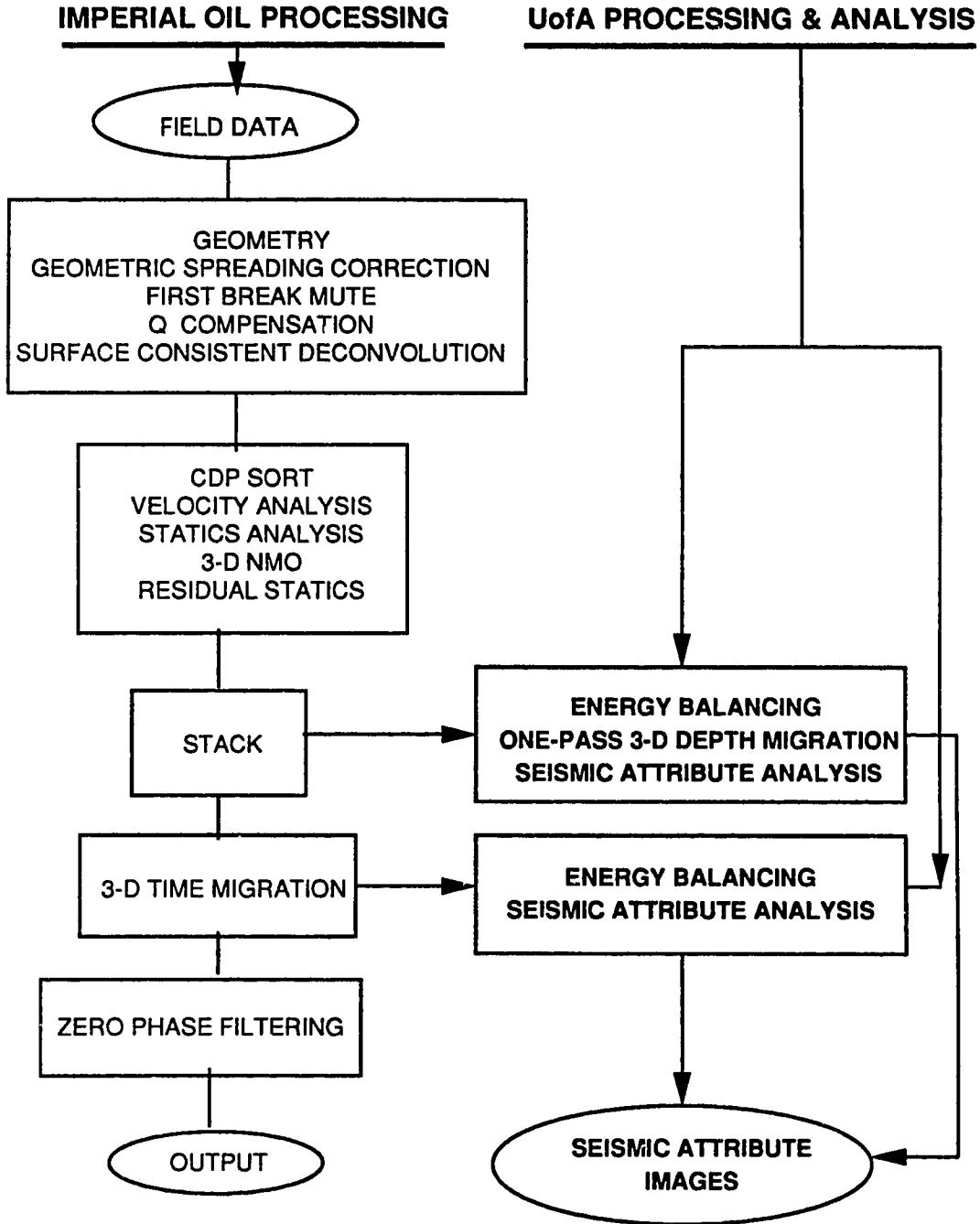
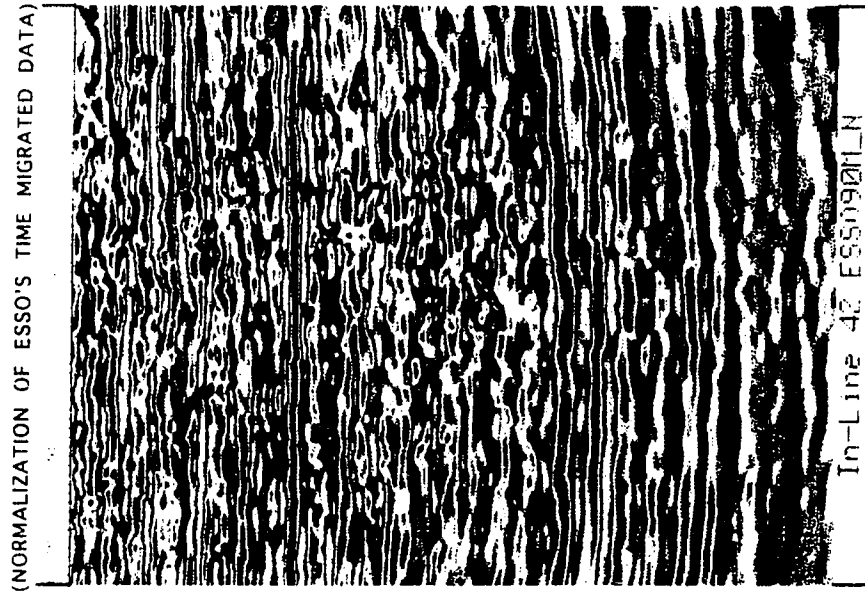


**Figure 6.3.12:** The processing flows as they were applied on both data sets (production 1990 and steam 1992) by Imperial Oil and the Seismology Laboratory, University of Alberta (this research).



(a)

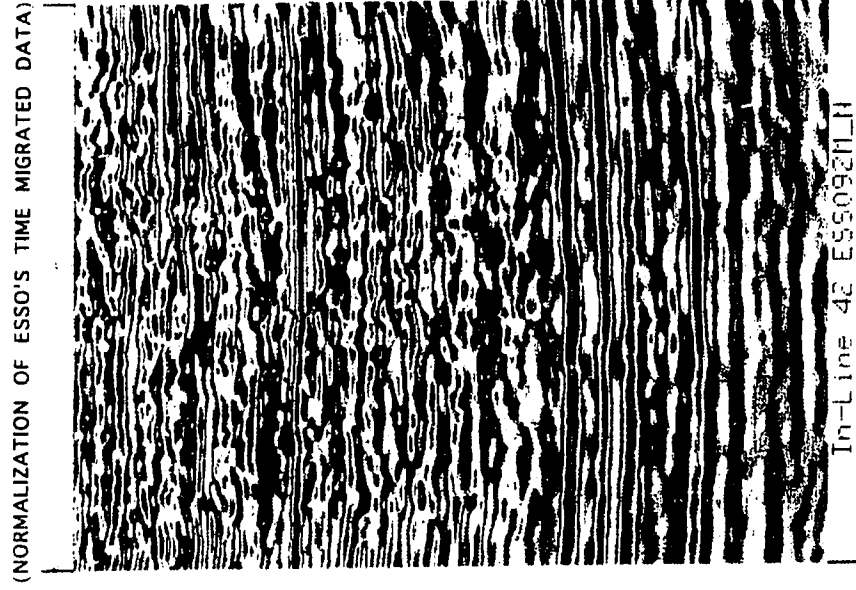
ESSO PRODUCTION 1990 : INLINE 42



TIME (SEC)

(b)

ESSO STEAM 1992 : INLINE 42



TIME (SEC)

Figure 6.3.13: Normalized time migrated data, inline 42 from: (a) the production (1990) and (b) the steam (1992).

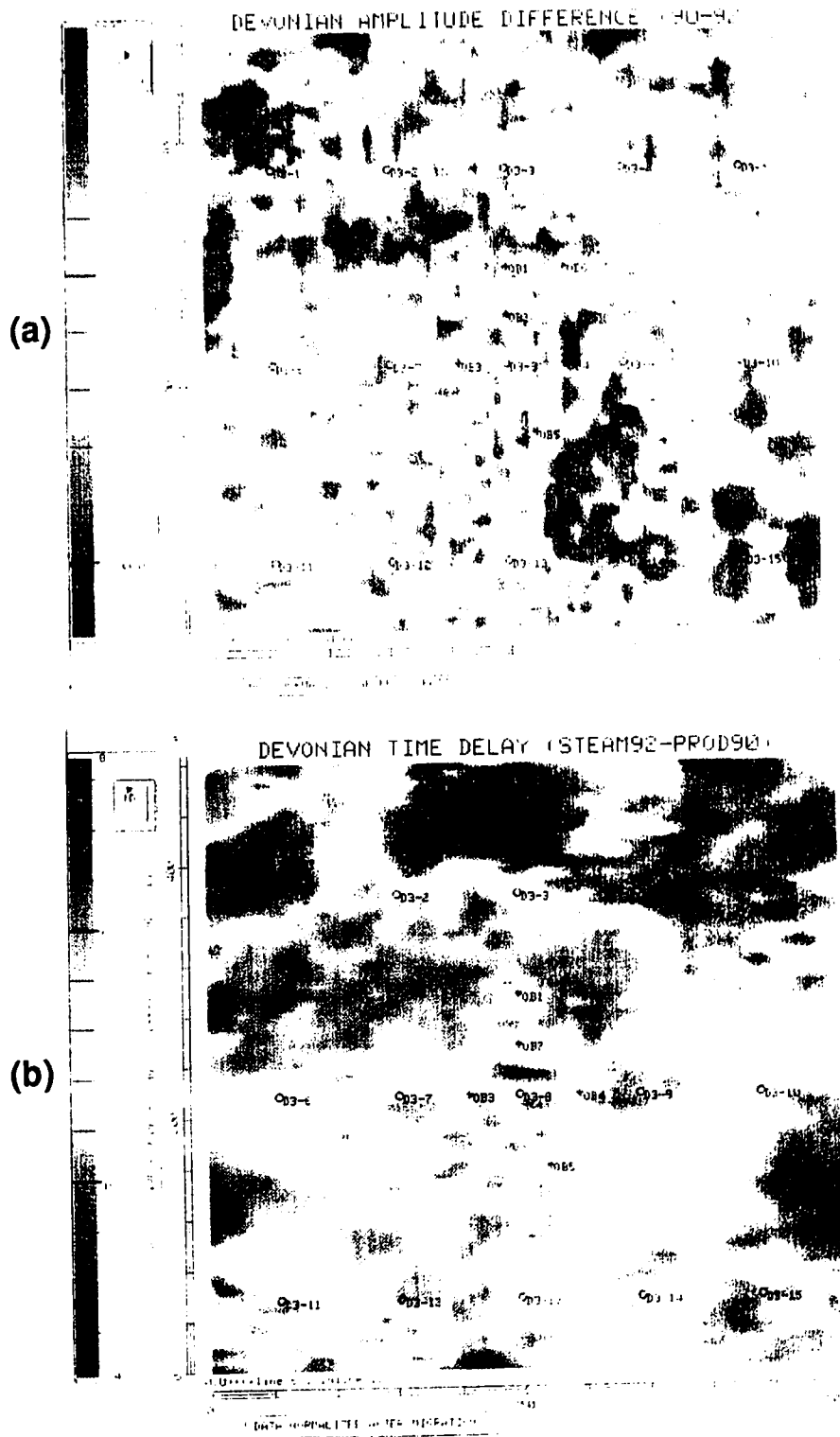


**Figure 6.3.14:** (a) Devonian amplitude difference and (b) Devonian two-way travel time delay (pushdown) between the steam (1990) and the production (1992) normalized time migrated data.

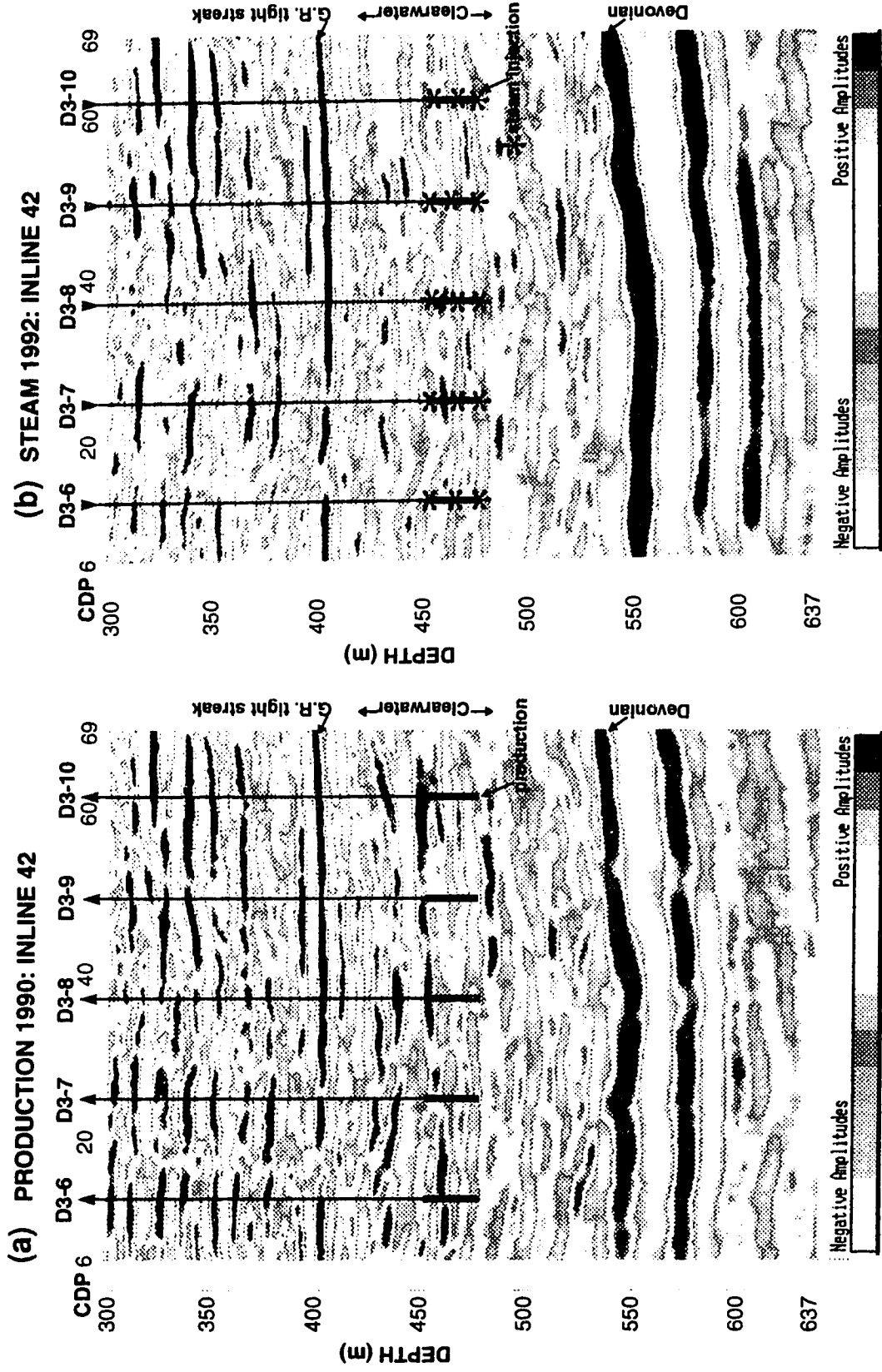
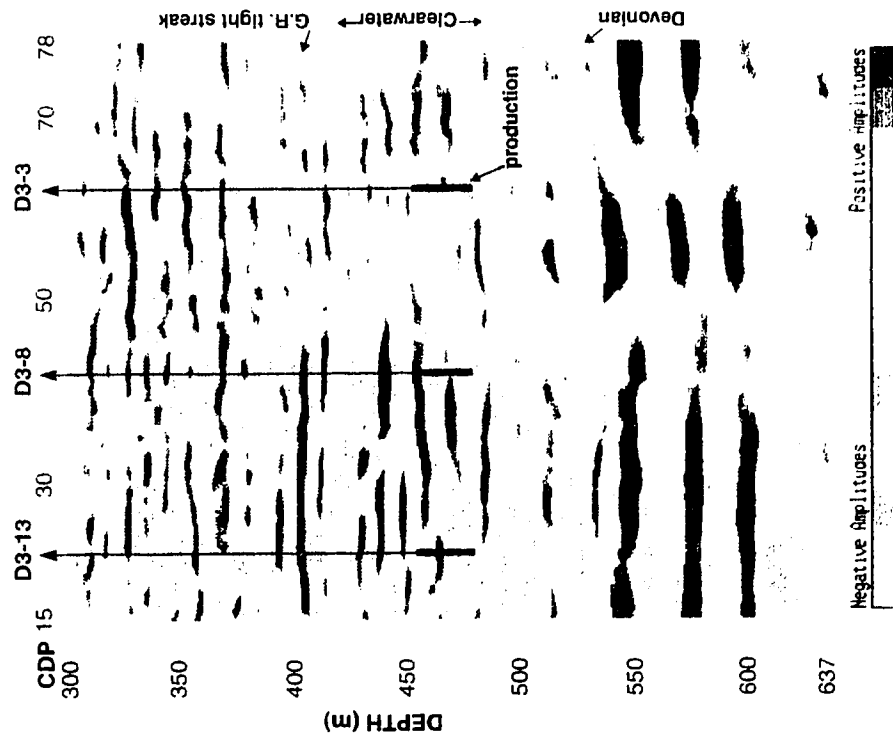


Figure 6.3.15: Inline 42 from: (a) the production (1990) and (b) the steam (1992) depth migrated data.

(a) PRODUCTION 1990: CROSS-LINE 37



(b) STEAM 1992: CROSS-LINE 37

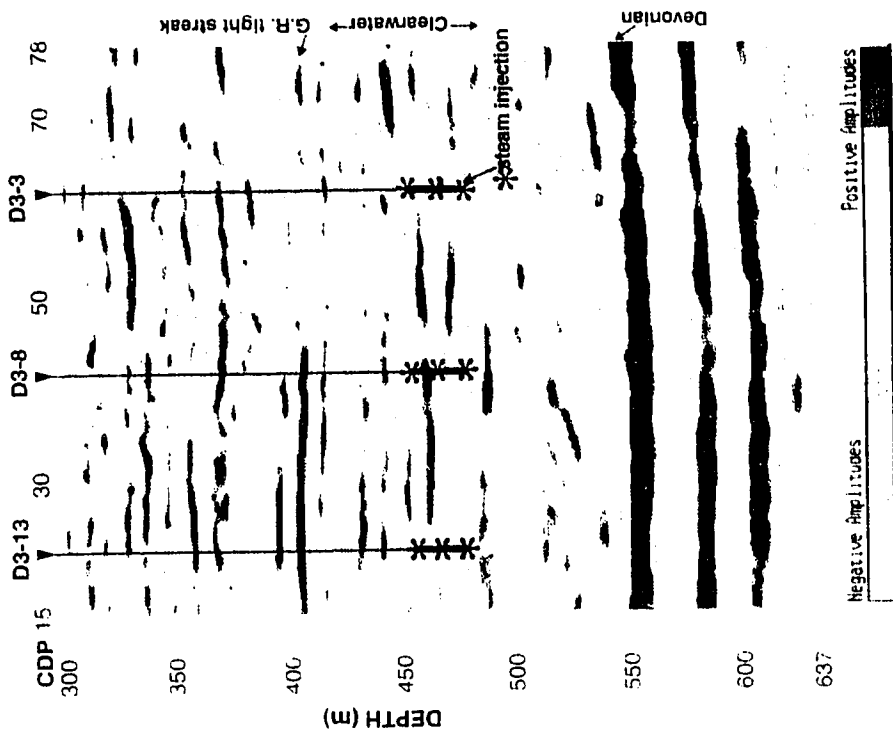
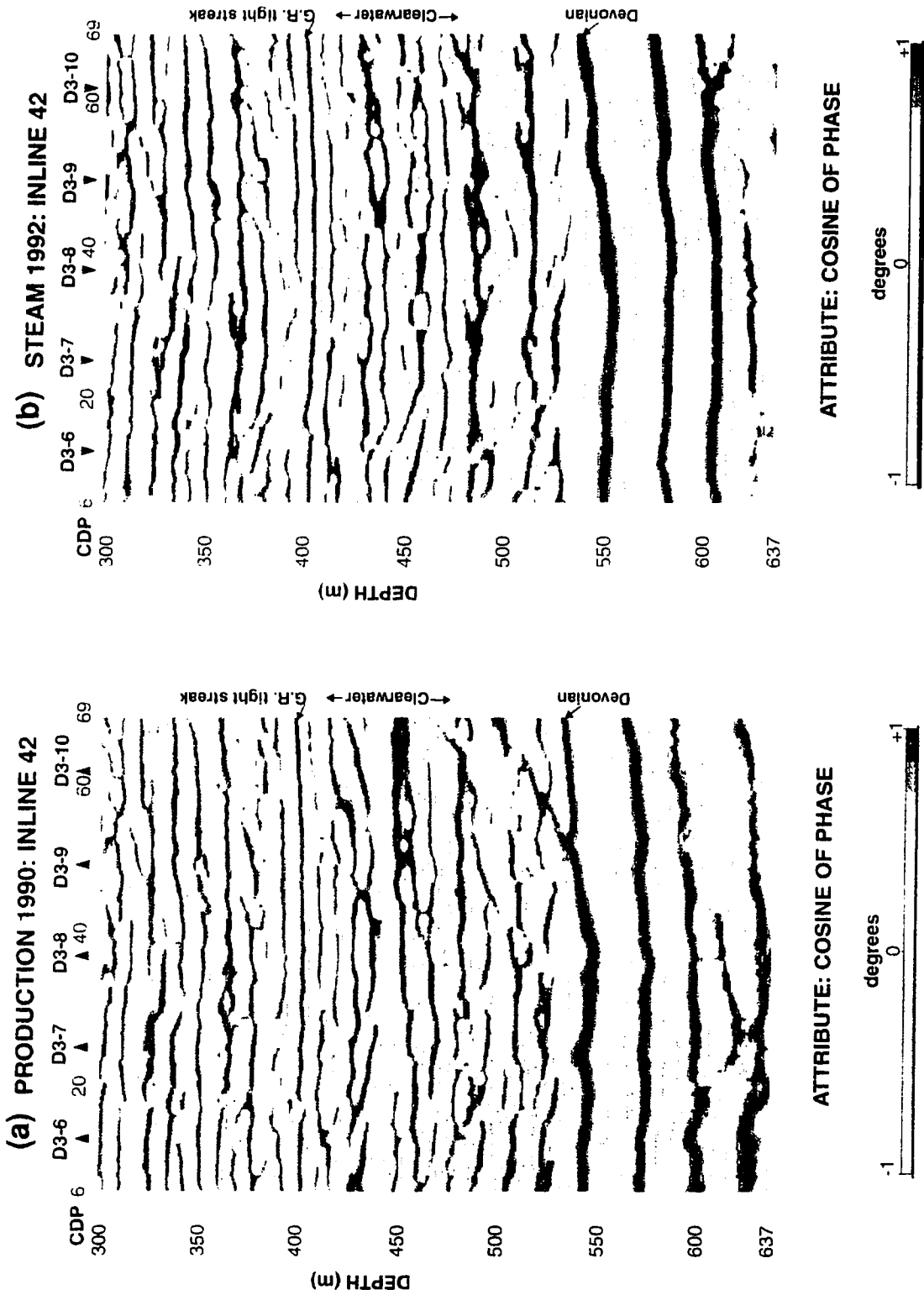
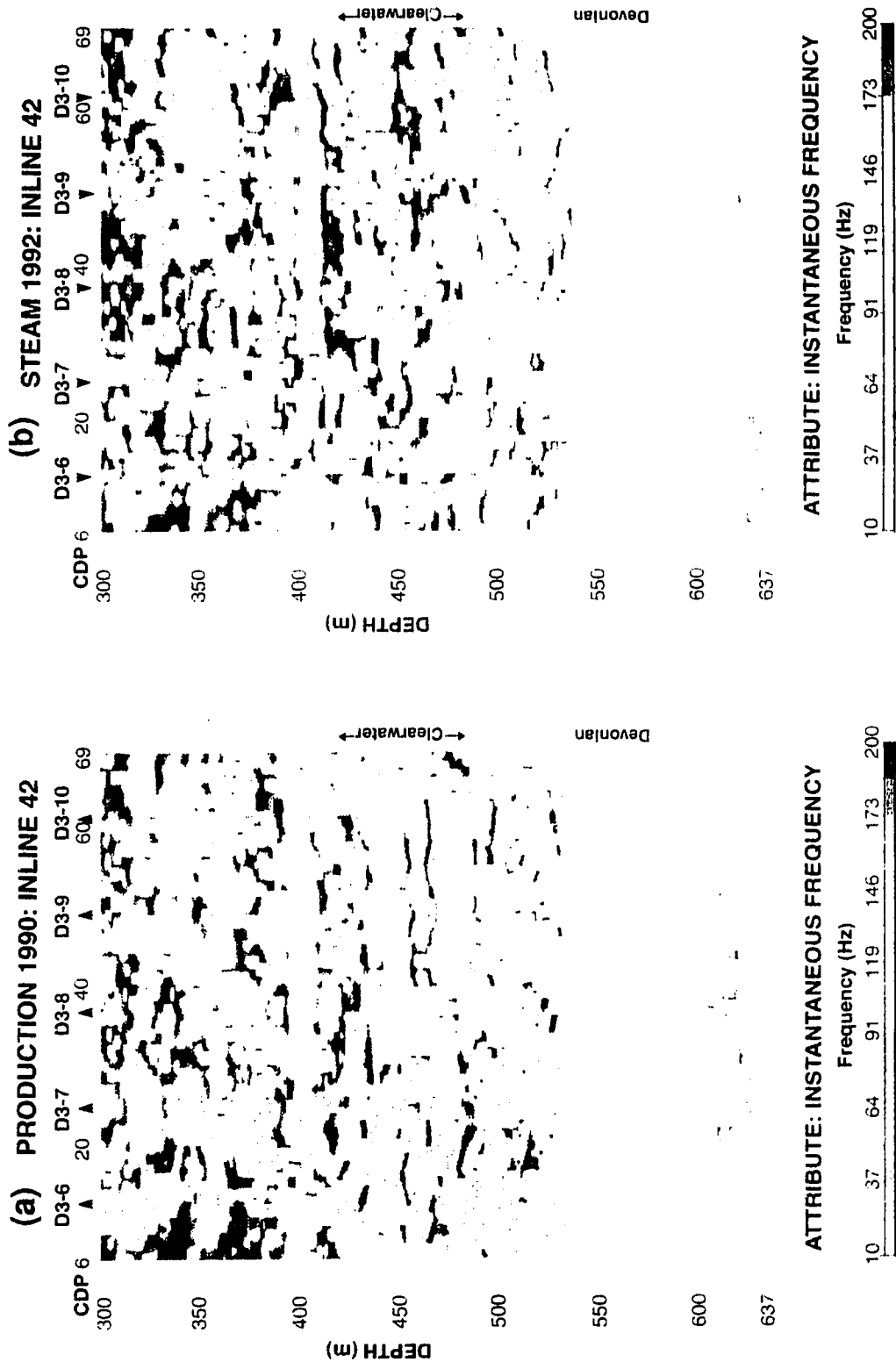


Figure 6.3.16: Crossline 37 from: (a) the production (1990) and (b) the steam (1992) depth migrated data.



**Figure 6.3.17:** Cosine of phase for inline 42 from: (a) the production (1990) and (b) the steam (1992) depth migrated data.



**Figure 6.3.18:** Instantaneous frequency for inline 42 from: (a) the production (1990) and (b) the steam (1992) depth migrated data.

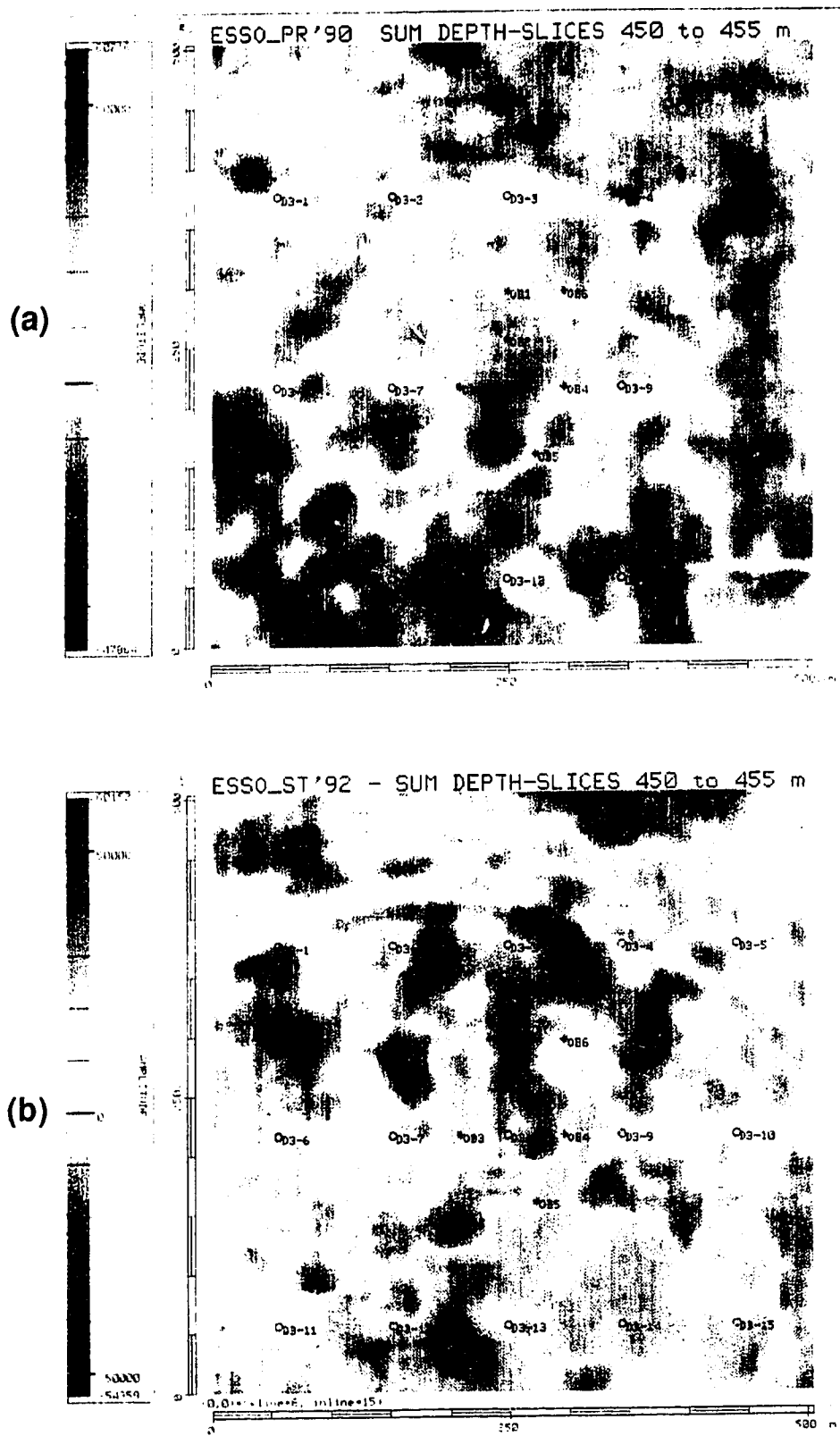


Figure 6.3.19: Depth slices summed over 5 m interval, 450~455 m, from: (a) the production (1990) and (b) the steam (1992) depth migrated data volumes.

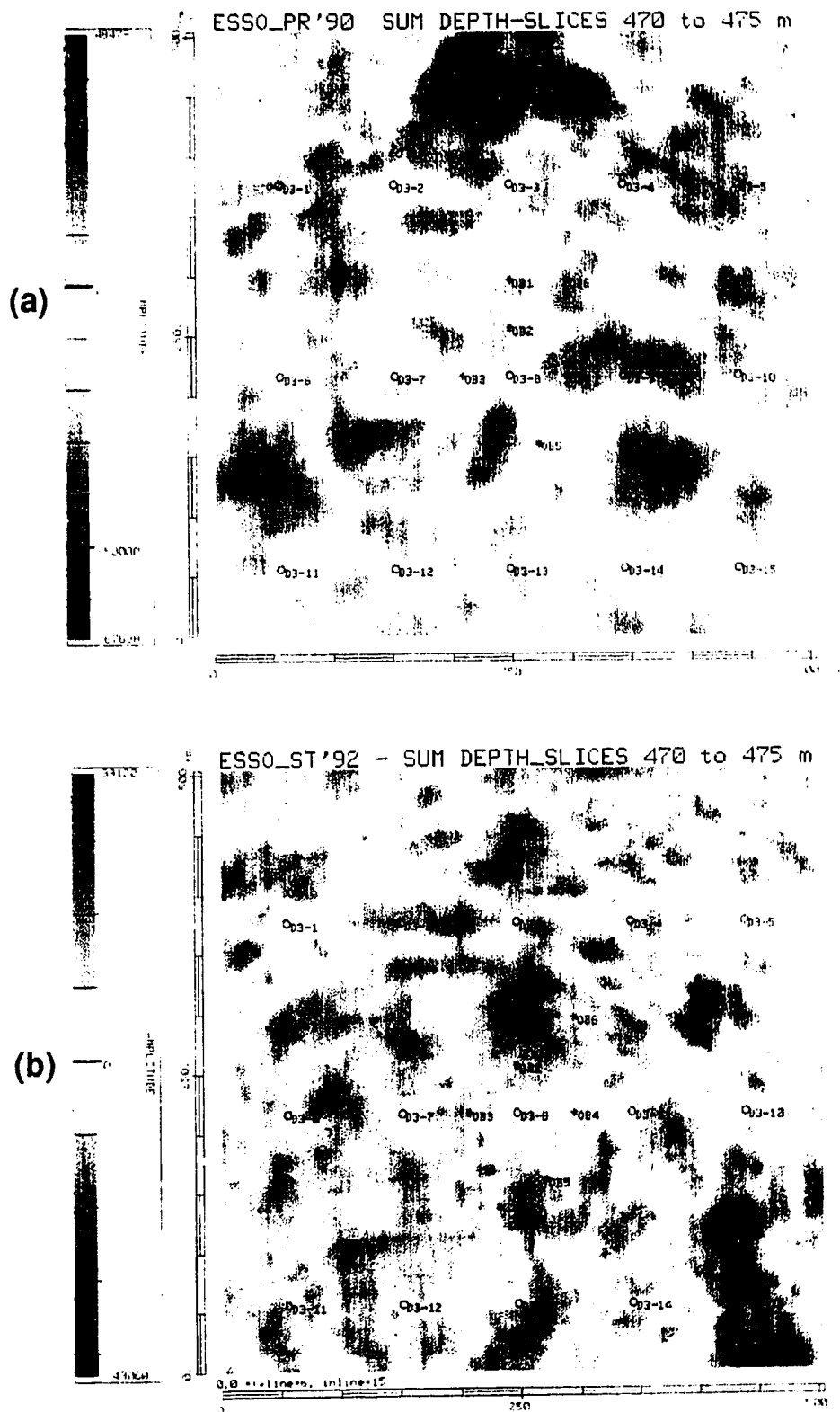
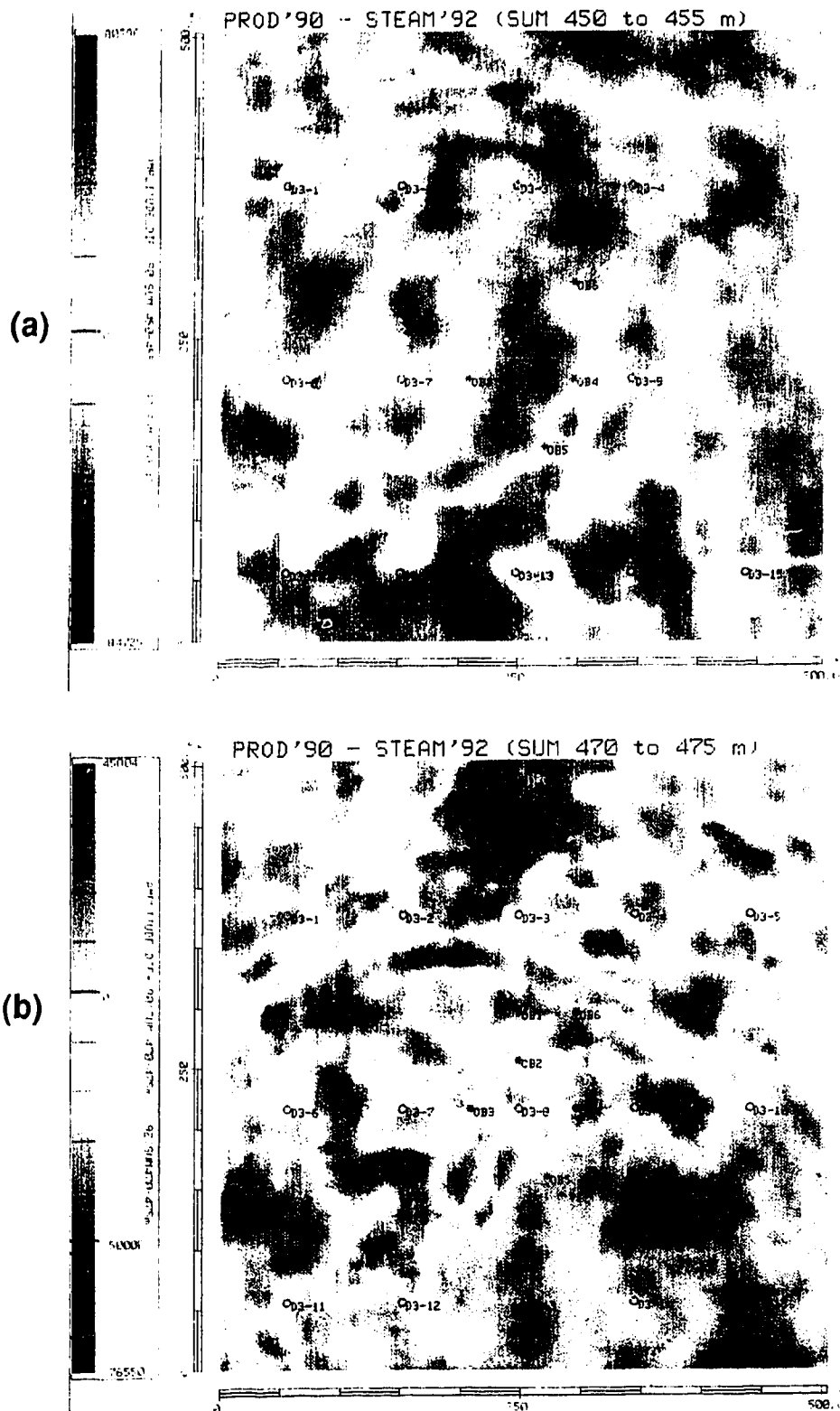


Figure 6.3.20: Depth slices summed over 5 m interval, 470~475 m, from: (a) the production (1990) and (b) the steam (1992) depth migrated data volumes.





**Figure 6.3.21:** Amplitude difference between the production (1990) and the steam (1992) depth migrated data over 5 m depth interval: (a) between 450 and 455 m, and (b) between 470 and 475 m.

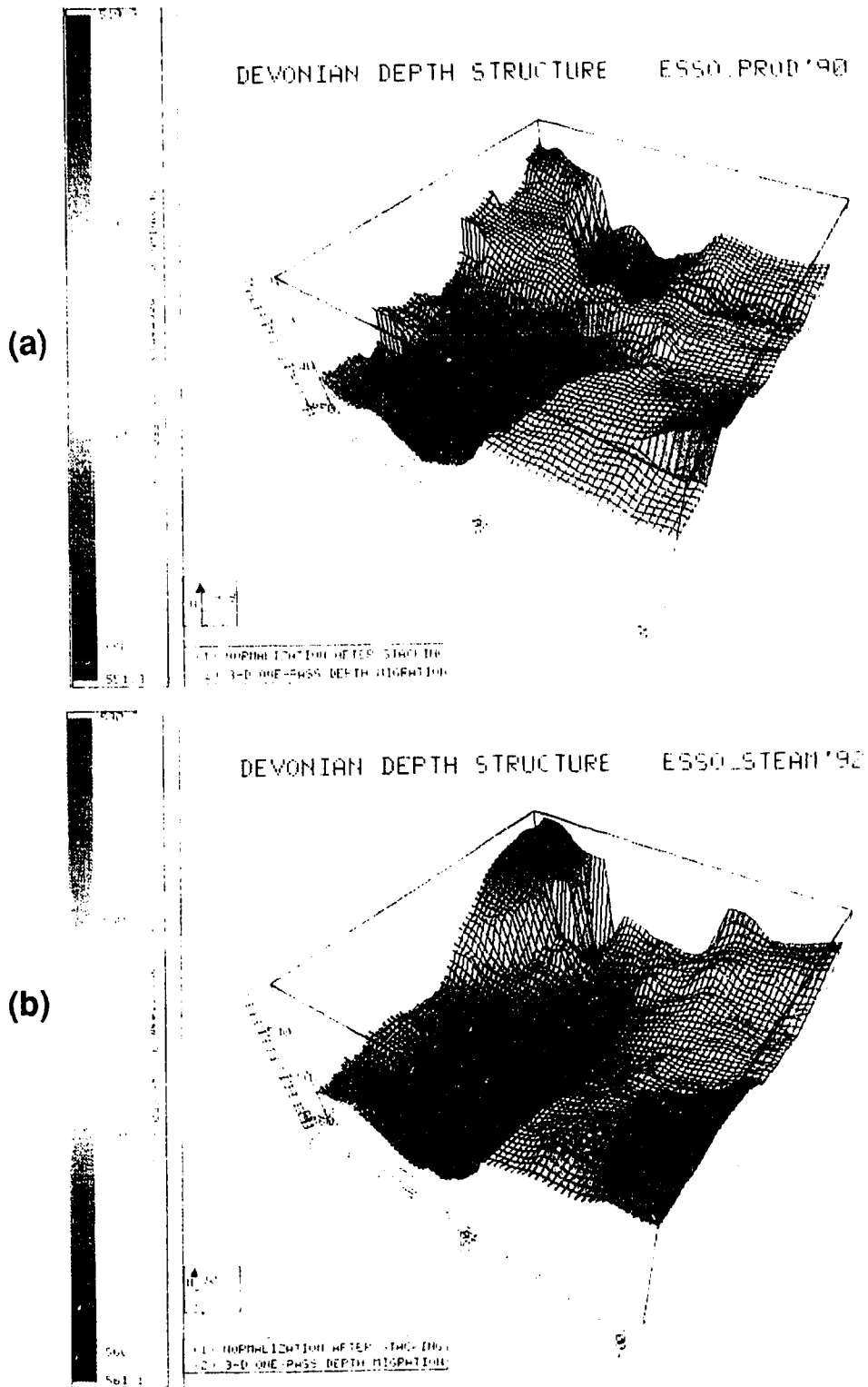


Figure 6.3.22: A 3-D perspective of the apparent depth structure of the Devonian horizon during the production 1990 (a) and the steam 1992 (b) cycles.

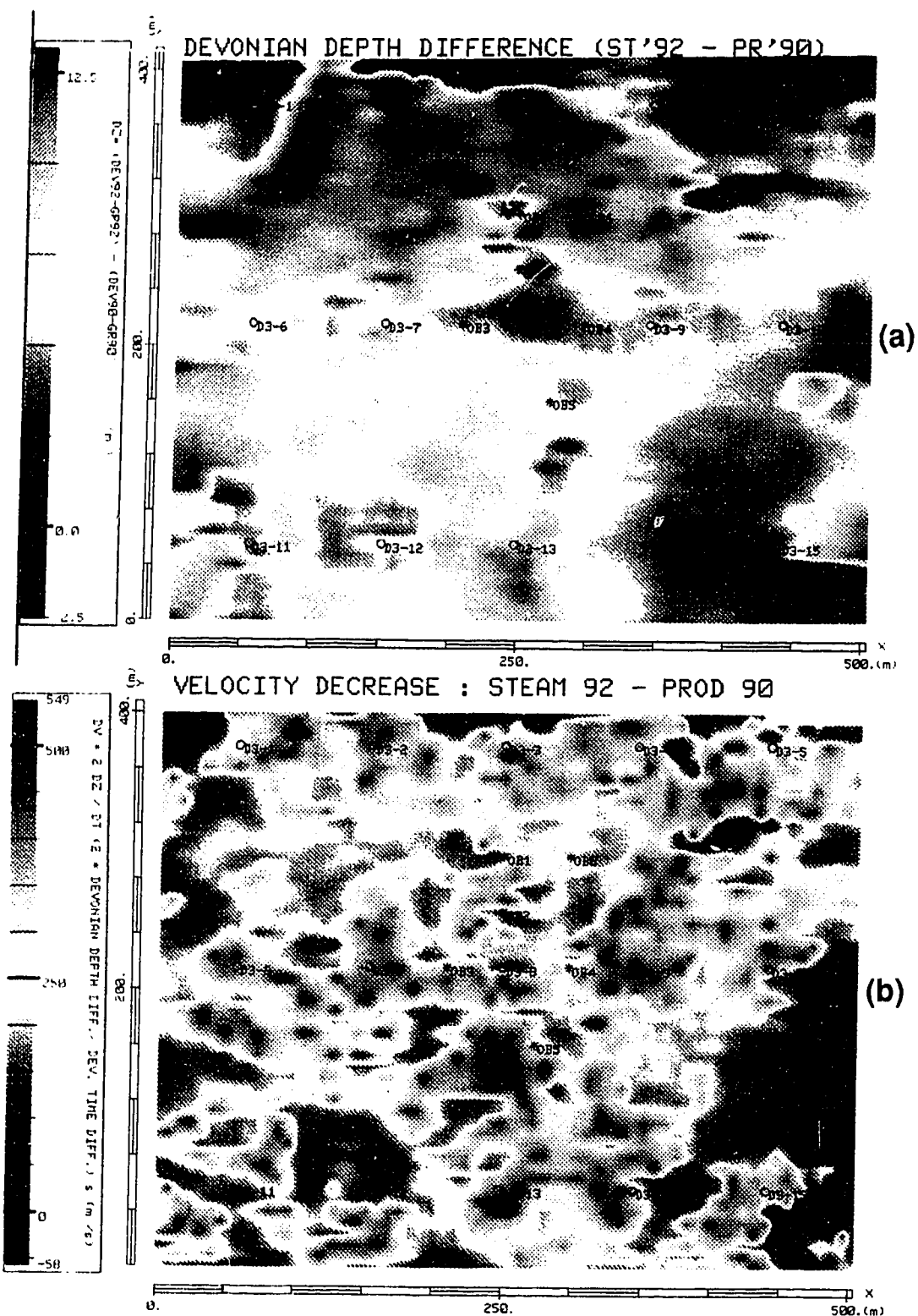
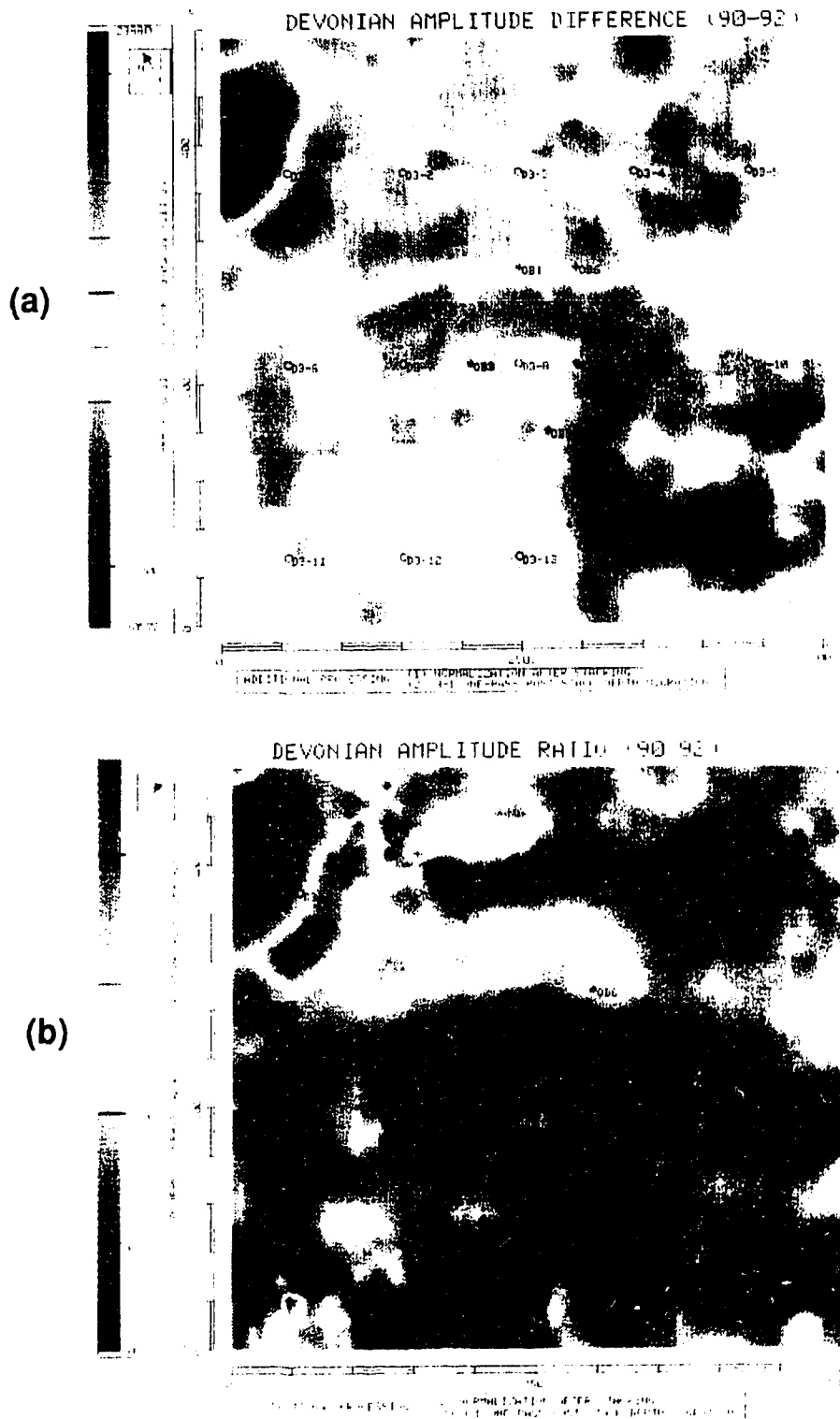


Figure 6.3.23: (a) Devonian apparent depth pushdown between steam (1992) and production (1990) depth migrated data. (b) The velocity reduction ( $\Delta v$ ) in the steam-heated reservoir as it is seen by the Devonian horizon.



**Figure 6.3.24:** Devonian amplitude difference (a) and ratio (b) between the production (1990) and the steam (1992) depth migrated data volumes.

### 6.3.6 Discussion of Imperial Oil Project's Results

We have implemented sophisticated and computationally efficient 2-D elastic and 3-D acoustic modeling algorithms on very detailed (2x2x2 m) and realistic velocity models from Imperial Oil's D3-pad which undergoes cyclic steam stimulation for bitumen recovery. The wave propagation simulations resolved all the geological structure and as well detected calcified tight streaks in the Clearwater reservoir. These tight streaks are of critical importance for the oil recovery process since they act as permeability barriers that impede vertical migration of the steam. Furthermore, wave simulations during different phases of the EOR process such as before any steaming (base), steam injection and production (monitors) were performed. The resultant realistic seismic sections were able to show the effects on reflections within and below the Clearwater reservoir due to the presence of an expanded steam heated zone.

The 3-D reverse time migration algorithm developed in Chapter 4 was tested with 3-D synthetic seismic data and a realistic velocity model (3-D GEOSET model) and proved that one can image accurately and define with high resolution (2 m in all directions, in this case) the Clearwater reservoir and the tight streaks within it. On the other hand, both the 2-D elastic and 3-D acoustic modeling algorithms developed in this thesis prove to be valuable tools in understanding seismic changes occurring during the steam stimulation process. These algorithms not only generated images with high resolution but also allowed computations to run as fast as the acquisition of the field seismic data. This suggests the valuable potential of wave propagation simulations since these can generate high quality seismic images before and during the cyclic steam stimulation which can help in the characterization of the reservoir as it evolves with time during the thermal process.

Additional processing was performed on the 3-D seismic data in order to remove all the effects not associated with the steam stimulation by normalizing the two monitor data sets (energy balancing). Furthermore, the one-pass 3-D implicit finite difference depth migration algorithm developed in this thesis was used to migrate both monitor seismic surveys resulting in high resolution depth seismic images (1 m vertical resolution).

Seismic attribute analysis and differencing was performed on both time migrated and depth migrated data. Seismic images within and below the reservoir are functions of a number of variables such as velocity, reflectivity and attenuation and can result in time or depth pushdowns, amplitude bright spots or dim spots, and spectral modifications. Images generated from time migrated and depth migrated data sets are in good agreement in terms of the anomalies that define. However, the images from the depth migrated data have better

resolution and more accuracy due to the better migration algorithms used and thus more emphasis was given to these data sets.

During production the reservoir conditions near the boreholes are at a local minimum in terms of fluid pressure (high effective stress  $\sim 9.5$  MPa) and temperature ( $150$  °C) but at a maximum in terms of gas saturation ( $> 5$  %). On the other hand, during the steam cycle the reservoir conditions are at a local maximum in terms of fluid pressure (12 MPa) (low effective stress  $\sim 2$  MPa) and temperature ( $315$  °C) but at a minimum in terms of gas saturation ( $\sim 2$  %). The changing conditions are a major potential source for alteration of the seismic signature and the cause of seismic anomalies during steam injection and production.

The generated images showed time delays and depth pushdowns anomalies that are associated with the expanding steam-heated zone during the steam injection phase and the gas presence during production. Also, amplitude anomalies were observed from differencing horizons between the steam and production cycles that are in spatial agreement with the time and depth delays. Furthermore, amplitude anomalies generated from differencing depth slices defined the steam front very well. Both images from the top (450-455 m) and the bottom of the reservoir (470-475 m) show amplitude anomalies that have areal conformance. Also, they suggest a vertical conformance of about 25 m.

Spectral attenuation was observed during production in comparison to the steam cycle. In terms of the conditions existing in the reservoir during production, the high gas saturation would affect seismic wave attenuation most.

Based on the described reservoir conditions during the thermal process, the time, depth and amplitude anomalies that result from the differencing of the seismic images between steam and production cycles are the combined result of a decrease in the effective stress, a temperature increase, and gas reduction during the steam phase with respect to the production phase.

It would had been easier to correlate the seismic changes between the monitors and a base survey (prior to the EOR process). Although the existence of the two monitor surveys allows a comparison of the seismic character of the reservoir and enables the mapping of the areal conformance of the steam stimulation, the existence of a base seismic survey could allow one to positively map the vertical conformance. However, such base survey was not performed on this pad.

## **6.4 SEISMIC MONITORING OF MOBIL'S PILOT EOR PROJECT**

### **6.4.1 The Vertical Pilot EOR project**

Mobil Oil of Canada had a 23 vertical well pilot (presently abandoned) in the Cold Lake area of Alberta where steam stimulation was used as an enhanced oil recovery method. In this experiment the steam was injected starting at a depth of approximately 360 m in three different levels of the Sparky sands that are separated by shales. The steam was injected at a constant rate of 200 m<sup>3</sup> CWE per day at wellhead pressures of 8 to 10 MPa. The injection pressure in some wells had to be gradually increased to maintain this injection rate which resulted in differential pressure states between some wells.

In the Mobil area of study, the Mannville Group consists of a sequence of sands and interbedded shales, containing the following formations: Colony, McLaren, Waseca, Sparky, G.P., Clearwater and McMurray. The best reservoirs are in the Sparky and Waseca formations. The Sparky consists of three sands separated by shales that result in the Upper Sparky, the Middle Sparky and the Lower Sparky.

### **6.4.2 3-D Seismic Reflection Surveys**

In 1987, Mobil Oil Canada initiated a 3-D high resolution seismic reflection acquisition program at the Cold Lake area of Alberta, Canada. The program consisted of a base survey carried out in October of 1987 and a monitor survey carried out in November of 1988 nearly at the end of the 2nd cycle. Both surveys were recorded over the same pad that included 23 injector-producer wells and 3 observation wells (Figure 6.4.1). At the time of the second survey only five wells (3, 6, 13, 16, 18) were under steam injection pressures, the rest were on flow back or drawdown pressures.

For both experiments the field acquisition geometry was identical. Each survey had 10 receiver lines laid out in E/W direction with line spacing of 88 m, group interval of 22 m and with each geophone array consisted of 18 geophones. Also, it had a total of 16 source lines laid out in N/S direction with source line spacing of 66 m, shot point interval of 22 m and a total number of 374 shots. The type of energy source was Vibroseis (2 vibrators) with a non-linear sweep over a frequency range of 8-178 Hz. The field data were recorded, 478 traces per record, with sample rate of 1 ms using a DFS VII system. After stacking, each survey has 73 inlines and 90 crosslines with bin size of 11x11 m (Figure 6.4.1).

Mobil Oil of Canada provided us with digital copies of the stacked data, paper copies

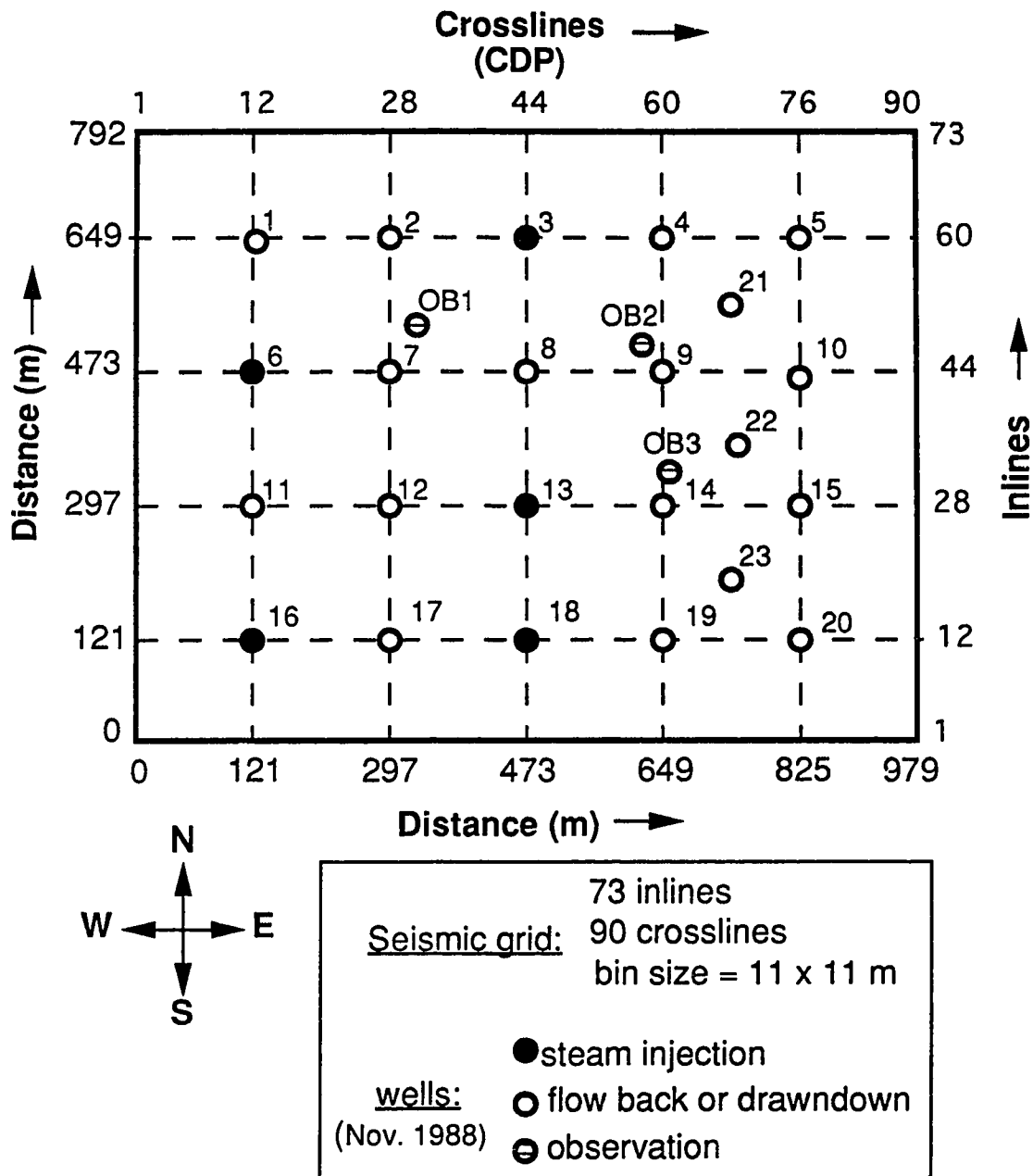


Figure 6.4.1 : The site map of Mobil's pilot project showing the locations of the injection/production and observation wells, and the seismic grid.



of the time migrated data for both surveys, and sonic logs.

### 6.4.3. Seismic Wave Propagation Simulations

Computer simulations of seismic wave propagation were essential for the interpretation of field data. Finite difference modeling of seismic waves in acoustic and elastic media in the region over the steam-heated zone was performed in order to examine the relation between reservoir conditions with seismic characteristics such as velocity, amplitude and frequency modification with time. For the generation of the velocity models (base) we used sonic logs, stacking velocities and time migrated sections. The models used in these simulations were modified until a reasonable match was obtained between the field and synthetic data.

In order to understand the effects that the steaming process caused on the seismic character, we introduced steam zones of various characteristics into our base model. In the field experiment the steam was injected at three perforation levels corresponding to the three Sparky Sands. However, there are two hydraulic reservoir systems; an upper system that consists of the Upper Sparky Sands with leakoff to the Waseca above and a lower system that consists of the Mid Sparky and the Lower Sparky with leakoff to the G.P (Siewert, 1993, personal communication). There is a thick shale between the Upper and Mid Sparky that acts as a very effective permeability barrier. The shale between the Mid and Lower Sparky is not as efficient and there is some cross-flow through joints and cracks. Also, the shale between the Lower Sparky and the G.P is very thin and permeable. For this reason, we introduced a double steam zone at each well location at the Sparky level (Figure 6.4.2). Both steam zones are semi-ellipses. The upper steam zone simulates the upper hydraulic system in the Upper Sparky Sands and it is 10 m thick. The lower steam zone simulates the lower hydraulic system in the Mid and Lower Sparky Sands and it is 14 m thick. In the modeling we did not include the high velocity shales that separate the steam zones.

## ACOUSTIC MODELING

Zero offset acoustic modeling was performed using a simplified flat multi-layer velocity model with and without the steam zone (Figure 6.4.2). The modeling was performed with a 2-D  $\omega$ -x algorithm that uses the Exploding Reflector Model (ERM) and a 65 degree approximation of the one-way scalar wave equation. In Figure 6.4.3.a the zero offset section is shown for the simplified model without the steam zones. In Figure 6.4.3.b

the zero offset section clearly resolves the steam-heated zones and shows the time delay (pushdown) of the reflectors below. Furthermore, Figure 6.4.3.c shows the depth migrated section with the steam zones clearly imaged and the reflectors below are corrected from the velocity sags.

## ELASTIC MODELING

Elastic wave (P-SV) computer simulations were performed on velocity models with and without steam zones. A P-wave line source with a Gaussian function as source of excitation with dominant frequencies of 50 to 100 Hz, was used to generate seismograms for multiple shot locations. Synthetic seismograms for vertical or horizontal components of particle velocity or stress components can be generated. The common shot gathers can directly compared with field shot gathers or after sorting into CMP gathers, NMO and stacking, the resultant stacked section can be migrated and compared to a field inline or crossline.

For the 2-D elastic modeling, the dimensions of the model was 968 m in the x-direction and 1200 m in the z-direction. The finite-difference mesh size was 2.75 m (1/4 of the CDP spacing) in the x-direction. The total numbers of grid nodes in the x-direction was 393 including 20 nodes at each side of the model for absorbing region. The mesh size in the z-direction was 2.5 m and the total number of nodes was 501 including the bottom absorbing region. The finite difference time step was 0.1 ms. The sampling interval was 1 ms and data were recorded for 0.8 s. Therefore, for this model a computational grid of 393 x 501 nodes and 8046 time steps were used. The elastic wave simulation for this model required 2.01 hours of CPU time on a Convex 210.

A 2-D velocity model (Figure 6.4.4.a) for the Mobil pad along the inline 12 of the seismic grid was generated using sonic wells from the pad and the impedances from the inversion of the base (before steam) migrated inline 12. This velocity model is considered as the base model from which we generated base (pre-steam) synthetic seismic data. Using this model and a 50 Hz gaussian line source, P-SV seismograms for the vertical component of the particle velocity were generated. Eight synthetic shot gathers were generated by setting the source along the model at 132 m spacing ( in the field experiment 16 shotlines with 66 m spacing were used). Figure 6.4.5.a shows the synthetic shot gather with the source in the middle of the model and with trace spacing of 11 m. We applied normal moveout (NMO) correction on the shot gathers using the same velocity function as the one applied on the real data and then we stacked with CDP spacing of 11 m and the same

muting pattern as the one applied on the real data. Figure 6.4.6.a shows the resulting stack section for the base model. Also, a realistic zero-offset section was generated but is not shown here.

Along the seismic inline 12 there are five injection/producer wells. Assuming that they are all steaming, we can simulate this by setting steam zones at the corresponding locations on the base velocity model. Thus, we generate a monitor velocity model on which elastic modeling is performed in order to generate monitor synthetic seismic data (Figure 6.4.5.b). Synthetic shot gathers, stacked and zero offset sections were generated for five different models that all had five steam injection wells but the steam-heated zones varied in areal dimensions (areal conformance) and in the degree of velocity decrease (compressibility increase) due to the combined effects of temperature (high), pressure (high fluid pressure - small effective stress) and gas (gas reduction - small gas saturation). However, here we present only one case.

In Figure 6.4.4.b shows the velocity model (monitor) with five steam injection wells. The steam-heated zones (two semi-ellipses) generated in the Sparky reservoir have a core (steam) of about 80 m areal extent and a 20% velocity and density reduction. However, the velocity and density continues to change gradually (heated area) to that of the surrounding material. Considering that the wells along the inline direction are 96 m apart, our modeled steam zone expansion may create communication paths between the low velocity steam-heated zones (Figure 6.4.4.b). Using the above model, we generated P-SV shot gathers for multiple shot locations (8) and one is shown in Figure 6.4.5.b. The eight generated shot gathers after NMO (applied as described earlier) were stacked to produce a stacked section that is shown in Figure 6.4.6.b. On both the shot gather and the stacked section we can clearly observe reflections and diffractions from the steam zones. Amplitude increases (bright spots) are generated on the top of the steam-heated zones (0.375 ms). Also, amplitude changes (dim spots) and time delays are observed at reflectors below such as the Devonian reflector at 0.5 s. These changes are more dramatic when the shot gather and the stacked section (Figures 6.4.5.b, 6.4.6.b) are compared with the corresponding ones (Figures 6.4.5.a, 6.4.6.a) from the model without steam-heated zones. Furthermore, when the amplitude spectrums (not shown here) of both shot gathers with and without steam zones are compared, a frequency attenuation is observed on the shot gather with steam zones in a 100 ms time window that includes the steam zones.

*(Text continued on page 227)*

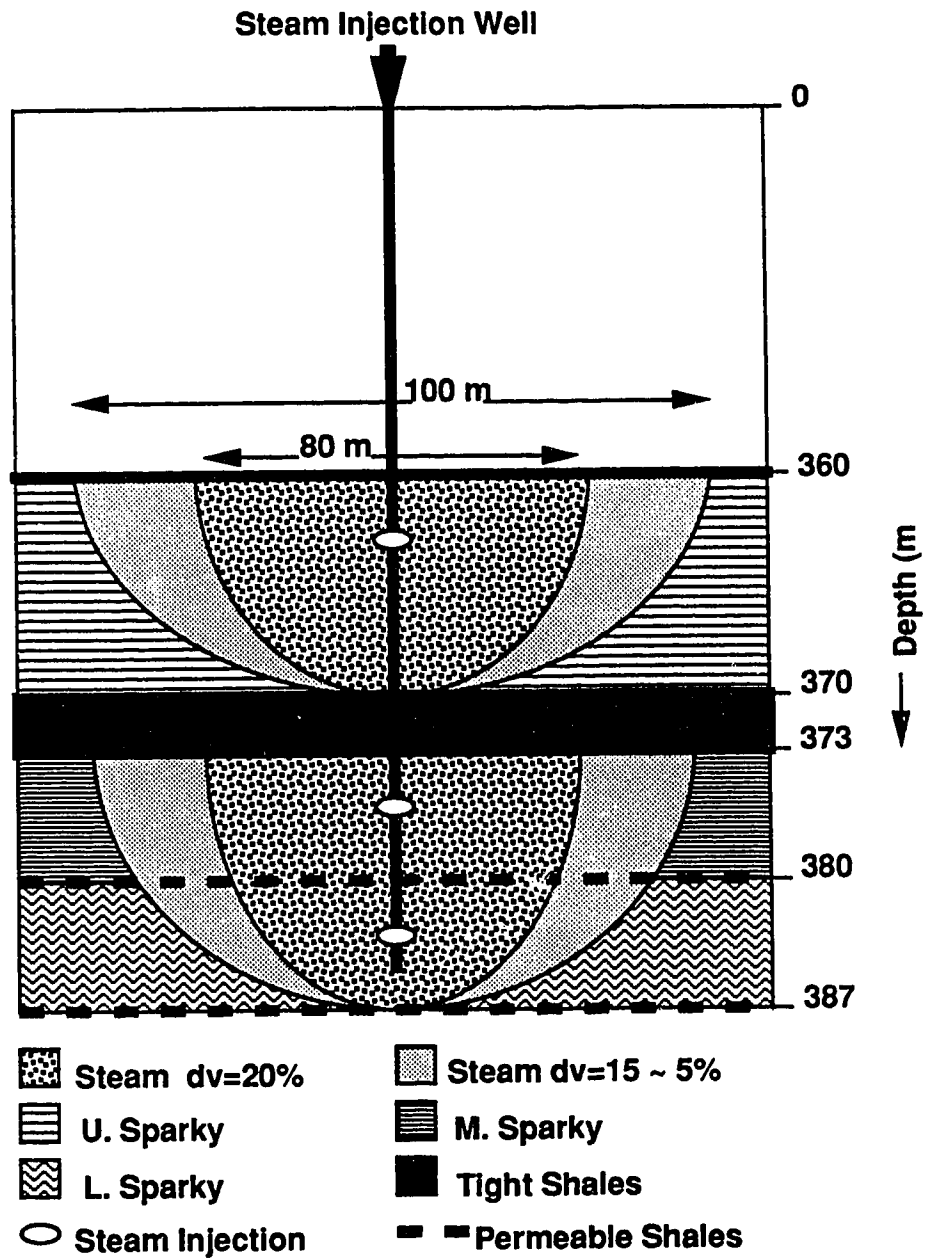
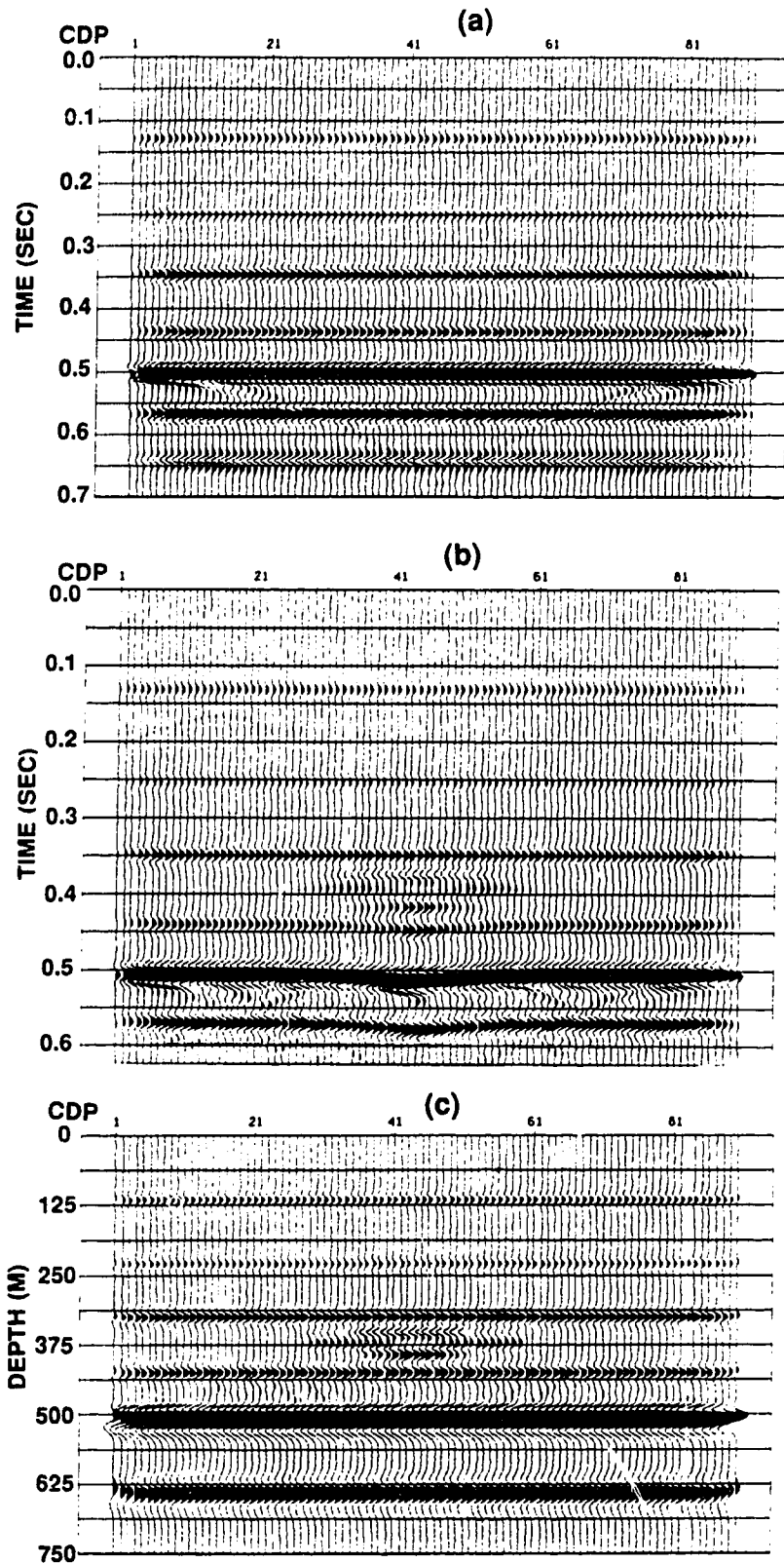


Figure 6.4.2: The steam zones used to simulate steam injection in the Sparky Sands.



**Figure 6.4.3:** Acoustic  $\omega$ - $x$  modeling generated zero offset sections without (a) and with steam zone (b). 2-D  $\omega$ - $x$  depth migration of the zero offset section with the steam zone generated the depth migrated section (c).

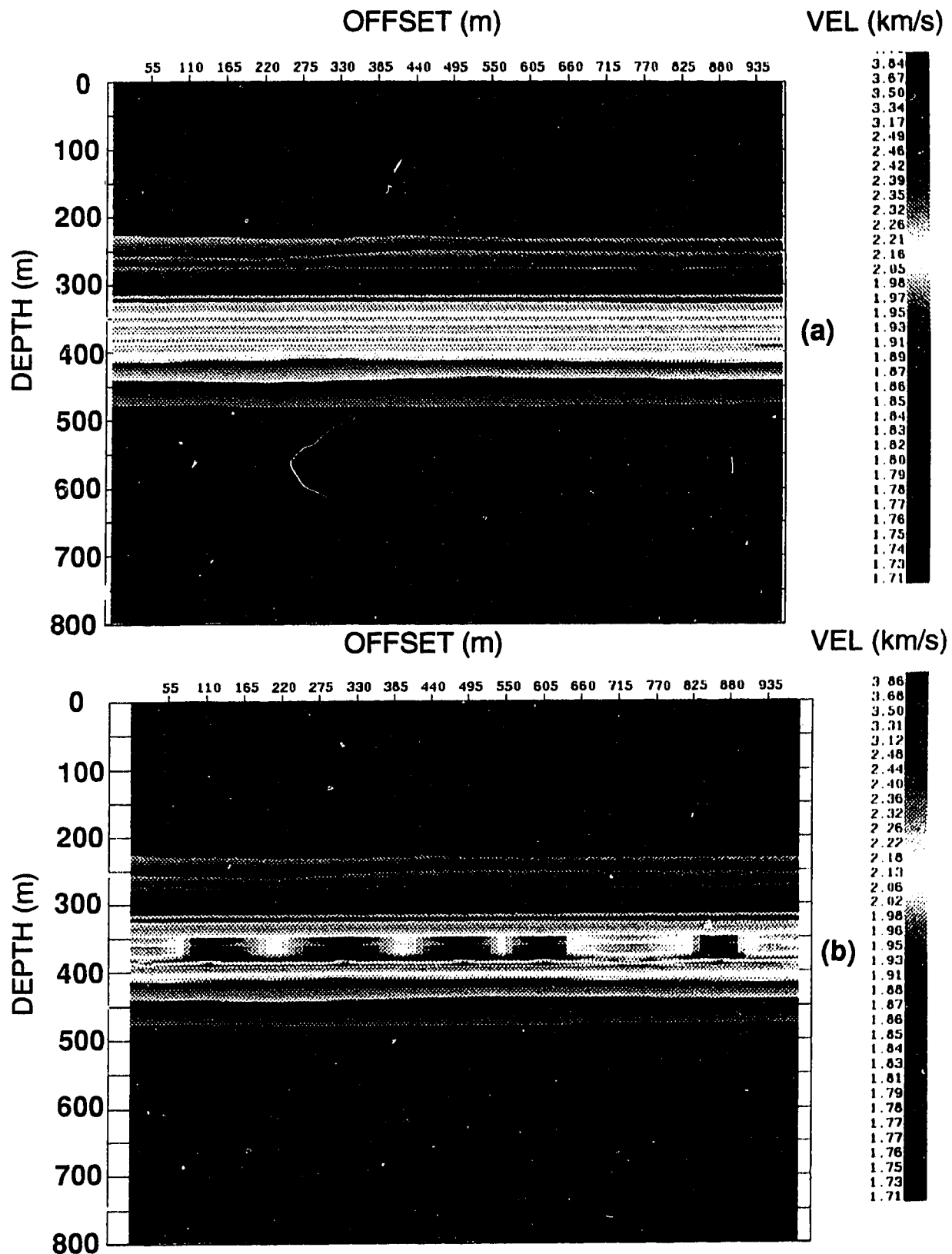
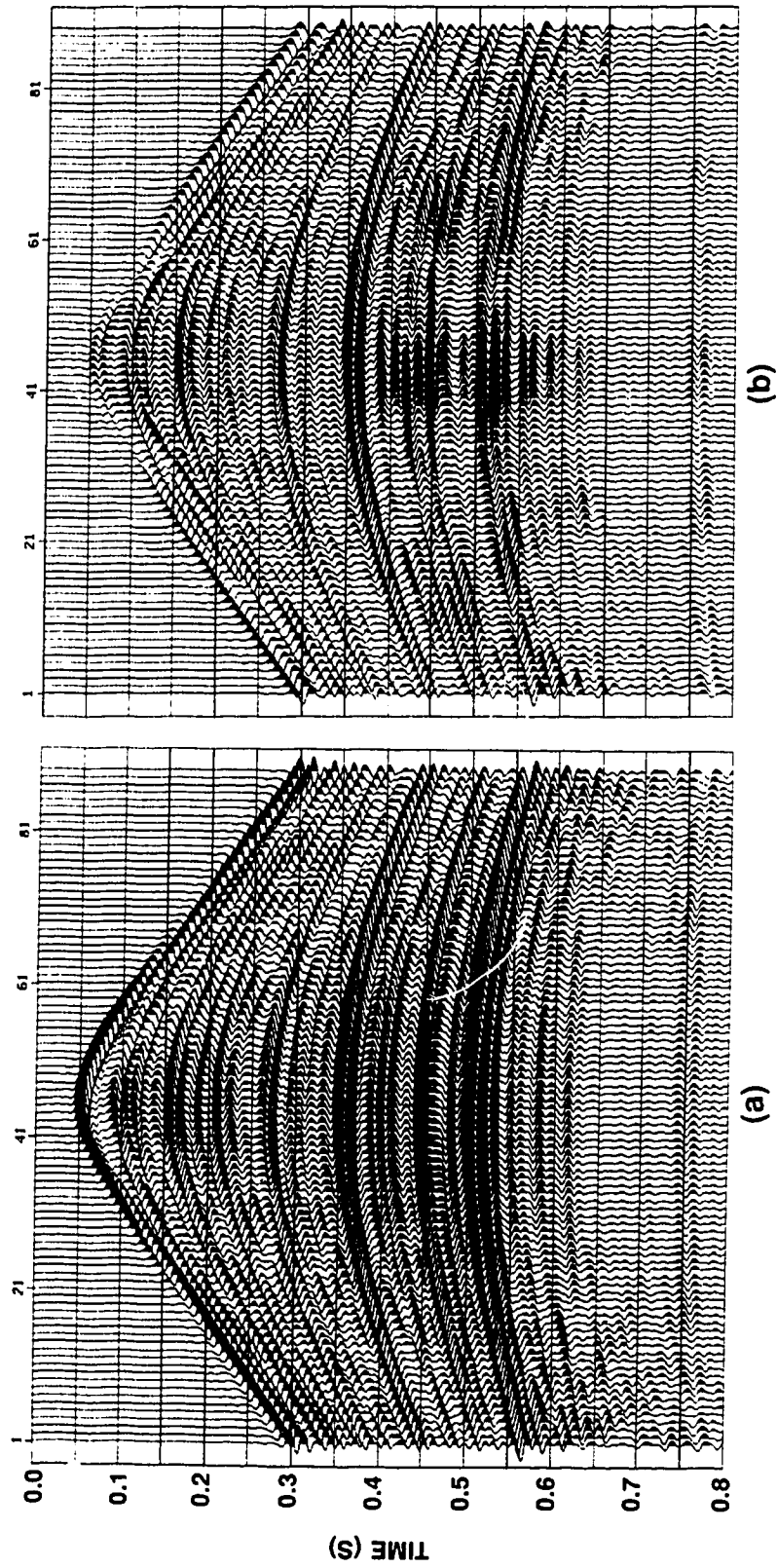
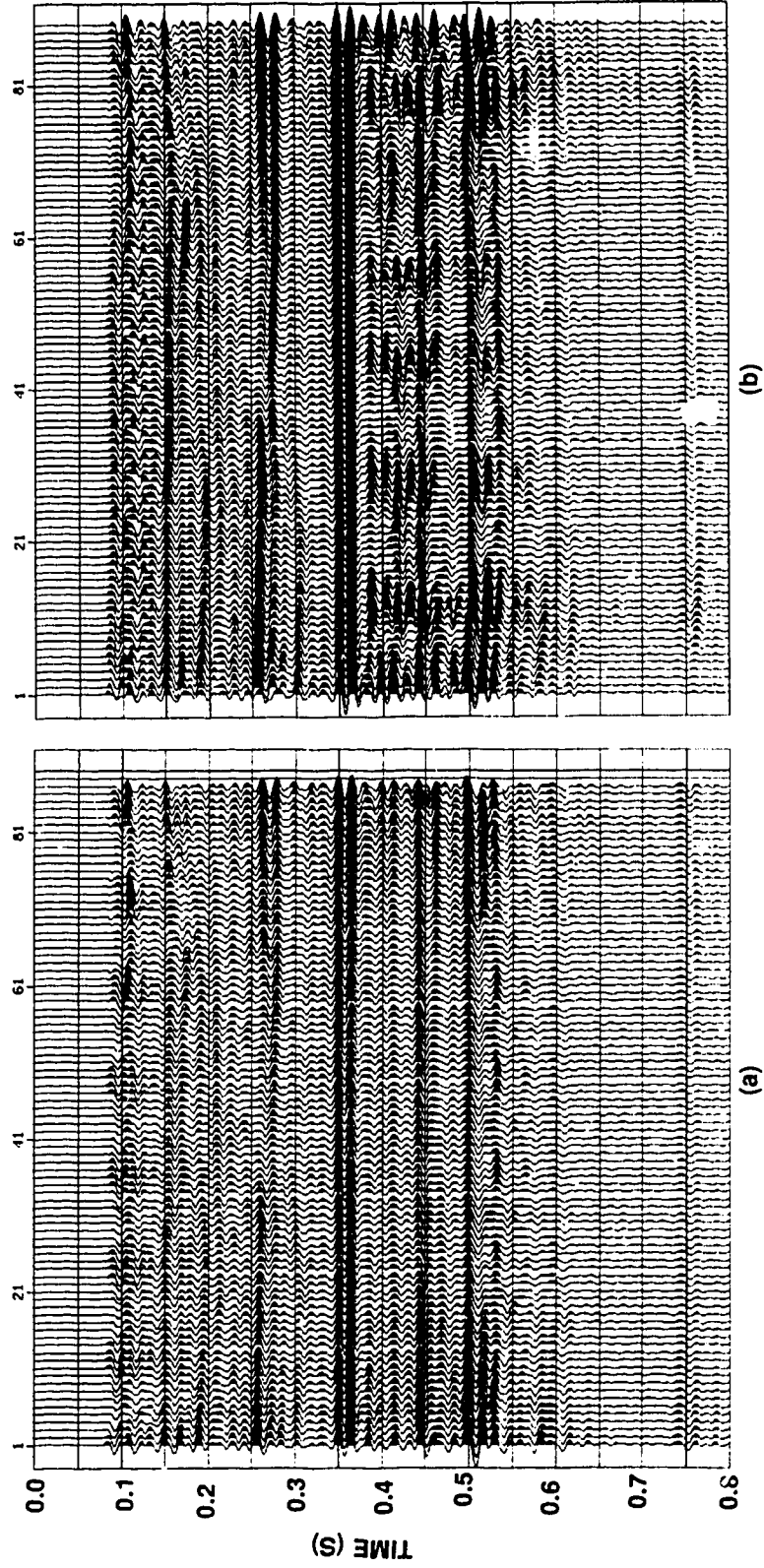


Figure 6.4.4: Velocity models used for 2-D elastic wave propagation simulations: (a) before the steaming process (base, no steam zones) and (b) during steam injection (monitor, steam zones).



**Figure 6.4.5:** Synthetic shot gathers (vertical particle velocity component) from elastic wave simulations for the models (Figure 6.4.4): (a) before the steaming process (base, no steam zones) and (b) during steam injection (monitor, steam zones)



**Figure 6.4.6 :** Stacked sections for the models (Figure 6.4.4): (a) before the steam stimulation process (base) and (b) during steam injection (monitor-steam).



#### 6.4.4 Processing of the 3-D Seismic Data

The processing sequence that was applied on both data sets (base and steam-monitor) by Mobil Oil was as follows: demultiplexing, static computations, true amplitude recovery, first break mute, deconvolution, dephase filter, equalization, velocity analysis (datum referenced), automatic surface consistent residual statics, big bin velocity analysis, normal moveout correction, CDP stack, dephase, filter, two-pass 3-D Kirchhoff f-k migration (dip controlled, stack velocity function), time invariant filter and equalization (Figure 6.4.7). On the other hand, our own processing involved energy balancing and one-pass 3-D depth migration of both base and steam-monitor stacked data volumes (Figure 6.4.7).

#### ENERGY BALANCING OF THE STACKED DATA

A global trace balancing was applied on both stacked sets (base 1987 and steam 1988) and it was calculated as follows. From the 3-D stacked data volume from the base survey a time window between 150 ms and 300 ms was selected. The reason for the selection of this time window is that within this interval the reflections are consistent and continuous and are located well above the steam-heated zone in the Sparky Sands. In a similar way as was described earlier, a *global factor* was calculated from the base data. Next for each trace in both data volumes (base and steam) a *trace factor* was computed. The ratio between the “global factor” and each “trace factor” results in a balancing factor (scaling factor) for that trace which is applied to all samples in the trace for both data sets. Consequently, both data sets have been normalized to a uniform amplitude energy. Therefore, differences between the two seismic monitors that may be due to differences in the source, water-table or any other effect not related to the EOR process should not be present anymore.

#### 3-D DEPTH MIGRATION OF THE ENERGY BALANCED STACKED DATA

3-D depth migration of both energy balanced stacked data volumes (base 1987 and steam 1988) was performed in order to generate seismic images with higher spatial and vertical resolution. Also, since we depth migrate the data the resultant seismic sections are in depth thus avoiding time to depth conversions and making the interpretation process easier. We used the one-pass 3-D depth migration algorithm (Chapter 4) with a small extrapolation step of 1 m which produces migrated images of high vertical resolution. Both

data sets were migrated using the same velocity model in order to preserve the differences in amplitude and time/depth of reflectors within and below the steam-heated reservoir. The migration was performed on 44 processors of a Myrias SPS3 parallel computer. The CPU time required for the migration (including I/O and FFT) of each data volume (90x73 CDPs and 1501 time samples) using 1500 depth steps and 250 frequencies was 9.16 hours.

#### **6.4.5 Attribute Analysis**

Prior to any processing we analysed the stacked data. Inline 12, from both stacked volumes (base 1987 and steam-monitor 1988), is shown in Figure 6.4.8. At the time of the monitor survey only two (16, 18) of the five wells along inline 12 were still steaming. We can observe clearly the amplitude anomalies (bright spots) associated with the steam injection when the monitor inline 12 is compared with the base. Furthermore, time delays are easily observed on the monitor for the reflectors below the reservoir (Sparky Sands between 0.375 and 0.4 s). This delay is more evident for the Devonian reflector (at about 0.5 s) and it is about 6 ms. Also, this is clearly seen when time slices from both base and steam data volumes are compared (Figure 6.4.9). Furthermore, when the amplitude spectrums (not shown here) of both base and monitor inline 12 are compared, a spectral attenuation was observed for the high frequencies on the steam inline within and below the Sparky reservoir.

We interpreted the Colony horizon (at about 0.34 s) on both base and steam data which is above the reservoir. The Colony travel time maps between the base and steam surveys were subtracted. The resultant time difference map (Figure 6.4.10.b) revealed significant time delays to the Colony during steaming although we expected no time delays on reflectors above the steam zones. Furthermore, the difference of the Colony horizon slices between monitor and base surveys show amplitude difference (Figure 6.4.10.a) with the Colony, during the monitor survey, having a decreased amplitude over most of the area. These amplitude changes and time delays on the Colony, indicate that effects other than the steaming ones exist and caused changes on the reflectors above the reservoir. Therefore, the changes that are observed on the reflectors within and below the reservoir are due to the combined steaming effects with others such as source changes and variations in the water table. Therefore, it is necessary to energy balance, to correct for the effects not related to the steaming process. Also, instead of comparing travel time maps that are referenced to the surface we should compare isochrone maps which are referenced to the Colony, in order to remove the time delays that are not due to the steaming effect.

The Devonian reflector was interpreted on both energy balanced stacked data volumes. The amplitude difference (Figure 6.4.11) between the two horizon slices (monitor-base) show that the Devonian has dimmed during steaming. The main anomaly is in agreement with the stress field in this area thus suggesting that the most of the steam is moving through preexisting fracturing paths. On the other hand, the difference between the Devonian isochrone maps (taken with respect to the Colony at each survey) from the base and steam surveys show a large time delay (Figure 6.4.11). This time delay correlates with the steaming wells at the time of the monitor survey (wells 16, 18, 13, 3, 6). However, the major time delay anomaly (blue colour, ~5 ms) does not correlate with the amplitude anomaly very well.

Next we analysed the depth migrated data volumes. In Figure 6.4.12 the inline 12 from both the base and steam migrated data is shown. Along this line only two wells (16, 18) were still steaming. The effect on the seismic reflections of the steam injection can be observed on the monitor inline 12 when compared to the base one. The amplitude of the reflectors within the Sparky reservoir in the vicinity of the steaming wells is increased, especially notice the bright spot around CDP 40 ( on inline 14, not shown here, the bright spot is on CDP 44). Furthermore, changes in the seismic signature such as amplitude decreases and depth pushdowns can be observed. For example, the Devonian shows an apparent depth pushdown in the steam data. Similar effects on the seismic reflectors within and below the reservoir can be observed on the monitor data such as on crossline 44 (Figure 6.4.13). Along this line three wells (18,13, 3) are still steaming. In addition increased fracturing is seen in the reservoir and the shale below it in the vicinity of well 3. Dramatic changes in the reflectors, such as time delays (velocity sags) and amplitude changes, within the reservoir can be observed on the monitor data (e.g., inline 60, Figure 6.4.14) as we move close to well 3 which is still steaming

Next, the Devonian reflector was interpreted on both base and monitor data. The Devonian isopach maps generated with respect to the Colony (above the reservoir) were differenced. The resultant apparent depth difference (pushdown) shows an anomaly that is mostly concentrated in the east side of the pad (Figure 6.4.15). However, pushdowns are observed in the vicinity of all steaming wells (16, 18, 13, 6, 3). Next, the Devonian horizon slices are differenced (base-monitor) to obtain an amplitude anomaly map. The resultant anomalies show the areal amplitude decrease of the Devonian during steam injection and they show large amplitude decreases in the vicinity of the steaming wells (3, 6, 13, 16, 18). Furthermore, semicircular anomalies propagate downwards (from north to south) may associated with an expanding steam zone from north to southeast due to the

high pressure in the center of the pad (wells 18, 13, 3) and very low pressure in the east side of the pad (drawdown wells). Both the amplitude and depth anomalies (Figure 6.4.16) are in general agreement with the corresponding anomalies observed on amplitude difference and time delay maps generated from the data before migration (Figure 6.4.11; opposite colour scale is used).

The Upper Sparky (about 355 m) horizon was interpreted on both base and monitor-steam depth migrated data volumes. The isopach maps generated with respect to the Colony (above the reservoir) were differenced (Figure 6.4.15). The resultant apparent depth difference (pushdown) shows an anomaly that is mostly concentrated in the east side of the pad. However, pushdowns are observed in the vicinity of all steaming wells (16, 18, 13, 6, 3). Additionally, the difference between the base and steam horizon slices shows anomalies associated with the steaming wells. Furthermore, semicircular anomalies propagate downwards (from north to south) and may be associated with an expanding steam front from north to southeast that is caused by the differential pressure between the high pressure in the center of the pad ( steam injection wells 18, 13, 3) and very low pressure in the east side of the pad (drawdown wells).

In addition to the above analysis, other horizons such as the Middle Sparky, the GP kick and the Clearwater were interpreted. Seismic attribute analysis, such as travel time and amplitude differencing, generated seismic images (not presented here) that show anomalies that correlated well to the pressure states of the wells and were in agreement with the anomalies discussed above.

#### **6.4.6 Discussion of Results from Mobil's Experiment**

By integrating all the available information detailed velocity models were constructed that represent reservoir condition prior to any steaming (base). Additionally, these models included steam zones that simulated the hydraulic reservoir systems in the Sparky Sands during steam stimulation. Using these models elastic wave simulations during different phases of the EOR process such as before any steaming (base) and during steam injection (steam-monitor) were performed. The resultant realistic seismic sections were able to show the effects on reflections within and below the Sparky reservoir due to the presence of an expanded steam-heated zone.

*(Text continued on page 241)*

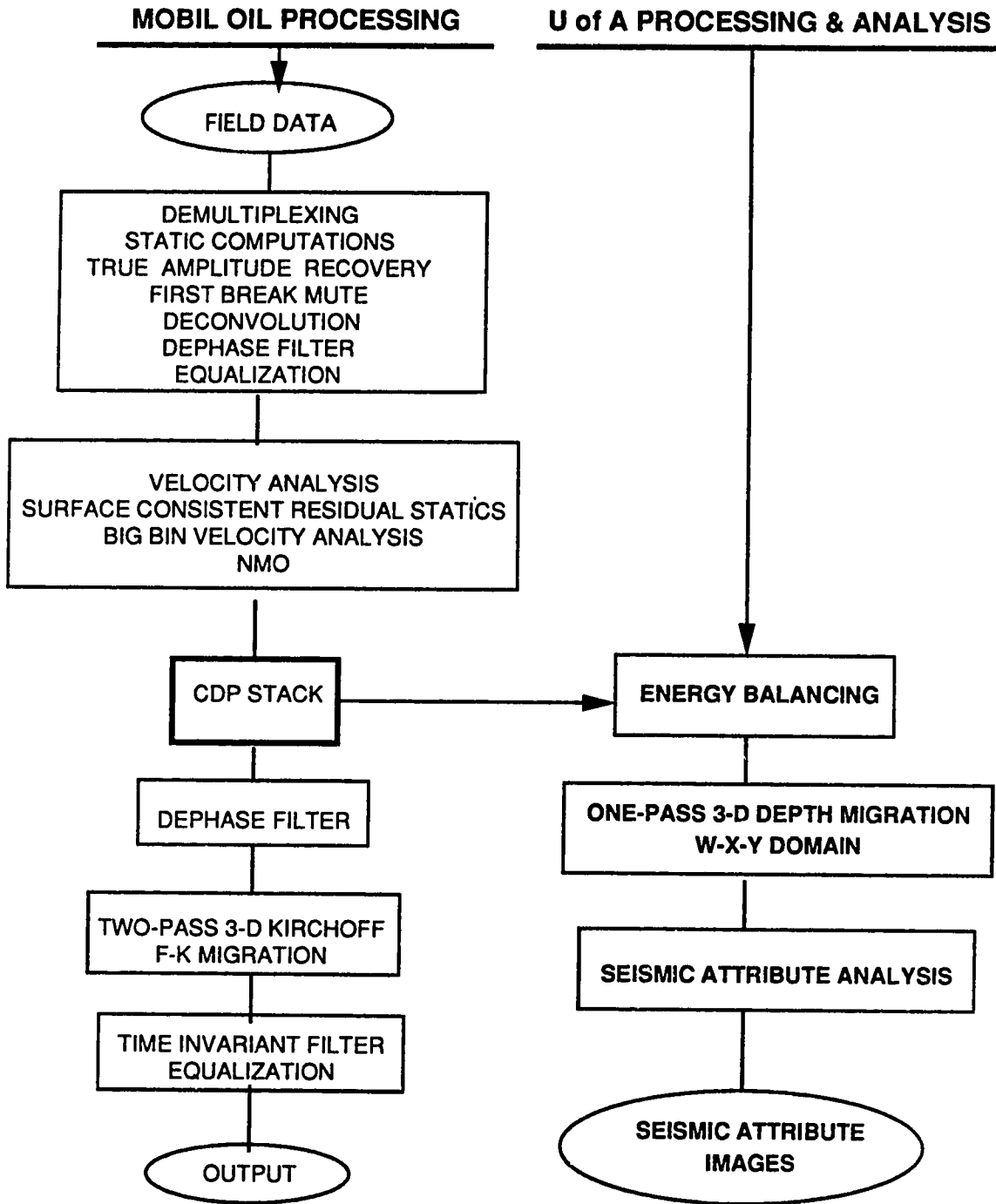


**Figure 6.4.7:** The processing flows as they were applied on both data sets (base and steam-monitor) by Mobil Oil and the Seismology Laboratory, University of Alberta (this research).

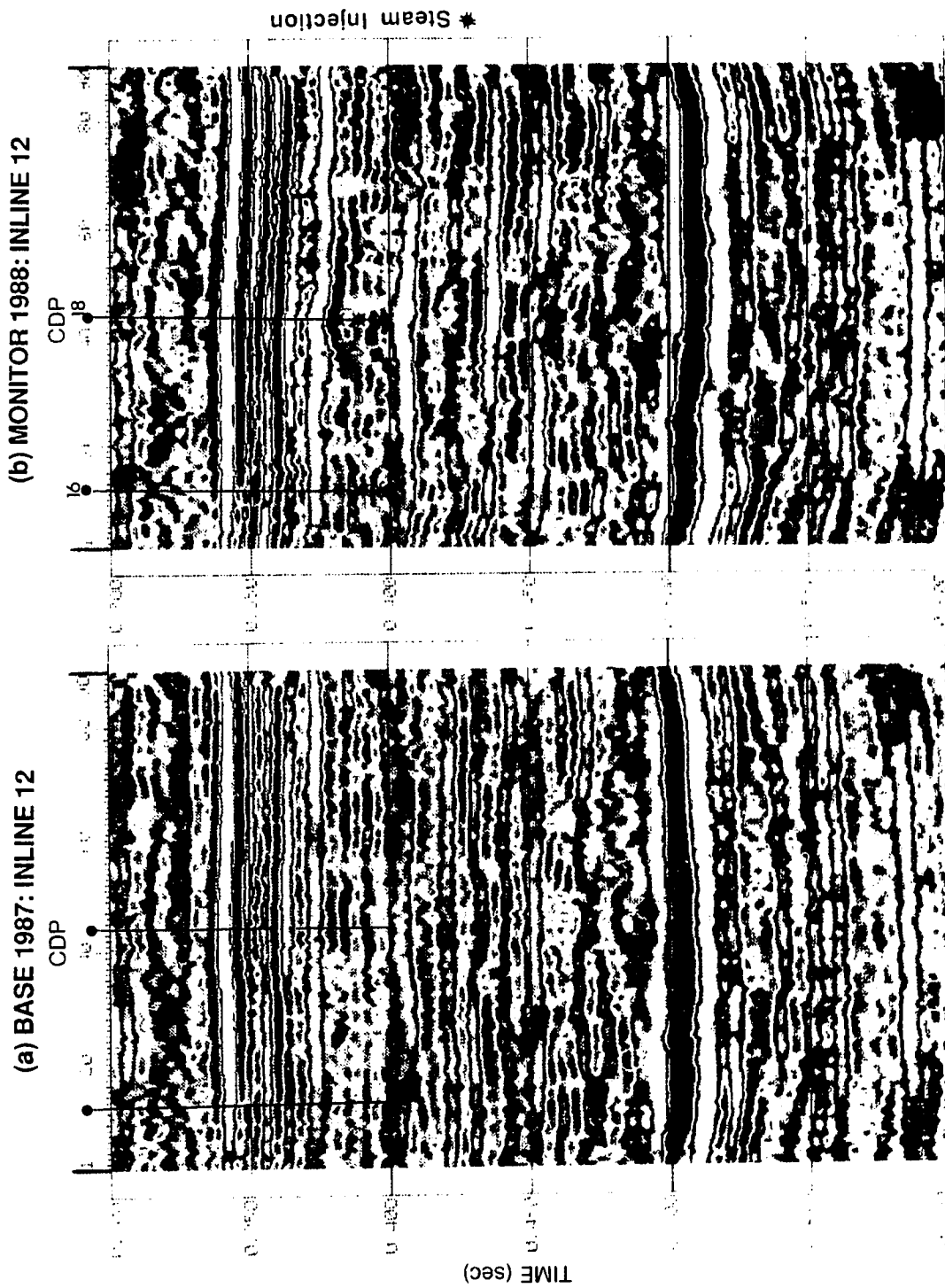


Figure 6.4.8: The inline 12 from the stacked data sets: (a) base and (b) steam-monitor.

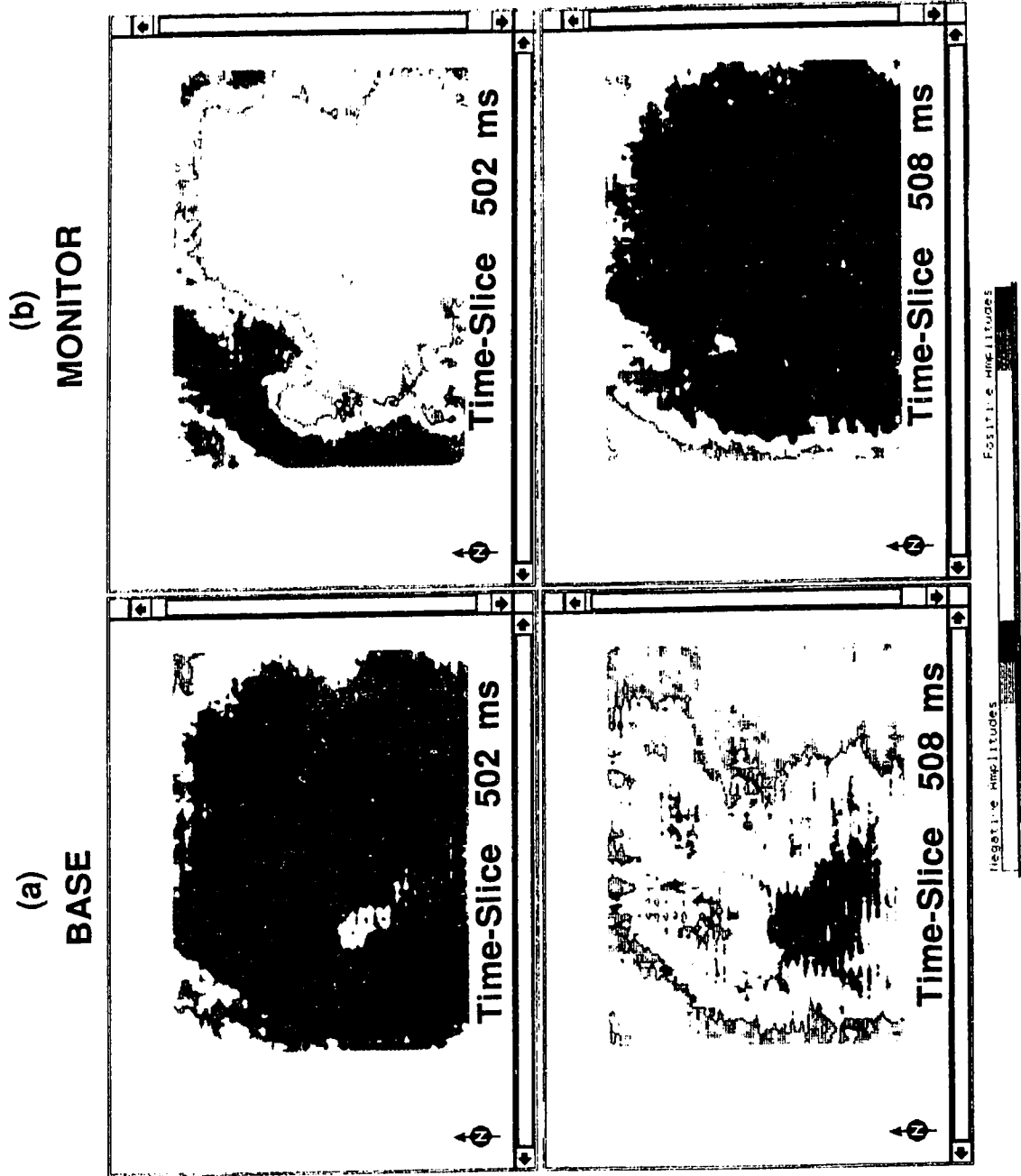


Figure 6.4.9: Time slices from the stacked data volumes: (a) base and (b) steam-monitor.

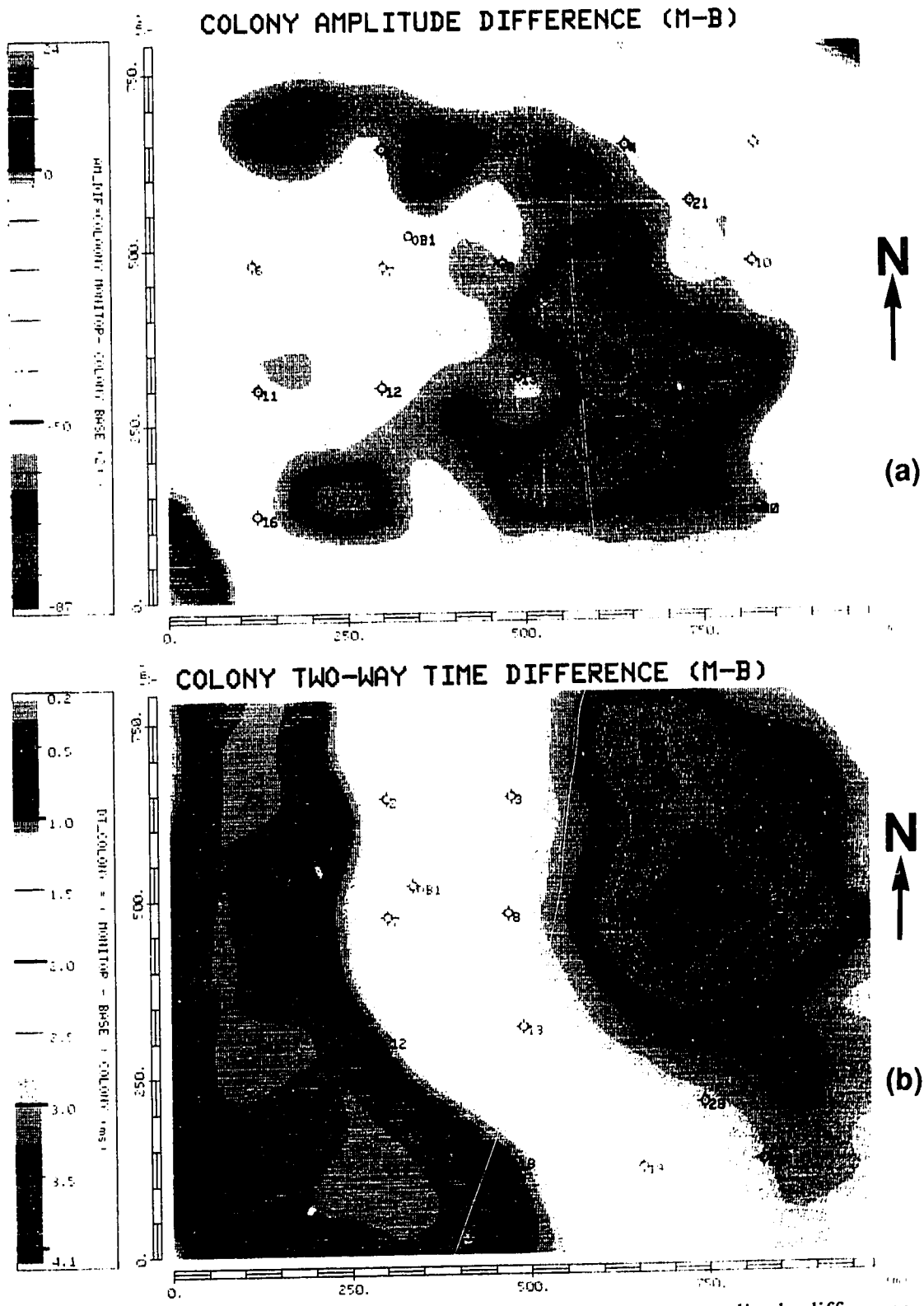
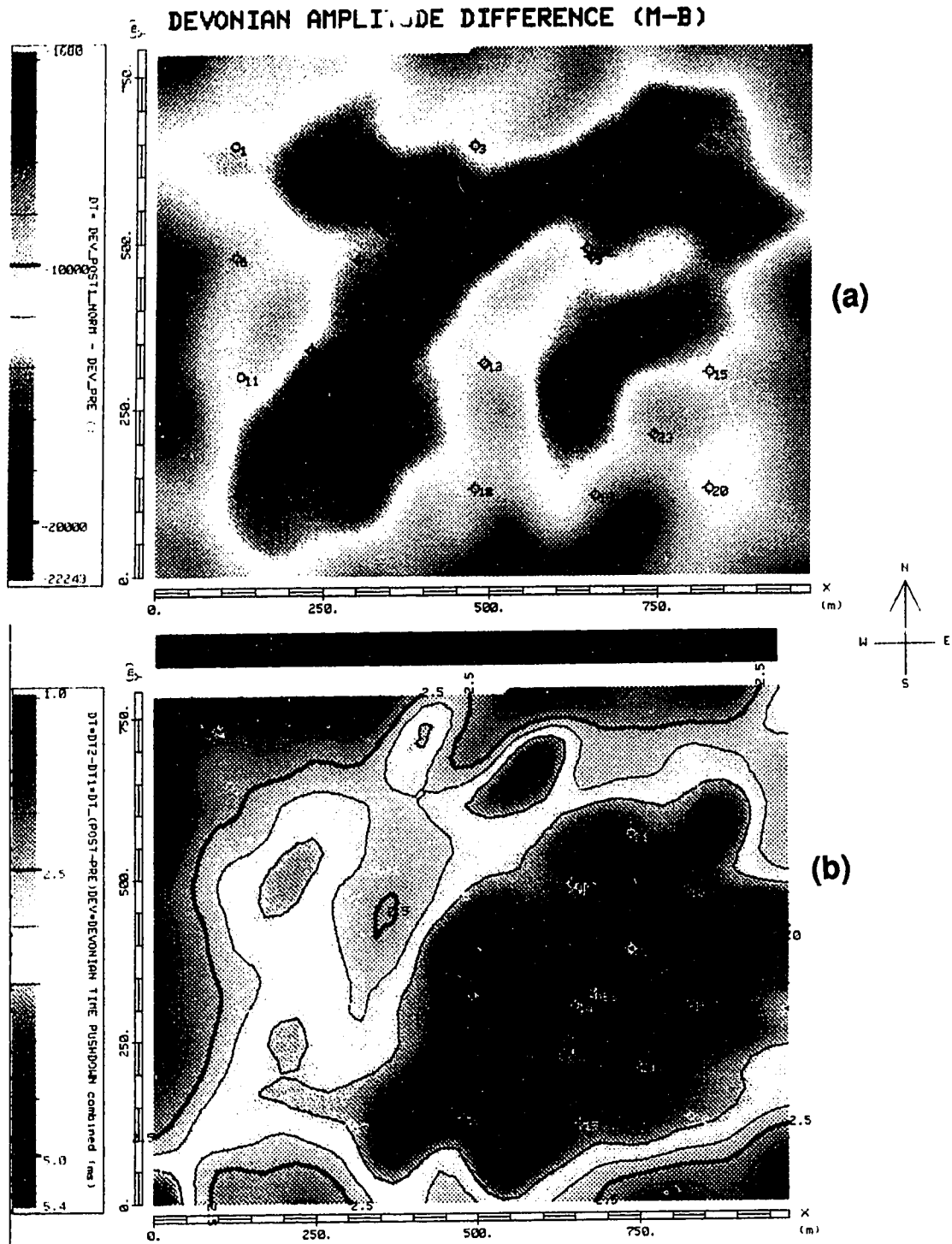


Figure 6.4.10: The Colony horizon from the stacked data: (a) the amplitude difference and (b) the time difference (pushdown) between the monitor and the base surveys.





**Figure 6.4.11:** The Devonian horizon from the stacked data after normalization: (a) the amplitude difference and (b) the time delay (pushdown) between monitor and base surveys.

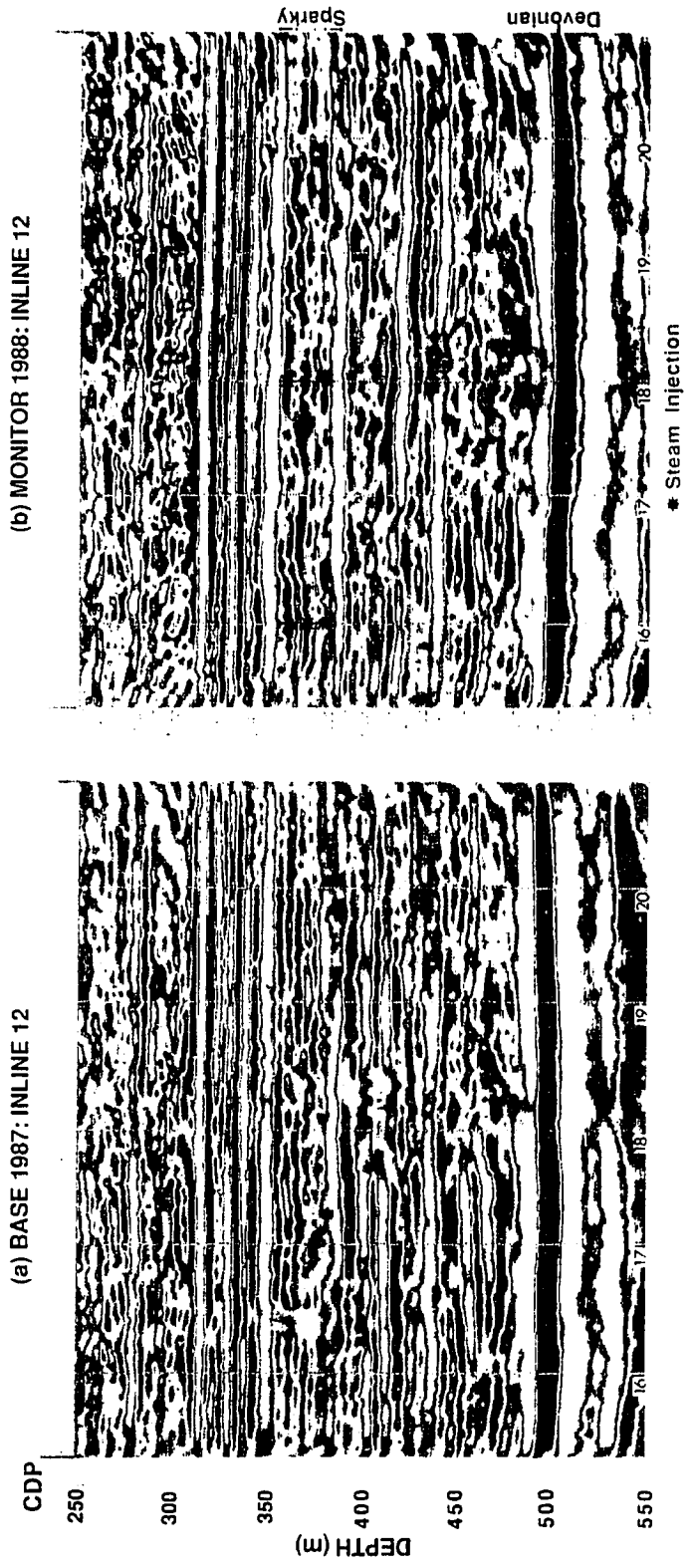


Figure 6.4.12: The inline 12 from the depth migrated data: (a) base (1987), and (b) steam-monitor (1988).

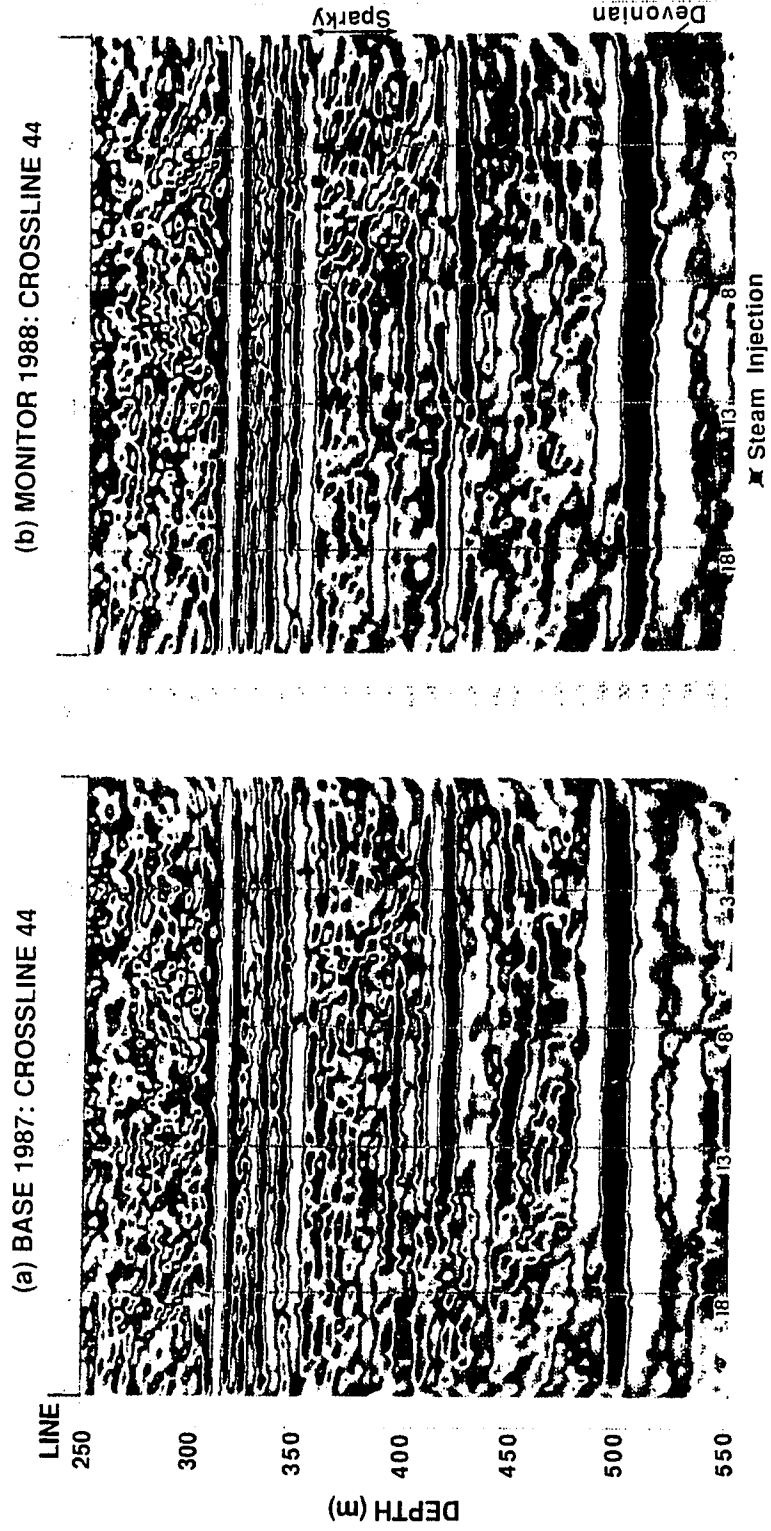


Figure 6.4.13: The crossline 44 from the depth migrated data: (a) base (1987), and (b) steam-monitor (1988).

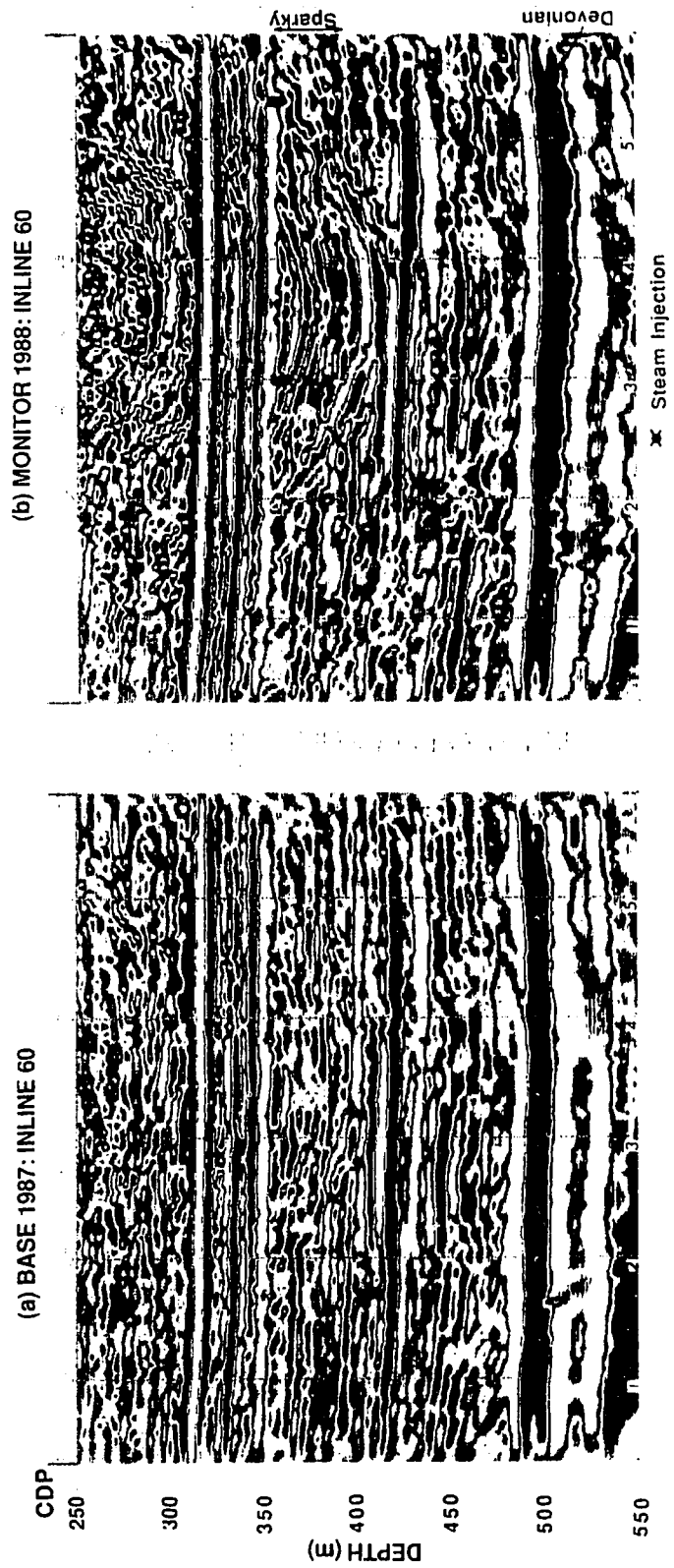


Figure 6.4.14: The inline 60 from the depth migrated data: (a) base (1987), and (b) steam-monitor (1988).

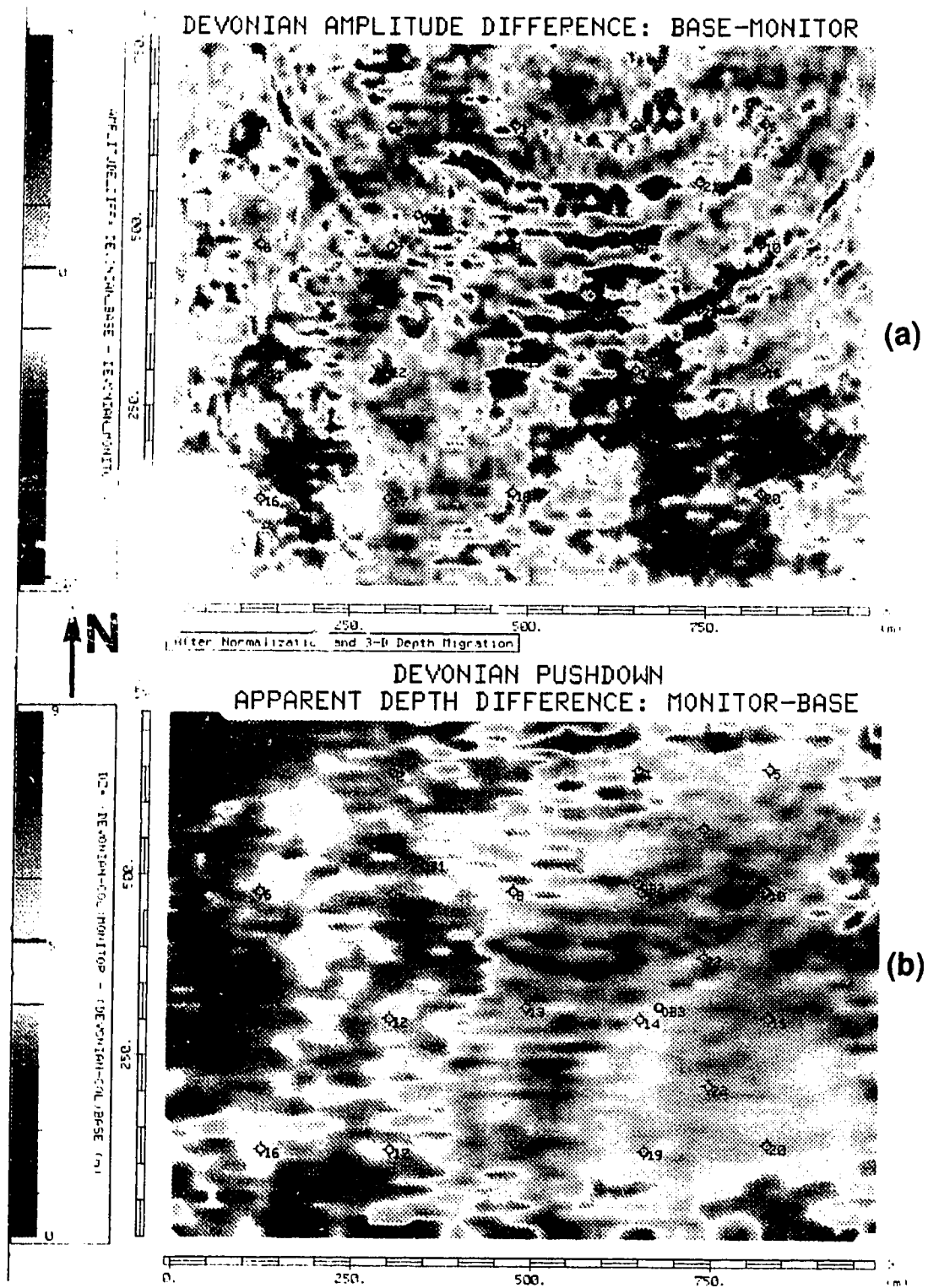


Figure 6.4.15: The Devonian horizon from the depth migrated data: (a) the amplitude difference between base and monitor and (b) the apparent depth pushdown between monitor and base.

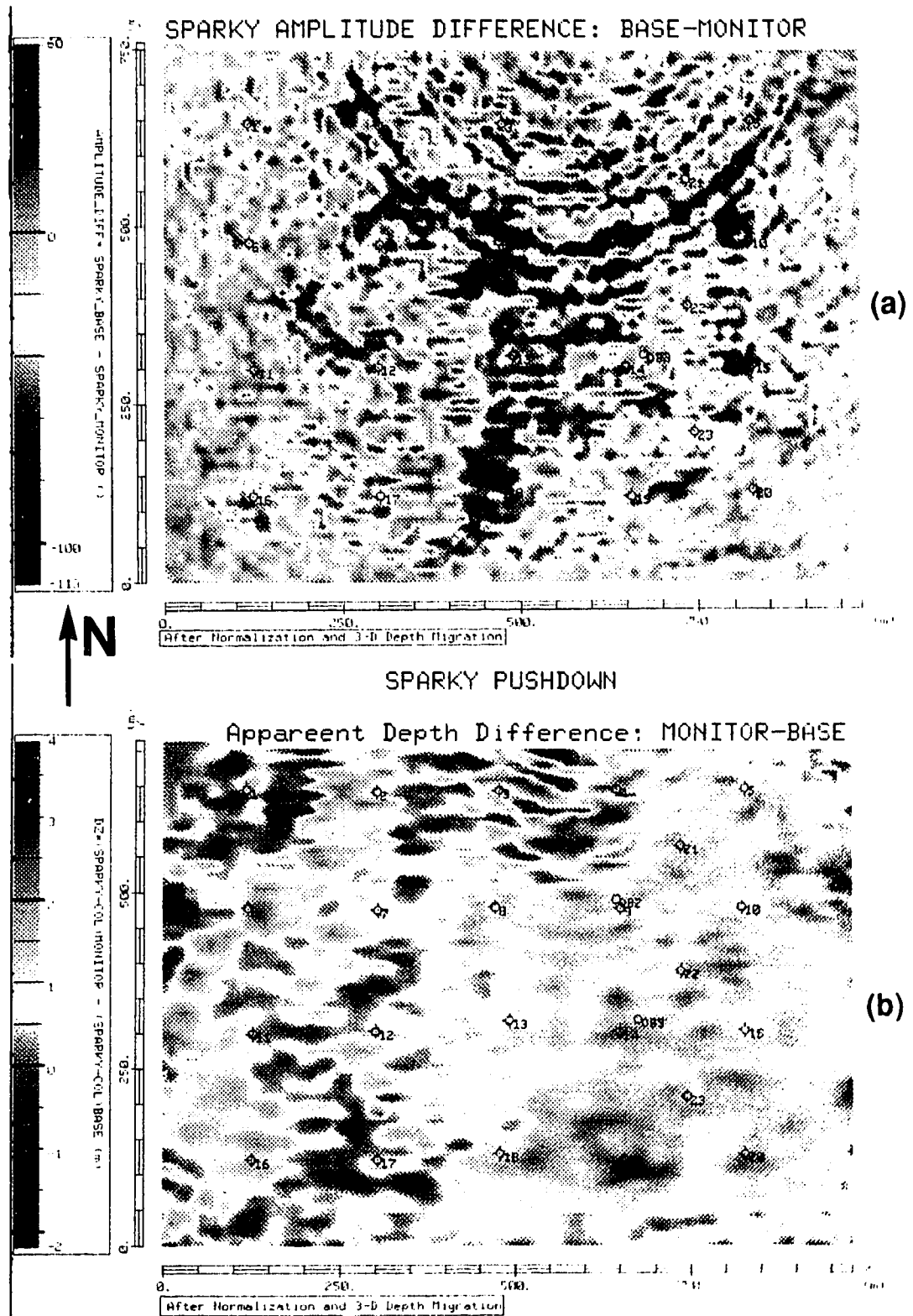


Figure 6.4.16: The Sparky horizon from the depth migrated data: (a) the amplitude difference between base and monitor and (b) the apparent depth pushdown between monitor and base.

Additional processing was performed on the 3-D seismic data in order to remove all the effects not associated with the steam stimulation by energy balancing the base and steam-monitor stacked data volumes. Furthermore, the one-pass 3-D implicit finite difference depth migration algorithm developed in this thesis was used to migrate both seismic surveys resulting in high resolution depth seismic images (1 m vertical resolution).

The analysis of the stacked data showed effects on the seismic attributes that were not related to the steam stimulation only thus showing the need of the energy balancing between the base and monitor surveys. Further analysis using the depth migrated data generated high resolution seismic images within and below the reservoir. The observed seismic attribute anomalies are functions of a number of variables such as velocity, reflectivity and attenuation and resulted in time or depth pushdowns, amplitude bright spots or dim spots, and spectral modifications. Anomalies observed within the reservoir in the vicinity of the steaming wells (high pressure) are the direct result of velocity decrease and amplitude increase associated with the rock and fluid compressibility increases which were caused by the high fluid pressures (small effective stress) and the high temperature (steam). Furthermore, anomalies (bright spots or dim spots) observed in the vicinity of drawdown wells (flow back, small pressures) may be associated with the higher gas saturation in those areas of the reservoir (gas evolution will produce a bright spot) or to residual effects from the completed steam cycle (for these wells) such as gas reduction (dim spot). In conclusion, the observed seismic attribute anomalies generally correlate well with the pressure and steaming states of the wells on the pad.

## **5. CONCLUSION ON SEISMIC MONITORING OF EOR PROCESSES**

High resolution realistic models (velocity, density) for Imperial Oil's D3-pad and Mobil Oil's vertical pilot site were generated before, during and after underwent cyclic steam stimulation for bitumen recovery for the Cold Lake oil sands. These models were generated by successfully integrating all available information such as sonic and density logs, 3-D seismic data, crosswell data, geologic data, and reservoir engineering data from observation wells. 2-D and 3-D acoustic and elastic wave simulations were carried out for these models by implementing the sophisticated and computationally efficient 2-D elastic and 3-D acoustic modeling algorithms developed in this thesis on powerful supercomputers. The generated synthetic seismic data resolved the geological structure and, as well, they displayed calcified tight streaks in the oil sands reservoirs. These tight shales are of critical importance for the oil recovery process since they act as permeability barriers

that impede vertical migration of the steam. Wave simulations were performed during different phases of the EOR process such as before any steaming (base), steam injection and production (monitors). The resultant sections showed the effects on the seismic signature of the reservoir conditions during the different phases of the EOR process. Also, they resolve the steam-heated zones. Furthermore, the wave simulations provided us with a better understanding, of the relation between the seismic characteristics such as velocity, amplitude and frequency with the reservoir conditions such as pressure, temperature and gas saturation that proved to be valuable during the interpretation of the real data. Therefore, the modeling algorithms developed in this thesis prove to be valuable tools in understanding seismic changes occurring during the steam stimulation process.

Additional processing was performed on the 3-D seismic data in order to remove all the effects not associated with steam stimulation by normalizing the two monitor data sets (energy balancing). Furthermore, the one-pass 3-D implicit finite difference depth migration algorithm developed in this thesis was used to migrate all 3-D seismic monitoring surveys resulting in high resolution seismic images.

During production the reservoir conditions near the boreholes are at a local minimum in terms of fluid pressure (high effective stress) and temperature but at a maximum in terms of gas saturation. On the other hand, during the steam cycle the reservoir conditions are at a local maximum in terms of fluid pressure and temperature but at a minimum in terms of gas saturation. The changing conditions are a major source for alteration of the seismic signature and the cause of seismic anomalies during steam injection and production.

Seismic attribute analysis was performed in a number of different ways on all data sets. The images from the depth migrated data have high resolution and more accuracy due to the better migration algorithms used and thus more emphasis was given to these data sets. The generated images showed seismic anomalies such as time delays, depth pushdowns, velocity decreases, spectral modifications and amplitude changes, that are associated with the expanding steam-heated zone during the steam injection phase and the gas presence during production. Also, these anomalies imaged the expanding steam front and suggested areal and vertical conformances. Furthermore, these anomalies were well correlated to the areal location of the pressure and temperature states of the wells on the pads. This suggested that the anomalies on the seismic signature, imaged from the seismic attribute analysis of the monitoring data (base, steam, production cycles), are the combined result of a decrease in the effective stress, a temperature increase, and gas reduction during the steam phase with respect to the production phase.

Overall, the generated seismic images correlate well with the observed field



performance behavior. However, a quantitative correlation is required in order to obtain estimates of reservoir properties such as saturation and permeability from the above seismic images. This may be possible with the utilization of geostatistical estimation methods such as kriging. Ideally, seismic surveys should have been conducted over shorter time intervals (e.g., 4 to 6 month intervals) to enable better forecasting of the steam front movement, and to assist in the balancing of reservoir voidage at the production wells in attempt to exercise some control over the reservoir sweep mechanism. Furthermore, a base survey (prior to any steaming) is of critical importance since it can provide a reference data set that can be used in conjunction with the monitor data sets for seismic attribute differencing analysis and the mapping of the vertical steam conformance.

The reported results imply that reservoir parameters may be detected *in-situ* using reflection seismology to map the spatial heterogeneity of porosity and permeability, detect anomalous pore pressure and its temporal variations, detect subsurface fractures, track thermal fronts, monitor the movement of gas caps and track the steam front in steam stimulation. We believe that with advent of the new vector and parallel computers and sophisticated interactive workstations, 3-D high resolution surface seismic time-lapse monitoring is a feasible and potentially powerful technique that can be used for the design and efficient management of the thermally enhanced oil (EOR) recovery from the enormous reserves in the tar sands at Cold Lake, Alberta.

## REFERENCES

- Britton, M.W., Martin, W.L., Leibrecht, R.J. and Harmon, R.A., 1983, Street ranch pilot test of fracture-assisted steamflood technology: *J. Petr. Tech.*, 35, 511-522.
- Eastwood, J., Lebel, P., Dilay, A., and Blakeslee, S., 1994, Seismic monitoring of steam-based recovery of bitumen: *The Leading Edge*, 13, No. 4, 242-251.
- Greaves, R.J. and Fulp, T.J., 1987, Three-dimensional seismic monitoring of an enhanced oil recovery process: *Geophysics*, 52, 1175-1187.
- Kalantzis, F., Kanasevich, E.R., Dai, N., and Udey, N., 1993a, 3-D seismic monitoring of thermal EOR processes, case I: initial results: CSEG National Convention, Calgary, Expanded Abstracts, 66-67.
- Kalantzis, F., Kanasevich, E.R., Dai, N., Kostyukevich, A., and Udey, N., 1993b, 3-D seismic reflection imaging over thermally enhanced oil recovery sites: SEG Summer Research Workshop, California, Expanded Abstracts, 382-385.

- Kalantzis, F., Kanasewich, E.R., Dai, N., Kostyukevich, A., and Udey, N., 1993c, Imaging of reflection seismic wavefields in thermally enhanced oil recovery projects: 63rd Annual Intern. Meeting, Soc. Expl. Geophys., Expanded Abstracts, 335- 338.
- Kalantzis, F., Kanasewich, E.R., Kostyukevich, A., and Udey, N., 1994, Integrated time-lapse reservoir monitoring: Modeling and Imaging: CSEG National Convention, Calgary, Expanded Abstracts, p. 122-123.
- Macrides, C.G., Kanasewich, E.R., and Bharatha, S., 1988, Multiborehole seismic imaging in steam injection heavy oil recovery projects: *Geophysics*, **53**, 65-75.
- Matthews, L., 1992, 3-D seismic monitoring of an in-situ thermal process: Athabasca Canada, *in* R. Sheriff (Ed.). *Reservoir Geophysics: Society of Exploration Geophysicists*.
- Paulson, B.N.P., Smith, M.E., Tucker, K.E., and Fairborn, J.W., 1992, Characterization of a steamed oil reservoir using cross-well seismology: *The Leading Edge*, **11**, No. 7, 24-32.
- Paulson, B.N.P., Meredith, J.A., Wang, Z., and Fairborn, J.W., 1994, The Steepbank crosswell seismic project: Reservoir definition and evaluation of steamflood technology in Alberta tar sands: *The Leading Edge*, **13**, No. 7, 737- 747.
- Siewert, A., 1993, 3-D seismic monitoring of a steam stimulation process under frac pressures at the Iron River vertical pilot, Cold Lake, Alberta: CSEG National Convention, Calgary, Expanded Abstracts, 64-65.
- Tsingas, C., 1991, Seismic reflection amplitude versus angle variations over a thermally enhanced oil recovery site: *Geophysics*, **56**, 292-301.

## CHAPTER 7

# IMAGING OF GROUND-PENETRATING RADAR DATA FOR CHARACTERIZATION OF NUCLEAR WASTE REPOSITORIES

### 7.1 INTRODUCTION

Ground-Penetrating Radar (GPR) is being used to map the earth's shallow subsurface in engineering applications, groundwater detection, environmental and archaeological site assessment. Annan et al. (1992) used GPR for monitoring dielectric permittivity of a dense non-aqueous phase liquid (DNAPL) migrating into a sandy aquifer. Roberts et al. (1992) used 3-D GPR for the detection of buried steel drums. GPR was also selected by Wood et al. (1993) as a potential technique for hazardous-waste investigations in southern California. Annan et al. (1991) used GPR to detect and map the water table. Friedel et al. (1991) used common offset radar for detecting small scale fractures in igneous rock. Imai et al. (1987) used ground-penetrating radar for archaeological investigations.

All the countries producing nuclear generated electrical power encounter the problem of management and disposal of the nuclear waste. At present many of these countries are researching methods for underground disposal of high level nuclear waste. As part of the Canadian Nuclear Fuel Waste Management Program, Atomic Energy of Canada Limited (AECL) is studying the plutonic rock of the Canadian Shield as a medium for disposal of nuclear waste (Dormuth et al., 1987). One important aspect of this research involves the determination of the structure and physical parameters of granitic rock.

A variety of geophysical methods are being used for identifying fractures and zones of structural weakness prior to underground excavation. Ground-penetrating radar surveys may be used to discover fracture zones in igneous bodies for distances of 100 m or more from the surface or from boreholes and mine shafts. The radar reflection method is based on backscattering from discontinuities in dielectric constants within a rock mass. Although the radar reflection method uses electromagnetic waves in the 10 to 1000 MHz frequency band, there are similarities to the seismic reflection method which uses viscoelastic waves in the 10 to 1000 Hz band. A radar profile is similar to a seismic shot gather or a CDP

stacked seismic section, depending on the radar survey geometry. Therefore, many of the processing techniques that have been developed for seismic data processing can be directly applied to radar data.

One of the most powerful methods among a large number of seismic processing techniques is the migration method. It positions dipping and diffracted data to their true subsurface location resulting in a correctly focused image with increased spatial resolution. Claerbout (1976, 1985) and Yilmaz (1987) have discussed extensively seismic migration and other processing methods. A number of investigators have applied seismic processing algorithms to radar data including, a number of different migrations such as split-step Fourier migration (Fisher et al., 1992; Hu, 1992), Kirchhoff migration (Hogan, 1988), reverse-time migration (Fisher et al., 1992),  $\omega$ -x depth migration (Kalantzis et al., 1994).

In this paper we apply both commercially available and our own seismic processing algorithms such as frequency-space depth migration to GPR data from AECL's Whiteshell research area in Manitoba in order to detect and image fracture zones in the plutonic rock.

## 7.2 GEOPHYSICAL METHODOLOGY

The Whiteshell research area (WRA) is located near Pinawa in southeastern Manitoba, Canada (Figure 7.1) and is one of AECL's principal geoscience research sites. An extensive drilling program has been carried out in the granitic Lac du Bonnet Batholith near the western margin of the the exposed Precambrian Shield. The Underground Research Laboratory (URL) has a vertical shaft and two main working levels (Figure 7.2) at 240 and 420 m depth. The research carried out at WRA has two main objectives: (1) to apply and refine geophysical methods for characterization of potential disposal vault sites in igneous rocks of the Canadian Shield and (2) to refine and calibrate the regional geosphere model for use in hypothetical disposal vault performance assessment calculations.

Geophysical techniques are used for site screening, evaluation and excavation-scale characterization (Soonawala et al., 1990). The methods used for site screening and evaluation are airborne and surface magnetic and electromagnetic (EM), surface gravity and surface seismic reflection. The methods used for site characterization, such as detecting, characterizing and mapping fractures zones within the plutonic rock mass (P-wave velocity 5000~6000 m/s, radar wave velocity  $1.2 \times 10^8$  m/s), are well logs, high resolution seismic reflection (1000 Hz), crosshole seismic tomography (5 kHz) (Hayles et al., 1994), mini-crosshole seismic tomography (50 kHz) (Hayles et al., 1991; Wong et al., 1985), surface radar (25~100 MHz) and borehole radar (20~60 MHz).

Fractures are characterized by one or more geophysical responses such as low resistivity, low acoustic velocity, low density, high apparent porosity. At URL the above methods have confirmed the existence of two major low dipping fracture zones (FZ-2, FZ-3) in the rock mass (Figure 7.2) which subcrop to the northwest of the shaft. One fracture zone (FZ-2) is located about 20 to 30 m below the 240 m level at the shaft of the URL site (Stevens et al., 1994).

Among the many geophysical experiments performed at WRA are surface reflection Ground Penetrating Radar (GPR) surveys over fracture zones in the upper 100 m of the granite, single-hole reflection and crosshole tomographic radar surveys from the URL excavation levels (Holloway et al., 1992; Stevens et al., 1994).

### **7.3 GEOLOGY OF THE WHITESHELL RESEARCH AREA**

The Lac du Bonnet Batholith is located in the southern part of the English River subprovince of the Superior Province of the Canadian Shield (Brown et al., 1989). It has an east-northeast direction and about 1500 km<sup>2</sup> of it are exposed east of the Paleozoic cover. It is a relatively homogeneous body mainly composed of pink, porphyritic granite-granodiorite and xenolith-bearing granite in the upper part and an impermeable grey granite-quartz monzonite below 350 m.

The outcrop surfaces are low relief and easily accessible for radar surveying. The structural features significant for the GPR studies are low-intermediate-dipping (0~20°; Brown et al., 1989) fractures that are scattered at the surface but reduce to well defined fault zones at depth. Borehole information in the vicinity of the GPR profiling areas often shows subhorizontal fracturing in the top 100 m of the granite. Radar profiles from the outcrops around these boreholes give information about the nature and areal extent of this fracturing.

### **7.4 GROUND-PENETRATING RADAR METHOD**

The radar reflection method is based on back scattering from discontinuities of the dielectric constant in the rock. Ground Penetrating Radar (GPR) systems transmit a short pulse of electromagnetic energy from an antenna into the ground. The reflected energy from a discontinuity depends on the contrast between the relative dielectric constant ( $\epsilon_r$ ) and the electrical conductivity ( $\sigma$ ) of the fracture with the host rock at the interface. The GPR system measures the total travel time and amplitude of the electromagnetic energy that has

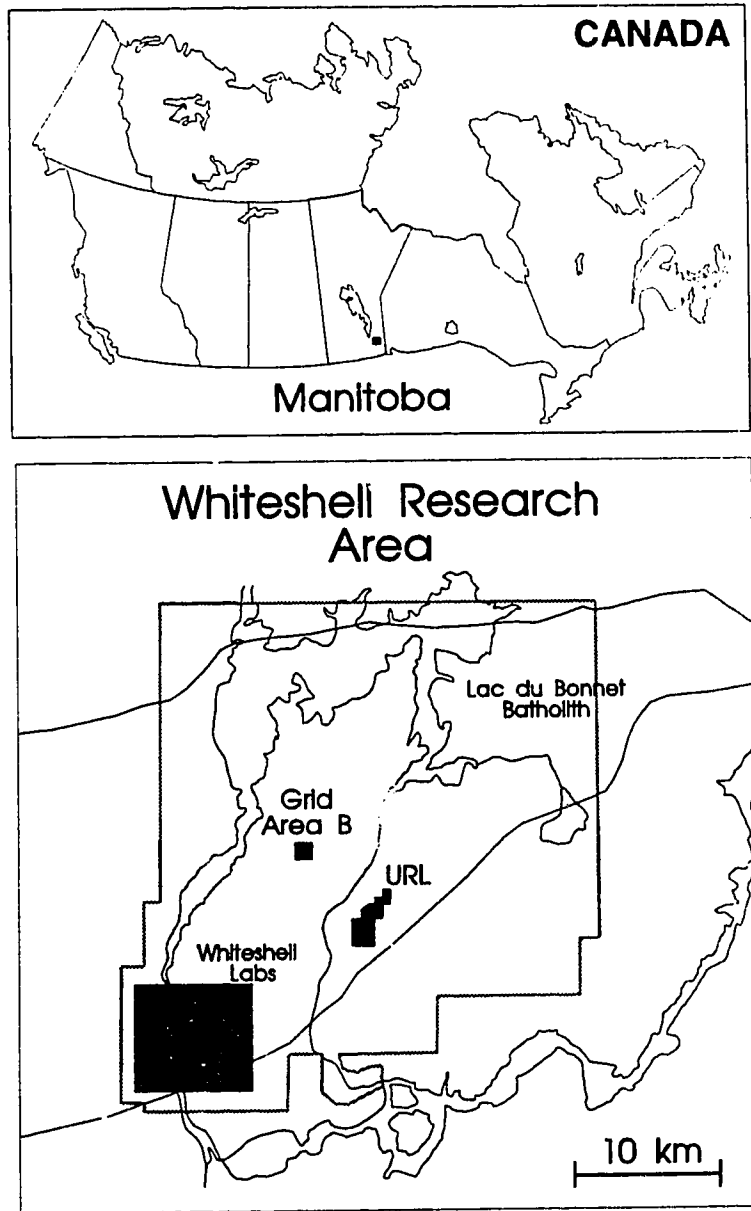


**Figure 7.1: Location and area map of AECL's (Atomic Energy of Canada Limited) Whiteshell Research Area and the Underground Research Lab in Manitoba, Canada.**

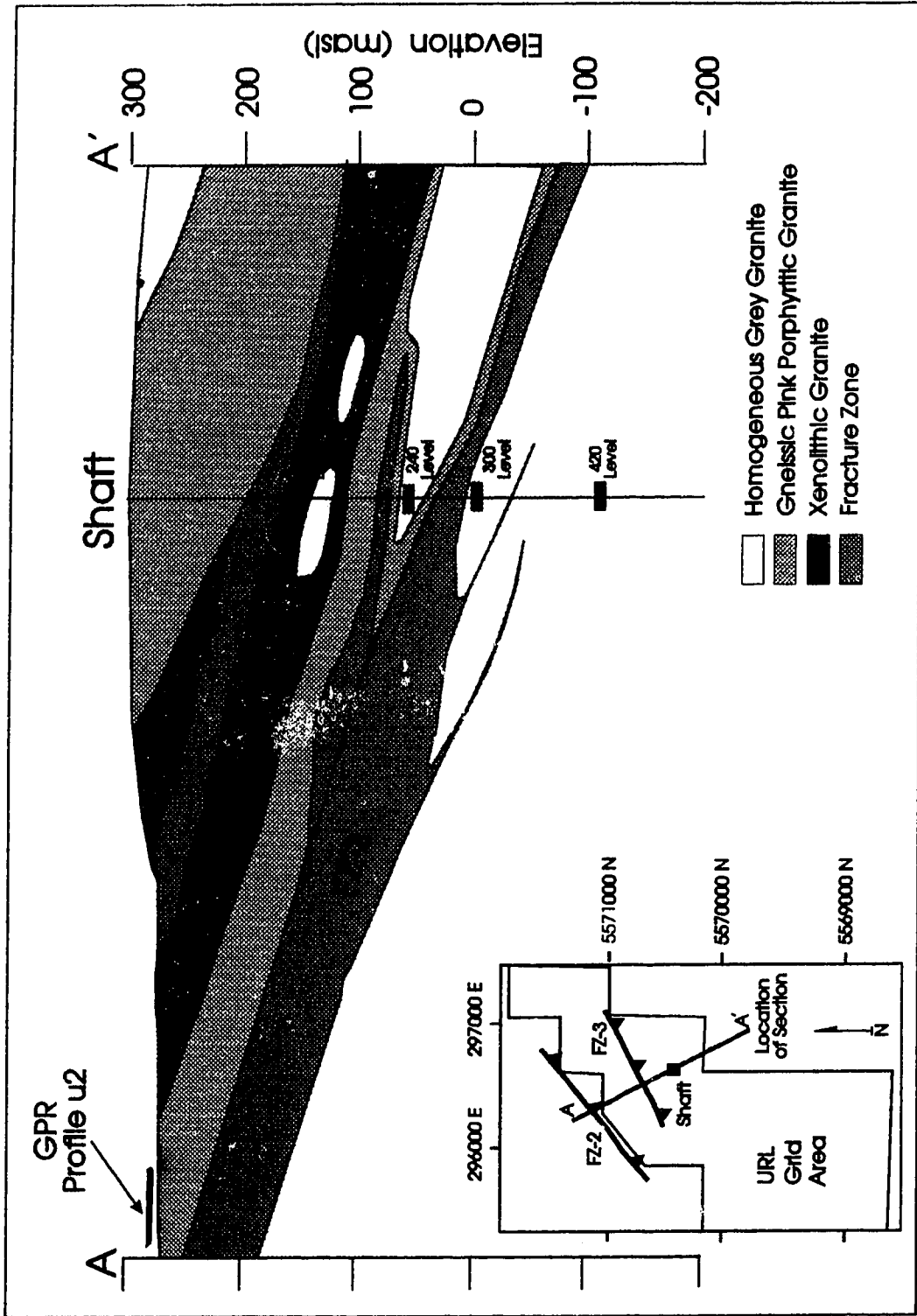


**Figure 7.2:** A cross section showing geological and structural features across the URL area and through the URL shaft. The major fracture zones shown have been confirmed by a number of different geophysical methods.

travelled from the transmitter antenna to the receiver antenna directly or after reflecting at discontinuities in the rock. A radar profile is produced by plotting amplitude and the two-way travel time versus the midpoint between the two antennas.

GPR systems operate at frequencies from 10 MHz to 1000 MHz. The frequency range and the amplitude of the initial signal and the electrical properties of the medium determine the resolution and effective penetration range of the radar survey. The maximum effective range of a GPR system depends on the radar system limitations and energy attenuation in the transmission medium. Higher survey frequencies result in greater resolution but smaller probing distances. The average attenuation rate of radar energy at a frequency of 22 MHz has been calculated by Olsson et al. (1987) to be 0.3 dB/m in granite.

The electromagnetic field generated by a radar antenna and transmitted into a medium can be described by Maxwell's equations. Formulations for the radar reflection method are given by Olsson et al. (1987) among others. From these formulations it arises that the magnitude of the electrical attenuation is defined as the skin depth distance  $\delta$ , over which the intensity of the plane wave is reduced by  $1/e$  (i.e., the field strength is  $\sim 37\%$  of that at the source). The skin depth is given by the equation

$$\delta = \frac{2}{\sigma} \sqrt{\frac{\epsilon}{\mu}} \quad (7.1)$$

where  $\sigma$  is the electrical conductivity of the medium,  $\epsilon$  the electrical permittivity of the medium and  $\mu$  the magnetic permeability of the free space.

According to Holloway et al. (1986), the propagation velocity of electromagnetic energy at GPR frequencies in the Lac du Bonnet granite is approximately 0.120~0.125 m/ns. Then using the following equation

$$\epsilon_r = \left(\frac{c}{V}\right)^2 \quad (7.2)$$

where  $\epsilon_r$  is the relative dielectric constant of the medium,  $c$  is the speed of light in vacuum ( $3 \times 10^8$  m/s) and  $V$  describes the velocity of the electromagnetic plane wave in the medium, the relative dielectric constant of the Lac du Bonnet granite has been determined to be approximately 6~6.5. However, the presence of water in the fractured granite will have a great effect on the dielectric constant and the conductivity of the rock. On the other hand the unfractured granite has only negligible amounts of water because of its very low porosity. The dielectric constant for granite varies from 4.8 to 18.9 and for water is 80.36



(Telford et al., 1976).

The signal wavelength is related to the frequency of the antenna and the transmission medium,

$$\lambda = \frac{c}{f\sqrt{\epsilon_r}} \quad (7.3)$$

where  $\lambda$  is the wavelength of the signal in the transmission medium and  $f$  is the centre frequency of the radar antenna. Assuming a dielectric constant ( $\epsilon_r$ ) of 6.5, the wavelength at 25 MHz frequency is about 4.7 m.

## 7.5 FREQUENCY-SPACE DEPTH MIGRATION FOR GPR DATA

One of the most advanced processing techniques applied to the seismic data is migration. The migration technique positions dipping and diffracted data to their true position resulting in an image which has greater spatial resolution. For example, a point scatterer that is buried in a constant velocity medium generates a zero offset seismic section that is a hyperbola in two dimensions. In this case, migration sums amplitudes along the diffraction hyperbola and then places the result at the apex of it. The kinematics of both seismic reflection and radar reflection methods are similar. Therefore we can use the seismic migration algorithms based on the scalar wave equation for migrating radar data.

In this thesis 2-D finite difference poststack depth migration in the frequency-space ( $\omega$ - $x$ ) domain was used for migration of GPR profiles. The algorithm was parallelized over frequencies and is described in Chapter 4. The algorithm was implemented on a 44-processor Myrias SPS3 MIMD parallel computer. The CPU time required for the migration of a GPR line was very small, e.g., for a problem of size 129 traces X 1126 time samples the CPU time required was 179 sec when 1001 depth steps ( $dz=0.1$  m) and 250 frequencies were used. Since the computational time required for the migration is small, it is practical to perform a number of depth migrations (iterative migration), updating the velocity field in search of an interpreted optimum migrated result.

## 7.6 ACQUISITION OF GPR DATA IN GRANITE

The upper 300 m of the Lac du Bonnet granite is a very good medium for propagation of electromagnetic energy at radar frequencies because it is highly resistive (greater than 10  $K\Omega$ -m). Also, water filled fracture zones are good reflectors of radar energy because of

their electrical contrast (lower resistivity and higher dielectric constant) with respect to the surrounding granite. Therefore, high frequency radar systems are well suited for the detection and characterization of fracture features in granite.

Surface, single-hole and crosshole radar surveys have been conducted at a number of sites in the Whiteshell research area. These experiments were conducted to identify and map fracture zones. Two types of radar systems are used by AECL: the RAMAC borehole system from ABEM Geoscience of Sweden and the PEIV surface radar system from Sensors and Software Inc. of Canada. The principles of both systems are similar.

The depth of penetration is inversely proportional to the profiling frequency and directly proportional to the strength of the output signal. Therefore, the success of a GPR survey depends on the antenna frequency and pulser voltage used which vary with depth of interest and reflector resolution required. A typical surface radar profile was recorded with a marching transmitter-receiver pair, spaced at a fixed distance, depending on the frequency used, along the survey line. The long axis of the antennas was oriented perpendicular to the survey line (transverse electric configuration). The pulser voltage was 1000 V. Signals were recorded at a constant interval (0.5~1 m) as the antenna pair was moved along the survey line. Each measurement consisted of a stacked pulsed radar signal (128 stacks) for an improved signal-to-noise ratio.

Figure 7.3 shows the location of the GPR lines and boreholes in Permit area B and in the URL area. In Figures 7.4 and 7.5 we show the raw data of four surface radar profiles. For all the profiles the antennas used had a centre frequency of 25 MHz, the transmitter-receiver antenna spacing was 3 m and the sampling interval was 1.6 ns. Automatic gain control (AGC) has been applied on the raw data so that the weaker and deeper reflections become visible. Otherwise only the direct arrival and the first reflector are visible.

Figure 7.4.a shows the raw data of radar profile-b3 from Permit area B (Figure 7.3.a). Borehole WB1 is about 40 m west of this radar line (Figure 7.3.a). The measurements were collected at 1 m intervals for a total of 152 raw traces corresponding to station 15 to 165 m. Figure 7.4.b shows radar profile-u2 from an outcrop survey in the northwest part of the URL area. A vertical borehole (M10) exists near the northwest end of the radar profile (Figure 7.3). The profile consists of 112 traces corresponding to station 0 to 55.5 m with the measurements recorded at 0.5 m intervals. Figure 7.5.a shows radar profile-pgl1 which is located in the URL area. The profile consists of 129 traces with trace spacing of 1 m. This profile is parallel to the strike of a local fracture zone. On the other hand, Figure 7.5.b shows radar profile-pgl3 which is essentially perpendicular to the strike of the same feature. All raw GPR profiles are plotted with AGC (0.2  $\mu$ s time window).

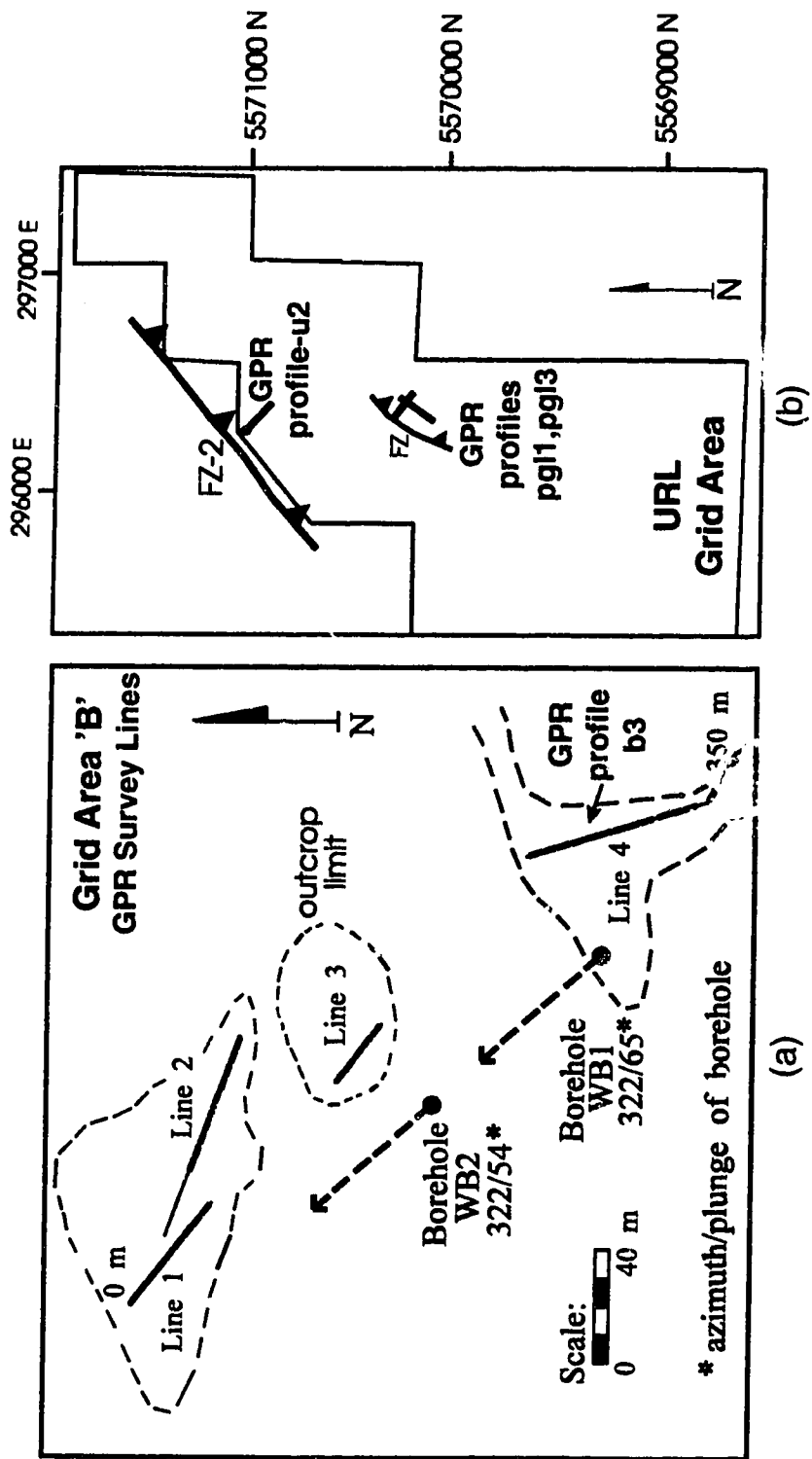
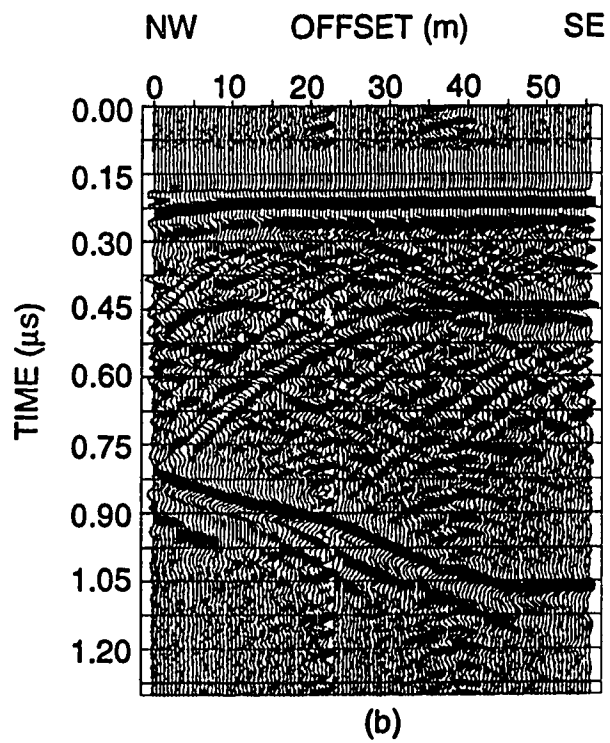
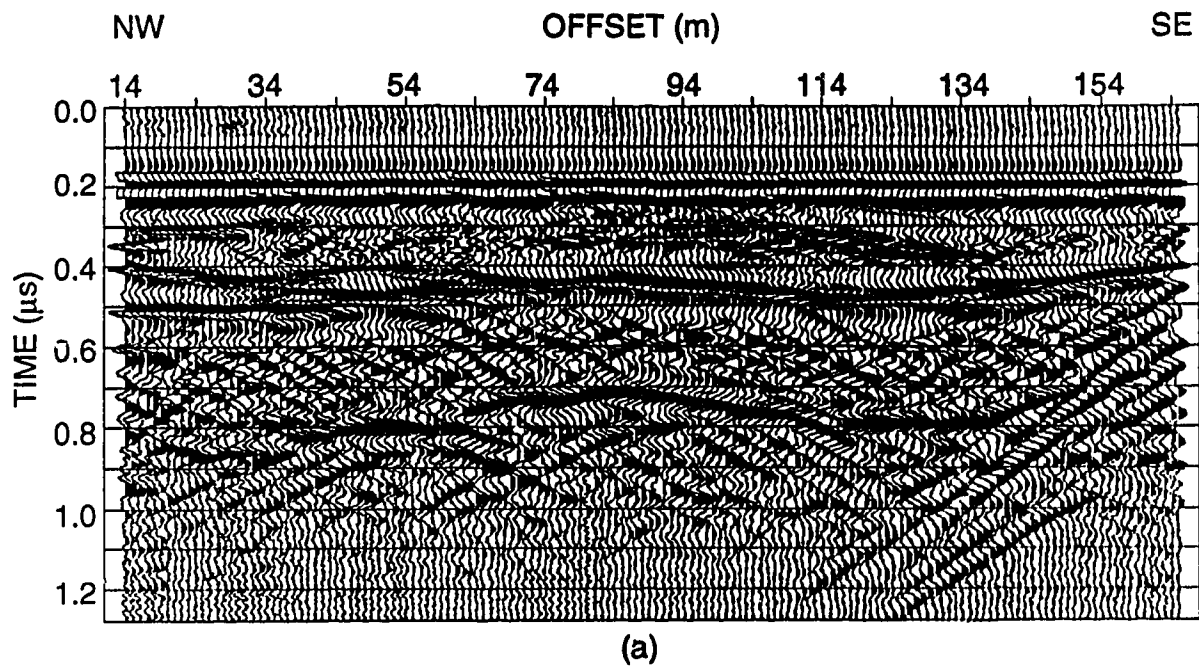
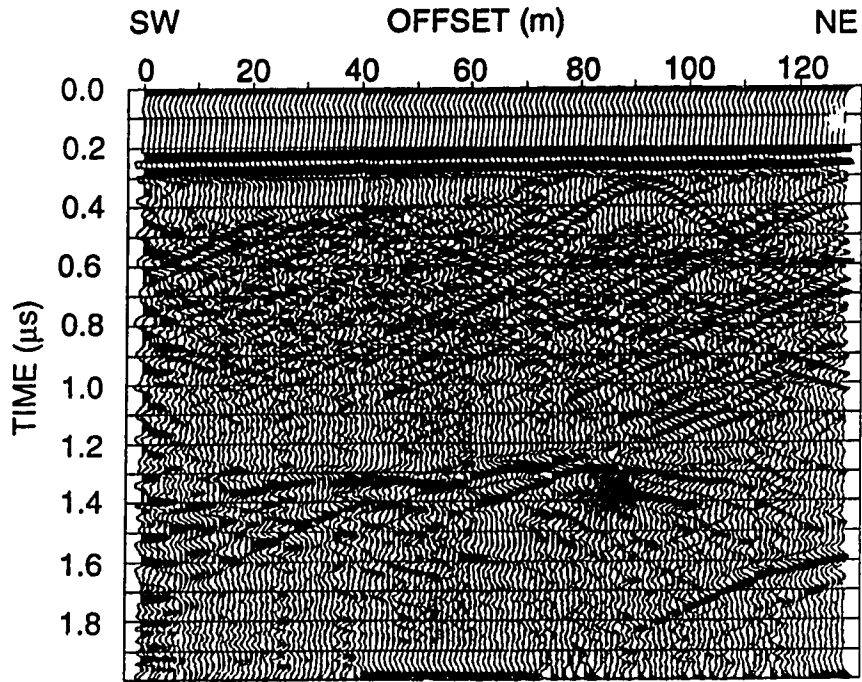


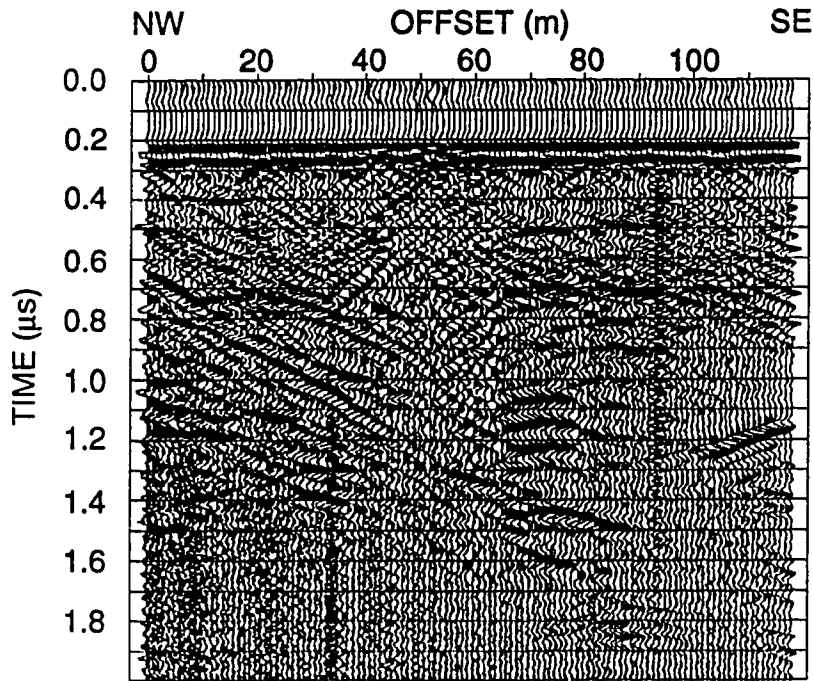
Figure 7.3: The location of the GPR profiles and boreholes in (a) Permitt area B and (b) the URL area.



**Figure 7.4:** Raw GPR profiles: (a) profile-b3 from the Permitt area B, and (b) profile-u2 from the URL area.



(a)



(b)

**Figure 7.5:** Raw GPR profiles: (a) profile-pg11 and (b) profile-pg13, both from the URL area.

## 7.7 PROCESSING OF GPR DATA USING SEISMIC ALGORITHMS

The principles of the radar reflection method are similar to the ones of the seismic reflection method. In the survey geometry that was used, a radar profile is similar to a one-fold common midpoint (CMP) stacked seismic section. The energy reflects at almost normal incidence from a reflecting interface because the transmitter-receiver separation (offset) is small (3 m for 25 MHz antenna) compared to the average probing depth in granite. Therefore, a radar profile can be compared to a zero-offset seismic section. However, some of the recorded energy is not from reflectors directly below the midpoint of the antenna pair or the point of recording.

Demultiplexing (from time slices to traces) is not needed since the data were recorded as traces (only one source and one receiver are used each time). Elevation statics are not used since the elevation in the survey area changes gradually with about a 2 m relief across each site. A static shift is applied to each of the raw traces to correct for the fact that recording was started before source excitation. Also, a time dependent gain function is applied on the data to compensate for energy losses due to geometrical spreading and ohmic attenuation of energy ( $\sim 0.3$  dB/m). Profile-u2 is processed with AGC applied on the data but not the above gain. The rest of the profiles are processed with the above gain applied on the data (no AGC is used).

Predictive deconvolution is applied for spiking the wavelet and suppressing short to medium period multiples. Next, band-pass filtering with an upper corner frequency near the antenna's third harmonic (75 MHz), is applied to remove the characteristic low and high frequency background noise components. Also, a signal to noise ratio (SNR) enhancement filter is applied via the Karhunen-Loeve transform. ITA/Insight algorithms were used for deconvolution and SNR enhancement in the above processing steps.

In Figure 7.6.a profile-u2 is plotted after the above processing flow with AGC (0.2  $\mu$ s). Also, in Figure 7.7.a profile-b3 is plotted after processing with gain (0.3 dB/m). We can observe that the quality of the radar profiles has improved. However, in order to collapse diffractions and focus the energy migration of the data is essential.

Velocity analysis was performed by AECL (Stevens et al., 1994). The near surface ground wave velocity was estimated to be about 0.120 m/ns using a wide angle reflection and refraction technique (WARR) on outcrops. Also, the average wave velocity of the rock in the upper 300 m was estimated from the slope of a best-fit line through crosswell radar data to be approximately 0.118 m/ns.

Prior to migration a smooth spatial and temporal taper is applied on both sides of the

radar profile to reduce generated artifacts due to the finite aperture. Our own frequency-space domain ( $\omega$ - $x$ ) depth migration algorithm, described in Chapter 4, was applied to the data using a constant velocity of 0.12 m/ns. For all profiles the wavefield was downward extrapolated using a depth step by automatic merging of 0.1 m. After migration and prior to plotting the final migrated results, random noise attenuation and trace balancing are applied. Figure 7.6.c shows the migrated radar profile-u2. The depth migrated radar profiles b3, pgl1 and pgl3 are shown in Figures 7.7.c, 7.8.a, 7.8.b, respectively, using colour to show the amplitude strength of the events. As we see on the migrated profiles with and without AGC, the diffractions have been collapsed, most of the energy has been focused and reflectors are more continuous and sharpened. Figure 9 shows the GPR data processing flow used.

## 7.8 INTERPRETATION OF THE GPR MIGRATED IMAGES

The first strong continuous event of the profiles is the direct arrival of the air-ground wave. The air wave is the fastest event in radar data (whereas it is the slowest in the seismic data) since it propagates at  $3 \times 10^8$  m/s. The other direct wave propagates along the air-rock interface at about  $1.2 \times 10^8$  m/s (radar velocity in granite).

On the depth migrated profile-u2 (Figure 7.6.c) the most significant feature is a strong continuous reflector at about 40 m at the northwest end of the profile and at about 55 m depth at the southeast end. This reflection corresponds to the location of the fracture zone FZ-2 (Figure 7.2), logged in borehole M-10 (Figure 7.6.b). Another feature is a reflection event at depths of about 15~20 m. It extends about 25 m laterally at the southeast of the profile and is most likely a fracture feature. The diffraction event generated from the termination or closure of this fracture seen on the raw data (Figure 7.4.b) has collapsed after migration.

On the depth migrated profile-b3 (Figure 7.7.c) a strong continuous reflector along the whole section exists at about 15~20 m depth. Another, less continuous reflector horizon exists at depths of about 30~40 m which is essentially subhorizontal and highly discontinuous possibly indicating echelon fracturing and/or regions of higher hydraulic permeability along the fracture zone. The proximity of this radar profiling line to borehole WB-1 has also made it possible to confirm the dip and the nature of these reflectors at corresponding depths in the borehole core log (Figure 7.7.b).

The migrated profile-pgl1 (Figure 7.8.a) clearly images a fracture zone (FZ) at depths of 60 to 80 m along the profile, essentially parallel to the strike of the feature. Also, the

migrated profile-pgl3 (Figure 7.8.b) images the same fracture zone perpendicularly to the strike. On both migrated profiles the diffractions seen on the raw data (Figure 7.5) have been collapsed and some of the dipping events have moved out of the area of the profile. On the profile-pgl3 (Figure 7.8.b) very strong reflections from the bottom and weaker reflections from the top of the fracture zone are ranging from 35 m depth near the outcrop edge at the northwest to 80 m depth at the southeast end of the profile. This fracture zone (FZ, Figure 7.3.b) has been confirmed in near-by boreholes. It is open to water flow to the northwest and closes to the southeast. The imaging results indicate that the fracture zone is about 25 m thick which could generate internal radar reflections as well as discrete reflectors from the top and bottom of the zone.

*(Text continued on page 263)*



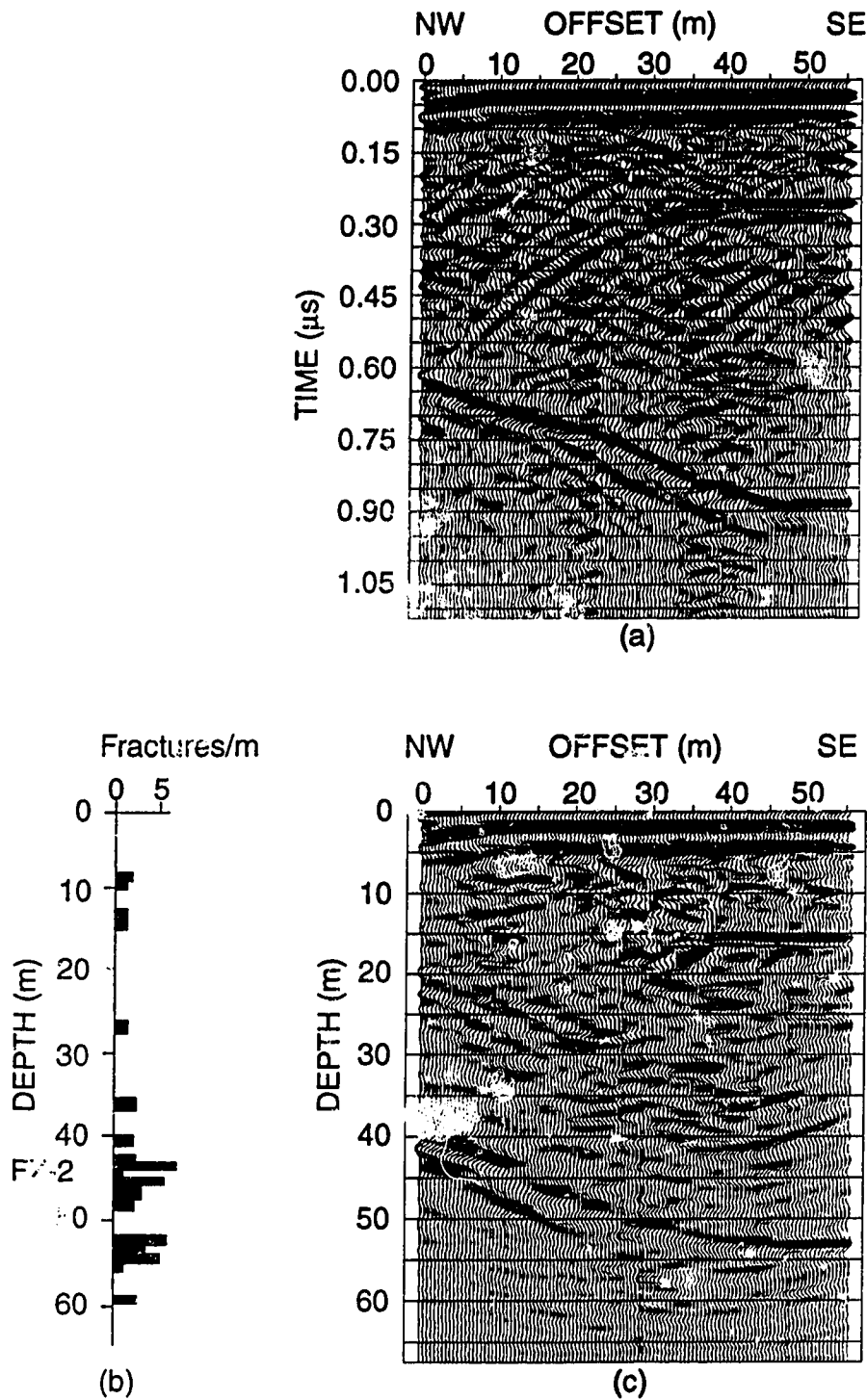


**Figure 7.6:** The GPR profile-u2 from the URL area: (a) The processed data after AGC, static shift, deconvolution, and bandpass and signal-to-noise ratio enhancement filtering; (b) The core log from borehole M-10 (near the northwest end of the profile); and (c) The depth migrated data after  $\omega$ -x finite difference migration, random noise attenuation and trace balancing.

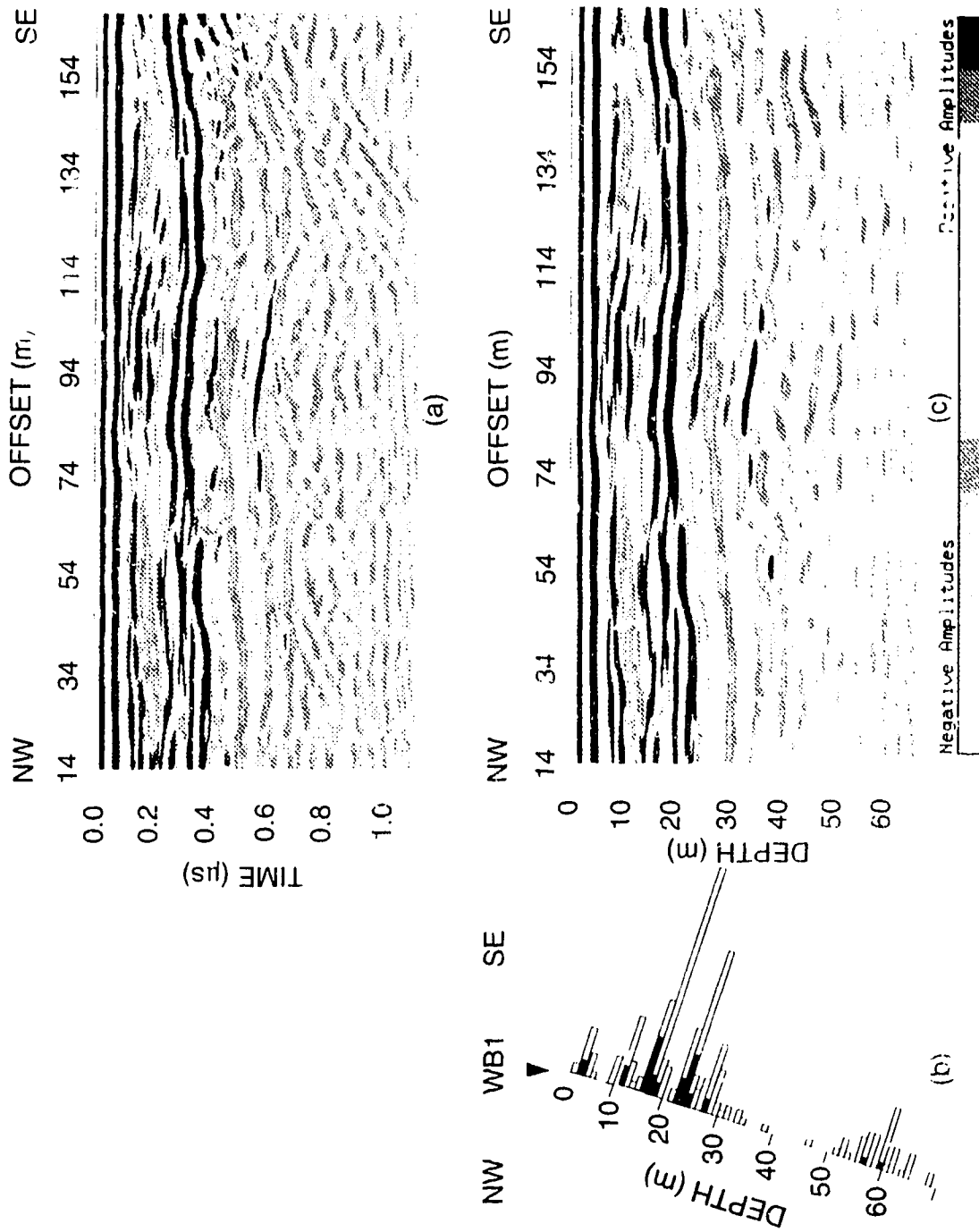


**Figure 7.7:** The GPR profile-b3 from area B: (a) The processed data after static shift, gain, deconvolution, and bandpass and signal-to-noise enhancement filtering; (b) The core log from borehole WB1 (about 40 m west from the profile); and (c) The depth migrated data after  $\omega$ -x finite difference migration, random noise attenuation and trace balancing.

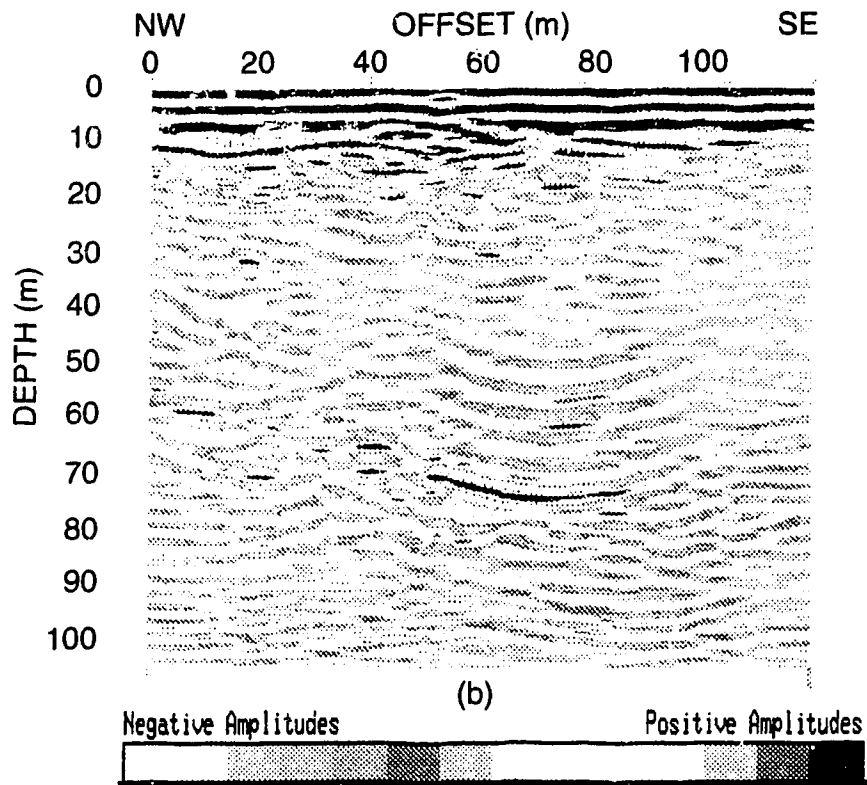
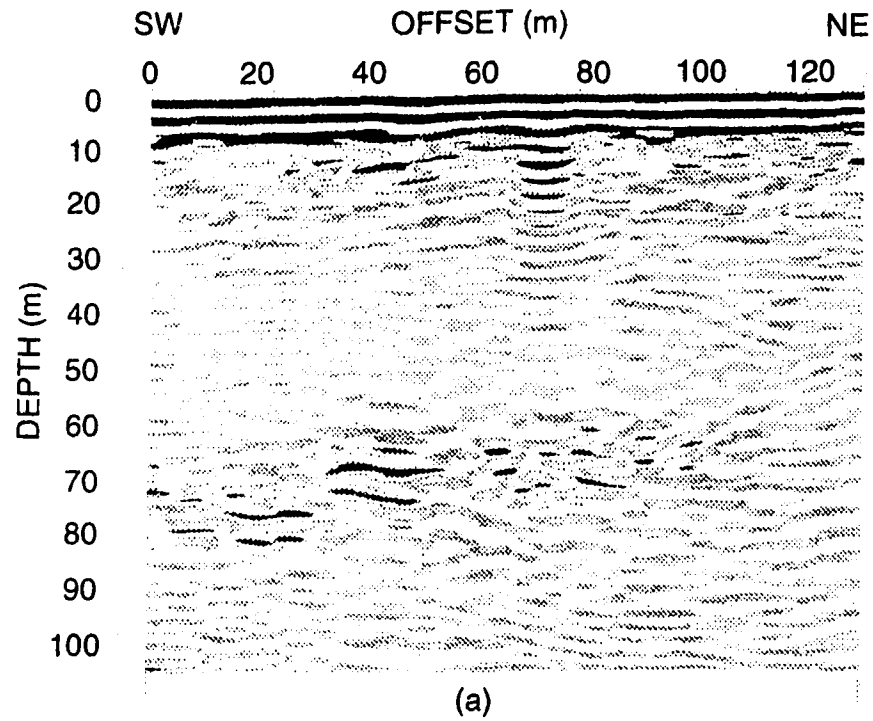


Figure 7.8: GPR profiles after processing and migration: (a) The depth migrated profile-pg11; and (b) The depth migrated profile-pg13.

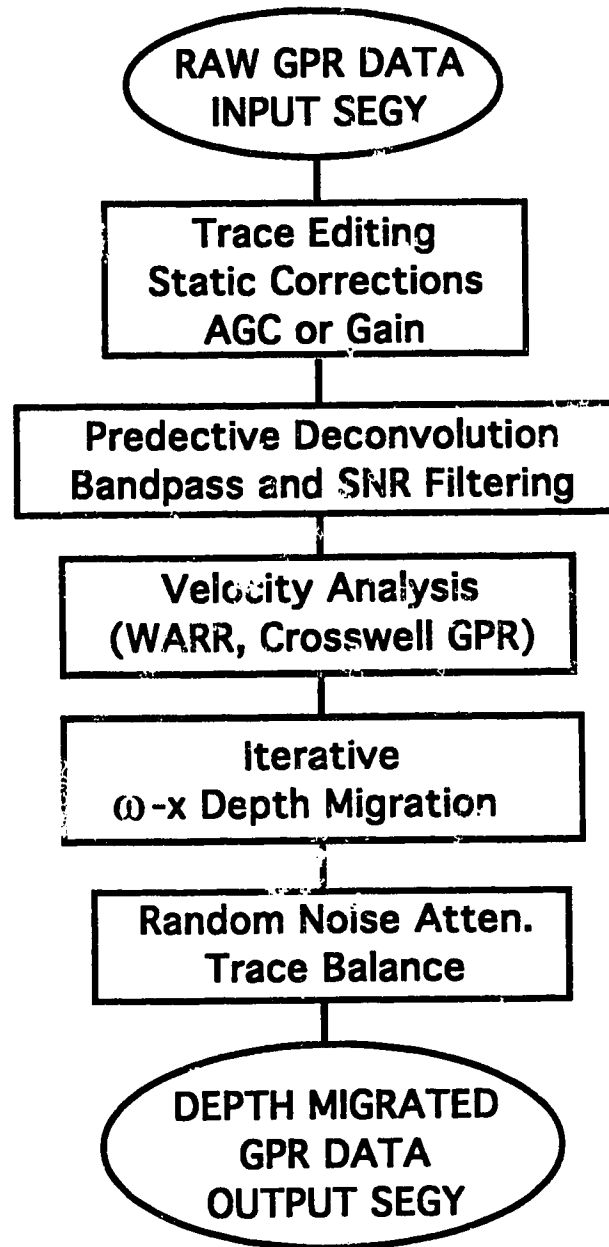


Figure 7.9: The algorithmic flow used for processing and migration of the GPR data.

## 6.9 CONCLUSION

The raw GPR profiles show an unfocused image of the fractured granite due to diffractions, noise and weak deeper reflections. The raw data were processed using seismic processing algorithms such as deconvolution, filtering and frequency-space depth migration. The only difference is the scale of the problem, the time in seismic migration is in the order of seconds ( $s$ ) whereas in radar migration the time is in the order of microseconds ( $\mu s$ ). The  $\omega$ - $x$  depth migration algorithm was capable of collapsing the diffractions, moving dipping events to their true subsurface location and focusing most of the energy. The final migrated results show significant improvements in signal to noise enhancement, depth of penetration, collapse of diffractions and imaging of fracture zones.

In the above processing flow an approximate time-dependent compensation has been applied for geometrical spreading and ohmic dissipation of energy. Thus, the migrated profiles accurately image the shape and location of the reflectors, collapse diffractions and move dipping events to their true positions but in terms of amplitude the images may not be absolutely reliable.

We applied successfully a 2-D processing flow to 2-D radar data (Figure 7.9). However, 3-D effects such as energy originating from places off the survey plane are not imaged properly with a 2-D migration. Also, with the above used poststack processing flow based on the zero-offset assumption and the exploding reflector model, multiple reflections and evanescent energy may not be totally corrected.

The ground-penetrating radar method at centre frequencies of 25 MHz in the granitic Lac du Bonnet Batholith has successfully imaged fractures to distances of at least 100 m below outcrop surfaces. Furthermore, all strong reflections detected on the radar profiles correlate well with open fracture zones logged in drill cores.

This study clearly demonstrates that seismic processing algorithms can be successfully applied to ground-penetrating radar data due to the kinematic similarities between radar reflection and seismic reflection methods. Furthermore, the paraxial approximation to the scalar wave equation can be used for the depth migration of radar data the same way as applied to seismic data.

## REFERENCES

Annan, A.P., Cosway, S.W. and Redman, J.D., 1991, Water Table Detection with

- Ground-Penetrating Radar: 61st Ann. Internat. Mtg., Soc. Expl. Geophys., Expanded Abstracts, 494-496.
- Annan, A.P., Brewster, M.L., Greenhouse, J.P., Redman, J.D., Schneider, G.W., Olhoeft, G.R. and Sander, K.A., 1992, Geophysical Monitoring of DNAPL Migration in a Sandy Aquifer: 62nd Ann. Internat. Mtg., Soc. Expl. Geophys., Expanded Abstracts, 344-347.
- Brown, A., Soonawala, N.M., Everitt, R.A., And Kamineni, D.C., 1989, Geology and geophysics of the Underground Research Laboratory Site, Lac du Bonnet, Manitoba: *Can. J. Earth Sci.*, **26**, 404-425.
- Claerbout, J. F., 1976, *Fundamentals of Geophysical Data Processing*, McGraw Hill Inc.
- Claerbout, J. F., 1985, *Imaging the Earth's Interior*: Blackwell Scientific Publications.
- Dormuth, K. W. and K. Nuttall, 1987, The Canadian Nuclear Waste Management Program: Radioactive Waste Management and the Nuclear Fuel Cycle, **8**, 93-104.
- Fisher, E., McMechan, G. A. and Annan, A.P., 1992, Acquisition and processing of wide-aperture ground-penetrating radar data: *Geophysics*, **57**, 495-504.
- Fisher, E., McMechan, G.A., Annan, A.P. and Cosway, S.W., 1992, Examples of reverse-time migration of single-channel, ground-penetrating radar profiles: *Geophysics*, **57**, 577-586.
- Hayles J. G., Stevens K. M., Serzu M. H. and Lodha G. S., 1991, Developments in the Mini-Charts system and field trial results in measuring excavation damage in granite: Proceeding of the 4th International MGLS/KEGS Symposium on Borehole Geophysics for Minerals, Geotechnical and Groundwater Applications, Toronto, Canada.
- Hayles J. G., Serzu M. H., Tomsons, D.K., Everitt, R.A., and Lodha G. S., 1994, Cross-hole seismic and single-hole geophysical surveys for characterizing an area of moderately fractured granite: CSEG and CSPG Joint National Convention, Exploration Update '94, Calgary, Alberta, Expanded Abstracts, 267-268.
- Hogan, G., 1988, Migration of ground-penetrating radar data: A technique for locating subsurface targets: 59th Ann. Internat. Mtg., Soc. Expl. Geophys., Expanded Abstracts, 345-347.
- Holloway A.L., Soonowala N.M. and Collet L.S., 1986, Three dimensional fracture mapping in granite excavations using ground-penetrating radar: *Canadian Institute of Mining Bulletin*, **79**, 54-59.
- Holloway A.L., Stevens K.M. and Lodha G.S., 1992, The results of the surface and borehole radar profiling from permit area B of the Whiteshell Research Area, Manitoba, Canada: Fourth International Conference on Ground Penetrating Radar, Special Paper

- 16, 329-337, Rovaniemi, Finland.
- Hu, L. Z., 1992, Imaging Pipeline in 3-D by Ground-Penetrating Radar: 62nd Ann. Internat. Mtg., Soc. Expl. Geophys., Expanded Abstracts, 352-355.
- Imai, T., Sakayaman, T. and Kanemori, T., 1987, Use of ground penetrating radar and resistivity surveys for archaeological investigations: *Geophysics*, **52**, 137-150.
- Kalantzis, F., Stevens, K.M., Kanasewich, E.R., and Lodha, G.S., Depth migration of ground-penetrating radar data: CSEG National Convention, Calgary, Expanded Abstracts, 251-252.
- Olsson O., Falk L., Forslund O., Lundmark L. and Sandberg E., 1987, Crosshole Investigations - Results from Borehole Radar Investigations. Stripa Project: KBS-SP-87-11, Swedish Nuclear Fuel and Waste Management Co, Stockholm, Sweden.
- Roberts, R. L. and Daniels, J.J., 1992, 3-D Data Collection and Analysis for High-Resolution GPR Studies: 62nd Ann. Internat. Mtg., Soc. Expl. Geophys., Expanded Abstracts, 360-363.
- Rocca, F., Cafforio, C. and Prati, C., 1989, Synthetic aperture radar: A new application for wave equation techniques: *Geophys. Prosp.*, **37**, 809-830.
- Soonawala, N.M., Holloway, A.L. and Tomsons, D.K., 1990, Geophysical Methodology for the Canadian Nuclear Waste Management Program, in: *Geotechnical and Environmental Geophysics, Volume I: Review and Tutorial*, Ward S.H. (ed), 309-331.
- Stevens K.M., Lodha G.S., Holloway A.L. and Soonawala N.M., 1994, The application of Ground Penetrating Radar for mapping fractures in plutonic rocks within the Whiteshell Research Area, Pinawa, Manitoba, Canada: Submitted for review to the *Journal of Applied Geophysics*, thematic issue on Ground Penetrating Radar.
- Telford, W. M., Geldart, L. P., Sheriff, R.E. and Key, D. A., 1976, *Applied Geophysics*: Cambridge University Press.
- Wong J., Hurley P. and West G. F., 1985, Investigation of subsurface geological structure at the Underground Research Laboratory with crosshole seismic scanning: The Geoscience Program - Proceeding of the 17th Information Meeting of the Nuclear Fuel Waste Management Program, Volume II, 593-608.
- Wood, L. and Hennon, K., 1993, Parameter Testing of Ground-Penetrating Radar for Geological Investigations in Poor-Data Area: 63rd Ann. Internat. Mtg., Soc. Expl. Geophys., Expanded Abstracts, 483-486.
- Yilmaz, O., 1987, *Seismic Data Processing*: Soc. Expl. Geophys.

## CHAPTER 8

### CONCLUSIONS

This thesis explored new and existing wave-equation modeling and migration methods. Innovative utilization of recent advances in computing based on the vector computations and the subdivision of the computational sequence into parallel components led to the development of highly vectorized and parallel algorithms. Many of the developed algorithms were vectorized using sophisticated approaches such as matrix multiplication by diagonals to take full advantage of the computational power of vector supercomputers. On the other hand, some of the algorithms were highly parallelized by utilizing the inherent parallelism in the frequency, space and partially in time domains that the seismic equations have and thus they took full advantage of the computational power of massively parallel computers and workstation clusters. Implementation of the above algorithms fully utilized the existing current supercomputer technology that we had access to such as vector and parallel supercomputers (e.g., a Convex 210 vector mini-supercomputer, a Fujitsu VPX 240/10 vector/parallel supercomputer, and a Myrias SPS-3 MIMD parallel computer) and single workstations and workstation clusters (e.g., SUN, IBM RISC 6000). This led to the implementation of more accurate and cost effective seismic imaging methods that were in the past impossible in practice.

A new 3-D acoustic modeling method was formulated and a computationally efficient algorithm was developed for it. The second order differential 3-D scalar wave equation was formulated into a first order hyperbolic system which was solved with explicit finite differences using the MacCormack splitting scheme. The numerical solution of the 3-D wave system provides a useful method for simulating the evolution of a pressure field which corresponds to the P or compressional type of body waves which is most frequently recorded. In the 3-D acoustic modeling algorithm both lateral and vertical variations of the acoustic (P-wave) velocity and density are allowed. The method accounts for many important wave phenomena such as diffraction, interference and generation of multiple reflections. Although the use of the acoustic wave equation rules out the generation of shear and surface waves, it still is accurate enough for many important exploration and production problems. Another advantage of 3-D modeling is that time slices (snap shots) come at no extra cost and they can enable us to examine the spatial configuration of the wavefield as it propagates through the 3-D earth model and reaches the surface at different times. Also, existing 2-D elastic modeling algorithms were modified and fine-tuned for



computationally efficient and realistic wave propagation simulations in complex structures.

The modeling algorithms were successfully vectorized and parallelized. Access to powerful vector/parallel supercomputers and massively parallel processors (MPPs) motivated this work towards simulations of wave propagation with higher accuracy in two and three dimensional inhomogeneous media. The result is a pronounced decrease in execution time, ability to handle quite large models and an increase in accuracy and resolution. Particularly, the implementation of the 3-D acoustic modeling algorithm on the Fujitsu VPX/240 supercomputer resulted in pronounced CPU and vectorization performance (up to 98 %) thus opening the avenues for large scale realistic wave propagation simulations in 3-D complex structures.

The 3-D modeling algorithm may easily be extended to simulate wave propagation in three dimensional anisotropic heterogeneous media. Furthermore, the computational performance of the algorithm suggests the possibility of large scale 3-D elastic wave simulations in realistic and complex media. However, both topics are beyond the scope of this thesis and are left for future research.

2-D poststack and prestack depth migration algorithms in the frequency-space domain using implicit finite differences were developed and implemented on a parallel computer. Furthermore, 3-D poststack and prestack depth migration parallel algorithms were developed in the frequency domain that use a one-pass or alternate direction implicit (ADI) finite difference method. The algorithms were highly parallelized by fully utilizing the inherent parallelism in the frequency and space domains that the seismic equations have and thus they took full advantage of the computational power of massively parallel computers. The one-pass 3-D depth migration algorithm was implemented on a Myrias SPS5 parallel computer for the migration of a number of real 3-D seismic data sets with pronounced execution times.

An original formulation of the 3-D reverse time migration method was developed employing either a full or a one-way wave hyperbolic system that is solved with explicit finite differences using the MacCormack scheme. This method is very accurate since it does not use any approximations to the one way equation such as the paraxial approximation used for one-pass 3-D implicit finite difference depth migration in the frequency domain. Furthermore, it does not suffer from the unwanted evanescent energy since extrapolation is performed in time and not in depth as in the case of the recursive depth extrapolation based migrations. The use of the full wave system for migration can result in imaging of dips beyond 90 degrees. On the other hand, the advantage of the one-way system is that it does not generate multiple energy. Based on this innovative formulation

of the reverse time migration method four new algorithms were developed for poststack and prestack depth migration of 3-D complex seismic data. All algorithms were vectorized and implemented on a Fujitsu VPX/240 supercomputer with pronounced CPU and vectorization performance.

The 3-D reverse time migration method when the full wave system is used does not have dip restrictions. Therefore, it should be able to migrate 3-D seismic data that contain turning waves generated in complex structures such as overhanging salt domes and intrusions of salt into faults. Also, the application of prestack reverse time migration can significantly simplify the processing of seismic data since there is no need for demultiplexing the data, sorting into common-midpoint gathers, elevation and near-surface static corrections, first break muting and removal of surface waves, and normal and dip moveout corrections since these operations are eliminated or are performed automatically and implicitly with the reverse time migration. Thus, the entire seismic processing sequence may be reduced to determining an accurate velocity model with some kind of velocity analysis method and depth imaging of the 3-D seismic data with the reverse time migration. However, this extraordinary potential of our 3-D reverse time migration algorithm has not yet been fully tested and explored. It is left for research in the immediate future.

This thesis not only developed and implemented new imaging methods but also utilized all the developed algorithms for imaging seismic and radar wavefields in a wide range of applications such as 3-D seismic monitoring of tar sands reservoirs during steam stimulation, crustal studies (LITHOPROBE Alberta Basement transect), and characterization of nuclear waste repositories. The 2-D migration algorithm was adapted for applications that range from deep crustal imaging of seismic wavefields that involve 18 seconds long travel times (50 Km depth) and frequencies in the order of 1~100 Hz, to imaging of radar wavefields that involve 2000 nano-seconds (ns) long travel times and frequencies in the order of 50 MHz. The one-pass 3-D depth migration was used for high resolution imaging of 3-D seismic monitoring data from EOR sites at Cold Lake, Alberta. The 2-D elastic and 3-D acoustic modeling algorithms were used extensively for wave propagation simulations in the reservoir before and during steam stimulation processes in oil sands. Also, the 3-D poststack reverse time migration was used for the migration of a 3-D synthetic seismic data volume generated over a Cold Lake model.

Atomic Energy of Canada is investigating the suitability of plutonic rocks of the Canadian Shield as a repository medium for nuclear wastes. Ground-Penetrating radar (GPR) data were recorded over the Lac du Bonnet granitic batholith in the Whiteshell Research Area near Pinawa, Manitoba, Canada. The stacked GPR profiles showed a

distorted, unfocused image of the fractured granite due to diffractions and noise in addition to interesting weak deeper reflections. The raw data were processed using seismic processing algorithms such as deconvolution, correction for attenuation, filtering and our own frequency-space depth migration algorithm. The results showed significant improvements in signal to noise enhancement, depth of penetration and collapse of diffractions. Water filled fracture zones were particularly well enhanced and weak reflectors showed improved continuity. Our migration algorithm enabled us to detect and image fracture zones in the plutonic rock with a resolution never before achieved. Furthermore, this study demonstrated that seismic processing algorithms can be successfully applied to ground-penetrating radar data due to the kinematic similarities between radar reflection and seismic reflection methods. Also, the paraxial approximation to the scalar wave equation can be used for the depth migration of radar data the same way as applied to seismic data.

As part of LITHOPROBE's Alberta Basement transect, deep crustal seismic reflection profiling (over 500 Km long) was undertaken in 1992 for probing the crust beneath the Western Canada Sedimentary basement. The 2-D depth migration described in this thesis was applied on some of the seismic data and succeed to image structures in the crust down to depths of 50 Km and the crust/mantle boundary (Moho) at about 40 Km depth.

Enormous reserves of bitumen or heavy oil are present in sands of Lower Cretaceous age in Alberta, Canada. Enhanced oil recovery (EOR) methods such as steam stimulation are used to reduce the viscosity of the bitumen and produce it by driving it into a production well. However, during the steaming process, the movement of fluids away from the heated sources at the perforation level is controlled by permeability heterogeneities and even small heterogeneities or anisotropy, caused from fracturing due to high pressure injected steam, can play an important factor in the efficiency of the EOR process. Therefore, it is important to image the shape and areal extent of the steam-heated zone and determine the direction and rate of movement of the thermal front.

An extensive overview of the state of the art knowledge of the seismic wave propagation phenomena in porous rocks and in particularly in oil sands was carried out. This suggested that petrophysical alterations in the heavy oil reservoirs during steam stimulation, as caused by pressure, temperature, the replacement of bitumen by steam or steam condensate, etc., contribute to velocity changes, attenuation and velocity dispersion of seismic waves in the effected reservoir. These changes on a seismic reflection record imply seismic attribute changes such as amplitude brightening of reflections from the top of the steam zone and travel time delays of reflectors within and below the steam invaded zone. Thus, non-invasive or remote sensing geophysical techniques, especially the surface

seismic reflection method can be used to continuously monitor reservoirs during the EOR process and map the expanded steam-heated zone.

Two case studies were performed in this thesis that involve steam stimulation projects (Mobil Oil Canada and Imperial Oil of Canada) in the heavy oil sands of Cold Lake, Alberta. Seismic monitoring of the reservoir during the thermal process (steam stimulation) is performed with 3-D surface high resolution seismic surveys repeated over specified time intervals carried out over the EOR sites. The modeling and migration algorithms developed here were used for advanced processing and interpretation of the recorded 3-D data volumes and integration of the seismic data with other geological and engineering data. Extensive 2-D elastic and 3-D acoustic wave propagation simulations were performed during different phases of the steam stimulation process in order to examine the relation between reservoir properties and conditions such as porosity, permeability and saturation, pressure and temperature with seismic characteristics such as velocity, amplitude and frequency modification with time. Furthermore, an extensive seismic attribute analysis was performed on all 3-D seismic (base and monitors) before and after our own processing such as one-pass 3-D depth migration. This resulted to high resolution seismic attribute images such as amplitude anomalies, time and depth pushdowns, and velocity reduction that mapped the areal and vertical extent of the steam-heated zones (areal and vertical conformance), tracked the steam front and detected some fractures. Furthermore, the attribute anomalies were correlated to the areal location and pressure and temperatures states of the wells. This suggests that the seismic images may be used as reservoir temperature, pressure and gas saturation diagnostic tools.

The generated seismic images correlated well with the observed field performance. However, a quantitative correlation is required in order to obtain estimates of the reservoir properties such as saturation and permeability. This may be possible with geostatistical methods such as kriging, but this is left for future research. A knowledge of the evolving reservoir properties and conditions in real time allows the possibility of controlling and modifying steam injection and production strategies. Thus, 3-D surface seismic monitoring has the potential of becoming a powerful tool for the efficient management of EOR projects.

In conclusion, we believe that by employing state of the art vector and parallel supercomputer technology, the imaging algorithms developed in this thesis can be powerful tools in all phases of exploration and development geophysics.

## APPENDIX A

### VECTOR AND PARALLEL SUPERCOMPUTERS

#### A.1 THE MYRIAS SPS3 PARALLEL COMPUTER

The finite difference migration and modeling algorithms such as the one-pass 3-D depth migration developed in this thesis were parallelized and implemented on a Myrias SPS3 parallel computer at the Canadian Network for Space Physics (CNSR) at the University of Alberta.

The Myrias SPS3 is a MIMD massively parallel computer (MPP). To date, the largest system assembled consists of 1044 processors. The one used in this research, is installed in an expandable configuration consisting of 48 Motorola 68040 processors with 8 Mbytes of memory each. The Myrias SPS3 in terms of hardware is a distributed-memory machine and is similar to nCUBE parallel computer. However, its operating system presents to the programmer/user a shared-memory machine.

The Parallel Application Management System (PAMS) is a comprehensive set of system management programs that support the execution of user programs (Parallel Programmer's Guide, 1991, Myrias Computer Technologies Inc). The PAMS is implemented on the Myrias SPS3 and can also be used on network workstations (workstation clusters) from which PAMS can extract the power of a massively-parallel computer. It is the operating system for the Myrias parallel platform that handles data, program synchronization, distribution and merging.

Since we used the Myrias SPS3 computer extensively in this research, we will present in some detail some of the functions that PAMS performs and the characteristics of the Myrias system. The Myrias programming paradigm is *deterministic*; a program will always produce the same results. This results in easier code development. It has a *coherent shared virtual memory*, that is, a single virtual address space used for all program memory. The memory is automatically distributed around the network and results to no programming need for data partitioning, distribution or coherence. However, many algorithms that use this style of shared memory will need to use *semaphores* for task synchronization. Generally, semaphores are used for two purposes: one, as guards on regions to avoid race conditions; and second, as gates on pages to avoid "jitter" where

pages get bounced around between concurrently executing tasks referencing the same set of pages.

The Myrias paradigm is a *task based model* which means that work is partitioned according to tasks, not processors. Tasks are executed in the most efficient location. This allows program portability to different system sizes. It is *non-intrusive* since parallelism is expressed by inserting a few compiler directives such as *PARDO* (for a parallel DO loop). The approach is similar to vectorization except that both fine-grained and coarse-grained parallelism can be exploited. Automation features keep lower-level parallel actions out of the source code. The same source code can be compiled for serial, vector or parallel execution.

*Transparent data distribution* allows data to be distributed as needed and when needed based on dynamic references. That results to normal programming, no need of data partitioning and distribution, and application portability. It uses *dynamic load balancing* since shared memory allows any task to run anywhere. Coherency rules allow tasks to run in any order. To balance work across processors, it begins with tasks that have not yet started and all nodes are kept doing work. Programs with widely-varying task lengths will still run efficiently. With *transparent latency hiding*, multiple tasks time share on each node to eliminate wait states. Transparent hierarchical data caching keeps times for data copying to a minimum.

The Myrias paradigm provides *dynamic parallelism* where memory distribution, task distribution and load balancing are all done dynamically in response to specific requirements of a given job. This allows parallelism to respond to specific input data conditions and allows the system to respond to interference from other jobs. *Uncached global memory* (all tasks modify the same page) and *message passing* are supported and can be intermixed with normal *PARDO* memory. The system maintains only one copy of an uncached global shared memory page and moves it between processors as it is referenced. The memory paradigms can be intermixed to allow incremental development with optimal results. Optimized subroutines can be used by naive users without seeing effects of lower paradigms.

The Myrias programming paradigm exploits control flow parallelism. This approach is to extend common programming languages with constructs that allow the expression and execution of parallelism. This makes parallelization similar to vectorization except that both fine and grain coarse parallelism can be exploited. Parallelism is primarily expressed in loops and are referred as *PARDO* (parallel do) loops ( Karpoff and Lake, 1993). A task is created for each iteration of the *PARDO* loop. Then, the tasks are automatically distributed

and load-balanced across available processors. PARDO's can be nested with arbitrary complexity such as nested and recursive parallelism. Each task created by a PARDO, child task, inherits a complete copy of the address space from the parent task's address space. When the child tasks are completed their address spaces are merged back (*mergeby sum*) into a single image and parent task resumes with an updated address space. The Myrias PARDO is similar to the FORALL statement of the Fortran-D (Fox et al., 1990) in that both create tasks which use a copy-merge model for semantics.

## A.2 THE FUJITSU VPX240/10 SUPERCOMPUTER

The 3-D acoustic modeling and reverse time migration algorithms presented in this thesis were implemented on a Fujitsu VPX240/10 supercomputer at the Calgary High Performance Computing Centre (HPCC).

The Fujitsu VPX240/10 is a single processor, pipelined SIMD (Single Instruction, Multiple Data) parallel computer with a peak computational capability of 2.5 Gflops (2.5 billion floating point operations per second). It is supported by a large central memory, fast and large secondary storage units and a large mass storage subsystem.

The CPU consists of a *Main Storage Unit (MSU)*, one *Vector Processing Unit* and one *Scalar Processing Unit*. The main storage unit contains up to 64 MWords (512 Mbytes) of 128-way interleaved memory (128 memory banks) with 35 ns access time. The main memory is backed up by a secondary storage unit of that consists of 1024 Mbytes (128 MWords) which can be configured as part of the file system with transfer rates between SSU and MSU for either reads or writes at bandwidths approaching 1 Gbytes/sec.

The VPX240/10 vector processing unit is an SIMD (single instruction, multiple data) pipelined parallel processor. The vector unit includes an ensemble of vector registers and replicated pipelines (each delivering two results per vector clock cycle). The maximum speedup available from pipelining is limited by the number of operand pairs that can be in the pipe simultaneously (~10); all additional performance must come from parallelism. Out of the seven pipelines that the VPX240 has (Figure 1), six can operate simultaneously: two load-store, two mask, and two arithmetic pipelines. The load-store pipelines can deliver two 64 bit words per vector unit clock cycle each. The multiply-add pipelines can execute up to two "multiply-adds" per vector clock cycle each when executes the compound multiply-add instruction on contiguous data elements. Thus the two multiply-add pipelines (four independent arithmetic pipes) concurrently can execute compound multiply-add instructions at a peak computational rate of 8 floating point operations (FLOPs) per 3.2 ns

clock period, which translates to 2.5 GFLOPS performance. This is the case when computing convolutions, solving linear equations, and performing matrix-matrix or matrix-vector operations.

In contrast to the vector times vector operations that was optimal on the CRAY-1, the optimal computation on the VPX240 is the matrix multiply computation defined by the following kernel:

```
do 4 j=1 , n
*VOCL LOOP, UNROLL (4)
do 4 k=1 , n
do 4 i= 1 , n
4      c(i , j) = c(i , j) + a(i , k) * b(k , j) .
```

The use of the compiler directive VOCL (Vector Optimization Control Line) to unroll the k loop to a depth of 4 increases the number of parallel floating point operations in the inner loop to 8 to match the 4-pipe architecture of the VPX240 without the need of changing the original code.

The 64 KB registers of the VPX240 can be reconfigured by the compiler to match the algorithmic characteristics of an application program. The size of the registers are matched to the inherent parallelism of the application. As the level of parallelism supported by the hardware increases, the vector length at which half the peak performance is attained has also increased. This is the so called  $n_{1/2}$ . When this value is small the computer behaves more like a serial computer and when it is large the computer behaves more like a massively parallel computer. The VPX240 has an  $n_{1/2}$  of approximately 150. The reconfigurable vector registers of the VPX240 allow short vector lengths to be matched with short vector lengths by lowering the  $n_{1/2}$  value for that particular kernel. This allows the computer to achieve higher peak performance for a wider range of problem sizes. One of the hardware characteristics that contributes to an increase in the value of  $n_{1/2}$  is the vector start-up overheads. The advantage of multiple vector registers in the pipelined architectures such the one of the VPX240 is that the startup overhead of a vector load is incurred only for the first elements in the loop. Subsequent loads and their overheads can be overlapped with computation. This is in contrast with the SIMD parallel arrays, which cannot overlap the communications overhead with computation.

Using Flynn's taxonomy of parallel processing, the VPX240 belongs to the SIMD family of parallel computers. Parallelism is defined at the loop level (fine-grained



parallelism as opposed to the routine or program level (coarse-grained parallelism). The VPX240 with its independent arithmetic pipes and use of pipelining is a hybrid implementation of both spatially and temporally multiplexed parallel processors.

The VPX240 has also a single scalar processing unit with a scalar clock running at 6.4 ns (twice the duration of the 3.2 ns vector clock). The operating system partitions the central memory into two regions. The vector processing unit is supported by a physical memory organization that is optimal for cpu-intensive computing. The scalar processing unit is supported by the virtual (paged) memory that is more suitable for an interactive workload.

### **A.3 THE CONVEX C210 VECTOR MINI-SUPERCOMPUTER**

Most of the 2-D elastic wave simulations for enhanced oil recovery (EOR) projects at Cold Lake Alberta presented in this thesis were performed on a Convex C210 mini-supercomputer at the University of Alberta.

The Convex C210 has a 64-bit vector uniprocessor with a cycle time of 40 ns. It has a peak speed of 50 Mflops, 128 Mbytes of real memory and 5.7 Gbytes of disk storage. Of this amount, 1.1 Gbytes is used to support virtual memory. Also, as we mentioned earlier, the Convex C-series computers belong to the MIMD shared-memory class of computers.

The Convex C210 has a vector processing unit with total of 8 vector registers with 128 elements each and 64 bits per element. There are three independent functional unit controllers: load and store, multiply and divide, add and logical. Chaining consists of directly routing the output of one functional unit to be the the input of another functional unit. A vector functional unit can start processing new input before finishing work on its previous input.

There are a number of properties associated with the vectorization of an application code. Loops containing array references that use loop induction variables as subscripts are good candidates for vectorization. A loop induction variable is a variable that is incremented or decremented by a constant value on each iteration of the loop (e.g., the loop control variable). Generally, when loops are nested, only the innermost loop can be vectorized. The compiler can sometimes distribute or interchange nested loops in order to improve vectorization performance. Some assignments into scalar values can be vectorized by the compiler using vector reduction operations (some loops can be vectorized even if the results of operations are not stored into arrays of data). Use of loop induction variables in calculations does not inhibit vectorization. Conditionals within loops can often be

vectorized.

There are a number of restrictions in the vectorization of a code on Convex supercomputers and generally on vector supercomputers. Vectorization of a loop can be inhibited if any of the following exist within the loop: Function or subroutine calls; I/O statements; Character data; multiple exits or entries; equivalence variables or arrays; recurrence. Recurrence exists when a new value assigned to one element of a vector operation depends upon the use of another result from the same vector operation. Results of a vector operation are never available for use by the same vector operation. When the value of a subscript cannot be determined, the compiler will not attempt vectorization in order to avoid a possible recurrence. The portions of the loop that inhibit vectorization are placed by the compiler in a separate loop and run in scalar. Also the compiler performs loop interchange in order to avoid recurrence in the inner loop, increase the iteration count for the vectorizable inner loop and achieve the most efficient vector stride in the inner loop.

## APPENDIX B

### FUNDAMENTALS OF SEISMIC WAVES

#### B.1 STRESS AND STRAIN

In seismology the theory of continuum mechanics is used to describe the propagation of seismic waves through the earth. *Newton's law*, in terms of the force and the mass per unit volume, can be written as

$$\mathbf{f}(\mathbf{r},t) = \rho \frac{\partial^2 \mathbf{u}(\mathbf{r},t)}{\partial t^2} = \rho \ddot{\mathbf{u}}(\mathbf{r},t) \quad (\text{B.1.1})$$

or as a system of equations, one for each component of the force and the displacement vectors,

$$f_i(\mathbf{r},t) = \rho \frac{\partial^2 u_i(\mathbf{r},t)}{\partial t^2} = \rho \ddot{u}_i(\mathbf{r},t) \quad (\text{B.1.2})$$

There are two types of forces that can act on an object. One is the body force, which acts everywhere within an object, resulting to a net force proportional to the volume of the object. The other is the surface force, which acts on the surface of an object, resulting to net force proportional to the surface area of the object.

We define the *traction vector*  $\mathbf{T}(\hat{\mathbf{n}})$ , as the limit of the surface force  $\mathbf{F}$  per unit area at any point as the area becomes infinitesimal. The traction vector has the same orientation as the force, and is a function of the unit normal vector  $\hat{\mathbf{n}}$  because it depends on the orientation of the surface. The system of surface forces acting on a volume is described by three traction vectors. The components of the three traction vectors are  $T_i^j$ , where the upper index (j) indicates the surface and the lower index (i) indicates the component.

The *stress tensor* completely describes the surface forces acting on a body and is given by

$$\sigma_{ij} = \begin{pmatrix} \sigma_{11} & \sigma_{12} & \sigma_{12} \\ \sigma_{21} & \sigma_{22} & \sigma_{23} \\ \sigma_{31} & \sigma_{32} & \sigma_{33} \end{pmatrix} = \begin{pmatrix} T_1^1 & T_2^1 & T_3^1 \\ T_1^2 & T_2^2 & T_3^2 \\ T_1^3 & T_2^3 & T_3^3 \end{pmatrix} \quad (\text{B.1.3})$$

The three diagonal components are called *normal stresses* and the six off-diagonal components are called *shear stresses*. Positive values of the normal tractions correspond to *tension* and negative values correspond to *compression*.

The stress tensor is symmetric ( $\sigma_{ij} = \sigma_{ji}$ ) and (B.1.3) can be written as

$$T_i = \sum_{j=1}^3 \sigma_{ij} n_j \quad \text{or} \quad \mathbf{T} = \boldsymbol{\sigma} \hat{\mathbf{n}} \quad (\text{B.1.4})$$

If the traction and normal vectors are parallel, then the shear components of the traction are zero. These surfaces are characterized by the *principal stress axes* and the normal stresses are called *principal stresses*. Equation (B.1.4) can be written as

$$T_i = \sigma_{ij} n_j = \lambda n_j \quad (\text{B.1.5})$$

Thus the principal stress axes  $\hat{\mathbf{n}}$  are the eigenvectors of the stress tensor and the principal stresses  $\lambda$  are the eigenvalues.

Now, if we write Newton's law in terms of body forces and stresses we have the *equation of motion*:

$$\frac{\partial \sigma_{ij}(\mathbf{r}, t)}{\partial x_j} + f_i(\mathbf{r}, t) = \rho \frac{\partial^2 u_i(\mathbf{r}, t)}{\partial t^2} \quad (\text{B.1.6})$$

that must be satisfied at every point in a continuous medium. If no body forces are applied then we have the *homogeneous equation of motion*,

$$\frac{\partial \sigma_{ij}(\mathbf{r}, t)}{\partial x_j} = \rho \frac{\partial^2 u_i(\mathbf{r}, t)}{\partial t^2} \quad (\text{B.1.7})$$

If stresses are applied to a non-rigid material they caused deformation. The deformations that result from the differential motion within the body are described by the *strain tensor*  $\epsilon_{ij}$ . The components of the strain tensor are the spatial derivatives of the

displacement field ( $\mathbf{u}(\mathbf{r})=(u_x, u_y, u_z)$ ). The strain tensor is given by the following equation,

$$\varepsilon_{ij} = \begin{bmatrix} \frac{\partial u_x}{\partial x} & \frac{1}{2}\left(\frac{\partial u_x}{\partial y} + \frac{\partial u_y}{\partial x}\right) & \frac{1}{2}\left(\frac{\partial u_x}{\partial z} + \frac{\partial u_z}{\partial x}\right) \\ \frac{1}{2}\left(\frac{\partial u_y}{\partial x} + \frac{\partial u_x}{\partial y}\right) & \frac{\partial u_y}{\partial y} & \frac{1}{2}\left(\frac{\partial u_y}{\partial z} + \frac{\partial u_z}{\partial y}\right) \\ \frac{1}{2}\left(\frac{\partial u_z}{\partial x} + \frac{\partial u_x}{\partial z}\right) & \frac{1}{2}\left(\frac{\partial u_z}{\partial y} + \frac{\partial u_y}{\partial z}\right) & \frac{\partial u_z}{\partial z} \end{bmatrix} \quad (\text{B.1.8})$$

*Dilation* is the divergence of the displacement field and is given by the sum of the diagonal components of the strain tensor,

$$\theta = \varepsilon_{ii} = \frac{\partial u_x}{\partial x} + \frac{\partial u_y}{\partial y} + \frac{\partial u_z}{\partial z} = \nabla \cdot \mathbf{u} \quad (\text{B.1.9})$$

*Hooke's law* gives the *stress-strain* relation which is the medium's *constitutive equation*,

$$\sigma_{ij} = c_{ijkl} \varepsilon_{kl} \quad (\text{B.1.10})$$

where the constants  $c_{ijkl}$  are the elastic moduli of the elastic medium. Generally, an elastic medium has 21 independent elastic constants. For an *isotropic* material (same properties regardless orientation) there are only two independent elastic moduli, which can be defined in different ways. One pair is the *Lame's parameters*  $\lambda$  and  $\mu$ . Then, the *constitutive equation for an isotropic elastic material* is written as

$$\sigma_{ij} = \lambda \varepsilon_{kk} \delta_{ij} + 2 \mu \varepsilon_{ij} = \lambda \theta \delta_{ij} + 2 \mu \varepsilon_{ij} \quad (\text{B.1.11})$$

where  $\delta_{ii}=0$ .

The *bulk modulus or incompressibility*  $K$  is defined as the ratio of the pressure applied to the resulted volumetric change. For an isotropic elastic body,

$$K = \frac{-dp}{d\theta} = \lambda + \frac{2}{3} \mu \quad (\text{B.1.12})$$

If we stress a body along only one axis we get a state of stress called uniaxial tension. The *Poisson's ratio* gives the ratio of the contraction along the other two axes to the extension along the axis with uniaxial tension,

$$\nu = -\frac{\epsilon_{yy}}{\epsilon_{xx}} = -\frac{\epsilon_{zz}}{\epsilon_{xx}} = \frac{\lambda}{2(\lambda + \mu)} \quad (\text{B.1.13})$$

If a medium has  $\lambda = \mu$ , then is called poisson solid and has poisson's ratio equal 0.25. The *Young's modulus* is defined as the ratio of the tensional stress to the resulting extensional stress,

$$E = \frac{\sigma_{xx}}{\epsilon_{xx}} = \frac{\mu(3\lambda + 2\mu)}{\lambda + \mu} \quad (\text{B.1.14})$$

*Boundary conditions* relate the displacements and tractions as the wave propagates from one medium to another. The earth's surface is considered a *free surface* and for the traction vector and the stress tensor the we have

$$T_i = \sigma_{ij} n_j = 0 \quad \text{and} \quad \sigma_{xz} = \sigma_{yz} = \sigma_{zz} \quad (\text{B.1.15})$$

On the other hand, at the interface between two solids, the three components of the *traction* vector and all the components of the *displacement* must be *continuous*.

## B.2 SEISMIC WAVES

For an *isotropic elastic medium*, the x-component of the *homogeneous* (no body force/source term) *equation of motion* is

$$\frac{\partial \sigma_{xx}(x,y,z,t)}{\partial x} + \frac{\partial \sigma_{xy}(x,y,z,t)}{\partial y} + \frac{\partial \sigma_{xz}(x,y,z,t)}{\partial z} = \rho \frac{\partial^2 u_x(x,y,z,t)}{\partial t^2} \quad (\text{B.2.1})$$

Using the constitutive equation (B.1.11), we obtain the following *stress-strain* relations:

$$\begin{aligned}
\sigma_{xx} &= \lambda\theta + 2\mu \frac{\partial u_x}{\partial x} \\
\sigma_{xy} &= \mu \left( \frac{\partial u_x}{\partial y} + \frac{\partial u_y}{\partial x} \right) \\
\sigma_{xz} &= \mu \left( \frac{\partial u_x}{\partial z} + \frac{\partial u_z}{\partial x} \right)
\end{aligned} \tag{B.2.2}$$

where  $\theta$  is the dilatation given by equation (B.1.9). Then, taking the derivatives of the stress components, assuming the medium is homogeneous (the elastic constants do not vary with position), using the definitions of dilatation  $\theta$  and the Laplacian

$$\nabla^2(u_x) = \frac{\partial^2 u_x}{\partial x^2} + \frac{\partial^2 u_x}{\partial y^2} + \frac{\partial^2 u_x}{\partial z^2} \tag{B.2.3}$$

and substituting into equation (B.2.1) we obtain the x-component of the equation of motion,

$$(\lambda + \mu) \frac{\partial \theta}{\partial x} + \mu \nabla^2(u_x) = \rho \frac{\partial^2 u_x}{\partial t^2} \tag{B.2.4}$$

Similarly, equations of motion for the two other components of displacement can be obtained. Then, using the vector Laplacian,  $\nabla^2 \mathbf{u} = (\nabla^2 u_x, \nabla^2 u_y, \nabla^2 u_z)$ , the three components of the equation of motion can be combined into a single vector equation:

$$(\lambda + 2\mu) \nabla (\nabla \cdot \mathbf{u}(x,y,z,t)) - \mu \nabla \times (\nabla \times \mathbf{u}(x,y,z,t)) = \rho \frac{\partial^2 \mathbf{u}(x,y,z,t)}{\partial t^2} \tag{B.2.5}$$

We can decompose the displacement field into a scalar potential  $\Phi(x,y,z,t)$  and a vector potential  $\Psi(x,y,z,t)$  such as

$$\mathbf{u}(x,y,z,t) = \nabla \Phi(x,y,z,t) + \nabla \times \Psi(x,y,z,t) \tag{B.2.6}$$

$$\nabla \cdot (\nabla \times \Psi) = 0 \quad \text{and} \quad \nabla \times (\nabla \Phi) = 0 \tag{B.2.7}$$

Then, by substituting into equation (B.2.5) and rearranging terms, we obtain

$$\nabla \left( (\lambda + 2\mu) \nabla^2 \Phi(x,y,z,t) - \rho \frac{\partial^2 \Phi(x,y,z,t)}{\partial t^2} \right) = -\nabla \times \left( \mu \nabla^2 \Psi(x,y,z,t) - \rho \frac{\partial^2 \Psi(x,y,z,t)}{\partial t^2} \right) \quad (\text{B.2.8})$$

A solution of this equation can be obtained if each of the terms in the brackets is zero. Then, the scalar potential satisfies the following equation

$$\nabla^2 \Phi(x,y,z,t) = \frac{1}{v_p^2} \frac{\partial^2 \Phi(x,y,z,t)}{\partial t^2} \quad (\text{B.2.9})$$

This equation is the *3-D scalar wave equation* and is associated with the propagation of a compressional or P-wave that propagates with velocity,

$$v_p = \left( \frac{\lambda + 2\mu}{\rho} \right)^{\frac{1}{2}} \quad (\text{B.2.10})$$

On the other hand, the vector potential satisfies equation

$$\nabla^2 \Psi(x,y,z,t) = \frac{1}{v_s^2} \frac{\partial^2 \Psi(x,y,z,t)}{\partial t^2} \quad (\text{B.2.11})$$

This equation is the *3-D vector wave equation* and is associated with the propagation of a shear or S-wave that propagates with velocity,

$$v_s = \left( \frac{\mu}{\rho} \right)^{\frac{1}{2}} \quad (\text{B.2.12})$$

The P-wave is associated with the scalar potential. As the wave propagates, the resulting displacements in the direction of the propagation cause the medium to be alternatively compressed and expand. Thus, the wave generated by a scalar potential results to a volumetric change and is called *longitudinal* or *compressional* wave. On the other hand, the shear wave do not cause volume change. The only displacement associated with



this propagating wave is perpendicular to the direction of the wave propagation. Thus, the wave generated by the vector potential is called *transverse* wave.

The S-wave polarizations are the SV for shear waves with displacement in the vertical plane (x-z) and the SH for the shear waves with displacement in the horizontal plane and in the y-direction. Also, shear waves cannot propagate through an ideal fluid.

### B.3 THE ACOUSTIC WAVE EQUATION

The acoustic wave equation describes sound waves in a fluid or gas. However, this equation is valid for waves in solid earth if the converted compressional to shear wave energy is negligible (usually for angle of incidence  $< 20^\circ$ ). Furthermore, it is true for SH-wave propagation.

Using Newton's law (mass per unit volume  $\times$  acceleration = force per unit volume = - pressure gradient)

$$\rho \frac{\partial^2 \mathbf{u}}{\partial t^2} = - \nabla P \quad (\text{B.3.1})$$

where  $\mathbf{u}$  is the particle displacement ;  $\rho$  is the density (mass per unit volume of the fluid) and  $P$  is the pressure of the fluid. The pressure  $P$  is equal to the product of the incompressibility  $K$  and the convergence of displacement  $\mathbf{u}$  (negative of the divergence):

$$P = - K \nabla \cdot \mathbf{u} \quad (\text{B.3.2})$$

We take the second time derivative of equation (B.3.2) and we have

$$\frac{\partial^2 P}{\partial t^2} = - K \nabla \cdot \frac{\partial^2 \mathbf{u}}{\partial t^2} \quad (\text{B.3.3})$$

Introducing (B.3.1) into the right side of equation (B.3.3) we have

$$\frac{\partial^2 P}{\partial t^2} = K \nabla \cdot \frac{\nabla P}{\rho} \quad (\text{B.3.4})$$

This is the *acoustic wave equation* and three dimensions it can be written as

$$\left( \frac{\partial}{\partial x} \frac{1}{\rho} \frac{\partial}{\partial x} + \frac{\partial}{\partial y} \frac{1}{\rho} \frac{\partial}{\partial y} + \frac{\partial}{\partial z} \frac{1}{\rho} \frac{\partial}{\partial z} \right) P(x,y,z,t) = \frac{1}{K(x,y,z)} \frac{\partial^2 P(x,y,z,t)}{\partial t^2} \quad (\text{B.3.5})$$

If we assume that the density is space independent ( $\rho \neq \rho(x,y,z)$ ), then we obtain the *scalar wave equation* in its usual form

$$\frac{\partial^2 P}{\partial t^2} = \frac{K}{\rho} \nabla^2 P \quad (\text{B.3.6})$$

The *3-D scalar wave equation* in its usual form is also written as

$$\frac{\partial^2 P(x,y,z,t)}{\partial x^2} + \frac{\partial^2 P(x,y,z,t)}{\partial y^2} + \frac{\partial^2 P(x,y,z,t)}{\partial z^2} = \frac{1}{v^2(x,y,z)} \frac{\partial^2 P(x,y,z,t)}{\partial t^2} \quad (\text{B.3.7})$$

where  $v(x,y,z)$  is the wave velocity in the medium and is given by the equation

$$v(x,y,z) = \left( \frac{K(x,y,z)}{\rho} \right)^{1/2} \quad (\text{B.3.8})$$

and the *2-D scalar wave equation* is written as

$$\frac{\partial^2 P(x,z,t)}{\partial x^2} + \frac{\partial^2 P(x,z,t)}{\partial z^2} = \frac{1}{v^2(x,z)} \frac{\partial^2 P(x,z,t)}{\partial t^2} \quad (\text{B.3.9})$$

## APPENDIX C

### 3-D EXPLICIT FINITE DIFFERENCE MODELING

#### C.1 THE MACCORMACK TYPE SPLITTING SCHEME

The MacCormack type of scheme in the x-direction (for equation 3.3.23) is given by equations (3.3.24) and (3.3.25) for the predictor and corrector, respectively, and when applied to the hyperbolic system of the 3-D acoustic wave equation (3.3.10) consists of :

a) for  $n=2k$  ;  $k=1,2,\dots$

for the pressure P, the predictor

$$P_{i,j,k}^{(1)} = P_{i,j,k}^{(n)} - \frac{\Delta t}{6 \Delta x} K_{i,j,k} \left( 7 (v_x)_{i,j,k}^{(n)} - 8 (v_x)_{i+1,j,k}^{(n)} + (v_x)_{i+2,j,k}^{(n)} \right) \quad (C.1.1)$$

and the corrector

$$P_{i,j,k}^{(n+1)} = \frac{1}{2} \left( P_{i,j,k}^{(1)} + P_{i,j,k}^{(n)} \right) + \frac{\Delta t}{12 \Delta x} K_{i,j,k} \left( 7 (v_x)_{i,j,k}^{(1)} - 8 (v_x)_{i-1,j,k}^{(1)} + (v_x)_{i-2,j,k}^{(1)} \right) \quad (C.1.2)$$

for the particle velocity component  $v_x$ , the predictor

$$(v_x)_{i,j,k}^{(1)} = (v_x)_{i,j,k}^{(n)} - \frac{\Delta t}{6 \Delta x} \rho_{i,j,k}^{-1} \left( 7 P_{i,j,k}^{(n)} - 8 P_{i+1,j,k}^{(n)} + P_{i+2,j,k}^{(n)} \right) \quad (C.1.3)$$

and the corrector

$$(v_x)_{i,j,k}^{(n+1)} = \frac{1}{2} \left( (v_x)_{i,j,k}^{(1)} + (v_x)_{i,j,k}^{(n)} \right) + \frac{\Delta t}{12 \Delta x} \rho_{i,j,k}^{-1} \left( 7 P_{i,j,k}^{(1)} - 8 P_{i-1,j,k}^{(1)} + P_{i-2,j,k}^{(1)} \right) \quad (C.1.4)$$

The above difference equations are employed in alternate time steps with the following ones resulting from equations (3.3.26) and (3.3.27) for the predictor and the corrector, respectively. Thus,

b) for  $n=2k+1$  ;  $k=0,1,2,\dots$

for the pressure P, the predictor is

$$P_{i,j,k}^{(1)} = P_{i,j,k}^{(n)} + \frac{\Delta t}{6 \Delta x} K_{i,j,k} \left( 7 (v_x)_{i,j,k}^{(n)} - 8 (v_x)_{i+1,j,k}^{(n)} + (v_x)_{i+2,j,k}^{(n)} \right) \quad (C.1.5)$$

and the corrector is

$$P_{i,j,k}^{(n+1)} = \frac{1}{2} \left( P_{i,j,k}^{(1)} + P_{i,j,k}^{(n)} \right) - \frac{\Delta t}{12 \Delta x} K_{i,j,k} \left( 7 (v_x)_{i,j,k}^{(1)} - 8 (v_x)_{i-1,j,k}^{(1)} + (v_x)_{i-2,j,k}^{(1)} \right) \quad (C.1.6)$$

for the particle velocity component  $v_x$ , the predictor is

$$(v_x)_{i,j,k}^{(1)} = (v_x)_{i,j,k}^{(n)} + \frac{\Delta t}{6 \Delta x} \rho_{i,j,k}^{-1} \left( 7 P_{i,j,k}^{(n)} - 8 P_{i+1,j,k}^{(n)} + P_{i+2,j,k}^{(n)} \right) \quad (C.1.7)$$

and the corrector is

$$(v_x)_{i,j,k}^{(n+1)} = \frac{1}{2} \left( (v_x)_{i,j,k}^{(1)} + (v_x)_{i,j,k}^{(n)} \right) - \frac{\Delta t}{12 \Delta x} \rho_{i,j,k}^{-1} \left( 7 P_{i,j,k}^{(1)} - 8 P_{i-1,j,k}^{(1)} + P_{i-2,j,k}^{(1)} \right) \quad (C.1.8)$$

The corresponding equations for the MacCormack scheme in the y-direction (for pressure and particle velocity component  $v_y$ ) and in the z-direction (for pressure and vertical partial velocity  $v_z$ ) are obtained similarly.

## APPENDIX D

### IMPLICIT FINITE-DIFFERENCE MIGRATION

#### D.1 IMPLICIT FINITE DIFFERENCE FOR THE 65<sup>0</sup> PARABOLIC APPROXIMATION

We want to compute the monochromatic wavefield  $Q(x,z,\omega_j)$  at  $(x,z)$  location and frequency  $\omega_j$ , where  $j=1,\dots,N\omega$  with  $N\omega$  total number of frequencies used. Thus, we discretize the differential equation (4.2.18) and approximate each harmonic component  $Q(x,z)$  by a mesh function  $q_n^m$  where  $m=i \Delta x$ , with  $i=1,\dots,Nx$  and  $n=k \Delta z$ , with  $k=1,\dots,Nz$ .  $\Delta x$  and  $\Delta z$  are the finite difference mesh grid spacings for the horizontal and vertical axes respectively.  $Nx$  indicates the number of traces in the gather and  $Nz$  the number of depth steps. Also, the value of  $m(x,z)=\omega_n/v(x,z)$  at the  $i$ -th trace ( $i\Delta x$  lateral location) and  $k$ -th depth step ( $k\Delta z$  depth location) is set  $m(i\Delta x,k\Delta z)=m$ .

Replacing the differentials of equation (4.2.18) by their respective finite differences and changing the sign of the  $z$  differentials to evaluate upgoing waves one has (4.2.20):

$$-\frac{i\beta}{\alpha m} \delta_{xx} \delta_z Q - \frac{im}{\alpha} \delta_z Q + \delta_{xx} Q = 0 \quad (D.1.1)$$

where  $\delta_z = \partial/\partial z$ ,  $\delta_{xx} = \partial^2/\partial x^2$ , and  $m=m(x,z)=\omega/v(x,z)$ .

A fourth order of accuracy for the approximation of the second order differential is the Douglas formula and is given by (Mitchell and Griffiths, 1980; Claerbout, 1985) :

$$\delta_{xx} = \frac{1}{\Delta x^2} \left( \frac{\delta^2}{1 + \gamma \delta} \right) \quad (D.1.2)$$

where  $\Delta x$  is the grid spacing and  $\gamma = 1/12$  (Mitchell and Griffiths, 1980) or  $1/6$  (Claerbout, 1985), and  $\delta^2$  is the operator  $(1, -2, 1)$ .

An implicit Crank-Nicolson (Mitchell and Griffiths, 1980; Claerbout 1976, 1985)

finite difference algorithm scheme is employed to solve the resultant difference equation. This algorithm is unconditionally stable (Mitchell and Griffiths, 1980) and involves more than one point at the advanced depth level centered at  $n+1/2$  according to :

$$q_{n+1/2}^m = \frac{1}{2} (q_{n+1}^m + q_n^m) \quad (D.1.3)$$

The finite difference approximation of the differential equation (D.1.1) employing equations (D.1.2) and (D.1.3) reads:

$$-\frac{i\beta}{\alpha m} \frac{1}{\Delta x^2} \left( \frac{\delta^2}{1 + \gamma \delta^2} \right) \left( \frac{q_{n+1}^m - q_n^m}{\Delta z} \right) - \frac{i m}{\alpha} \left( \frac{q_{n+1}^m - q_n^m}{\Delta z} \right) + \frac{1}{\Delta x^2} \left( \frac{\delta^2}{1 + \gamma \delta^2} \right) \frac{1}{2} (q_{n+1}^m + q_n^m) = 0 \quad (D.1.4)$$

Multiply throughout by  $\Delta x^2 (1 + \gamma \delta^2)$  we have:

$$-\frac{i\beta}{\alpha m} \frac{\delta^2}{\Delta z} (q_{n+1}^m - q_n^m) - \frac{i m \Delta x^2}{\alpha \Delta z} (1 + \gamma \delta^2) (q_{n+1}^m - q_n^m) + \frac{\delta^2}{2} (q_{n+1}^m + q_n^m) = 0 \quad (D.1.5)$$

Simplifying by setting the laterally varying coefficients as:  $A = \frac{i\beta}{\alpha m \Delta z}$  and

$B = \frac{i m \Delta x^2}{\alpha \Delta z}$ , and apply the operator  $\delta^2 = (1, -2, 1)$  we have:

$$\begin{aligned} & -A q_{n+1}^{m+1} + 2A q_{n+1}^m - A q_{n+1}^{m-1} + A q_n^{m+1} - 2A q_n^m + A q_n^{m-1} \\ & + \frac{1}{2} q_{n+1}^{m+1} - q_{n+1}^m + \frac{1}{2} q_{n+1}^{m-1} + \frac{1}{2} q_n^{m+1} - q_n^m + \frac{1}{2} q_n^{m-1} \\ & - B q_{n+1}^m + B q_n^m - B \gamma q_{n+1}^{m+1} + 2B \gamma q_{n+1}^m - B \gamma q_{n+1}^{m-1} \\ & + B \gamma q_n^{m+1} - 2B \gamma q_n^m + B \gamma q_n^{m-1} = 0 \end{aligned} \quad (D.1.6)$$

After separating the terms with index  $n+1$  to the left hand side and the terms with index  $n$  to the right hand side, we have:

$$\left( -A + \frac{1}{2} - B \gamma \right) q_{n+1}^{m+1} + (2A - 1 - B + 2B\gamma) q_{n+1}^m +$$

$$\begin{aligned}
& + \left(-A + \frac{1}{2} - B\gamma\right) q_{n+1}^{m-1} = \\
& \left(-A - \frac{1}{2} - B\gamma\right) q_n^{m+1} + (2A + 1 - B + 2B\gamma) q_n^m + \\
& + \left(-A - \frac{1}{2} - B\gamma\right) q_n^{m-1}
\end{aligned} \tag{D.1.7}$$

We can define the coefficients:

$$\begin{aligned}
\bar{A} &= \left(-A + \frac{1}{2} - B\gamma\right) \\
\bar{B} &= (2A - 1 - B + 2B\gamma) \\
\bar{C} &= \left(-A - \frac{1}{2} - B\gamma\right) \\
\bar{D} &= (2A + 1 - B + 2B\gamma)
\end{aligned} \tag{D.1.8}$$

and equation (D.1.7) becomes

$$\bar{A} q_{n+1}^{m+1} + \bar{B} q_{n+1}^m + \bar{C} q_{n+1}^{m-1} = \bar{C} q_n^{m+1} + \bar{D} q_n^m + \bar{C} q_n^{m-1} \tag{D.1.9}$$

Then, if the wavefield is extrapolated from the “n” depth position (“n” present values are known) to the “n+1” depth level (the “n+1” values are the unknowns), we can set a system of simultaneous equations for all “m” lateral locations given as follows:

$$\begin{bmatrix}
\bar{b} & \bar{A} & 0 & \dots & 0 \\
\bar{A} & \bar{B} & \bar{A} & \dots & 0 \\
0 & \bar{A} & \bar{B} & \bar{A} & \dots & 0 \\
\dots & \dots & \dots & \dots & \dots & 0 \\
0 & \dots & \dots & \bar{A} & \bar{B} & \bar{A} \\
0 & 0 & \dots & \dots & \bar{A} & \bar{b}
\end{bmatrix}
\begin{bmatrix}
q_{n+1}^1 \\
q_{n+1}^2 \\
\vdots \\
\vdots \\
q_{n+1}^{m-1} \\
q_{n+1}^m
\end{bmatrix}
=
\begin{bmatrix}
d_n^1 \\
d_n^2 \\
\vdots \\
\vdots \\
d_n^{m-1} \\
d_n^m
\end{bmatrix} \tag{D.1.10}$$

where

$$d_n^m = \bar{C} q_n^{m+1} + \bar{D} q_n^m + \bar{C} q_n^{m-1} \tag{D.1.11}$$

The  $b_l$  and  $b_r$  are adjustable and are evaluated according to the boundary conditions. The above system is a tridiagonal system that is, except for three diagonals all the elements of the matrix in (D.1.10) are zero.

We follow the same approach for the one-pass 3-D finite difference depth migration since the diffraction term, using the splitting approach, consists of the diffraction term in the  $x$  direction (4.3.14) and the diffraction term in the  $y$ -direction (4.3.15). Each of these equations are the same as the one solved above (4.2.20 or D.1.1). An alternating direction implicit (ADI) Crank-Nicolson scheme is employed for the solution of both diffraction terms where at each depth step the equations are solved alternatively along the  $x$  and  $y$  direction.

## D.2 SOLUTION OF THE TRIDIAGONAL SYSTEM OF EQUATIONS

The tridiagonal system (D.1.10) is solved using the following method (Claerbout, 1985). Let the simultaneous equations be written as a difference equation:

$$a_j q_{j+1} + b_j q_j + c_j q_{j-1} = d_j \quad (D.2.1)$$

with  $j = 1, \dots, m$ , where  $m$  is the number of traces in the gather. Next, we introduce two new variables  $e_j$  and  $f_j$  along with an equation

$$q_j = e_j q_{j+1} + f_j \quad (D.2.2)$$

which with shifted index can be written:

$$q_{j-1} = e_{j-1} q_j + f_{j-1} \quad (D.2.3)$$

By inserting (D.2.3) into (D.2.1), we have :

$$a_j q_{j+1} + b_j q_j + c_j (e_{j-1} q_j + f_{j-1}) = d_j \quad (D.2.4)$$

Now, we rearrange (D.2.4) to resemble (D.2.2) :



$$q_j = \frac{-a_j}{b_j + c_j e_{j-1}} q_{j+1} + \frac{d_j - c_j f_{j-1}}{b_j + c_j e_{j-1}} \quad (D.2.5)$$

Compare (D.2.5) with (D.2.2) , we can see that recursion for  $e_j$  and  $f_j$  can be obtained as :

$$e_j = \frac{-a_j}{b_j + c_j e_{j-1}} \quad \text{and} \quad f_j = \frac{d_j - c_j f_{j-1}}{b_j + c_j e_{j-1}} \quad (D.2.6)$$

with  $e_1 = -a_1 / b_1$  and  $f_1 = d_1 / b_1$ . Then, for the right hand boundary we have from (D.2.10) that:

$$A_{m-1} q_{m-1} + b_r q_m = d_m \quad (D.2.7)$$

and from (D.2.3) replacing  $j$  by  $m$  we get:

$$q_{m-1} - e_{m-1} q_m = f_{m-1} \quad (D.2.8)$$

Solving the system of the two equations for  $q_m$  we have:

$$q_m = \frac{d_m - A_{m-1} f_{m-1}}{b_r + A_{m-1} e_{m-1}} \quad (D.2.9)$$

where  $b_r$  is evaluated using the 15<sup>0</sup> absorbing boundary condition, Clayton and Engquist, (1980). Having  $e_j$  and  $f_j$  we can compute the rest of  $q_j$  's from equation (D.2.3) going backwards.

### D.3 STABILITY ANALYSIS FOR THE 65<sup>0</sup> PARABOLIC APPROXIMATION

The problem of stability of a finite difference calculation used to solve equations (4.2.20 or 4.3.14 or 4.3.15) consists of finding a condition under which the difference:

$$q_n^m - \overline{q_n^m} = (Z_n^m) \quad (D.3.1)$$

between the theoretical and numerical solutions of the difference equation bounded as  $n$  tends to infinity, (Mitchell and Griffiths, 1980).

The von Neumann procedure consists of considering an harmonic decomposition of the error  $Z_n^m$  at grid points at a given depth level leading to error function

$$E(x) = \sum_j A_j e^{i b_j x} \quad (D.3.2)$$

where in general the frequencies  $|b_j|$  and  $j$  are arbitrary.

It is necessary to consider only the single term  $e^{ibx}$  where  $b$  is a any real number. For convenience, suppose that the depth being considered is  $z=0$ . To investigate the error propagation as  $z$  increases, it is necessary to find a solution of the finite difference equation (D.1.1) which reduces to  $e^{ibx}$  where  $z=0$ . Let such a solution be:  $e^{az} e^{ibx}$  where  $a = a(b)$  is complex in general. The original error component will not grow with increasing depth if  $|e^{ak}| \leq 1$  for all  $a$ .

Boundary conditions are neglected in the von Neumann method (Mitchell and Griffiths, 1980), which applies in theory only to pure initial value problems. It does however provide necessary conditions for stability of constant coefficient problems regardless of the type of boundary conditions. Substitute:  $Z_n^m = e^{ank} e^{ibmh}$  where  $k = \Delta z$  and  $h = \Delta x$ , into the difference equation (D.1.6) with  $A=-A$  and  $B = -B$  indicating downgoing waves and divide by  $e^{ank} e^{ibmh}$ . We have:

$$\begin{aligned} & A e^{ak} e^{ibh} - 2 A e^{ak} + A e^{ak} e^{-ibh} \\ & - A e^{ibh} + 2 A - A e^{-ibh} + \frac{1}{2} e^{ak} e^{ibh} - e^{ak} + \frac{1}{2} e^{ak} e^{-ibh} + \\ & + \frac{1}{2} e^{ibh} - 1 + \frac{1}{2} e^{-ibh} + B e^{ak} - B + B\gamma e^{ak} e^{ibh} - 2 B\gamma e^{ak} + B\gamma e^{ak} e^{-ibh} - \\ & - B\gamma e^{ibh} + 2 B\gamma + B\gamma e^{-ibh} = 0 \end{aligned} \quad (D.3.3)$$

Multiplying by  $e^{ak}$  throughout and recognizing that exponential terms can be expressed as cosines we have:

$$\begin{aligned} & A e^{2ak} (2 \cos(bh) - 2) - A e^{ak} (2 \cos(bh) - 2) + \frac{1}{2} e^{2ak} (2 \cos(bh) - 2) + \frac{1}{2} e^{ak} (2 \cos(bh) - 2) \\ & + B e^{2ak} - B e^{ak} + B\gamma e^{2ak} (2 \cos(bh) - 2) - B\gamma e^{ak} (2 \cos(bh) - 2) = 0 \end{aligned} \quad (D.3.4)$$

Recognizing that  $(1 - \cos(t)) = 2 \sin^2(t/2)$  and simplifying by denoting  $\xi = e^{ak}$  and

multiplying by -1 throughout we have:

$$4 A \xi^2 \sin^2 (b h / 2) - 4 A \xi \sin^2 (b h / 2) + 2 \xi^2 \sin^2 (b h / 2) + 2 \xi \sin^2 (b h / 2) - B \xi^2 + B \xi + 4 B \gamma \xi^2 \sin^2 (b h / 2) - 4 B \gamma \xi \sin^2 (b h / 2) = 0 \quad (D.3.5)$$

Factoring out  $\xi^2$  and  $\xi$  we get a second order polynomial equation in  $\xi$  as:

$$\xi^2 (4 A \sin^2 (b h / 2) + 2 \sin^2 (b h / 2) - B + 4 B \gamma \sin^2 (b h / 2)) + \xi (-4 A \sin^2 (b h / 2) + 2 \sin^2 (b h / 2) + B - 4 B \gamma \sin^2 (b h / 2)) = 0 \quad (D.3.6)$$

Setting  $S = \sin^2 (b h / 2)$  and recognizing that the coefficients of  $\xi^2$  and  $\xi$  are the same except the  $-2 S$  and  $+2 S$  terms we get a simplified equation:

$$\xi^2 (C + 2 S) - \xi (C - 2 S) = 0 \quad (D.3.7)$$

Solving for  $\xi$  we get the two solutions  $\xi_1 = 0$  and  $\xi_2 = (C - 2 S) / (C + 2 S)$ . Since  $C$  is a pure imaginary number the amplification factor  $\xi$  then takes the form of a complex number divided by its complex conjugate. Expressing the complex number in polar form it becomes clear that such a number has a magnitude of unity. Hence,  $|\xi| = 1$  and this satisfies the unconditional stability criterion,  $|\xi| \leq 1$ .

#### D.4 ABSORBING BOUNDARY CONDITIONS

We used the so called 15° paraxial absorbing boundary conditions in the solution of equation (D.1.10) based on Clayton and Enquist (1980). The effectiveness of these conditions can be shown by comparing their effective reflection coefficients at the boundaries. The 2-D scalar wave equation is given by:

$$P_{xx} + P_{zz} = \frac{1}{v^2} P_{tt} \quad (D.4.1)$$

Taking the 15 degree paraxial approximation we have:

$$P_x + \frac{1}{v}P_t = 0 \quad (D.4.2)$$

Consider an *incident* plane wave travelling at the -z, +x direction according to

$$P_i = e^{(ik_x x - ik_z z - i\omega t)} \quad (D.4.3)$$

which initiates a *reflection* from the right boundary of the form

$$P_r = r e^{(-ik_x x - ik_z z - i\omega t)} \quad (D.4.5)$$

where r is the effective reflection coefficient. Locally near the boundary the wave field ( $P_i + P_r$ ) will satisfy the boundary condition given above thus obtaining:

$$ik_x - irk_x - i\frac{\omega}{v} - ir\frac{\omega}{v} = 0 \quad (D.4.6)$$

or

$$r = \frac{k_x - \frac{\omega}{v}}{k_x + \frac{\omega}{v}} \quad (D.4.7)$$

Recognizing that  $k_x = k \sin(\theta)$  where  $k = \omega/v$  and  $\theta$  is the angle between the travelling wave and the vertical side boundary we have:

$$r = \frac{\sin(\theta) - 1}{\sin(\theta) + 1} \quad (D.4.8)$$

Therefore, when the wave hits the boundary with  $\theta=0^\circ$  (the wave travels in the vertical direction), then  $r=-1$ . These boundary conditions are match with the exact paraxial wave equation (Clayton and Enquist, 1980). Similarly, when the wave hits the boundary with greater angles then we can see that the effective reflection coefficient decreases.

## APPENDIX E

### LITHOPROBE ALBERTA BASEMENT TRANSECT

#### E.1 ACQUISITION

The first part of deep crustal seismic reflection profiling of Alberta (LITHOPROBE Alberta Basement transect) was carried out in the summer of 1992. The goal of this project is to probe the crust beneath the Western Canada Sedimentary Basin and study the origin of the continent and the influence of basement structure on the sedimentary section above.

The program consisted of a 2-D reflection experiment complemented by a 3-D reflection experiment and a long-offset expanding spread (wide angle) experiment. The 2-D reflection data were recorded in north-south and east-west profiles (10 lines) that covered an area of over 500 Km (from west of Edmonton to the Alberta-Saskatchewan border). Each reflection spread consisted of 240 receiver arrays with nine in-line geophones over 42 m per array. The group interval (receiver array spacing from center) was 50 m. The source interval was 100 m (every two receiver stations). This geometry resulted in an average of 60 fold per CMP (6000% CMP coverage). The source was Vibroseis (4 vibrators, each with 44,000 lb peak force). At each source location (shot point) each vibrator would vibrate eight times moving by 7.14 m (drag) each time and thus the generated output signal from each vibrator consisted of eight linear sweeps (14 s, 10~56 Hz). The recorded data were 18 s long with 4 ms sampling rate.

The 3-D reflection experiment covered a 12 Km x 12 km area. The three-dimensional grid of CMPs after bin stacking with 100 m x 100 m bins resulted into a 121 x 121 grid (800 %). The long offset expanding spread experiment was performed in four stages during the normal recording of the regular 2-D data using 480 channel geometry and acquired offsets of 48 Km long.

#### E.2 PROCESSING AND IMAGING

The data were processed by Pulsonic Geophysical Ltd. with a standard processing stream for the entire data set similar to that used in conventional seismic data processing for hydrocarbon exploration targets. This processing flow included deconvolution, spectral

balancing, refraction static corrections, surface consistent residual statics, muting, velocity analysis, normal moveout correction, CDP stacking, finite difference migration and filtering.

Additional processing of the data was performed by the Seismology Laboratory that included normalization, depth migration and filtering. Prior to migration the data were normalized (amplitude and time) to the Second White Specs (Rong et al., 1994), padded on both sides of the section and tapered on the bottom of the section. The 2-D  $\omega$ - $x$  finite difference depth migration algorithm developed in this thesis was used for the migration of three profiles (lines) of the 2-D reflection experiment. The optimal depth step used after taking into account large dips, the velocity function, sampling interval in time and space and the frequency content of the data, was 10 m. The CDP spacing was 25 m.

Our migration succeeded in imaging the geologic structure very well. It focussed the energy of dipping layers sharply at the Precambrian and Cambrian unconformities. The main reflectors along with number of faults are clearly imaged. Also, the depth migrated profiles revealed a number of anomalies including basement-cover interactions and lateral amplitude changes (Rong et al., 1994). The discovery of these anomalies is important in understanding the structural formation and deformation of the Precambrian rocks during the last 600 million years. Figure E.1 shows portions of the depth migrated sections that image clearly the structure down to depths of 5 Km. Furthermore, migration of the 18 s long sections images the structure of the earth underneath central Alberta to depths of 50 Km and the crust/mantle boundary (Moho) at about 40 Km depth.

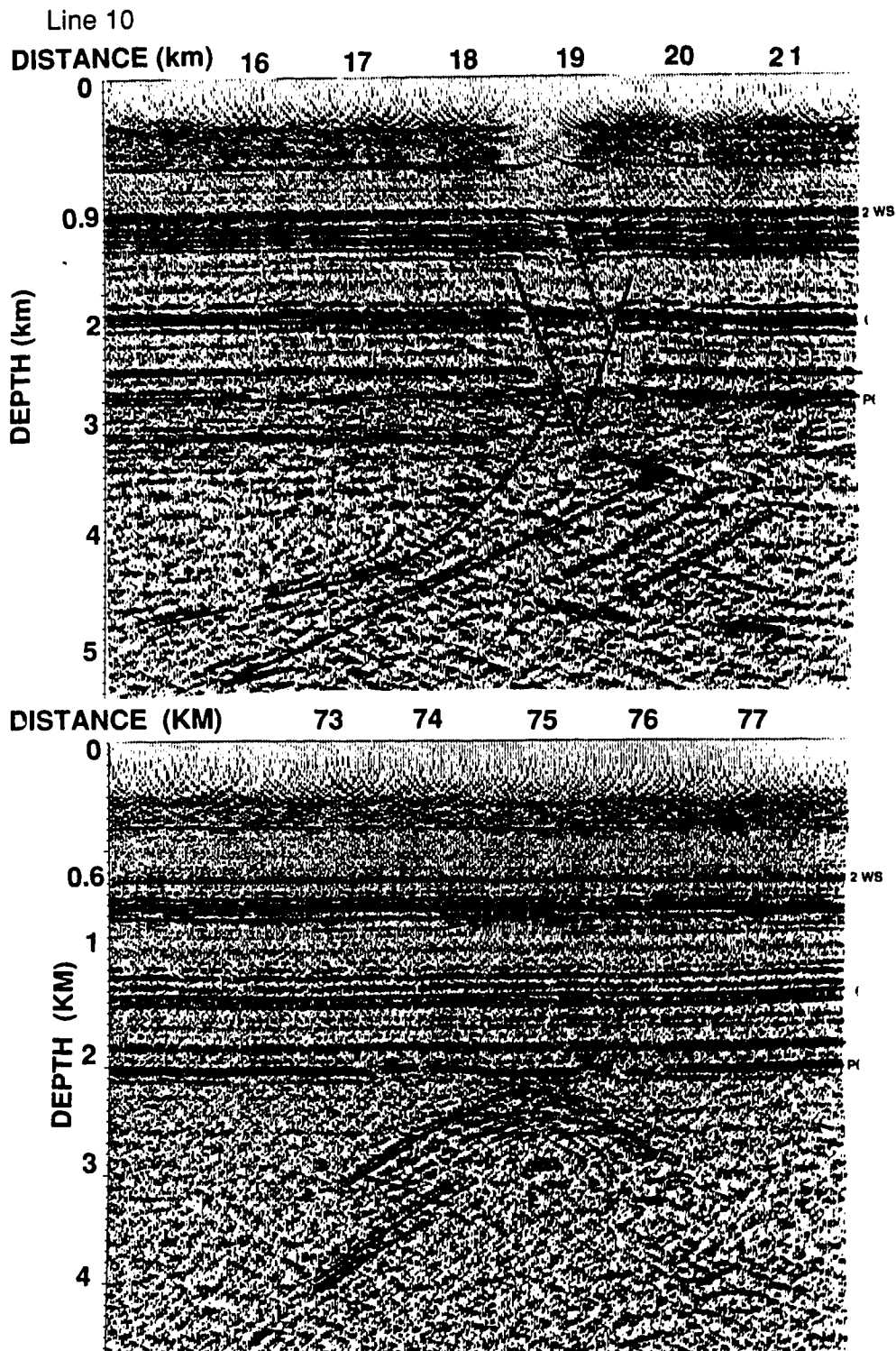


Figure E.1: Portions of the depth migrated line 10 (LITHOPROBE Alberta Basement transect) with interpretation (Seismology Laboratory, University of Alberta)